UNIVERSITY OF CALIFORNIA

Santa Barbara

The Chemical Composition of the Continental Crust: Investigations of Major Elements and Halogens

A dissertation submitted in partial satisfaction of the requirements for the degree Doctor of Philosophy in Earth Science

by

Peng-Yuan Han

Committee in charge:

Professor Roberta L. Rudnick, Chair

Professor Matthew G. Jackson

Professor Francis A. Macdonald

June 2025

The dissertation of Peng-Yuan Han is approved.

_____

Francis A. Macdonald

_____

Matthew G. Jackson

_____

Roberta L. Rudnick, Committee Chair

May 2025

The Chemical Composition of the Continental Crust:

Investigations of Major Elements and Halogens

ACKNOWLEDGEMENTS

The dissertation marks the end of a long journey—one I couldn't have completed without the help and support of so many people.

First and foremost, I would like to thank my advisor, Roberta Rudnick, for her unwavering support and guidance throughout my PhD. I am particularly thankful for her patience in helping me improve my pronunciation, her encouragement during difficult and challenging times, the trips and hikes we took to appreciate the beauty of nature, the space she gave me to engage in open and thoughtful discussions, and her generous sharing of wisdom and life lessons. I truly believe that the mentorship she provided will continue to shape my future—both professionally and personally.

My appreciation also extends to my committee members, Matthew Jackson and Francis Macdonald. Their expertise in the field, sharp questions, and insightful feedback consistently pushed me to re-examine the assumptions and approaches used in our research, as well as to consider its broader geological implications. This experience has taught me to approach geological processes from multiple perspectives and has helped me become a more critical and creative thinker.

I would also like to acknowledge the faculty at UCSB who have shaped my academic journey. Matthew Rioux is a beloved instructor and mentor. I have learned so much from his classes, not only as a student but also as a teaching assistant working alongside him for many quarters. The interactions with other faculty members like John Cottle, Phil Gans, Douglas Wilson, Lorraine Lisiecki, and Susannah Porter have also been very enriching. Further thanks to the department staff (Yann Ricard, Quinlan Dougherty, Jaima Ortega, Patricia

Machuca, Jorge Pichardo, Todd Penniman, Shannon Dalton, and Alicia Magallanes) for their logistical support.

Many friends and students have also warmed my life here, especially Francisco Apen, Judy Pu, Mary Ringwood, Lindsay Buff, Ruixia Bai, Yifan Du, Suoya Fan, Lingyu Zhao, and Kunlong Liu. I have also been very fortunate to work with brilliant undergraduate students: Jacquie Hoot, Madison Huising, and Ruben Underwood-Aguilar, whose curiosity, enthusiasm, and dedication continually inspired me. Last but not the least, Dr. Murphy (Roberta's dog), thank you for bringing much-needed comfort and joy along the way.

I am also indebted to my collaborators. In particular, I would like to thank Zhao-Chu Hu, Jaime Barnes, Michael Marks, Tao He, and Kang Chen for their help in funding acquisition, data analysis, and stimulating discussions. If possible, please forgive me for sending so many samples for analysis, and thanks sincerely for your patience, support, and generous assistance throughout the process. I also extend my thanks to Richard Gaschnig, Shui-Jiong Wang, Fernando Bea for sharing samples/data and providing valuable insights into the projects.

I must express my deepest thanks to Shan Gao (1962–2016), my master's advisor. I am profoundly grateful for the passion he instilled in me for continental geochemistry. I would not be on this journey without him. I am also grateful to other members of the group at that time, especially Yong-Sheng Liu, Zhao-Chu Hu, Ming Li, Jing-Liang Guo, Kang Chen, and Gui-Rong Hu. Thank you very much for all your support and companionship during that difficult time.

Lastly, I owe everything to my family, my mom (1971–2007), my dad, and my brother. Thank you for all the love you have given me, which has shaped who I am today. Mom, we are all doing well down here, and I hope you are doing great too. Miss you so much!

VITA OF PENG-YUAN HAN

May 2025

EDUCATION

2019–2025 Ph.D. Earth Science, University of California, Santa Barbara

2014–2017 M.S. Geochemistry, China University of Geosciences, Wuhan

2010–2014 B.Sc. Geology, China University of Geosciences, Wuhan

PROFESSIONAL EMPLOYMENT

2019–2025 Teaching Assistant and Graduate Student Researcher, UC Santa Barbara

2017–2019 Research Assistant, China University of Geosciences, Wuhan

2014–2017 Graduate Student Researcher, China University of Geosciences, Wuhan

2013–2014 Undergraduate Researcher, China University of Geosciences, Wuhan

AWARDS & FELLOWSHIPS

George Tunell Endowed Fellowship, UC Santa Barbara (2024)

Harry Glicken Memorial Graduate Fellowship, UC Santa Barbara (2023)

Richard and Eleanor Migues Field Research Prize, UC Santa Barbara (2023)

Goldschmidt Travel Grant, Geochemical Society (2022)

George Tunell Endowed Fellowship, UC Santa Barbara (2022)

Coast Geological Society Scholarship Award, Coast Geological Society (2021)

Outstanding Thesis Award, China University of Geosciences, Wuhan (2017)

Excellent Graduate Student, China University of Geosciences, Wuhan (2016)

Excellent Zhoukoudian Fieldtrip Intern, China University of Geosciences, Wuhan (2012)

TEACHING

**Outstanding Teaching Assistant Award, UCSB Academic Senate, 2023 (nominated)

**Undergraduate's choice Teaching Assistant, UCSB Earth Science, 2021, 2022

Earth 102C: Metamorphic Petrology, 2021S and 2023S, UC Santa Barbara

Earth 104A: Field Studies in Geological Methods, 2022S, UC Santa Barbara

Earth 114: Geomaterials, 2019F, 2020F, 2021F, and 2022F, UC Santa Barbara

Earth 115: Analytical Methods in Geomaterials, 2021W, UC Santa Barbara

Earth 124IG: Introduction to Geochemistry, 2020W, UC Santa Barbara

Earth 177: Ore Deposits, 2022W, UC Santa Barbara

MENTORING

Madison Huising, Senior thesis, co-supervise (w/ Prof. Rudnick), 2023–2024

Ruben Underwood-Aguilar, Senior thesis, co-supervise (w/ Prof. Rudnick), 2023–2024

Jacquie Hoot, Senior thesis, co-supervise (w/ Prof. Rudnick), 2021–2022

PUBLICATIONS

Han, P.Y., Husing, M. Rudnick, R.L., Barnes, J.D., Marks, M.A.W., He, T., Bea, F., Hu, Z.C., Halogen behavior during high-grade metamorphism and partial melting in the deep continental crust (Ivrea Zone, NW Italy). *In Prep. for Earth and Planetary Science Letters.*

Han, P.Y., Chen, K., Rudnick, R.L., Hu, Z.C., Average major element composition of the upper continental crust derived from an integrated study of sedimentary and igneous rocks. *Under review at Geochimica et Cosmochimica Acta*.

Han, P.Y., Rudnick, R.L., Hu, Z.C., Marks, M.A.W., He, T., Chen, K., Halogen (F, Cl, Br, and I) enrichments on the continental surface: a perspective from loess. *Geochemical Perspective Letters*, 32, 52–57.

Han, P.Y., Rudnick, R.L., He, T., Marks, M A.W., Wang, S.J., Gaschnig, R.M., Hu, Z.C. (2023). Halogen (F, Cl, Br, and I) concentrations of the upper continental crust through time as recorded in ancient glacial diamictite composites. *Geochimica et Cosmochimica Acta*, 341, 28–45.

Han, P.Y., Guo, J.L., Chen, K., Huang, H., Zong, K.Q., Liu, Y.S., Hu, Z.C., Gao, S. (2017). Widespread Neoarchean (~ 2.7–2.6 Ga) magmatism of the Yangtze craton, South China, as revealed by modern river detrital zircons. *Gondwana Research*, 42, 1–12.

CONFERENCE ABSTACTS

Han, P.Y., Chen, K., Rudnick, R.L., Hu, Z.C., A new estimate of major elements in the average upper continental crust: a holistic study of igneous and sedimentary rocks with implications for surface processes evolution, Goldschmidt conference, Prague, 2025.

Huising, M., **Han, P.Y.**, Rudnick, R. L., Bea, F., He, T., Hu, Z.C., Marks, M.A.W., Behavior of halogens (F, Cl, Br, and I) during medium- to high-grade metamorphism: evidence from the Ivrea-Verbano Zone, Italian Alps, Goldschmidt conference, Chicago, 2024.

Han, P.Y., Rudnick, R.L., Hu, Z.C., He, T., Marks, M.A.W., Chen, K., Halogen (F, Cl, Br, and I) systematics in loess: Implications for halogen enrichments at Earth's land surface, AGU Fall meeting, San Francisco, 2023.

Han, P.Y., Rudnick, R. L., He, T., Marks, M.A.W., Wang, S.J., Gaschnig, R.M., Hu, Z.C., The role of continental crust in the global halogen cycle: Insights from halogen concentrations (F, Cl, Br, and I) of ancient glacial deposits, Goldschmidt conference, Hawaii, 2022.

Han, P.Y., Guo, J. L., Gao, S., Dominant 2.6–2.7 Ga magmatism in the Kongling terrane and its implication for Neoarchean evolution of the Yangtze craton, South China. AGU Fall meeting, San Francisco, 2016.

Han, P.Y., Guo, J.L., Chen, K., Huang, H., Gao, S., Widespread 2.6–2.7 Ga magmatism in the Yangtze craton. China Geoscience Union meeting, Beijing, 2016.

ABSTRACT

The Chemical Composition of the Continental Crust:

Investigations of Major Elements and Halogens

by

Peng-Yuan Han

The continental crust is an important geochemical reservoir, and its average composition provides critical insights into the processes of its formation, crust-mantle recycling, and interactions with other reservoirs such as the atmosphere, oceans, and mantle. However, due to its inherent heterogeneity, the existing estimates are subject to significant uncertainties, whether for major or trace elements. By systematically examining element concentrations and ratios in crustal igneous, sedimentary, and select metamorphic rocks, I reevaluated the concentrations of major elements and halogens in the continental crust, as well as their behavior during geological processes related to crust formation, differentiation, and evolution.

Chapter I presents a study focusing on the major elements of the upper continental crust (UCC). Based on a suite of newly analyzed loess samples, as well as compiled data from fine-grained siliciclastic sedimentary rocks (loess, glacial diamictites, and shales) and a large dataset of continental igneous rocks, this study explored a new approach to estimate the major element composition of the UCC. Compared to previous methods, this new approach

avoids biases such as oversampling of mafic rocks when averaging igneous rocks and the incorporation of weathering signatures in estimates based on sedimentary rocks and/or large-scale sampling. The new results confirm an evolved, granodiorite composition for the UCC and also suggest that continental weathering exerts a significant control on seawater composition for many elements.

Chapter II focuses on the analysis of halogen (F, Cl, Br, and I) concentrations in a suite of ancient glacial diamictite composites. With systematically low I concentrations in most composites, these samples are inferred to have predominantly sampled the crystalline bedrocks. Based on linear correlations between halogens and other elements, a new estimate for the present-day crystalline UCC is derived. The new results are used to quantify magmatic degassing during continental formation and the loss of Cl from continents through chemical weathering. Further calculations suggest that weathering alone is insufficient to account for the Cl inventory in the oceans, which may instead be primarily derived from mantle outgassing and/or late volatile accretion.

Chapter III examines halogen (F, Cl, Br, and I) concentrations in a set of worldwide loess samples. With systematically higher concentrations than those of glacial diamictite composites, the loess samples reflect a systematic enrichment of halogens on the continental surface, with estimated enriched following the trend: $F \approx Cl < Br << I$. Additionally, the halogen ratios (Br/Cl, I/Cl, and Br/I) of loess samples are similar to those of organic-rich soils/sediments but distinct from those of glacial diamictites, suggesting that another process (beyond biological influence) may be responsible for fractionating halogens in the glacial diamictites. Using a mixing model, it is estimated that the materials composing loess are predominantly (>80–90%) sourced from crystalline bedrocks.

Chapter IV investigates the behavior of halogens (F, Cl, Br, I, and Cl isotopes) during high-grade metamorphism and partial melting in the deep continental crust, based on a well characterized suite of samples from the Ivrea Zone, Northwestern Italy, which experienced amphibolite- to granulite-facies metamorphism. The results show that F, I, and possibly Br are lost during prograde metamorphism. By contrast, Cl appears to be influenced by the input of externally derived Cl-rich fluids during granulite-facies metamorphism, possibly introduced by underplating magmas. These halogens, present in the lower continental crust, may have played a crucial role in the formation of granitic magmas, thereby contributing to the differentiation of the continental crust.

Contents

Introduction

Earth is unique in the solar system, distinguished by its bimodal topography, which features a thin, dense, mafic oceanic crust and a relatively thick, buoyant, and more differentiated continental crust with an average "andesitic" composition (Taylor and McLennan, 1985; Rudnick and Gao, 2003). In contrast to the oceanic crust, which is continuously recycled by plate tectonics and is ≤ 200 Ma, the continental crust has largely survived subduction due to its greater chemical buoyancy, preserving rocks dating back as far as 4 billion years (Bowring and Williams, 1999; Wilde et al., 2001). Throughout Earth's history, the continental crust has undergone significant secular changes, not only in the mechanism(s) responsible for its formation, but also in its chemical composition (e.g., Taylor and McLennan, 1985; Hawkesworth et al., 2010; Cawood et al., 2013; Tang et al., 2016). Additionally, it has extensively interacted with other reservoirs, including the atmosphere, oceans, and mantle, playing a crucial role in global geochemical cycles and shaping Earth's habitability (e.g., Amiotte Suchet et al., 2003; Willbold and Stracke, 2006; Jackson et al., 2007; Gaschnig et al., 2014; Macdonald et al., 2019).

The average composition of the continental crust provides a useful baseline for evaluating the above processes, and studying the abundances and distributions of elements in Earth's crust has been an ongoing endeavor since the first rock analyses (Clarke, 1889). However, this task is far from simple—if not nearly impossible—given the inherent heterogeneity in rock distribution and composition, even in its most accessible part, the upper continental crust (UCC). To address these challenges, researchers have employed various methods, including averaging igneous rocks (e.g., Clarke, 1889; Clarke and Washington, 1924; Pease et al., 2023), analyzing fine-grained sediments such as glacial tills, shales, loess, mud-rocks,

and river sediments (e.g., Goldschmidt, 1933; Nance and Taylor, 1976; Taylor et al., 1983; Kamber et al., 2005; Bayon et al., 2015; Gaschnig et al., 2016), conducting large-scale sampling of exposed rocks in specific regions (e.g., Shaw et al., 1967; Fahrig and Eade, 1968; Ronov and Migdisov, 1970; Gao et al., 1998; Borodin, 1999), and using various model-based calculations (e.g., Ronov and Yaroshevsky, 1976; Ronov et al., 1991; Condie, 1993; Borodin, 1999; Sammon and McDonough, 2021). Through these efforts, significant advances have been made in constraining the average composition of the UCC, though notable uncertainties remain (Rudnick and Gao, 2003 and references therein).

Among the estimates for the UCC, major elements are generally considered well-constrained, with values obtained from different methods generally consistent with each other. By compiling and averaging previously reported values, Rudnick and Gao (2003) derived a new estimate, with most previous values falling within 20% of it. However, this estimate still carries significant uncertainty originating from earlier studies, including analytical errors, local heterogeneity, and assumptions underlying various UCC models. The significant uncertainties in existing UCC estimates also leave some fundamental questions inadequately addressed: What is the end product of magmatic differentiation in the continental crust (or the average igneous composition of the UCC)? How much sedimentary rock is contained within the UCC? And how does continental weathering influence the composition and evolution of the continental crust?

Chapter I re-evaluates the average major element composition of the UCC. Based on a suite of newly analyzed loess samples (n = 139) from around the globe, as well as compiled data for fine-grained siliciclastic sedimentary rocks (loess, glacial diamictites, and shales) and a large dataset of continental igneous rocks, we propose a new compositional estimate

for the average UCC, with uncertainties of <5% (two standard errors) for all major elements. This new estimate aligns well with elemental trends observed in fine-grained sedimentary rocks, particularly in loess, demonstrating efficient mixing in loess relative to shales and glacial diamictites. Compared to previous studies, this new approach avoids biases such as oversampling of mafic rocks when averaging igneous rocks and the incorporation of weathering signatures in estimates based on sedimentary rocks and/or large-scale sampling. The new results confirm the evolved, granodioritic composition of the UCC. From mass balance, the contribution of sediments to the UCC (whether contained in the sedimentary cover or incorporated into the crystalline bedrocks) is estimated to be less than 40%, suggesting that the UCC maintains a predominantly igneous composition despite modifications over geologic history. The solubility of major elements during continental weathering is ranked as (Ca, Na, Mg) > (K, Mn, P) >> (Si, Ti, Fe, Al), exerting a significant control on seawater chemistry for many elements.

In addition to major elements, the average concentrations of trace elements in the UCC is also subject to considerable uncertainties, particularly for elements that are not routinely analyzed, such as platinum-group elements, chalcophile elements, and halogens (Rudnick and Gao, 2003; Hu and Gao, 2008; Gao, 2010; Chen et al., 2016). Halogens, an important group of lithophile and volatile elements, are known to profoundly influence Earth's habitability (e.g., Clay et al., 2017; Kendrick et al., 2017; Broadley et al., 2018b; Kendrick, 2024). Additionally, because halogens preferentially partition into aqueous fluids and organic matter (especially Br and I), relative to silicate minerals and melts, they can serve as useful tracers of various geological processes, including magmatic degassing (Bureau et al., 2000; Balcone-Boissard et al., 2010), metamorphic devolatilization (John et al., 2011; Kendrick et

al., 2013; Pagé et al., 2016; Beaudoin et al., 2024), chemical weathering (Han et al., 2023), and/or biological activity (Fehn et al., 2006; Muramatsu et al., 2007; Han et al., 2024).

The role of the continental crust in the global halogen cycle remains poorly understood, partly due to the lack of high-quality compositional data for halogens in crustal rocks. Prior to my work, there are only four independent estimates of halogen concentrations in the UCC (Shaw et al., 1967; Wedepohl, 1995; Gao et al., 1998; Muramatsu and Wedepohl, 1998) and three estimates for the lower continental crust (Wedepohl, 1995; Gao et al., 1998; Muramatsu and Wedepohl, 1998), with difference among different the estimates varying by up to a factor of ~10. To address this gap, halogen concentrations in the fine-grained matrix of glacial diamictite composites (Chapter II) and loess (Chapter III) were determined using two advanced analytical methods: (1) combustion ion chromatography (C-IC) analysis for F, Cl, and Br (Epp et al., 2019), and NH_4HF_2 digestion and ICPMS analysis (N-ICPMS) for Cl, Br, and I (He et al., 2019). These analyses were used to estimate halogen abundances in the UCC and to investigate their behavior during chemical weathering and biological enrichment. Chapter IV also examined halogen concentrations and chlorine isotopic composition of metamorphic rocks from the Ivrea Zone (Alps, Northwest Italy), a cross-section through the middle to lower continental crust, to investigate halogen behaviors during high-grade metamorphism and partial melting.

Chapter I. Average Major Element Composition of the Upper Continental Crust Derived from An Integrated Study of Sedimentary and Igneous Rocks

Under review at *Geochimica et Cosmochimica Acta* in 2025

With co-authors Kang Chen[2], Roberta L. Rudnick[1], Zhao-Chu Hu[2]

[1]Department of Earth Science and Earth Research Institute, University of California - Santa Barbara, Santa Barbara, CA 93106, USA

[2]State Key Laboratory of Geological Processes and Mineral Resources, China University of Geosciences, Wuhan, 430074, PR China

Abstract

A systematic analysis of the compositions of fine-grained sedimentary rocks (loess, glacial diamictites, and shales) and a large dataset of continental igneous rocks was conducted to determine the major element composition of the average upper continental crust (UCC). Starting from a restricted range of Al_2O_3 in crustal igneous rocks and by exploring the elemental relationships (their concentrations and ratios) in both sedimentary and igneous rocks, we derive a new estimate with associated two standard errors for the major element composition of the UCC: SiO_2 = 63.55 ± 0.62 wt.%, TiO_2 = 0.74 ± 0.03 wt.%, Al_2O_3 = 15.24 ± 0.51 wt.%, FeO_T = 5.26 ± 0.20 wt.%, MnO = 0.10 ± 0.01 wt.%, MgO = 2.54 ± 0.10 wt.%, CaO = 4.84 ± 0.19 wt.%, Na_2O = 3.35 ± 0.11 wt.%, K_2O = 3.06 ± 0.11 wt.%, P_2O_5 = 0.22 ± 0.01 wt.%, and LOI = 1.10 ± 0.04 wt.%. The new estimate is consistent with the element correlations and ratios observed in sedimentary rocks, though the signals in such rocks can be affected by varying degrees of chemical weathering and/or mineral sorting. Compared to previous estimates, our new estimate has lower compatible element concentrations (e.g., TiO_2, CaO, FeO_T, MnO, and MgO) than those derived from averaging igneous rocks, but higher soluble element concentrations (e.g., Na_2O, CaO, and P_2O_5) than those obtained by large-scale surface sampling. These differences could reflect biases in earlier approaches: averaging igneous rocks may oversample mafic rocks, while large-scale surface sampling may be affected by local heterogeneity and chemical weathering. Overall, our new methodology should provide a more accurate estimate of the average igneous UCC composition. The new results confirm the evolved, granodioritic composition of the UCC. Based on the mass balance between the igneous UCC composition proposed here and previous UCC estimates that incorporated sedimentary rocks (e.g., estimates based on large-

scale sampling), the contribution of sediments to the UCC—whether contained in the sedimentary cover or incorporated into crystalline bedrocks—is typically less than 40%. This suggests that the UCC maintains a predominantly igneous composition despite modifications over geological history. We estimate the solubility of major elements during chemical weathering as (Ca, Na, Mg) > (K, Mn, P) >> (Si, Ti, Fe, Al), which exerts a significant control on seawater chemistry for many elements.

1.1. Introduction

The continental crust is a unique feature of Earth, characterized by a relatively differentiated composition and a history dating back approximately 4 billion years (e.g., Taylor and McLennan, 1985; Rudnick and Gao, 2003; Hawkesworth et al., 2010). It was primarily formed by melts derived from Earth's mantle that were generated in both arc and intraplate settings, and later modified by crustal recycling, chemical weathering, and metamorphism (Taylor and McLennan, 1985; Rudnick, 1995). Tectonic activity also continuously alters the volume and mass of the continental crust through processes such as arc accretion, lower crustal delamination (or foundering), and/or relamination, along with the cyclical assembly and breakup of supercontinents (e.g., Kay and Kay, 1993; Bradley, 2011; Hacker et al., 2011). Via these processes, the continental crust has undergone extensive geochemical exchange with Earth's other reservoirs, such as the atmosphere, oceans, and mantle, playing a crucial role in the global geochemical cycle and in regulating Earth's habitability. An essential step in gauging the relative influence of these processes is to obtain an accurate estimate of the average composition of the continental crust. This goal has been a persistent pursuit for generations of geochemists since the pioneering work of Clarke (1889).

The continental crust has an average thickness of ~40 km and is bounded by the lithospheric mantle at the Mohorovicic discontinuity. It is generally thought to gradually transition from more mafic compositions at the base to more felsic ones at the surface. Accordingly, the continental crust is often divided into either two layers (upper and lower crust) (e.g., Taylor and McLennan, 1985; Wedepohl, 1995; Hacker et al., 2011) or three layers (upper, middle, and lower crust) (e.g., Rudnick and Fountain, 1995; Mooney et al., 1998; Rudnick and Gao, 2003). Another inherent characteristic of Earth's continental crust is

its heterogeneity, both vertically and horizontally, which makes it challenging to derive a meaningful average composition, even for its most accessible part, the upper continental crust (UCC).

Despite the challenges, significant progress has been made over decades of research in estimating the continental crust's composition, although considerable uncertainties persist in existing models (Rudnick and Gao, 2003 and references therein). For the major element composition of the UCC, which is the focus of this study, there are four primary approaches to determining its average composition: (1) averaging the composition of igneous rocks, (2) using the geochemistry of fine-grained siliciclastic sediments and sedimentary rocks, (3) large-scale sampling, and (4) miscellaneous calculations. These approaches are briefly reviewed below:

(1) *Averaging igneous rocks*. This method was first utilized by Clarke (1889) as the initial effort to systematically estimate the composition of Earth's crust. Assuming the crust to be a solid outer shell cooled from deeply derived magma, Clarke believed that Earth's crust (essentially what we now refer to as the UCC) was "made up almost wholly of igneous rocks" (Clarke and Washington, 1924). Thus, his calculations are primarily based on igneous rocks (both volcanic and plutonic), along with some metamorphic rocks like gneiss and schist, while explicitly excluding sedimentary rocks (Clarke, 1889; Clarke and Washington, 1924). This approach was recently expanded upon by Pease et al. (2023), who derived a new UCC compositional model based on a larger dataset of continental igneous rocks compiled by Keller and Schoene (2012), as well as incorporating geophysical constraints from seismic data.

(2) *Using the geochemistry of fine-grained siliciclastic sediments and sedimentary rocks*. This method is based on the concept that sedimentation processes can average wide areas of exposed crust. Originally, this approach was introduced using glacial loams (Goldschmidt, 1933), but later extended to fine-grained sedimentary rocks, such as shales (Nance and Taylor, 1976; Gromet et al., 1984), loess (Taylor et al., 1983; Gallet et al., 1998; Chauvel et al., 2014; Xiao et al., 2022), alluvial sediments (Kamber et al., 2005; Bayon et al., 2015), and glacial diamictites (Canil and Lacourse, 2011; Gaschnig et al., 2016). However, due to the potential loss of soluble elements (e.g., Ca, Na, and Mg) from siliciclastic sedimentary rocks, estimates obtained from this approach essentially represent the eroded/weathered UCC, rather than the crystalline bedrocks, as demonstrated by Kamber et al. (2005), Bayon et al. (2015), and Gaschnig et al. (2016). In this sense, analyses of such rocks provide insights only into the concentrations of insoluble elements (e.g., Ti, Al, Fe, La, Th) in the crystalline UCC (e.g., Taylor and McLennan, 1985; McLennan, 2001; Hu and Gao, 2008).

(3) *Large-scale sampling*. This approach is similar to the first one but includes sedimentary rocks. Large-scale sampling and weighted averaging of the wide variety of rocks exposed in a given area can provide a useful estimate of the area's average composition. Large-scale sampling campaigns were popular in the 1960s–1990s and have been conducted in North America (Canadian shield, Shaw et al., 1967; Fahrig and Eade, 1968), Europe (Baltic and Ukrainian shields, Ronov and Migdisov, 1970), and Asia (Eastern China and Japanese arc, Gao et al., 1998; Togashi et al., 2000). Of these studies,

the results from the Canadian shield are most widely used in other UCC compositional models (e.g., Taylor and McLennan, 1985; Wedepohl, 1995). However, it remains an open question how representative these results are for the global present-day UCC, especially when considering the disparities among estimates from different regions (Fig. 1b).

(4) *Miscellaneous calculations*. Some studies derived their UCC compositional models based on previously reported data and various assumptions. These assumptions could be based on either map distributions of different rock types, crustal structure, tectonic settings, or the depth extent of weathered UCC (e.g., Ronov and Yaroshevsky, 1976; Ronov et al., 1991; Condie, 1993; Borodin, 1999; Yaroshevsky, 2006; Sammon and McDonough, 2021). Also, the most cited compositional model, from Rudnick and Gao (2003), is an average of the existing models (derived from different approaches) before 2003. Such estimates carry not only the uncertainties from the original analyses, but also those introduced from model assumptions, and therefore, should be used with caution.

Different average UCC compositional models derived from various approaches are summarized in Table 1 and shown in Fig. 1. The results for the global subducting sediments (GLOSS) are also included, as they represent the average composition of trench sediments primarily eroded from the UCC and thus offer valuable insights into the composition of the continental crust (Plank and Langmuir, 1998; Plank, 2014). These previous UCC estimates vary significantly, demonstrating the challenge in estimating the composition of the UCC. Additionally, a careful examination of these estimates and approaches reveals significant

variations in the UCC definitions from different studies (see Table 1). Some studies focus primarily on the igneous component of the UCC (as exemplified by the first approach), while others emphasize the weathered/eroded UCC (as in the second approach). Estimates derived from large-scale sampling or model calculations that include variable proportions of igneous and sedimentary rocks also implicitly incorporate a chemical weathering signature in their compositional models. This complicates our ability to quantitatively analyze the processes governing the formation and evolution of the continental crust and its interaction with other geochemical reservoirs like Earth's atmosphere, oceans, and mantle.

In this study, we report the major element composition of a new set of loess samples collected from four continents (Europe, Asia, North America, and South America). By systematically examining elemental concentrations and ratios within these data, as well as those previously reported for sedimentary (e.g., loess, glacial diamictites, and shales) and continental igneous rocks, we propose a new framework for estimating the average composition of the UCC.

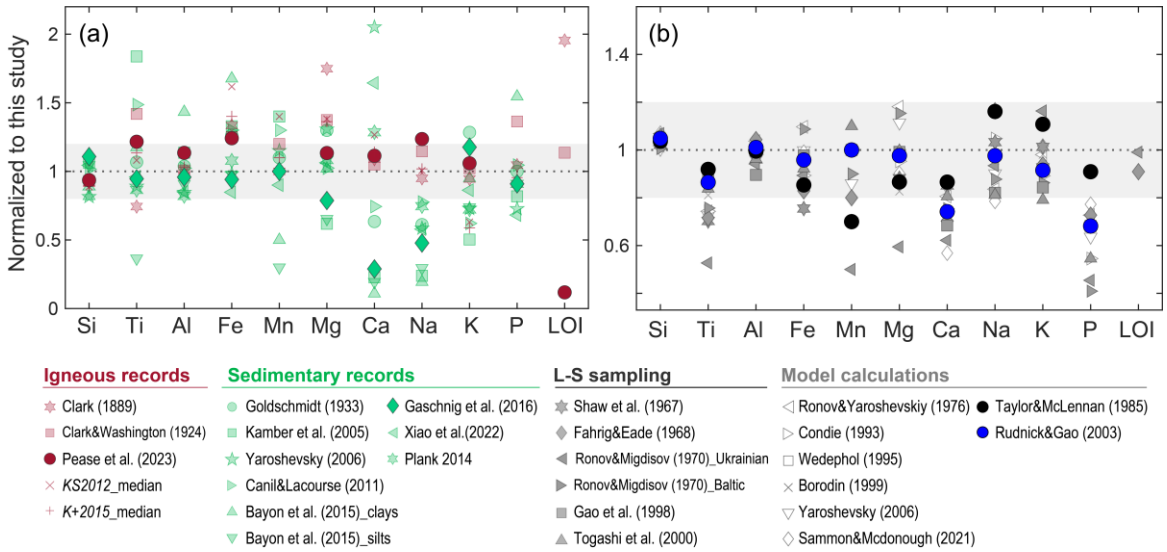

Fig. 1. Previous UCC estimates normalized to the estimate provided in this study (see Table 1). (**a**) UCC estimates obtained from igneous (red symbols) and sedimentary (green symbols) rocks. (**b**) Estimates based on large-scale (L-S) sampling (gray symbols) and model calculations (open symbols, except for those of Taylor and McLennan (1985) and Rudnick and Gao (2003)). The dashed line represents estimates from this study, and the gray horizontal band is 20% uncertainty.

Table 1. Summary of previous UCC estimates

Group and references	Sampling/calculation method	UCC definition	SiO_2 wt.%	TiO_2 wt.%	Al_2O_3 wt.%	FeO_T* wt.%	MnO wt.%	MgO wt.%	CaO wt.%	Na_2O wt.%	K_2O wt.%	P_2O_5 wt.%	LOI% wt.%	Sum wt.%	CIA# -
Averaging igneous records															
Clarke (1889)	Averaging igneous/metamorphic rocks	UCC (igneous)	58.31	0.55	14.76	7.02	0.1	4.44	5.27	3.18	2.89	0.23	2.2	98.9	52.1
Clarke and Washington (1924)	Averaging igneous/metamorphic rocks	UCC (igneous)	59.12	1.05	15.34	6.58	0.12	3.49	5.08	3.84	3.13	0.3	1.3	99.3	49.0
Pease et al. (2023)	Igneous rocks + geophysical constraints	UCC (igneous)	59.5	0.9	17.3	6.53	-	2.88	5.39	4.14	3.24	-	0.1	100.	49.2
Median of *K+2015*@	Median of compiled igneous rocks	UCC (igneous)	56.91	0.84	15.72	7.37	0.11	3.46	5.52	3.41	1.80	0.21	-	95.4	54.3
Median of *KS2012*@	Median of compiled igneous rocks	UCC (igneous)	56.34	0.80	15.19	8.51	0.14	3.51	6.13	3.37	1.93	0.20	1.6	97.7	53.4
Fine-grained sedimentary rocks															
Goldschmidt (1933)	Glacial loams	UCC (weathered)	59.19	0.79	15.82	6.65	0.11	3.3	3.07	2.05	3.93	0.22	3.7	98.8	59.4
Yaroshevsky (2006)	Sediments and lithology model	UCC-sedimentary shell	51.82	0.66	12.89	5.16	0.12	3.32	9.93	1.96	2.23	0.16	11.8	100.	59.4
Kamber et al. (2005)	Alluvial sediments	weathered UCC	67.53	1.36	17.31	6.99	0.14	1.57	1.1	0.8	1.54	0.18	-	98.5	81.2
Canil and Lacourse (2011)	Glacial diamictites	Juvenile UCC (weathered)	64.6	1.1	15.6	6.84	0.13	2.6	3.6	2.6	1.9	0.23	-	99.2	59.7
Bayon et al. (2015)	World river average silts	Eroded UCC	66.44	0.27	13.84	5.14	0.03	1.66	0.94	0.99	2.26	0.84	6.9	99.3	78.2
Bayon et al. (2015)	World river average clays	Weathered UCC	52.09	0.87	21.84	8.82	0.05	2.59	0.53	0.65	2.91	0.34	10.6	101.3	82.6
Gaschnig et al. (2016)	Glacial diamictites (carbonate-filtered)	Weathered UCC	70.4	0.7	14.6	4.95	0.1	2.	1.4	1.6	3.6	0.2	-	99.6	62.0
Xiao et al. (2022)	Loess (China)	UCC (carbonate-bearing)	66.37	0.71	12.98	4.46	0.09	2.7	7.96	1.94	2.64	0.15	-	100.	58.5
Plank and Langmuir (1998)	averaging trench sediments	GLOSS-I&	58.57	0.62	11.91	5.21	0.32	2.48	5.95	2.43	2.04	0.19	10.3	100.	49.2
Plank (2014)	averaging trench sediments	GLOSS-II&	56.6	0.64	12.51	5.67	0.43	2.75	6.22	2.5	2.21	0.2	10.2	99.9	54.2
Large-scale sampling															
Shaw et al. (1967)	Canadian shield	UCC (crystalline + sediments)	64.93	0.52	14.63	3.97	0.07	2.24	4.12	3.46	3.1	0.15	2.4	99.6	49.4
Fahrig and Eade (1968)	Canadian shield	UCC (crystalline + sediments)	65.3	0.53	15.9	4.36	0.08	2.2	3.4	3.9	2.87	0.16	1.	99.7	49.5
Ronov and Migdisov (1970)	Baltic shield	UCC (crystalline + sediments)	63.94	0.56	15.22	5.72	0.09	2.93	3.65	2.94	2.64	0.09	2.	99.8	54.3
Ronov and Migdisov (1970)	Ukrainian shield	UCC (crystalline + sediments)	67.89	0.39	14.35	4.7	0.05	1.51	3.01	3.13	3.56	0.1	1.1	99.8	49.8
Gao et al. (1998)	Eastern China	UCC (crystalline + sediments)	65.46	0.65	13.65	5.14	0.1	2.52	3.31	2.75	2.58	0.15	3.3	99.6	53.3
Togashi et al. (2000)	Japan Arc	UCC (crystalline + sediments)	67.53	0.62	14.67	4.85	0.11	2.53	3.9	2.72	2.42	0.12	-	99.5	55.5
Miscellaneous calculations															
Ronov and Yaroshevsky (1976)	Map-lithology model	UCC (crystalline + sediments)	64.7	0.55	15.8	5.77	0.1	3.	3.9	2.8	3.	0.16	-	99.8	55.7
Taylor and McLennan (1985)	derived from Shaw's work	UCC (crystalline + sediments)	65.89	0.68	15.17	4.49	0.07	2.2	4.19	3.89	3.39	0.2	-	100.2	47.7
Yaroshevsky (2006)	Lithology model	UCC-Granite-metamorphic shell	63.81	0.54	14.92	5.25	0.09	2.83	4.08	3.02	2.84	0.14	2.4	99.9	53.1
Condie (1993)	Map-lithology model	UCC (crystalline + sediments)	66.21	0.55	14.96	4.7	-	2.42	3.6	3.51	2.73	0.12		98.8	50.2
Wedepohl (1995)	derived from Shaw's work	UCC (crystalline + sediments)	64.93	0.52	14.63	3.97	0.07	2.24	4.12	3.46	3.1	0.15	2.4	99.6	49.4
Borodin (1999)	70% shield, 20% orogenic granitoids, and 10% continental margin tonalites	UCC (crystalline)	67.	0.6	15.5	4.93	-	2.1	3.5	3.2	3.	-	-	99.8	51.9
Rudnick and Gao (2003)	averaging previous UCC estimates	UCC (crystalline + sediments)	66.62	0.64	15.4	5.04	0.1	2.48	3.59	3.27	2.8	0.15	-	100.1	52.4
Sammon and McDonough (2021)	1/3 Gaschnig et al. (2016) and 2/3 Rudnick and Gao (2003)	UCC (crystalline + sediments)	68.	0.66	15.1	5.21	0.1	2.29	2.75	2.63	3.11	0.17	-	100.	55.6
	Median of previous UCC estimates:		64.93	0.65	15.17	5.16	0.1	2.53	3.65	3.02	2.87	0.16	2.4	-	53.4
	± 2 s.e.		1.89	0.09	0.64	0.50	0.01	0.26	0.77	0.37	0.22	0.06	1.8	-	3.7

This study	Elemental relationships within igneous and sedimentary rocks	**UCC (igneous)**	**63.55**	**0.74**	**15.24**	**5.26**	**0.10**	**2.54**	**4.84**	**3.35**	**3.06**	**0.22**	**1.10**	**100.**	**51.4**
		± 2 s.e.	**0.61**	**0.03**	**0.51**	**0.20**	**0.01**	**0.10**	**0.19**	**0.11**	**0.11**	**0.01**	**0.04**	**-**	**-**

***** FeO_T: Total ferrous (Fe^{2+}) iron. If ferric (Fe_2O_3) iron was reported in the original study, it was converted to FeO_T by multiplying 0.8998.

[#] CIA = molar Al_2O_3 / (Al_2O_3 + CaO^* + K_2O + Na_2O), where CaO^* is corrected for carbonate and apatite (Nesbitt and Young, 1982). The carbonate correction is based on the approach of McLennan (1993).

[%] LOI: Loss on ignition; when multiple volatile components (e.g., H_2O, CO_2, and S) were reported in previous studies, they were summed into a single LOI value.

[@] Median values of the compiled igneous datasets in this study, *KS2012* and *K+2015*, which are filtered from those reported by Keller and Schoene (2012) and Keller et al. (2015), respectively (see text for details).

[&] GLOSS: global subducting sediment (Plank and Langmuir, 1998; Plank, 2014).

1.2. Samples

Loess is a widespread, wind-blown dust that covers 10% of the continental surface (Muhs and Bettis, 2003). It is dominated by silt-sized particles (2–65 μm) and consists mainly of minerals such as quartz, feldspar, carbonate (calcite and dolomite), mica/clays, as well as various oxides and heavy minerals (Pye, 1995; Smalley, 1995). Here we report the major and selected trace elements for 139 loess samples collected from four continents: Europe (Germany and Switzerland), North America (United States), South America (Argentina), and Asia (China and Kazakhstan). Platinum-group elements and halogen concentrations (F, Cl, Br, I) for some of these samples have been previously reported in Park et al. (2012) and Han et al. (2024), respectively. The latitude and longitude of the loess sections, along with references to the original investigations of these units, are given in Table 2, and sample locations are plotted in Fig. 2. The loess samples from Europe and North America are mainly derived from the periglacial environment, where silts are produced from the mechanical grinding of the crust by either continental or mountain glaciers during the Quaternary period, followed by transport over limited distances by wind (Bettis III et al., 2003; Muhs et al., 2008; Rousseau et al., 2014; Lehmkuhl et al., 2021). In South America, loess is similarly periglacial and was produced through glacial erosion of the Andes, with additional local inputs from volcanic eruptions (Gallet et al., 1998; Schellenberger and Veit, 2006). Loess from Asia (China and Kazakhstan), however, is directly sourced from nearby large desert areas, where the silt is further contributed by high-mountain processes (glacial grinding and/or frost weathering) in the surrounding Central Asian Orogenic Belt and Northwestern Tibetan Plateau (Sun, 2002; Sun et al., 2022; Zhang et al., 2022). Consequently, the Asian loess deposits have been transported over longer distances by wind.

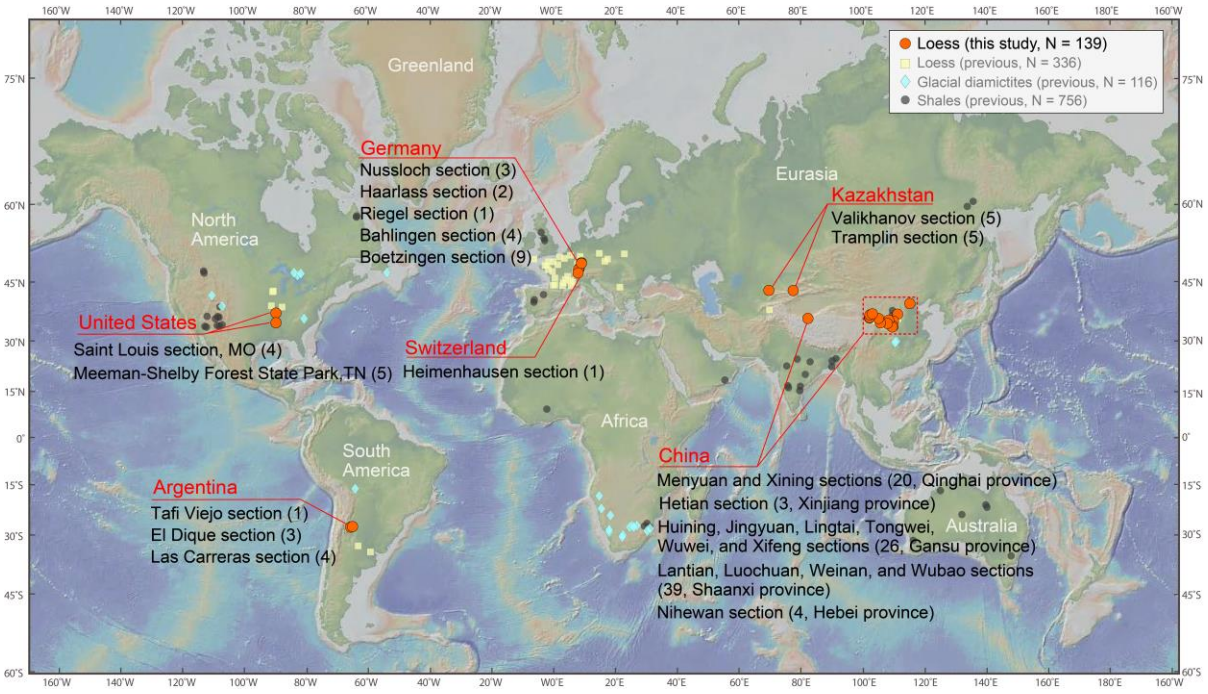

Fig. 2. World map showing the locations of fine-grained sedimentary rocks (loess, glacial diamictites, and shales) for which geochemical data are used in this study. Orange circles represent new loess samples analyzed in this study, with the number in parentheses after each section indicating the number of samples analyzed. Yellow squares and gray circles indicate previously studied loess and shale samples (see supplementary Table S1 for literature sources). Cyan diamonds represent glacial diamictite samples (Gaschnig et al., 2014; 2016).

Table 2. Major element composition of loess samples analyzed in this study

Samples	Locations	Latitude	Longitude	References	SiO_2	TiO_2	Al_2O_3	FeO_T*	MnO	MgO	CaO	Na_2O	K_2O	P_2O_5	LOI	Sum	CIA
					wt.%	wt.%	wt.%	wt.%	wt.%	wt.%	wt.%	wt.%	wt.%	wt.%	wt.%	wt.%	-
11K01	Germany, Riegel	48.145633°N	7.752706°E	Schulze et al. (2022)	46.35	0.41	6.55	2.22	0.08	2.44	19.45	0.73	1.28	0.12	19.7	99.6	64.4
11K02	Germany, Bahlingen	48.126214°N	7.735417°E	Schulze et al. (2022)	52.49	0.44	7.18	2.33	0.08	2.64	15.45	1.24	1.31	0.18	16.7	100.3	57.6
11K03	Germany, Bahlingen	48.126214°N	7.735417°E	Schulze et al. (2022)	69.76	0.65	10.95	3.76	0.11	1.47	3.34	1.42	1.83	0.10	6.0	99.8	62.2
11K04	Germany, Bahlingen	48.126214°N	7.735417°E	Schulze et al. (2022)	46.78	0.38	5.84	2.14	0.07	2.93	19.79	1.05	1.04	0.13	19.4	99.8	56.8
11K05	Germany, Bahlingen	48.126214°N	7.735417°E	Schulze et al. (2022)	47.58	0.39	6.36	2.34	0.07	2.84	18.98	1.00	1.08	0.13	18.6	99.6	59.5
11K06	Germany, Oberschaffhansen Boetzingen hohlweg	48.070461°N	7.704783°E	Schulze et al. (2022)	49.81	0.37	5.96	1.90	0.07	3.29	17.90	1.10	1.15	0.13	17.9	99.8	55.7
11K07	Germany, Oberschaffhansen Boetzingen hohlweg	48.070461°N	7.704783°E	Schulze et al. (2022)	47.62	0.38	6.03	1.96	0.06	3.32	18.78	0.93	1.17	0.12	19.0	99.6	58.9
11K08	Germany, Oberschaffhansen Boetzingen hohlweg	48.070461°N	7.704783°E	Schulze et al. (2022)	46.84	0.39	5.97	2.03	0.07	3.56	19.05	0.89	1.13	0.12	19.2	99.5	59.8
11K09	Germany, Oberschaffhansen Boetzingen hohlweg	48.070461°N	7.704783°E	Schulze et al. (2022)	48.40	0.38	5.92	2.01	0.07	3.36	18.55	0.89	1.12	0.12	19.1	100.2	59.6
11K10	Germany, Oberschaffhansen Boetzingen hohlweg	48.070461°N	7.704783°E	Schulze et al. (2022)	49.81	0.42	6.21	2.11	0.07	3.11	17.59	0.92	1.18	0.12	17.8	99.6	59.8
11K11	Germany, Oberschaffhansen Boetzingen hohlweg	48.070461°N	7.704783°E	Schulze et al. (2022)	48.28	0.39	5.90	2.04	0.07	2.94	18.94	0.87	1.08	0.12	18.6	99.5	60.2
11K12	Germany, Oberschaffhansen Boetzingen hohlweg	48.070461°N	7.704783°E	Schulze et al. (2022)	62.07	0.56	10.36	3.50	0.09	2.05	7.86	1.27	1.75	0.17	9.5	99.6	63.8
11K14	Germany, Oberschaffhansen Boetzingen hohlweg	48.070461°N	7.704783°E	Schulze et al. (2022)	44.13	0.35	5.60	1.87	0.06	1.67	23.39	0.72	1.05	0.13	20.8	100.0	62.8
11K15	Germany, Oberschaffhansen Boetzingen hohlweg	48.070461°N	7.704783°E	Schulze et al. (2022)	59.02	0.50	7.56	2.52	0.09	1.01	13.32	0.84	1.51	0.14	13.0	99.8	64.2
11H01	Germany, Nussloch	49.321783°N	8.70915°E	Antoine et al. (2009)	54.43	0.39	6.26	1.84	0.07	2.85	15.32	1.15	1.39	0.14	15.8	99.9	54.9
11H02	Germany, Nussloch	49.321783°N	8.70915°E	Antoine et al. (2009)	52.76	0.42	6.26	1.88	0.07	3.02	15.99	1.06	1.34	0.13	16.5	99.6	56.6
11H03	Germany, Nussloch	49.321783°N	8.70915°E	Antoine et al. (2009)	53.06	0.40	6.63	1.92	0.07	2.89	15.63	1.24	1.41	0.14	15.9	99.5	54.7
11H04	Germany, Haarlass	49.420917°N	8.728183°E	Jovanovič et al. (2014)	54.37	0.51	7.20	2.37	0.07	2.84	14.51	0.95	1.47	0.13	15.2	99.8	61.2
11H05	Germany, Haarlass	49.420917°N	8.728183°E	Jovanovič et al. (2014)	57.61	0.54	7.35	2.39	0.07	2.51	12.57	1.01	1.50	0.13	13.6	99.6	60.4
VE1	Switzerland, Heimenhausen	47.216667°N	7.7°E	Martignier et al. (2015)	76.99	0.61	10.76	3.07	0.11	1.11	0.53	1.45	1.93	0.11	3.3	100.4	67.5
Peoria-1	USA, Meeman Shelby Forest State Park, TN	35.31701°N	90.061°W	Rodbell et al. (1997)	64.87	0.66	8.18	2.90	0.08	4.06	5.84	1.37	1.84	0.13	9.9	100.1	56.0
Peoria-2	USA, Meeman Shelby Forest State Park, TN	35.31701°N	90.061°W	Rodbell et al. (1997)	63.03	0.60	8.13	2.65	0.07	4.49	6.50	1.39	1.91	0.13	10.7	99.9	55.3
Peoria-3	USA, Meeman Shelby Forest State Park, TN	35.31701°N	90.061°W	Rodbell et al. (1997)	58.53	0.54	7.30	2.29	0.07	5.69	8.26	1.31	1.92	0.12	13.6	99.8	53.6
Peoria-4	USA, Meeman Shelby Forest State Park, TN	35.31701°N	90.061°W	Rodbell et al. (1997)	58.24	0.56	7.53	2.37	0.07	5.92	8.48	1.42	1.82	0.13	13.3	100.1	53.4
Peoria-old	USA, Meeman Shelby Forest State Park, TN	35.31701°N	90.061°W	Rodbell et al. (1997)	57.95	0.53	7.23	2.24	0.07	5.89	8.41	1.27	1.90	0.12	14.0	99.9	54.0
MSL-1	USA, St Louis, MO	37.7485°N	90.0032°W	Wang et al. (2000)	54.65	0.39	6.39	2.32	0.10	5.63	11.11	1.02	1.72	0.09	15.9	99.5	55.2
MSL-2	USA, St Louis, MO	37.7485°N	90.0032°W	Wang et al. (2000)	59.95	0.51	7.53	2.51	0.07	4.79	7.90	1.19	1.89	0.12	12.8	99.5	56.2
MSL-4	USA, St Louis, MO	37.7485°N	90.0032°W	Wang et al. (2000)	54.78	0.43	6.28	2.23	0.07	6.06	10.94	1.10	1.69	0.10	15.7	99.6	53.8
MSL-5	USA, St Louis, MO	37.7485°N	90.0032°W	Wang et al. (2000)	67.25	0.59	8.71	2.94	0.15	3.11	4.87	1.38	2.03	0.15	8.3	99.8	56.8
AS1/3	Argentina, El Dique	26.933333°S	65.683333°W	Schellenberger and Veit (2006)	62.31	0.74	15.09	4.56	0.09	2.18	3.98	2.42	3.10	0.12	5.2	100.3	56.9
AS1/8	Argentina, El Dique	26.933333°S	65.683333°W	Schellenberger and Veit (2006)	61.77	0.74	15.33	4.65	0.09	2.09	4.17	2.44	3.10	0.18	5.4	100.5	57.4
AS1/13	Argentina, El Dique	26.933333°S	65.683333°W	Schellenberger and Veit (2006)	62.98	0.57	14.23	3.67	0.09	1.65	4.46	2.69	3.48	0.18	5.7	100.1	52.9
AS4/A20	Argentina, Las Carreras	26.95°S	65.766667°W	Schellenberger and Veit (2006)	63.17	0.89	16.40	5.38	0.10	1.80	2.15	2.31	3.11	0.30	4.0	100.3	61.3
AS4/A22	Argentina, Las Carreras	26.95°S	65.766667°W	Schellenberger and Veit (2006)	62.89	0.84	16.48	5.43	0.11	1.94	2.42	2.35	3.07	0.25	3.8	100.2	60.0
AS4/A26	Argentina, Las Carreras	26.95°S	65.766667°W	Schellenberger and Veit (2006)	63.49	0.88	16.48	5.36	0.11	1.85	1.97	2.40	3.10	0.14	3.7	100.1	61.0
AS4/A30	Argentina, Las Carreras	26.95°S	65.766667°W	Schellenberger and Veit (2006)	63.46	0.86	16.74	5.42	0.11	1.81	1.87	2.29	3.08	0.12	4.0	100.3	62.1
JU1/19	Argentina, Tafi Viejo	26.733333°S	65.266667°W	Sayago (1995)	65.02	0.76	14.93	4.90	0.10	1.76	2.12	2.01	3.28	0.12	4.8	100.4	59.4
TR688-690	Kazakhstan, Tramplin	43.208511°N	76.933639°E	Feng et al. (2011)	54.96	0.60	11.99	4.02	0.08	2.96	9.31	2.22	2.41	0.16	10.4	99.6	54.7
TR708-710	Kazakhstan, Tramplin	43.208511°N	76.933639°E	Feng et al. (2011)	55.32	0.60	12.03	4.09	0.08	2.98	9.73	2.06	2.40	0.16	10.1	100.0	56.3
TR728-730	Kazakhstan, Tramplin	43.208511°N	76.933639°E	Feng et al. (2011)	56.00	0.61	12.00	4.02	0.08	2.89	8.84	2.18	2.42	0.16	9.9	99.5	55.1
TR748-750	Kazakhstan, Tramplin	43.208511°N	76.933639°E	Feng et al. (2011)	55.94	0.64	12.15	4.12	0.09	2.86	8.90	2.15	2.40	0.16	9.7	99.5	55.7
TR759-760	Kazakhstan, Tramplin	43.208511°N	76.933639°E	Feng et al. (2011)	55.97	0.62	12.03	4.03	0.08	2.86	9.05	2.15	2.44	0.16	9.7	99.5	55.4
VA146-150	Kazakhstan, Valikhanov	43.1749°N	69.317111°E	Feng et al. (2011)	53.78	0.53	10.30	3.40	0.07	2.50	12.27	1.68	2.05	0.14	12.7	99.8	57.2
VA226-230	Kazakhstan, Valikhanov	43.1749°N	69.317111°E	Feng et al. (2011)	56.48	0.58	10.78	3.57	0.07	2.49	10.75	1.74	2.19	0.13	11.1	100.3	57.1
VA351-355	Kazakhstan, Valikhanov	43.1749°N	69.317111°E	Feng et al. (2011)	54.35	0.56	10.71	3.56	0.07	2.59	11.69	1.73	2.14	0.14	11.9	99.8	57.3
VA596-600	Kazakhstan, Valikhanov	43.1749°N	69.317111°E	Feng et al. (2011)	60.74	0.53	10.87	3.27	0.08	2.25	8.34	1.97	2.34	0.13	8.7	99.6	54.6

VA616-620	Kazakhstan, Valikhanov	43.1749°N	69.317111°E	Feng et al. (2011)	57.50	0.54	10.96	3.50	0.08	2.45	9.98	1.79	2.22	0.14	10.3	99.9	57.0
HN0430	China, GanSu, Huining Hepan	36.112528°N	104.858389°E	Ding et al. (1999)	59.19	0.60	11.42	3.82	0.08	2.63	8.16	1.80	2.27	0.15	9.2	99.7	57.8
HN0505	China, GanSu, Huining Hepan	36.112528°N	104.858389°E	Ding et al. (1999)	58.87	0.60	11.56	3.84	0.08	2.65	8.25	1.81	2.36	0.15	9.0	99.6	57.7
HN0515	China, GanSu, Huining Hepan	36.112528°N	104.858389°E	Ding et al. (1999)	58.74	0.60	11.54	3.87	0.08	2.67	8.31	1.83	2.34	0.15	8.9	99.5	57.6
HN1230	China, GanSu, Huining Hepan	36.112528°N	104.858389°E	Ding et al. (1999)	56.87	0.59	11.68	3.96	0.08	2.78	8.96	1.88	2.34	0.14	9.8	99.5	57.3
HN1310	China, GanSu, Huining Hepan	36.112528°N	104.858389°E	Ding et al. (1999)	57.60	0.59	11.80	3.98	0.09	2.74	8.58	1.89	2.39	0.15	9.3	99.6	57.4
CX0280	China, GanSu, Jingyuan Caoxian	36.367228°N	104.622428°E	Che and Li (2013)	60.61	0.58	11.30	3.71	0.08	2.43	7.80	2.20	2.29	0.15	8.1	99.6	53.7
CX0360	China, GanSu, Jingyuan Caoxian	36.367228°N	104.622428°E	Che and Li (2013)	61.05	0.59	11.20	3.67	0.08	2.42	7.66	1.86	2.26	0.16	8.2	99.6	56.8
CX0400	China, GanSu, Jingyuan Caoxian	36.367228°N	104.622428°E	Che and Li (2013)	60.81	0.58	11.17	3.64	0.08	2.42	7.75	1.83	2.26	0.16	8.4	99.5	57.1
CX1060	China, GanSu, Jingyuan Caoxian	36.367228°N	104.622428°E	Che and Li (2013)	59.99	0.59	11.37	3.81	0.08	2.52	8.15	1.90	2.28	0.16	8.6	99.9	56.8
CX1160	China, GanSu, Jingyuan Caoxian	36.367228°N	104.622428°E	Che and Li (2013)	59.90	0.60	11.49	3.82	0.08	2.53	7.78	1.93	2.35	0.16	8.5	99.5	56.5
L-1	China, GanSu, Lingtai Renjiapo	35.033333°N	107.4°E	Sun et al. (1998)	59.21	0.68	12.97	4.55	0.09	2.20	6.61	1.67	2.60	0.17	8.6	99.9	61.3
L-15-1	China, GanSu, Lingtai Renjiapo	35.033333°N	107.4°E	Sun et al. (1998)	50.02	0.53	10.43	3.53	0.08	1.52	15.14	1.27	2.08	0.21	14.3	99.5	62.9
L-15-2	China, GanSu, Lingtai Renjiapo	35.033333°N	107.4°E	Sun et al. (1998)	61.56	0.68	12.61	4.33	0.09	1.80	6.00	1.49	2.54	0.17	7.9	99.6	62.7
LT-L-33	China, GanSu, Lingtai Renjiapo	35.033333°N	107.4°E	Sun et al. (1998)	60.51	0.72	13.63	4.77	0.10	2.15	5.19	1.36	2.69	0.16	7.9	99.7	65.3
TW0415	China, GanSu, Tongwei pingxiang	35.154583°N	105.190472°E	Derbyshire et al. (1998)	55.21	0.59	11.23	3.77	0.08	2.36	9.97	1.65	2.25	0.14	12.4	100.1	59.0
TW0455	China, GanSu, Tongwei pingxiang	35.154583°N	105.190472°E	Derbyshire et al. (1998)	57.15	0.60	11.99	4.04	0.09	2.70	8.44	1.73	2.43	0.14	9.9	99.6	59.1
TW0535	China, GanSu, Tongwei pingxiang	35.154583°N	105.190472°E	Derbyshire et al. (1998)	56.54	0.60	12.08	4.11	0.09	2.63	8.89	1.73	2.46	0.13	10.2	99.9	59.2
TW0580	China, GanSu, Tongwei pingxiang	35.154583°N	105.190472°E	Derbyshire et al. (1998)	55.86	0.60	12.02	4.07	0.08	2.51	9.26	1.68	2.39	0.13	10.5	99.6	59.8
TW860	China, GanSu, Tongwei pingxiang	35.154583°N	105.190472°E	Derbyshire et al. (1998)	55.62	0.59	11.76	4.02	0.08	2.53	9.70	1.68	2.32	0.14	10.7	99.6	59.5
BY0520	China, GanSu, Wuwei Zhangyi	37.532056°N	102.792167°E	Yu et al. (2012)	59.13	0.65	12.30	4.41	0.09	2.96	6.95	2.13	2.47	0.17	8.3	100.1	56.1
BY0595	China, GanSu, Wuwei Zhangyi	37.532056°N	102.792167°E	Yu et al. (2012)	58.95	0.59	11.40	3.84	0.08	2.64	8.15	1.87	2.37	0.15	9.0	99.5	56.8
BY1660	China, GanSu, Wuwei Zhangyi	37.532056°N	102.792167°E	Yu et al. (2012)	55.99	0.62	11.80	4.15	0.09	2.86	9.06	1.85	2.41	0.15	10.1	99.6	57.7
BY1695	China, GanSu, Wuwei Zhangyi	37.532056°N	102.792167°E	Yu et al. (2012)	58.04	0.64	12.28	4.28	0.09	2.83	7.99	1.84	2.42	0.15	9.2	100.3	58.7
BY1925	China, GanSu, Wuwei Zhangyi	37.532056°N	102.792167°E	Yu et al. (2012)	61.29	0.61	11.02	3.80	0.08	2.69	7.42	1.85	2.23	0.15	8.3	99.9	56.6
06XF17	China, GanSu, Xifeng	35.883333°N	107.966667°E	Guo et al. (2000)	58.53	0.59	11.42	3.82	0.08	2.29	9.16	1.75	2.20	0.15	9.9	100.3	58.6
06XF80	China, GanSu, Xifeng	35.883333°N	107.966667°E	Guo et al. (2000)	63.21	0.72	13.89	4.91	0.10	2.17	3.99	1.69	2.58	0.14	6.3	100.2	62.6
LT-DJ-L1-1	China, Shaanxi, Lantian Duanjiapo	34.1875°N	109.232778°E	Sun et al. (1997)	55.70	0.67	13.00	4.57	0.09	2.05	9.09	1.47	2.27	0.12	10.5	100.0	64.2
LT-DJ-L1-5	China, Shaanxi, Lantian Duanjiapo	34.1875°N	109.232778°E	Sun et al. (1997)	61.53	0.76	14.71	5.28	0.10	2.16	3.49	1.49	2.46	0.11	7.2	99.9	66.1
LT-DJ-L1-8	China, Shaanxi, Lantian Duanjiapo	34.1875°N	109.232778°E	Sun et al. (1997)	55.72	0.68	13.34	4.72	0.09	1.95	8.72	1.32	2.21	0.11	10.7	100.1	66.6
LT-DJ-L1-10	China, Shaanxi, Lantian Duanjiapo	34.1875°N	109.232778°E	Sun et al. (1997)	59.89	0.74	14.31	5.07	0.10	2.06	4.68	1.46	2.42	0.11	8.1	99.5	65.9
LT-DJ-L1-14	China, Shaanxi, Lantian Duanjiapo	34.1875°N	109.232778°E	Sun et al. (1997)	55.13	0.65	12.69	4.46	0.09	1.98	9.44	1.47	2.23	0.13	10.8	99.6	63.8
LT-DJ-L2-1	China, Shaanxi, Lantian Duanjiapo	34.1875°N	109.232778°E	Sun et al. (1997)	66.52	0.77	14.73	5.06	0.10	1.99	1.08	1.50	2.62	0.13	4.5	99.5	67.9
LT-DJ-L2-4	China, Shaanxi, Lantian Duanjiapo	34.1875°N	109.232778°E	Sun et al. (1997)	65.58	0.77	14.93	5.25	0.10	2.06	1.10	1.62	2.83	0.13	4.6	99.6	66.8
LT-DJ-L2-8	China, Shaanxi, Lantian Duanjiapo	34.1875°N	109.232778°E	Sun et al. (1997)	65.86	0.79	14.88	5.17	0.10	2.04	1.11	1.64	2.85	0.13	4.4	99.5	66.5
LT-DJ-L2-14	China, Shaanxi, Lantian Duanjiapo	34.1875°N	109.232778°E	Sun et al. (1997)	54.06	0.62	12.05	4.19	0.09	2.06	10.69	1.43	2.28	0.16	11.7	99.8	63.1
LT-DJ-L2-17	China, Shaanxi, Lantian Duanjiapo	34.1875°N	109.232778°E	Sun et al. (1997)	65.93	0.80	14.83	5.21	0.11	2.07	1.08	1.52	2.74	0.14	4.9	100.0	67.6
L1-Luo-1	China, Shaanxi, Luochuan Heimugou	35.75°N	109.416667°E	An et al. (1991)	57.92	0.63	12.23	4.18	0.09	2.29	7.99	1.79	2.50	0.15	9.3	99.5	58.9
L1-Luo-2	China, Shaanxi, Luochuan Heimugou	35.75°N	109.416667°E	An et al. (1991)	58.67	0.64	12.27	4.21	0.09	2.30	7.91	1.84	2.51	0.15	9.0	100.1	58.4
L1-Luo-3	China, Shaanxi, Luochuan Heimugou	35.75°N	109.416667°E	An et al. (1991)	58.56	0.60	11.82	3.97	0.08	2.17	8.41	1.77	2.38	0.15	9.2	99.5	58.6
L1-Luo-4	China, Shaanxi, Luochuan Heimugou	35.75°N	109.416667°E	An et al. (1991)	58.47	0.61	11.76	3.94	0.08	2.19	8.61	1.84	2.37	0.15	9.2	99.7	57.8
L1-Luo-5	China, Shaanxi, Luochuan Heimugou	35.75°N	109.416667°E	An et al. (1991)	57.03	0.61	11.87	4.00	0.08	2.23	9.41	1.73	2.42	0.15	10.2	100.1	59.0
L1-Luo-6	China, Shaanxi, Luochuan Heimugou	35.75°N	109.416667°E	An et al. (1991)	57.92	0.62	11.84	4.02	0.08	2.22	8.80	1.75	2.42	0.15	9.9	100.1	58.7
L1-Luo-7	China, Shaanxi, Luochuan Heimugou	35.75°N	109.416667°E	An et al. (1991)	58.13	0.60	11.60	3.87	0.08	2.17	8.82	1.78	2.37	0.15	9.5	99.5	58.1
L1-Luo-8	China, Shaanxi, Luochuan Heimugou	35.75°N	109.416667°E	An et al. (1991)	58.06	0.63	12.21	4.18	0.09	2.29	8.09	1.75	2.46	0.15	9.3	99.7	59.3
L1-Luo-9	China, Shaanxi, Luochuan Heimugou	35.75°N	109.416667°E	An et al. (1991)	57.98	0.61	11.92	4.07	0.09	2.24	8.73	1.73	2.38	0.15	9.7	100.1	59.2
L1-Luo-10	China, Shaanxi, Luochuan Heimugou	35.75°N	109.416667°E	An et al. (1991)	57.00	0.58	11.24	3.76	0.08	2.12	9.86	1.76	2.25	0.16	10.3	99.5	58.0
GSS-8	China, Shaanxi, Luochuan Heimugou	35.75°N	109.416667°E	An et al. (1991)	58.67	0.63	11.90	4.00	0.08	2.31	8.19	1.72	2.42	0.17	9.3	99.8	59.3
GSS-25	China, Shaanxi, Luochuan Heimugou	35.75°N	109.416667°E	An et al. (1991)	61.02	0.63	11.72	3.87	0.08	1.96	7.14	1.75	2.29	0.18	8.7	99.8	59.1
10GJ-80	China, Shaanxi, Weinan	34.35°N	109.516667°E	Guo et al. (1994)	53.05	0.58	11.57	3.94	0.08	1.98	11.97	1.47	2.17	0.15	12.2	99.6	62.0
10NJ-243	China, Shaanxi, Weinan	34.35°N	109.516667°E	Guo et al. (1994)	66.77	0.79	15.00	5.34	0.10	1.92	1.10	1.42	2.67	0.13	4.4	100.3	68.4

10NJ-307	China, Shaanxi, Weinan	34.35°N	109.516667°E	Guo et al. (1994)	64.24	0.74	14.35	5.03	0.10	2.19	2.53	1.56	2.68	0.13	5.4	99.5	64.2
10YG-337	China, Shaanxi, Weinan	34.35°N	109.516667°E	Guo et al. (1994)	68.63	0.72	13.95	4.74	0.09	1.91	1.15	1.77	2.53	0.14	3.9	100.1	65.3
10YG-418	China, Shaanxi, Weinan	34.35°N	109.516667°E	Guo et al. (1994)	66.22	0.81	14.87	5.22	0.11	1.74	1.30	1.44	2.57	0.13	5.4	100.4	67.4
10YG-588	China, Shaanxi, Weinan	34.35°N	109.516667°E	Guo et al. (1994)	55.60	0.58	11.54	3.93	0.08	2.03	10.63	1.56	2.24	0.17	10.8	99.6	60.9
10YG-732	China, Shaanxi, Weinan	34.35°N	109.516667°E	Guo et al. (1994)	54.11	0.60	11.74	4.05	0.08	2.10	11.18	1.49	2.26	0.18	11.6	99.8	62.1
10YG-828	China, Shaanxi, Weinan	34.35°N	109.516667°E	Guo et al. (1994)	65.64	0.77	15.33	5.47	0.10	1.93	1.20	1.35	2.81	0.13	5.0	100.3	68.2
10YG-868	China, Shaanxi, Weinan	34.35°N	109.516667°E	Guo et al. (1994)	59.71	0.67	13.09	4.57	0.09	2.10	6.92	1.51	2.41	0.16	8.5	100.2	63.7
L1-Wb-001-1.2.3	China, Shaanxi, Wubao Xingzita	37.5°N	110.7°E	Guan et al. (2008)	59.89	0.60	11.30	3.70	0.08	2.38	8.16	1.87	2.27	0.13	8.9	99.7	56.7
L1-Wb-002-1.2	China, Shaanxi, Wubao Xingzita	37.5°N	110.7°E	Guan et al. (2008)	60.41	0.59	11.30	3.66	0.08	2.37	8.04	1.88	2.26	0.13	8.9	100.0	56.7
L1-Wb-003-4	China, Shaanxi, Wubao Xingzita	37.5°N	110.7°E	Guan et al. (2008)	60.59	0.61	11.42	3.75	0.08	2.43	7.82	1.95	2.28	0.14	8.5	100.0	56.2
L1-Wb-004-5.6	China, Shaanxi, Wubao Xingzita	37.5°N	110.7°E	Guan et al. (2008)	60.61	0.61	11.47	3.78	0.08	2.45	7.83	1.90	2.27	0.14	8.5	100.0	56.9
L1-Wb-005-1.2	China, Shaanxi, Wubao Xingzita	37.5°N	110.7°E	Guan et al. (2008)	60.57	0.60	11.44	3.75	0.08	2.47	7.67	1.94	2.30	0.14	8.5	99.9	56.3
L1-Wb-006-1.2.3	China, Shaanxi, Wubao Xingzita	37.5°N	110.7°E	Guan et al. (2008)	60.92	0.61	11.45	3.79	0.08	2.52	7.67	1.92	2.29	0.14	8.4	100.2	56.6
L1-Wb-007-4.5	China, Shaanxi, Wubao Xingzita	37.5°N	110.7°E	Guan et al. (2008)	60.73	0.60	11.46	3.78	0.08	2.46	7.75	1.93	2.27	0.14	8.4	100.1	56.5
L1-Wb-009-1.2	China, Shaanxi, Wubao Xingzita	37.5°N	110.7°E	Guan et al. (2008)	60.41	0.62	11.48	3.82	0.08	2.47	7.94	1.88	2.29	0.15	8.7	100.2	57.1
CJB-L1	China, Qinghai, Xining Caijiabao	36.725°N	101.841667°E	Jahn et al. (2001)	59.96	0.55	11.14	3.55	0.08	2.43	8.77	1.85	2.30	0.15	9.0	100.2	56.6
10SPC	China, Qinghai, Xining Zongzhai	36.516667°N	101.691667°E	Jahn et al. (2001)	58.41	0.55	11.15	3.67	0.08	2.67	9.52	1.83	2.23	0.15	9.6	100.2	57.1
15MY18	China, Qinghai, Menyuan	37.330008°N	101.81955°E	Xiao et al. (2023)	56.70	0.61	11.36	3.94	0.08	2.83	9.42	1.77	2.29	0.12	10.5	100.1	57.7
15MY43	China, Qinghai, Menyuan	37.330008°N	101.81955°E	Xiao et al. (2023)	60.95	0.66	12.15	4.36	0.09	2.39	6.85	1.79	2.44	0.14	7.9	100.2	58.8
15MY91	China, Qinghai, Menyuan	37.330008°N	101.81955°E	Xiao et al. (2023)	59.31	0.62	11.44	3.95	0.09	2.59	8.02	1.85	2.31	0.14	8.9	99.7	57.2
15MY139	China, Qinghai, Menyuan	37.330008°N	101.81955°E	Xiao et al. (2023)	58.42	0.64	11.85	4.21	0.09	2.70	7.97	1.74	2.42	0.15	9.1	99.7	58.9
15MY194	China, Qinghai, Menyuan	37.330008°N	101.81955°E	Xiao et al. (2023)	58.08	0.60	11.54	3.94	0.08	2.67	8.55	1.79	2.35	0.15	9.4	99.6	57.9
15MY281	China, Qinghai, Menyuan	37.330008°N	101.81955°E	Xiao et al. (2023)	56.74	0.60	11.56	4.04	0.08	2.56	9.16	1.70	2.31	0.13	10.3	99.6	58.9
15MY297	China, Qinghai, Menyuan	37.330008°N	101.81955°E	Xiao et al. (2023)	57.93	0.61	11.40	3.93	0.08	2.66	8.83	1.75	2.28	0.15	9.6	99.7	58.3
15MY317	China, Qinghai, Menyuan	37.330008°N	101.81955°E	Xiao et al. (2023)	57.72	0.62	11.83	4.11	0.09	2.70	8.54	1.76	2.37	0.16	9.6	99.9	58.8
15MY411	China, Qinghai, Menyuan	37.330008°N	101.81955°E	Xiao et al. (2023)	58.32	0.61	11.72	4.04	0.09	2.67	8.09	1.84	2.40	0.15	9.1	99.5	57.6
15MY555	China, Qinghai, Menyuan	37.330008°N	101.81955°E	Xiao et al. (2023)	59.70	0.59	11.30	3.79	0.08	2.42	8.23	1.85	2.29	0.14	8.9	99.7	56.9
15MY625	China, Qinghai, Menyuan	37.330008°N	101.81955°E	Xiao et al. (2023)	57.19	0.60	11.60	3.98	0.09	2.65	8.96	1.72	2.37	0.15	9.9	99.7	58.7
15MY680	China, Qinghai, Menyuan	37.330008°N	101.81955°E	Xiao et al. (2023)	59.42	0.63	11.74	4.02	0.09	2.64	7.84	1.89	2.36	0.14	8.6	99.8	57.3
15MY713	China, Qinghai, Menyuan	37.330008°N	101.81955°E	Xiao et al. (2023)	62.47	0.71	13.46	4.85	0.10	2.42	4.51	1.76	2.75	0.16	6.3	100.1	60.8
15MY741	China, Qinghai, Menyuan	37.330008°N	101.81955°E	Xiao et al. (2023)	57.56	0.64	12.84	4.53	0.09	2.77	7.45	1.69	2.62	0.15	8.9	99.7	60.7
15MY764	China, Qinghai, Menyuan	37.330008°N	101.81955°E	Xiao et al. (2023)	57.17	0.61	11.47	4.03	0.08	2.61	9.37	1.68	2.30	0.15	10.1	100.0	59.1
15MY784	China, Qinghai, Menyuan	37.330008°N	101.81955°E	Xiao et al. (2023)	54.29	0.60	11.92	4.16	0.09	2.79	10.29	1.61	2.44	0.15	11.2	100.0	60.3
15MY808	China, Qinghai, Menyuan	37.330008°N	101.81955°E	Xiao et al. (2023)	59.11	0.64	12.93	4.49	0.09	2.74	6.65	1.74	2.61	0.15	8.2	99.9	60.4
15MY-840	China, Qinghai, Menyuan	37.330008°N	101.81955°E	Xiao et al. (2023)	59.27	0.59	12.27	4.03	0.08	2.45	7.49	1.61	2.43	0.14	9.1	99.9	60.9
DBBS-01	China, Xinjiang, Hetian	36.398722°N	81.933833°E	Li et al. (2015)	57.69	0.53	10.61	3.35	0.07	2.74	10.04	2.05	2.21	0.15	9.8	99.6	53.7
DBBS-02	China, Xinjiang, Hetian	36.398722°N	81.933833°E	Li et al. (2015)	57.36	0.53	10.64	3.37	0.08	2.75	9.85	1.90	2.23	0.15	10.3	99.5	55.2
DBBS-03	China, Xinjiang, Hetian	36.398722°N	81.933833°E	Li et al. (2015)	59.02	0.52	10.49	3.26	0.07	2.59	9.30	1.96	2.23	0.15	9.6	99.5	54.3
NHW1.2m	China, Hebei, Nihewan	40.216667°N	114.666667°E	Zhao et al. (2010)	61.97	0.62	11.55	3.71	0.07	2.43	6.91	1.95	2.24	0.13	7.8	100.4	56.6
NHW2.4m	China, Hebei, Nihewan	40.216667°N	114.666667°E	Zhao et al. (2010)	61.48	0.64	11.91	3.98	0.08	2.42	6.56	2.14	2.24	0.13	7.8	99.8	55.6
NHW4.5m	China, Hebei, Nihewan	40.216667°N	114.666667°E	Zhao et al. (2010)	59.84	0.69	12.50	4.41	0.09	2.36	6.90	1.98	2.29	0.12	8.1	99.8	58.0
NHW6m	China, Hebei, Nihewan	40.216667°N	114.666667°E	Zhao et al. (2010)	57.35	0.66	12.34	4.33	0.08	2.68	7.58	2.39	2.21	0.12	9.6	99.8	54.3

*FeO_T: Total FeO, originally analyzed as total Fe_2O_3, but converted to FeO_T by multiplying by a factor of 0.8998.

In addition to the newly analyzed loess, previously reported data on loess (n = 336), the fine-grained matrix of glacial diamictites (n = 116), and shales (n = 756) are also used in this study (see supplementary Table S1). The latter two sediment types differ from loess in several ways. Though glacial diamictites are similar to loess in that they are also products of mechanical grinding when glaciers traverse the continental surface, they do not undergo subsequent wind transport. Instead, they are typically deposited as subaerial glacial tills or, more generally, on submarine continental margins, resulting in poorly sorted sediments that often contain a muddy to sandy matrix with clasts ranging from pebble to cobble size. The glacial diamictite data used in this study primarily come from Gaschnig et al. (2014, 2016). In those samples, clasts larger than ~5 mm were manually removed by hand-picking, and only the fine-grained matrix was analyzed, as it is assumed to be more representative of the average composition of the source rocks. Shale, on the other hand, is a well-sorted, fine-grained sedimentary rock predominantly composed of clay minerals (e.g., illite, kaolinite, and montmorillonite), along with some quartz, feldspar, carbonate, and organic matter (Shaw and Weaver, 1965). The source material for shale is primarily derived from continental erosion of rocks that experienced extensive chemical weathering; transport of these fine-grained minerals results in hydrodynamic mineral sorting before their final deposition in low-energy aquatic environments. As a result, shales typically exhibit higher chemical index of alteration (CIA) values (see footnote of Table 1 for formula) compared to glacial diamictites and loess (Fig. 3). In addition, while loess is mainly confined to the Pleistocene epoch, glacial diamictites and shales have been preserved throughout Earth's history, particularly shales. To eliminate potential crustal evolutionary signals present in ancient glacial diamictites (Gaschnig et al., 2014; 2016) and shales (Taylor and McLennan, 1985), only

post-Archean samples are compiled and used here. Note that eight glacial diamictite samples from the western Dwyka group are also excluded from the diamictite dataset, as their sources primarily sampled the Archean interior of the Kaapvaal craton, with minor inputs from the Paleoproterozoic Bushveld Complex (Gaschnig et al., 2014; 2016; 2022).

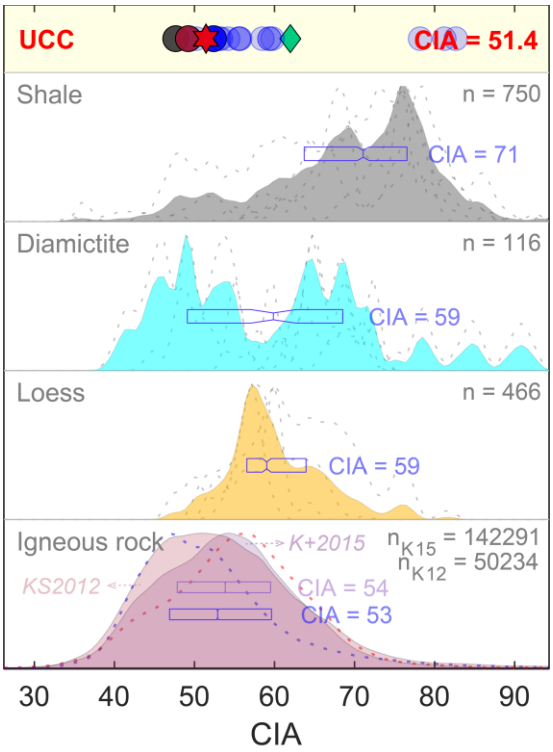

Fig. 3. Probability histogram of the chemical index of alteration (CIA) in the compiled datasets, including igneous rocks (*KS2012*—K12 and *K+2015*—K15), loess, glacial diamictites, and shales. Thin dotted lines for the loess, glacial diamictite, and shale datasets represent samples from different continents (e.g., Europe, Asia, South Africa, North America, South America, and Australia). In the igneous dataset, the blue and red dotted lines correspond to the plutonic and volcanic sub-datasets from Keller et al. (2015) (*K+2015*). The box plot shows the median along with the first and third quartiles for each dataset. The yellow bar at the top of the graph summarizes previous average UCC estimates, with the red star representing the result of this study (see Table 3), the blue circle (Rudnick and Gao, 2003), the dark gray circle (Taylor and McLennan, 1985), the purple circle (Pease et al., 2023), the green diamond (Gaschnig et al., 2016), and pale blue circles (which appear darker when they overlap) for all other previous estimates.

Two continental igneous datasets compiled by Keller and Schoene (2012) (*KS2012*) and Keller et al. (2015) (*K+2015*) are used here to investigate elemental concentration distributions and evolutionary trends with magmatic differentiation (Fig. 4). These data are, in turn, mainly sourced from EarthChem (http://www.earthchem.org) and previous studies (Condie, 2008; Condie and O'Neill, 2010; Moyen, 2011). The dataset from Keller et al. (2015) contains 122,751 plutonic and 171,690 volcanic whole-rock samples and is much larger than the 68,696 igneous samples in Keller and Schoene (2012). However, many of the samples in Keller et al. (2015) lack age constraints, which may introduce some uncertainties in interpreting their geological significance. Additionally, to remove potential regional and age biases within the large igneous dataset, we applied a spatiotemporal equation from Keller and Schoene (2012) to assign a weighting factor to each sample, which was later used to resample the two datasets. After these adjustments, 50,852 (out of 68,696) whole-rock samples from *KS2012* and 231,250 (out of 294,441) samples from *K+2015* were ultimately included in the analysis. The median values for major elements in these two datasets are also calculated and presented in Table 1 for comparison with previous UCC estimates. As shown, their median SiO_2 concentrations are around 56 wt.%, significantly lower than most estimates of the average UCC, including those derived from large-scale sampling campaigns (Table 1), suggesting that these two datasets may be biased toward a more mafic composition.

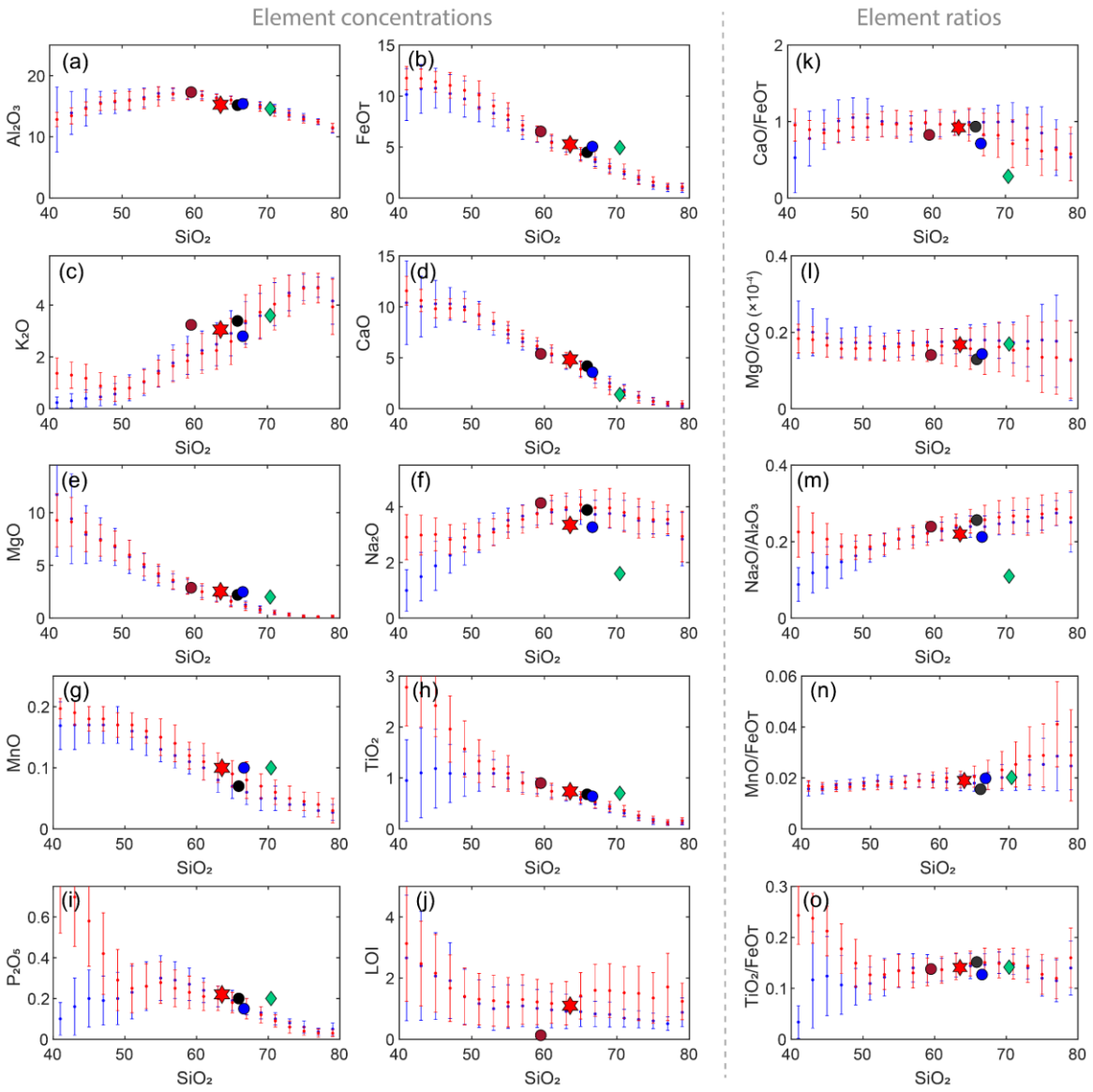

Fig. 4. Trends of element (**a-j**) concentrations (in wt.%) and (**k-o**) ratios with increasing SiO_2 in the *K+2015* igneous dataset. Shown are the median values, with uncertainties represented by median absolute deviations (MAD), for plutonic (blue) and volcanic (red) rocks. The average UCC estimates from this study, Pease et al. (2023), Gaschnig et al. (2016), Rudnick and Gao (2003), and Taylor and McLennan (1985) are also plotted for comparison, with symbols the same as those in Fig. 1.

1.3. Methodology and uncertainties

1.3.1. Chemical analyses of loess

Loess samples were powdered in an agate mortar (RS200, Retsch, Germany) prior to analysis. Loss on ignition (LOI) was first determined at 1000 °C. The resulting anhydrous powder was mixed with lithium tetraborate flux to form glass disks, which were then used for major element analyses via X-ray fluorescence (RIX2100, Japan) at Northwest University in Xi'an, China. Reference materials BCR-2 (basalt, USGS) and GSR-3 (basalt, Chinese National Standard) analyzed at the same time as the loess indicate that precision and accuracy are better than 5 % (Park et al., 2012; see also supplementary Table S2). Trace elements were analyzed by ICP-MS (Agilent 7900) after high-pressure acid digestion of samples in Teflon bombs at the State Key Laboratory of Geological Processes and Mineral Resources (GPMR), China University of Geosciences, Wuhan. About 50 mg of sample powder was weighed into a Teflon bomb, and then 1 ml of concentrated HNO_3 and 1 ml of concentrated HF were added. The sealed bomb was heated at 190 °C in the oven for 72 hours. After cooling, the solution was evaporated to dryness at ~120 °C. This was followed by the addition of 1 ml of concentrated HNO_3 and subsequent evaporation to dryness again. The resultant salt was re-dissolved in 1 ml of HNO_3, 1 ml of Milli-Q water (18.2 MΩ), and 1 ml of 1 μg/ml indium internal standard solution. The solution was then resealed and heated in the bomb at 190 °C for ~24 hours. The final solution was diluted to ~100 g with 2 % HNO_3 for ICP-MS analysis. Total procedure blanks are below detection limits. The results for the reference materials (BCR-2, BHVO-2, AGV-2, and SCo-1), as reported by Park et al. (2012), are within 10% of the recommended values for most elements and are within 5 % for the rare earth elements and Co used in this study (Table S2).

1.3.2. A mixing and dilution model

Siliciclastic sediments are derived from the chemical weathering and erosion of igneous rocks (and their metamorphic equivalents) exposed in the UCC, with the potential for one or more stages of sedimentary cycles (i.e., weathering, erosion, transportation, deposition, and diagenesis) (Taylor and McLennan, 1985). In addition to regional provenance differences, chemical elements in siliciclastic sediments can also be fractionated from one another during several geological processes, such as chemical weathering, mineral sorting, biological/anthropogenic activities, and even diagenesis and metamorphism. Therefore, they may not fully represent the average UCC. Additionally, the absolute elemental concentrations of sediments are often influenced by the presence of quartz and carbonate (calcite and dolomite), which are commonly found in sedimentary provenances (Plank and Langmuir, 1998; Carpentier et al., 2013; Gaschnig et al., 2016). To account for these potential influencing factors, we employ a mixing and dilution model to examine the elemental relationships within the fine-grained sedimentary rocks utilized here (loess, glacial diamictites, and shales; see section 1.4.1). In this model, we assume these sediments have sampled the average UCC, which is then diluted by incorporating variable amounts of quartz and carbonate (calcite and dolomite). Details about the calculations of the UCC composition can be found in the following discussion, and the compositions of quartz, calcite, and dolomite are based on their chemical formulae (SiO_2, $CaCO_3$, and $CaMg(CO_3)_2$).

1.3.3. Calculation of uncertainties

Crustal heterogeneity not only poses challenges in estimating average elemental concentrations but also in quantifying their uncertainties. In previous studies, the uncertainties have largely been ignored (e.g., Taylor and McLennan, 1985; Wedepohl, 1995), or, if considered, are derived by calculating the standard deviation of the average of previous estimates (Rudnick and Gao, 2003) or from a limited number of investigated samples (e.g., Barth et al., 2000; Teng et al., 2004; Chen et al., 2016; Gaschnig et al., 2016; Han et al., 2023). In this study, we explore a new approach for calculating the uncertainties of UCC estimates: examining the distribution of the median of elemental concentrations and/or ratios by MATLAB bootstrapping within the five compiled datasets (continental igneous rocks: *KS2012* and *K+2015*; loess; glacial diamictites; and shales). For a selected dataset, bootstrapping allows us to assess the distribution of its medians by randomly resampling the original dataset multiple times, as done in this study with 10,000 resampling trials. The final estimated elemental concentration/ratio in the UCC is averaged from the 10,000*N resampling median results, where N represents the number of datasets selected (N ranges from 1 to 5). Uncertainties are calculated as two standard deviations of the resampling medians, which essentially represent two standard errors for the final results. Additionally, uncertainty propagation must be made when calculating the abundance of an unknown element based on the concentration of a known element and their elemental ratios. In this case, we first generate a population of 10,000 values for both the known element and the elemental ratio, incorporating their uncertainties. By multiplying these two populations, a distribution for the concentrations of the unknown element is obtained, consisting of 10,000

results. The two standard deviations of this distribution are then used to represent the uncertainties.

1.4. Results and Discussion

1.4.1. Estimating UCC abundances

1.4.1.1. Aluminum (Al_2O_3)

Aluminum is a moderately incompatible element derived from Al-rich minerals (spinel, garnet, and clinopyroxene) in mantle peridotite during partial melting. During crystallization, Al_2O_3 in the melt may be buffered by Al-bearing phases like feldspar and amphibole, resulting in a relatively constant Al_2O_3 content throughout the igneous differentiation series (Uto, 1986; Zen, 1986; Favero and Jobstraibizer, 1996). Evidence of this is seen in the limited range of median Al_2O_3 content (mainly 12–17 wt.%) in both volcanic and plutonic rocks from the *K+2015* dataset as SiO_2 increases (Fig. 4a). The Al_2O_3 content of the igneous datasets also shows a Gaussian-like distribution, with a median value of 15.24 ± 0.51 wt.% from *KS2012* (Fig. 5a-b) and 15.80 ± 0.51 wt.% (2 s.e.) from *K+2015* (Fig. S1). These values are consistent with the average Al_2O_3 estimates for the UCC reported in previous studies, 15.17 ± 0.64 wt.% (2 s.e., Table 1). Given the potential bias present in *K+2015* (see above), we used the *KS2012* Al_2O_3 value (15.24 ± 0.51 wt.%) as representative for the UCC.

Except for a few Argentinian loess samples that may be influenced by regional heterogeneity (see discussion below), the maximum Al_2O_3 content in other newly analyzed samples is 15.33 wt.% (Table 2 and Fig. 6), which falls within the uncertainty of the suggested UCC Al_2O_3 abundance. This also supports the assumption in our mixing-dilution model that loess represents an average of the UCC, with dilution caused by variable amounts

of quartz and carbonate. In addition, because Al is relatively immobile during chemical weathering (Middelburg et al., 1988; Nesbitt and Wilson, 1992), except in some extreme scenarios involving organic matter (Ma et al., 2007), the average Al_2O_3 content could serve as a reference point for examining relative gains or losses of other elements during chemical weathering and/or mineral sorting. In Fig. 6, we plotted other elements against Al_2O_3, along with the mixing and dilution trends, to investigate elemental trends in the compiled loess, glacial diamictite, and shale data.

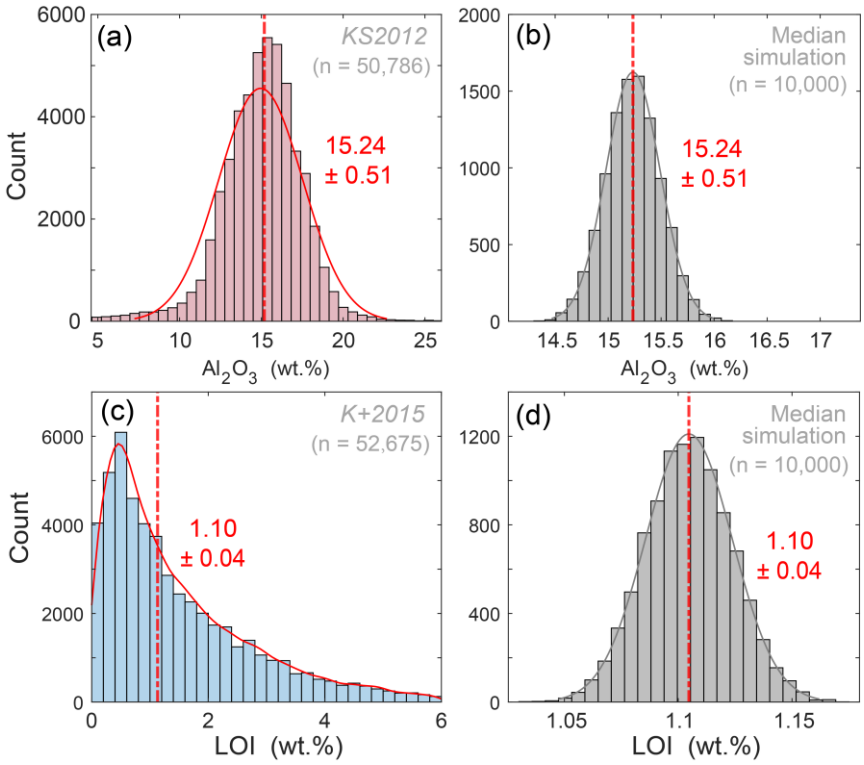

Fig. 5. (**a**, **c**) Concentration histograms of Al_2O_3 and LOI in igneous datasets, with thin dashed lines representing the median values calculated from 10,000 bootstrapping simulations (**b**, **d**). In (**a**), the more filtered Keller and Schoene (2012) dataset (*KS2012*) is used instead of *K+2015*, though they yield similar median Al_2O_3 contents within uncertainties (median Al_2O_3 in *K+2015* = 15.80 ± 0.51 wt.%, see supplementary material). LOI data is only available in the *K+2015* dataset.

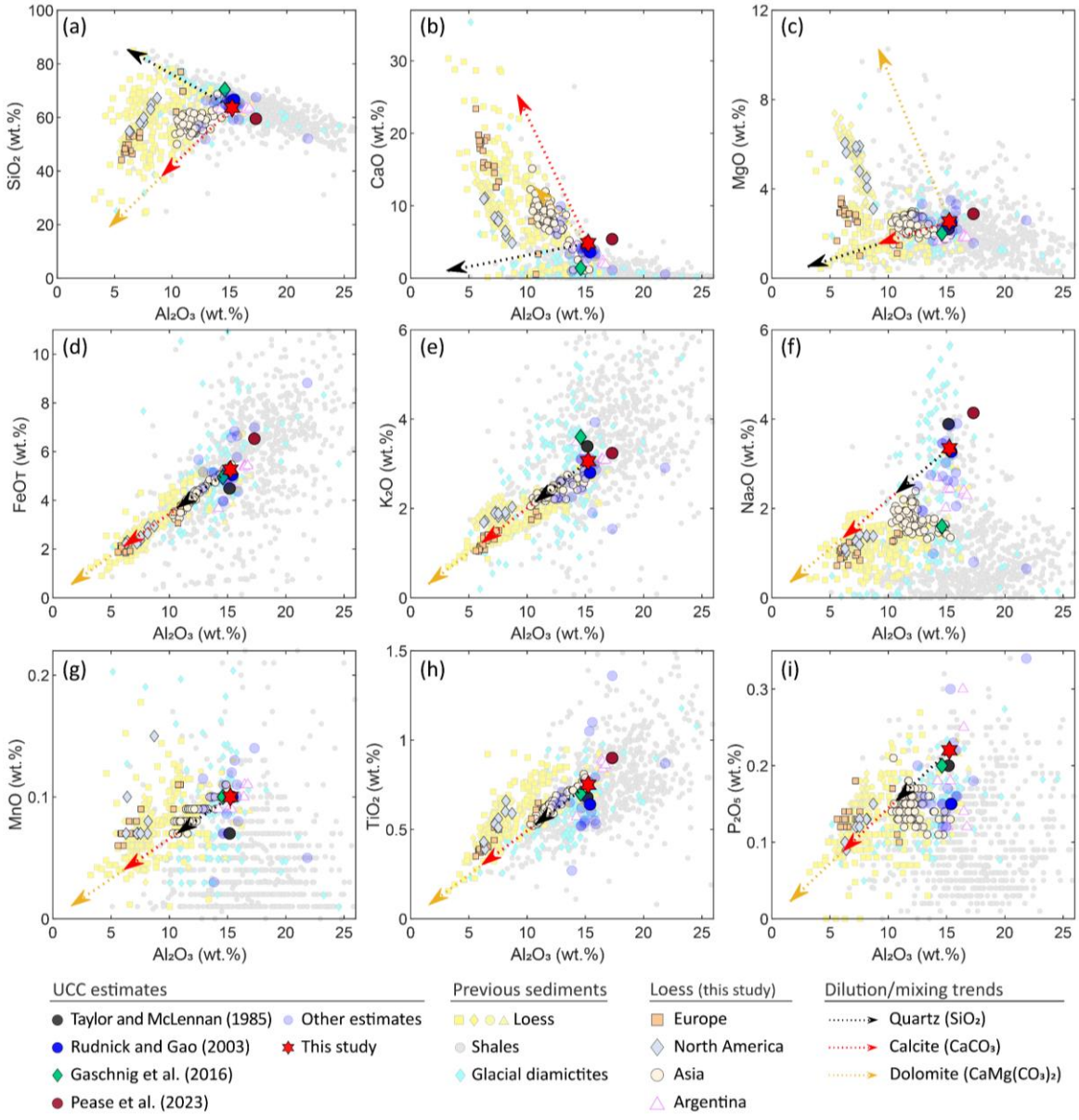

Fig. 6. Al_2O_3 contents vs. element concentrations in the compiled fine-grained sedimentary rocks. UCC estimates from different studies are also plotted for comparison. The results of this study are shown with two standard errors (red cross), although these are often too small to be visible. Using the average composition proposed in this study, dilution and mixing trends resulting from quartz and carbonate (e.g., calcite and dolomite) are depicted with dashed lines in different colors.

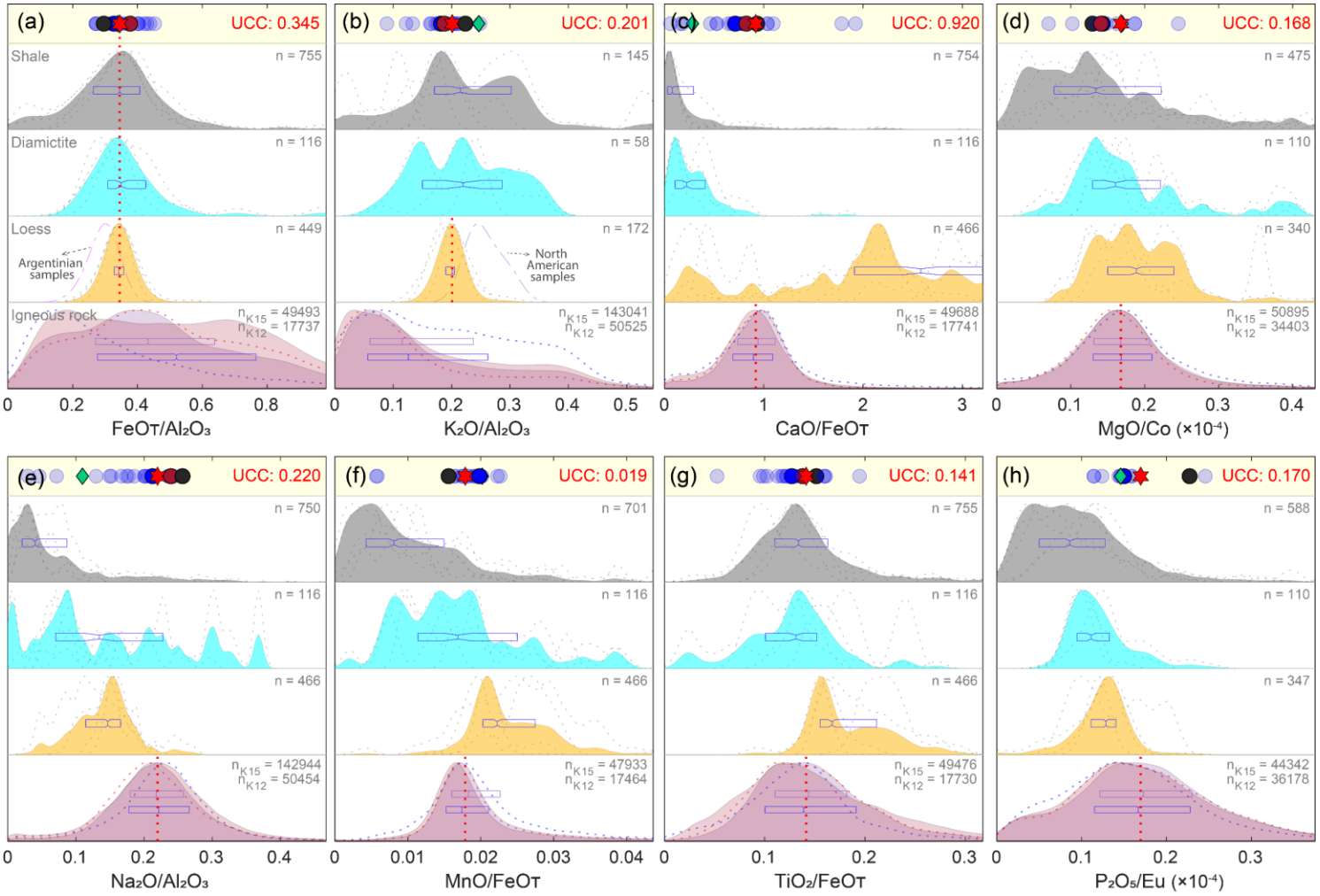

Fig. 7. Probability histogram of elemental ratios in our compiled datasets. The symbols in these plots follows that of Fig. 3. The estimate from this study is determined from the average of the medians of selected datasets, as indicated by a vertical red dashed line. The selections of datasets used for the calculations and associated caveats are described in detail in the text and briefly summarized below: (**a**) FeO_T/Al_2O_3, averaged from the

medians of shales, glacial diamictites, and loess (Argentinian loess samples excluded); (**b**) K_2O/Al_2O_3, derived from loess samples, excluding samples from North America and those with CIA > 60; (**c**) CaO/FeO_T, (**d**) MgO/Co, (**e**) Na_2O/Al_2O_3, (**f**) MnO/FeO_T, (**g**) TiO_2/FeO_T, and (**h**) P_2O_5/Eu: averaged from the medians of the two igneous datasets, *KS2012* (K12) and *K+2015* (K15). The Co and Eu in the UCC are estimated to be 15.1 ± 0.6 ppm (see Fig. S3) and 1.3 ± 0.1 ppm (see Fig. S7), respectively.

1.4.1.2. Iron (FeO_T)

Iron is a multivalent element that commonly occurs as ferrous iron (Fe^{2+}) or ferric iron (Fe^{3+}) in crustal rocks and sediments, with their relative proportions linked to the oxygen fugacity of the surrounding environments (e.g., Canfield et al., 2005; Lee et al., 2010; Dauphas et al., 2014). Previous estimates of Fe abundance are reported as Fe_2O_3, FeO, or a mixture of both, making direct comparisons challenging. As ferrous iron predominates in crystalline crustal rocks (Shaw et al., 1967; Fahrig and Eade, 1968), we have normalized all estimates to total FeO (FeO_T) in this study, as presented in Table 1.

As a compatible element, Fe content in igneous rocks decreases with increasing SiO_2 (Fig. 4b). This monotonic decrease makes it difficult to derive a meaningful average from the igneous datasets alone, as the relative proportions of rock samples with different SiO_2 content are unknown. However, Fe correlates positively with Al_2O_3 in all three sedimentary rock datasets investigated (loess, glacial diamictites, and shales) (Fig. 6d), suggesting that Fe, like Al, is conservative during chemical weathering, consistent with previous studies (Middelburg et al., 1988; Nesbitt and Wilson, 1992). Also, unlike the relatively scattered distributions seen for previously reported data for glacial diamictites, shales, and loess, the newly analyzed loess samples show a much tighter correlation, except for the samples from Argentina (Fig. 6d). Such correlations could result from the following: (1) Relative to glacial diamictites and shales, loess is more efficiently mixed during transport and thus records less regional variability. This is further supported by the homogeneous and more confined Fe isotopic composition observed in loess samples ($\delta^{56}Fe = 0.09 \pm 0.03‰$, Gong et al., 2017) compared to that of other clastic sediments ($\delta^{56}Fe = 0.12 \pm 0.13$ ‰, Beard and Johnson, 2004; Liu et al., 2022); (2) Some scatter seen in published sedimentary rock data may result from

analytical uncertainties and biases across different laboratories, which is especially evident when comparing the results of previously published data for loess with our new analyses; and (3) the deviation of Argentinian loess samples observed in both previously published data and our analyses likely reflects source heterogeneity inherent in these samples (Gallet et al., 1998; Schellenberger and Veit, 2006; Chauvel et al., 2014).

To calculate the Fe abundance in the UCC, we used the median FeO_T/Al_2O_3 ratios in the three sedimentary rock datasets, which yielded 0.345 ± 0.010 for shales, 0.348 ± 0.017 for glacial diamictites, and 0.342 ± 0.002 for loess (excluding the Argentinian samples), respectively. By averaging these medians, a FeO_T/Al_2O_3 ratio of 0.345 ± 0.007 is obtained (Fig. 7a), which corresponds to a FeO_T abundance of 5.26 ± 0.20 wt.% (Table 3).

1.4.1.3. Potassium (K_2O)

Potassium is highly incompatible, and concentrates in melts during partial melting; the K in the melts is not generally incorporated into crystallizing minerals until the very last stages of igneous differentiation (Fig. 4c). Additionally, K is soluble and can undergo complex reactions during chemical weathering, such as being released to solutions and/or absorbed onto clays like illite (e.g., Li et al., 2019; Teng et al., 2020; Li et al., 2021).

In the compiled sedimentary samples, K_2O positively correlates with Al_2O_3 (Fig. 6e). However, the data for glacial diamictites and shales are much more scattered compared to those of loess, and K_2O/Al_2O_3 ratios within the three datasets show that shales and glacial diamictites have slightly higher median ratios than most loess samples (Fig. 7b). This K enhancement cannot be explained by chemical weathering, in which K is typically removed, as glacial diamictites and shales have typically undergone more extensive weathering than

loess (Fig. 3). Instead, this discrepancy could result from two non-mutually exclusive processes: (1) preferential concentration of K-rich clays in the fine-grained fraction of sediments due to hydrodynamic mineral sorting (Nesbitt et al., 1996), and (2) potential K metasomatism through reaction with K^+-bearing pore waters during burial diagenesis or low-temperature metamorphism of shales and glacial diamictites (Rainbird et al., 1990; Fedo et al., 1995). Although loess may have also been influenced by the above two processes, the much lower and less variable K_2O/Al_2O_3 ratios in loess compared to those of glacial diamictites and shales (Fig. 7b) suggest that any potential K enrichment in loess, if it exists, is likely minimal. Thus, loess may serve as a representative proxy of the average UCC.

Within the loess data, North American samples exhibit significantly higher K_2O/Al_2O_3 ratios (0.22–0.32) compared to samples from other regions (~0.20) (Fig. 7b and 8e). These samples also show elevated Ba/Al_2O_3 (Fig. S2). These trends are observed not only in our newly analyzed loess samples but also in those compiled by Muhs et al. (2018) (see Table S1). Since both K and Ba are commonly associated with K-feldspar, and K-feldspar has K_2O/Al_2O_3 ratios between 0.4 and 0.8 (Deer et al., 2013), which are higher than most UCC estimates (0.10–0.25, Table 1), we attribute the higher K_2O/Al_2O_3 in the North American samples to an enrichment of K-feldspar. It is an open question how widespread this signal is across the North American continent and what its potential geological implications may be. However, as shown in Muhs et al. (2013), some loess samples from Nebraska exhibit relatively lower K/Rb and Ba/Rb ratios compared to those from northwestern Iowa, which were explained as a lower concentration of K-feldspar versus micas in their sources. If their explanation is correct, it would suggest that the K-feldspar enrichment observed in our North American samples is merely a local signature within the North American continent.

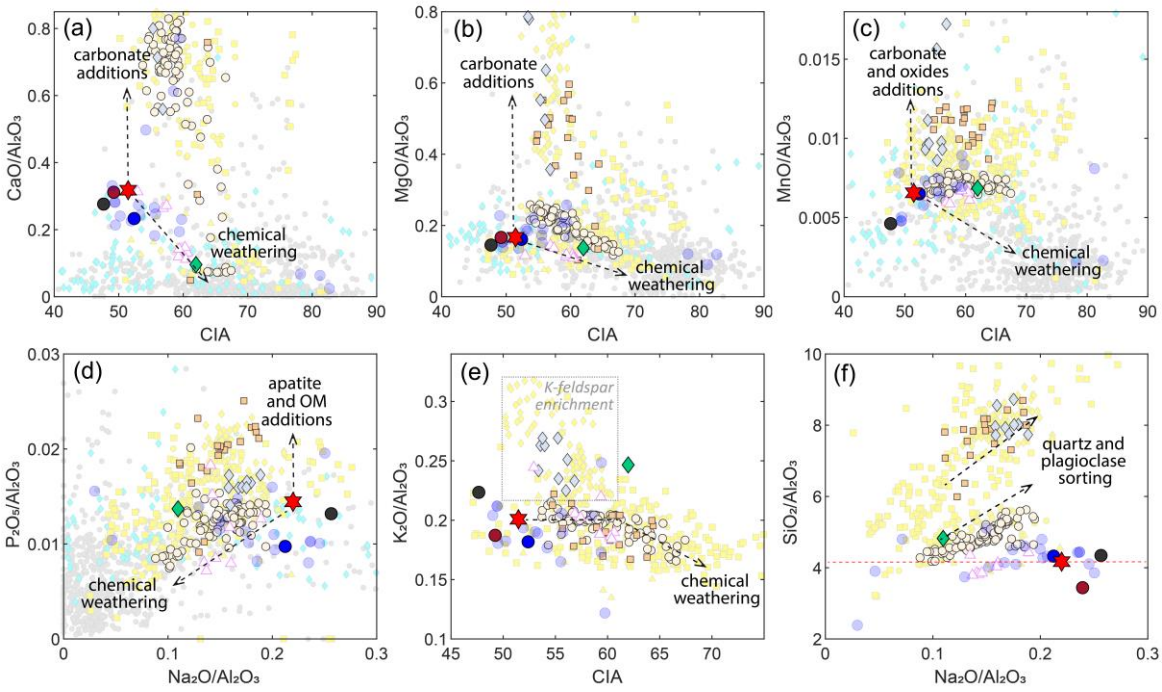

Fig. 8. Elemental ratio trends in compiled sedimentary rock samples. Symbols as in Fig. 6. In plot (**d**), OM refers to organic matter. Only loess samples are shown in **(e)** and **(f)** for simplicity. The gray-dotted square in (**e**) highlights North American loess samples exhibiting relatively high K_2O/Al_2O_3 ratios, likely due to K-feldspar enrichment. The horizontal red dotted line in (**f**) represents the newly estimated SiO_2/Al_2O_3 in average UCC composition. See the text for detailed discussions of each plot.

Finally, a study of K isotopes in loess observed that samples with lower K_2O/Al_2O_3 ratios tended to have lower $\delta^{41}K$ values, which were attributed to the preferential loss of the heavier K isotope (^{41}K relative to ^{39}K) into water during chemical weathering (Huang et al., 2020). Upon carefully examining the trend of K_2O/Al_2O_3 ratios against CIA values, we identified a slight decrease of K_2O/Al_2O_3 ratios when CIA exceeds 60, except for samples from North America (Fig. 8e), indicating potential K loss due to chemical weathering under more advanced weathering conditions. Thus, to calculate the K_2O abundance in the UCC, we excluded the loess samples from North America and those with CIA > 60. This results in a

median K_2O/Al_2O_3 ratio of 0.201 ± 0.001 for the loess dataset, leading to a calculated K_2O abundance of 3.06 ± 0.10 wt.% (Fig. 7b and Table 3).

1.4.1.4. Calcium (CaO) and magnesium (MgO)

Calcium and Mg are two alkaline earth elements that are soluble and can be released to the fluid during the chemical weathering of major rock-forming minerals such as pyroxene, amphibole, and feldspar. These elements subsequently precipitate in carbonates, such as calcite and dolomite, by reacting with dissolved CO_2 in the form of carbonic acid (H_2CO_3), thereby playing a crucial role in modulating Earth's climate (Berner and Berner, 1997).

In the compiled sedimentary rock data, shales and glacial diamictites exhibit generally lower CaO/Al_2O_3 and MgO/Al_2O_3 ratios than loess (Fig. 6b and 6c), reflecting the loss of Ca and Mg during chemical weathering. By contrast, loess samples display significantly higher CaO/Al_2O_3 and MgO/Al_2O_3 ratios, likely due to more limited chemical weathering of their source materials (Fig. 3) and more significant incorporation of carbonates (Pye, 1995; Xiao et al., 2022). Notably, carbonate in loess is not always primary (or detrital), i.e., produced mainly from the physical erosion of source rocks. A significant portion of carbonate can also be secondary, formed through biotic and pedogenic processes acting on loess deposits (Pye, 1995; Li et al., 2013). While determining the proportions of carbonate with different origins in loess is beyond the scope of this study, these carbonates are expected to produce similar mixing and dilution effects as described here.

The solubility and precipitation of Ca and Mg in sedimentary systems make it difficult to derive their averages in the UCC from sedimentary rocks; we therefore turn to igneous rocks. As compatible elements, both Ca and Mg decrease with increasing SiO_2 (Fig. 4d and 4e).

While calculating their averages from individual igneous rocks is similarly challenging, the ratios of CaO/FeO_T and MgO/Co are relatively constant during magmatic differentiation (Fig. 4k and 4l) and exhibit Gaussian-like distributions in the igneous datasets (Fig. 7c and 7d). Assuming the median values of these igneous datasets (0.92 for CaO/FeO_T and 0.17 for MgO/Co) are representative of the average UCC, we calculated CaO and MgO abundances in the average UCC as 4.84 ± 0.19 wt.% and 2.54 ± 0.10 wt.%, respectively. These calculations are based on the previously determined FeO_T abundance (5.26 ± 0.20 wt.%) and an inferred Co concentration (15.1 ± 0.6 ppm) derived from the median Co/FeO_T of loess samples (see section 1.4.1.2 above, and Fig. S3, respectively). Examining loess data for CaO and MgO contents reveals that most fall within the mixing region between the suggested average UCC with quartz and carbonate (calcite and dolomite) (Fig. 6b and 6c). Some samples, however, plot below the mixing-dilution lines, likely due to weathering losses, as evidenced by their relatively high CIA values (Fig. 8a and 8b). Collectively, this suggests that these new estimates derived from igneous rocks provide robust constraints on the composition of the average UCC.

1.4.1.5. Sodium (Na_2O)

Sodium is primarily hosted in feldspar (plagioclase—K-feldspar), the most abundant mineral in the exposed continental crust (Nesbitt and Young, 1984). Sodium is released to solution when feldspar undergoes incongruent chemical weathering to form clays (Nesbitt and Young, 1989). While most Na is eventually transported to the ocean, contributing to its salinity, some may precipitate as halite during evaporation, similar to the behavior of Ca and Mg in carbonates. However, unlike carbonate, which is stable on Earth's surface and

commonly found in siliciclastic sediments, halite has a more restricted distribution due to its high solubility and is limited to environments with relatively high salinities in arid regions.

In the compiled sedimentary rock data, shales exhibit the lowest Na_2O/Al_2O_3 ratios (Fig. 6f and Fig. 7e), likely due to the extensive chemical weathering that was a prerequisite to their formation. Glacial diamictites show more scattered Na_2O/Al_2O_3, which could mainly result from source heterogeneity associated with variable plagioclase content (Gaschnig et al., 2016; Han et al., 2023). By contrast, loess samples display much higher Na_2O/Al_2O_3 ratios, which may reflect reduced Na loss due to chemical weathering and/or halite addition. Mineralogical analysis of loess samples indicates that halite is not commonly present (e.g., Pye, 1995; Jeong et al., 2008; Xiao et al., 2022). Moreover, grain-size analyses of Chinese loess samples reveal that Na mainly resides in coarse-grained size fractions (Yang et al., 2006; Liang et al., 2013), which are predominantly composed of phases like quartz and feldspar. These observations suggest that the elevated Na_2O/Al_2O_3 in loess primarily reflects more limited weathering of their source rocks, and any contribution from halite, if present, is likely minimal. Based on the maximum Na_2O/Al_2O_3 ratio (0.19) observed in the newly analyzed loess samples, a minimum Na_2O concentration of 2.90 wt.% is inferred for the unweathered UCC. It should be noted that some previously analyzed European loess samples plot at slightly higher Na_2O contents than the mixing and dilution line of our proposed UCC composition (pale-yellow squares in Fig. 6f), and the much higher Na_2O/Al_2O_3 ratios in those samples (as high as 0.27) suggest that Na_2O in the UCC may even reach 4.11 wt.%. However, given the potential regional heterogeneity and analytical uncertainties across different labs, caution should be exercised when using these samples to provide any constraints.

Within the igneous dataset, Na_2O increases with increasing SiO_2, suggesting incompatible behavior during magmatic differentiation (Fig. 4f). This is also supported by the increasing Na_2O/Al_2O_3 ratio as SiO_2 increases (Fig. 4m). The Na_2O/Al_2O_3 ratios in the two igneous datasets show Gaussian-like distributions, with a median of 0.22 (Fig. 7e), which translates to a Na_2O concentration of 3.35 wt.% in the UCC. Given the potential bias of these igneous datasets toward more mafic compositions (see above), which could result in lower Na_2O/Al_2O_3 ratios (as the ratio decreases at lower SiO_2, Fig. 4m), the calculated Na_2O/Al_2O_3 ratio and Na_2O concentration should be considered as minimum constraints for the average UCC. This UCC Na_2O concentration of 3.35 wt.% is higher than the 2.90 wt.% obtained from the maximum Na_2O/Al_2O_3 ratio of the newly analyzed loess samples (see above), which aligns with the weathered nature of loess source rocks (Gallet et al., 1998). Therefore, we adopt the Na_2O estimate ($Na_2O = 3.35 \pm 0.11$ wt.%) calculated from the median igneous Na_2O/Al_2O_3 ratio (0.22 ± 0.001) as the minimum constraint for the Na_2O concentration in average UCC.

1.4.1.6. Manganese (MnO)

Manganese is a transition metal that can exhibit valence states ranging from -3 to +7 (White, 2018). Among these valence states, Mn^{2+}, Mn^{3+}, and Mn^{4+} are the most common in natural systems. Mn^{2+} typically associates with Fe in ferromanganese minerals such as olivine, pyroxene, clinopyroxene, garnet, and amphibolite, while Mn^{3+} and Mn^{4+} generally occur as oxides (Post, 1999; White, 2018). During chemical weathering, Mn^{2+} is soluble and can be released from silicates under anoxic conditions. However, its mobility greatly decreases when oxidized to Mn^{3+} and/or Mn^{4+} (Middelburg et al., 1988; Morgan, 2005). In

addition, Mn^{2+} can react with CO_2 to form Mn carbonates (e.g., rhodochrosite, $MnCO_3$), which are commonly found in sediments (Pedersen and Price, 1982; Okita, 1992).

Manganese has a compatibility similar to Fe (Qin and Humayun, 2008), so the MnO/FeO_T ratio in igneous rocks remains relatively constant during magmatic differentiation, except for rocks with SiO_2 > ~70 wt.% (Fig. 4n). The more scattered MnO/FeO_T ratios in high-Si igneous rocks could be due to the very low concentrations of both Fe and Mn in these rocks (Fig. 4b and 4g), caused by the crystallization of early mafic minerals and oxides during magmatic differentiation. Assuming that the Fe and Mn concentrations in the UCC are predominantly contributed by mafic and intermediate rocks, the influences of more differentiated rocks on the crustal MnO/FeO_T ratio should be limited. Thus, we adopt the median value of the igneous datasets, $MnO/FeO_T = 0.019$, as representative of the average UCC (Fig. 7f), which corresponds to a MnO concentration of 0.10 ± 0.01 wt.% (Table 3).

It is evident that shales and many glacial diamictites have relatively lower MnO/Al_2O_3 (and MnO/FeO_T) ratios compared to the average UCC (Fig. 6g), suggesting significant Mn loss during chemical weathering. By contrast, loess exhibits relatively higher MnO/Al_2O_3 (and MnO/FeO_T) ratios, with most samples plotting along or above the mixing and dilution line leading from the average UCC, particularly in those from Europe and North America (Fig. 6g). This pattern suggests limited Mn loss due to chemical weathering in loess sources. Additionally, a positive correlation between CaO/Al_2O_3 and MnO/Al_2O_3 (Fig. S4) indicates that carbonate may contribute to Mn enrichment in loess, which is consistent with the findings of Li et al. (2013), who proposed that detrital carbonate in loess is typically Mn-rich. Furthermore, the agreement between the lower bound of MnO/Al_2O_3 ratios in the newly

analyzed loess samples and the estimate obtained from igneous rocks (Fig. 6g) supports the robustness of our estimate.

1.4.1.7. Titanium (TiO_2)

Titanium, a transition metal, is often concentrated in accessory phases such as ilmenite, rutile, and titanite in crustal rocks. Additionally, silicates like biotite and amphibole can also host significant amounts of Ti due to their abundance, despite relatively lower concentrations (Force, 1976). During chemical weathering, the primary carriers of Ti are either stable (e.g., Fe-Ti oxides) or readily transformed into new phases (e.g., biotite and amphibole → clays), resulting in minimal weathering-related gain/loss (Middelburg et al., 1988; Taboada et al., 2006). Consequently, Ti, like Al, has been widely used as an insoluble reference element for investigating elemental leaching in weathering profiles (e.g., Nesbitt, 1979; Middelburg et al., 1988). However, due to the weathering-resistant nature of many Fe-Ti oxides, it has been suggested that hydraulic sorting may lead to fractionation of both Ti concentration and its isotopic composition between coarse- and fine-grained sediments (Klaver et al., 2021; Aarons et al., 2023).

In the compiled sedimentary rock data, TiO_2 positively correlates with Al_2O_3, demonstrating their similar behavior during chemical weathering (Fig. 6h). The TiO_2/Al_2O_3 ratios in loess are generally higher than those in shales and glacial diamictites, likely reflecting Ti enrichment in loess caused by mineral sorting (higher density minerals, such as zircon, tend to concentrate as 'lag' deposits; work in preparation). To evaluate the degree of mineral sorting in sedimentary systems and provide a robust average UCC TiO_2 estimate, we examined the TiO_2/FeO_T ratios of igneous rocks. Although Ti is generally considered a

moderately incompatible element, its concentration decreases with increasing SiO_2 (Fig, 4h), likely driven by its incorporation into fractionating Fe-Ti oxides (Deng et al., 2019). As shown in Fig. 4o, the TiO_2/FeO_T ratios in igneous rocks remain nearly constant during differentiation, except in rocks with SiO_2 < 50 wt.%. In these low-SiO_2 rocks, there is a clear disparity between plutonic and volcanic rocks, with volcanic rocks exhibiting overall higher TiO_2/FeO_T ratios. This likely reflects the influence of highly eruptive peralkaline volcanic rocks, which typically contain higher concentrations of incompatible elements than their intrusive equivalents (Keller et al., 2015). The median TiO_2/FeO_T ratio derived from the total igneous datasets is 0.141 ± 0.001 (Fig. 7g), slightly higher than the ratio of 0.135 ± 0.001 for rocks with > 50 wt. % SiO_2 (Fig. S5). Both values are higher than the medians for shales (0.134 ± 0.003) and glacial diamictites (0.131 ± 0.005) but significantly lower than that of loess (0.168 ± 0.006). These results suggest that coarser-grained sediments like loess are strongly affected by mineral sorting, whereas this effect is more limited in fine-grained sediments like shales and glacial diamictites.

Based on the calculated TiO_2/FeO_T ratios, 0.141 ± 0.001 for all igneous rocks and 0.135 ± 0.001 for rocks with SiO_2 > 50 wt.%, from the igneous datasets, the average UCC TiO_2 estimate is calculated as 0.74 ± 0.03 wt.% and 0.71 ± 0.03 wt.%, respectively, assuming a FeO_T concentration of 5.26 ± 0.20 wt.% (see above). The former estimate aligns more closely with the TiO_2 = 0.76 ± 0.04 wt.% reported by Plank and Langmuir (1998), derived from the correlation between Al_2O_3 and TiO_2 in trench sediments, and is therefore adopted here. This new estimate also yields a TiO_2/Al_2O_3 ratio of 0.049 ± 0.003, aligning with the minimum TiO_2/Al_2O_3 (0.048) observed in our newly analyzed loess samples (Argentinian loess samples excluded) (Table 2). This not only highlights the general Ti enrichment in loess

samples, likely introduced by the enrichment of Fe-Ti oxides, but also demonstrates the robustness of our new estimate (TiO_2 = 0.74 ± 0.03 wt.%) for the average UCC.

1.4.1.8. Phosphorus (P_2O_5)

Phosphorus is an incompatible element that is primarily hosted in apatite ($Ca_5(PO_4)_3(OH, F, Cl)$) in crustal rocks. During chemical weathering, apatite can react with dissolved carbon dioxide (e.g., H_2CO_3) and undergo congruent weathering (i.e., complete dissolution) (Filippelli, 2008; Hao et al., 2020). As a nutrient, the released P can transform into organic forms and become involved in the biogeochemical cycle, playing key roles in photosynthesis and metabolism (Reinhard et al., 2017; Cox et al., 2018). The incorporation of P into organic matter also promotes its preservation in sediments, which serve as another important source of P during continental weathering (Ruttenberg, 2003).

Sedimentary rock samples are highly scattered in the plot of P_2O_5 versus Al_2O_3, with the P_2O_5/Al_2O_3 ratios of shales generally lower than those of glacial diamictites and loess (Fig. 6i). This likely reflects variable degrees of P loss during chemical weathering. It remains an open question whether apatite behaves like other heavy minerals such as zircons and Fe-Ti oxides (see above), undergoing mineral sorting in siliciclastic sedimentary systems and enrichment in loess.

Because of the scatter in the sedimentary rock data, we use the P_2O_5/Eu ratio in igneous rocks to infer P_2O_5 concentration in the UCC and further investigate its behavior within sedimentary rocks. During magmatic differentiation, P and Eu are primarily controlled by the crystallization of apatite and plagioclase, respectively. When plotting P_2O_5/Eu ratios, a nearly constant trend is observed for igneous rocks with SiO_2 < 65 wt.%, followed by a sharp

decline at higher SiO_2 (Fig. S6). This decline likely reflects the preferential incorporation of P into apatite, relative to Eu into plagioclase, as SiO_2 increases beyond 65 wt.%. Assuming that SiO_2-rich rocks do not significantly influence the P_2O_5/Eu ratio of the average UCC because of their relatively low P_2O_5 and Eu contents, the median value of 0.17 ± 0.01 derived from the igneous datasets (Fig. 7h) can be considered representative of the UCC. Using an estimated Eu concentration of 1.3 ± 0.1 ppm (detailed calculations see Fig. S7), the P_2O_5 concentration in the UCC is calculated to be 0.22 ± 0.01 wt.% (Table 3).

Using this new estimate, we note that most sedimentary rocks plot below the mixing-dilution line of Qz-Cal-Dol (Fig. 6i), supporting a dominant weathering-related loss of P in these samples. By contrast, loess samples from Europe and North America exhibit generally higher P_2O_5/Al_2O_3 ratios, which could result from the enrichment of either P-rich organic matter or apatite. Given the much lower total organic carbon (TOC) content in the loess samples (~0.22 wt.%, Han et al., 2024) compared to shales (~1 wt.%, Shaw and Weaver, 1965), we suggest that the elevated P in some loess samples is primarily contributed by apatite, likely concentrated through mineral density sorting during loess formation. Additionally, P_2O_5/Al_2O_3 and Na_2O/Al_2O_3 positively correlate in all the investigated sediments, likely reflecting a dominant weathering trend, with a potential increase in P_2O_5/Al_2O_3 from the incorporation of both P-rich organic matter and apatite (Fig. 8d). Notably, our newly proposed UCC composition aligns with the lower bound of the $[P_2O_5/Al_2O_3]/[Na_2O/Al_2O_3]$ slope for the majority of sedimentary rocks (Fig. 8d), further supporting the validity of our new estimates for both P and Na.

1.4.1.9. Loss on Ignition (LOI)

Loss on ignition is a general term referring to the volatile components in rocks, such as H_2O, CO_2, organic C, and S, that are released when the rock is heated to a high temperature (typically ~1000°C) (Lechler and Desilets, 1987). LOI values are not always reported in previous UCC estimates (Table 1). Some studies have also normalized their major element concentrations to be LOI-free to enable direct comparison between estimates derived from different approaches (e.g., Taylor and McLennan, 1985; Rudnick and Gao, 2003; Kamber et al., 2005; Gaschnig et al., 2016). However, a side effect of this normalization is an indirect increase in the concentrations of other elements in varying proportions, with SiO_2 being most affected due to its relatively high abundance. In our compilation (Table 1), we recorded the original values as reported, without additional normalization. When multiple volatile components (e.g., H_2O, CO_2, and S) were reported in previous studies, they were summed into a single LOI value.

In comparing the available LOI data from previous studies it is evident that average UCC compositions based on sedimentary rocks typically show higher LOI values (~3.7 to 11.8 wt.%) compared to those derived from igneous rocks and large-scale sampling (0.1 to 3.3 wt.%) (Table 1). This discrepancy can largely be attributed to continental weathering, during which anhydrous silicates like plagioclase from crystalline bedrocks incongruently weather to form hydrous phases like clays (Nesbitt and Young, 1989). In addition, other volatile-bearing phases, such as carbonates and organic matter, may also be incorporated into sedimentary rocks, resulting in elevated LOI values. To provide an estimate of the UCC crystalline bedrocks, we examined the LOI concentrations in igneous rocks. As shown in Fig. 4j, LOI content decreases with increasing SiO_2, likely reflecting control by magmatic

exsolution/degassing during igneous differentiation (Plank et al., 2013; Annen and Burgisser, 2021). This uneven distribution results in a relatively skewed frequency distribution of LOI in the dataset, with most samples having LOI values between 0 and 2 wt.% (Fig. 5c). Using bootstrapping, the median LOI value is determined to be 1.10 ± 0.04 wt.%, which we propose as the baseline for the average UCC crystalline bedrocks (Table 3).

In the compiled sedimentary rock data, LOI contents for shales and glacial diamictites typically range from 2 to 7 wt.%, while loess samples exhibit significantly higher LOI values, reaching up to ~30 wt.% (Fig. 9). These much higher LOI values coincide with the incorporation of volatile-bearing phases (e.g., carbonates) into sediments, relative to crystalline bedrock, as seen by positive correlations between LOI and CaO (Fig. 9). The trends between LOI and CaO can be modeled by mixing an average siliciclastic source (with 6–8 wt.% LOI) with dolomite and calcite (Fig. 9; see Fig. S8 for the mixing results between LOI and MgO). Interestingly, the inferred siliciclastic source LOI range coincides with the ~7 wt.% LOI value for the "eroded UCC" proposed by Bayon et al. (2015), which was derived by averaging the silt fractions of worldwide river sediments, after carbonates were removed through acid leaching. Therefore, it seems reasonable to conclude that siliciclastic sediments on the continental surface, formed by chemical weathering and erosion of crystalline bedrocks, have an average LOI content of ~7 wt.%.

This raises a question, however, of why most shales and glacial diamictites have LOI values lower than ~7 wt.% (Fig. S9), if they are similar to loess and have sampled the weathered continental surface. We attribute this discrepancy to volatile loss during post-depositional diagenesis and low-grade metamorphism from these samples (Fig. S9). Indeed, unlike loess, which occurs as loose and unlithified sediment, shales and glacial diamictites

have been compacted into rocks and, in some cases, subjected to metamorphism (e.g., Nance and Taylor, 1976; Gromet et al., 1984; Gaschnig et al., 2016). These processes would inevitably cause dehydration, as well as dissolution of carbonate, thus reducing the LOI values of these sedimentary rocks (e.g., Segonzac, 1970; Wintsch and Kvale, 1994; Qiu et al., 2009; Stepanov, 2021).

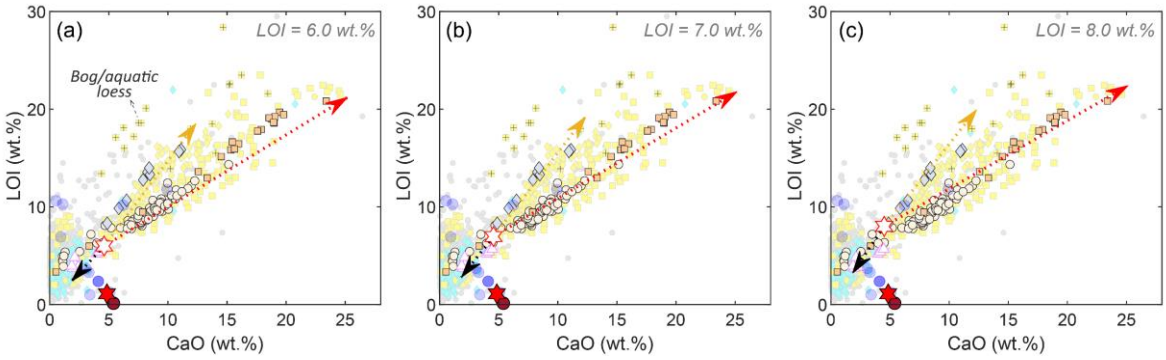

Fig. 9. LOI versus CaO in the compiled sedimentary rock samples. Trends in loess can be modeled by mixing an average siliciclastic source with 6–8 wt.% LOI (**a-c**, open red star) with dolomite and calcite. Samples falling off the mixing trends include a few European loess samples collected from bog or aquatic environments (Kühn et al., 2013). These samples exhibit relatively high LOI/CaO ratios (represented by pale yellow squares with a plus sign), possibly due to post-depositional water addition.

1.4.1.10. Silicon (SiO_2)

Silicon is the second most abundant element in Earth's continental crust after oxygen and is widely distributed in silicate minerals (e.g., olivine, pyroxene, amphibole, feldspar, quartz, and mica) of crustal rocks. During chemical weathering, Si hosted in silicate minerals can be partially released into solution to form H_2SiO_4. However, Si in quartz is more stable and tends to concentrate in weathering residues (Middelburg et al., 1988; Nesbitt and Wilson,

1992). Additionally, the weathering-resistant nature of quartz allows it to become more concentrated in coarse-grained sediments (e.g., sands) through mineral sorting during erosion and transportation, while clays, the weathering products of more weatherable silicates, are concentrated in fine-grained sediments (e.g., muds) (Nesbitt et al., 1996).

In this study, the SiO_2 concentration of the average UCC is calculated by subtracting the sum of all other elements (plus LOI) from 100%, which yields a value of 63.55 ± 0.62 wt.% (Table 3). This corresponds to a SiO_2/Al_2O_3 ratio of 4.17 ± 0.15 (2 s.e.) in the UCC, which interestingly aligns with the lowest SiO_2/Al_2O_3 ratio, 4.18, observed in the newly analyzed loess samples, as well as in most previously reported loess data (Fig. 6a and Fig. 8f). Most other loess samples, however, exhibit much higher SiO_2/Al_2O_3 ratios and plot typically between the carbonate and quartz dilution lines (Fig. 6a). This is likely due to variable enrichment of quartz in these samples. By contrast, glacial diamictites and shales show more scattered distributions, with many samples exhibiting much lower SiO_2/Al_2O_3 ratios, especially for shales. The decreased SiO_2/Al_2O_3 ratio in these samples may result from two non-mutually exclusive processes: (1) quartz being physically sorted out during erosion and transportation, and (2) potential silicon loss due to more extensive weathering.

The consistency between our SiO_2 estimate and the lower boundary of SiO_2/Al_2O_3 in loess samples appears to support its validity. This inference, however, requires minimal Si loss in the loess source. To investigate whether Si in loess has been affected by chemical weathering, we examined the relationship between SiO_2/Al_2O_3 and Na_2O/Al_2O_3 ratios, as well as the Si isotopic composition reported by Savage et al. (2013). As shown in Fig. 8f, SiO_2/Al_2O_3 positively correlates with Na_2O/Al_2O_3 for loess samples from different regions, with variations in SiO_2/Al_2O_3 ratios exceeding a factor of 2, corresponding to a ~30 wt.%

change in SiO_2 concentration. Such differences are unlikely to result from chemical weathering. Instead, we interpret the correlation as primarily caused by the mixing and enrichment of quartz and plagioclase during loess formation. These two minerals preferentially concentrate in coarse grain sizes (Yang et al., 2006; Liang et al., 2013), and their concentrations in loess are strongly regulated by fluctuations of paleo-monsoon intensity, which acts as the driving force for mineral sorting (Sun et al., 2006; He et al., 2016). In addition, Si isotope analysis reveals that loess has an isotopic composition of $\delta^{30}Si$ = -0.22 ± 0.07‰ (Savage et al., 2013), which is indistinguishable from that of granitic rocks ($\delta^{30}Si$ = -0.23 ± 0.15‰, Savage et al., 2012), but significantly higher than that of highly weathered shales ($\delta^{30}Si$ = -0.37 ± 0.47‰) and river clays ($\delta^{30}Si$ = -0.57 ± 0.60‰) (Savage et al., 2012; Bayon et al., 2018). These results suggest that the degree of Si weathering loss in the loess source, if present, is likely minimal. Overall, the close fit between our estimate and the lowest SiO_2/Al_2O_3 ratio observed in the newly analyzed loess samples suggests that our estimated SiO_2 = 63.55 ± 0.62 wt.% should provide a reasonable average for the UCC, which represents a lower bound if there has been any SiO_2 loss from loess due to chemical weathering.

1.4.1.11. Summary

The calculation process for different major elements in average UCC is summarized in Table 3 and depicted in Fig. 10. Except for Al_2O_3 and LOI, whose concentrations are directly calculated from the igneous datasets, the concentrations of other elements are primarily derived from elemental ratios using either igneous or sedimentary rock datasets, with the final SiO_2 inferred as the difference from the sum to 100%. The UCC concentrations and

corresponding elemental ratios align well with the trends observed in the collected fine-grained sedimentary rocks, further supporting the robustness of our estimates. Additionally, among these sedimentary rocks, loess samples exhibit lower degrees of chemical weathering in their source materials and a relatively homogeneous composition, likely resulting from more efficient mixing in the aerodynamic environment that forms loess. Therefore, loess likely serves as a better proxy in estimating the UCC composition, compared to glacial diamictites and shales, for many elements, though caution is still required to account for potential effects from chemical weathering and mineral sorting in samples from different regions.

Table 3. A new compositional model for the average UCC.

Element	wt.%	2 s.e.	Notes	
			elemental ratio	**calculation description***
SiO_2	63.55	0.62	-	subtracting the sum of all other elements from 100%
TiO_2	0.74	0.03	$TiO_2/FeO_T = 0.141 \pm 0.002$	averaging IG medians (*KS2012*, *K+2015*)
Al_2O_3	15.24	0.51	-	median of IG (*KS2012*)
FeO_T	5.26	0.20	$FeO_T/Al_2O_3 = 0.345 \pm 0.007$	averaging SH-GD-LS medians
MnO	0.10	0.01	$MnO/FeO_T = 0.019 \pm 0.0001$	averaging IG medians (*KS2012*, *K+2015*)
MgO	2.54	0.10	$MgO/Co = 0.168 \pm 0.001$ *(Co = 15.1 ± 0.6 ppm)*[#]	averaging IG medians (*KS2012*, *K+2015*)
CaO	4.84	0.19	$CaO/FeO_T = 0.920 \pm 0.003$	averaging IG medians (*KS2012*, *K+2015*)
Na_2O	3.35	0.11	$Na_2O/Al_2O_3 = 0.220 \pm 0.001$	averaging IG medians (*KS2012*, *K+2015*)
K_2O	3.06	0.11	$K_2O/Al_2O_3 = 0.201 \pm 0.001$	LS median (excluding North American and CIA > 60 samples)
P_2O_5	0.22	0.01	$P_2O_5/Eu = 0.170 \pm 0.001$ *(Eu = 1.3 ± 0.1 ppm)*[#]	averaging IG medians (*KS2012*, *K+2015*)
LOI	1.10	0.04	-	median of IG (*K+2015*)
Sum	100	-	-	-

*The dataset of igneous rocks is abbreviated as IG, shales as SH, glacial diamictites as GD, and loess as LS.

[#]The calculation for the updated Co estimate in the UCC is shown in Fig. S3; for the updated Eu estimate, see Fig. S7

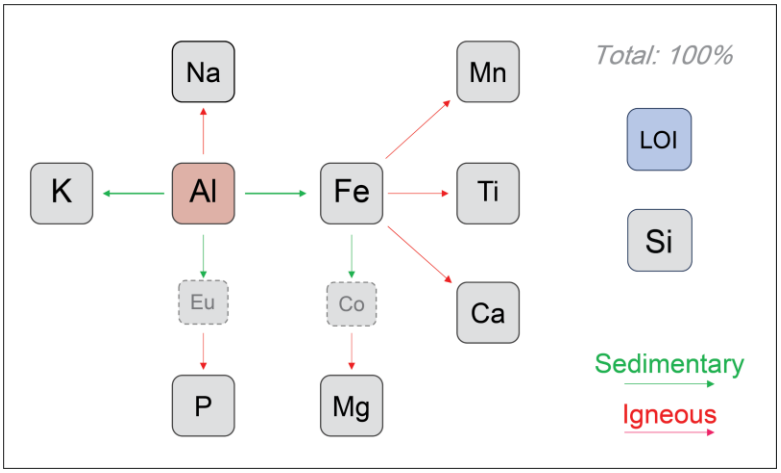

Fig. 10. Diagram showing the calculation methods used in this study to estimate each major element concentration in the average UCC. The Al_2O_3 and LOI contents are calculated directly from the igneous dataset (Fig. 5), while the concentrations of other elements are primarily derived from elemental ratios using either sedimentary (green arrow) or igneous (red arrow) rock data compilations. The final SiO_2 is inferred as the difference from the sum of the other elements to 100%. For more information, refer to the text and Table 3.

1.4.2. Comparison to previous estimates

The new average UCC estimate plots in the field of granodiorite on the total alkali versus silica (TAS) diagram (Fig. 11a), suggesting that the UCC has a relatively evolved, granodioritic composition. This is consistent with many previous results obtained from large-scaling sampling and model calculations (e.g., Shaw et al., 1967; Taylor and McLennan, 1985; Condie, 1993; Gao et al., 1998). In comparison, the estimates derived from igneous datasets exhibit systematically lower SiO_2, ranging from 56 to 60 wt.% (Clarke, 1889; Clarke and Washington, 1924; Pease et al., 2023). This likely reflects a bias to more mafic compositions in the igneous datasets, as discussed above, an inference further supported by the elevated concentrations of compatible elements such as CaO, FeO_T, MgO, and TiO_2 in

these igneous-related estimates (see Fig. 1a). The reason for such bias is unclear but could result from the oversampling of volcanic rocks, which are predominantly mafic and tend to cover larger land areas than deep-seated plutonic rocks due to their lower viscosity and higher eruptibility.

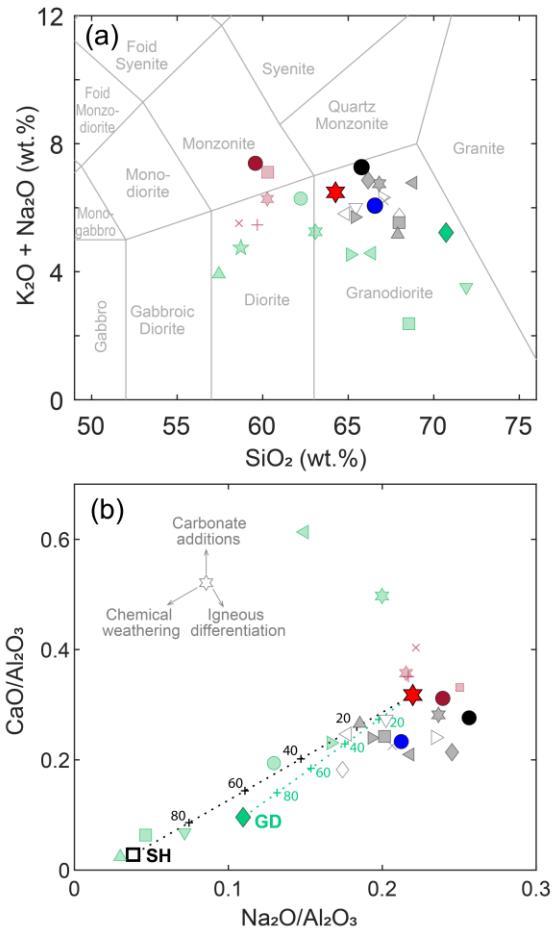

Fig. 11. (a) Total alkalis ($Na_2O + K_2O$) versus (SiO_2) contents of the compiled UCC estimates. The total alkali versus silica (TAS) diagram is after Middlemost (1994). **(b)** CaO/Al_2O_3 versus Na_2O/Al_2O_3 ratios. The dotted line represents the mixing between the average igneous UCC (as determined in this study) and the median of either ancient glacial diamictite composites (carbonates-filtered) reported by Gaschnig et al. (2016) (GD, green diamond) or shales derived from our collected data (Table S3; SH, black square). Each cross along the mixing line represents a 20% interval, with the numbers indicating the proportion of sediments incorporated into the igneous crust. Symbols as in Fig. 1. All UCC estimates plotted here have been normalized to 100% anhydrous.

By contrast, the average UCC estimates obtained from sedimentary rocks display a much wider range of SiO_2 contents, from 52 to 70 wt.% (Table 1). A primary reason for this large variation is the LOI value, although it was not consistently reported in previous studies. Studies with SiO_2 values lower than our estimate have generally higher LOI values, for example, 3.7 wt.% LOI in Goldschmidt (1933), 10.6 wt.% in Bayon et al. (2015), and 11.8 wt.% in Yaroshevsky (2006), as well as ~10 wt.% in Plank and Langmuir (1998) and Plank (2014). Additionally, estimates derived primarily from fine-grained siliciclastic sediments (e.g., Goldschmidt, 1933 for glacial clays; Bayon et al., 2015 for river clays) may have lower SiO_2 due to the focus on clay components. Other estimates, however, yield SiO_2 values higher than 64 wt.%, especially when normalized to 100% anhydrous (Fig. 11a). This indicates a general increase in SiO_2 concentrations in sediments, likely due to the removal of more soluble elements during chemical weathering. This interpretation aligns with the relative depletions of soluble elements such as Na_2O, Ca_2O, MgO, and P_2O_5 observed in sedimentary rock-derived estimates (Fig. 1a). The weathering effect may also explain the correlated decreasing trend of CaO/Al_2O_3 and Na_2O/Al_2O_3 observed for most sedimentary-derived UCC estimates, except for a few with elevated CaO/Al_2O_3 ratios, which likely reflect the incorporation of carbonates (Fig. 11b).

UCC model compositions derived from large-scale sampling and lithology-model calculations display relatively higher SiO_2 but lower concentrations of soluble elements such as CaO and Na_2O than our estimate (Fig. 11b). These characteristics resemble features observed in sediment-derived estimates, potentially due to the incorporation of weathering signatures by including variable proportions of (meta)sedimentary samples in these estimates. Some estimates, however, still exhibit elevated Na_2O concentrations, such as those

reported by Shaw et al. (1967) and Fahrig and Eade (1968) based on large-scale sampling of the Canadian shield, with their results later adopted by Taylor and McLennan (1985) and Wedepohl (1995). This contrasts with the expected loss of Na associated with chemical weathering, and similar results are not observed in large-scale sampling from other areas, such as the Baltic and Ukrainian shields (Ronov and Migdisov, 1970), Eastern China (Gao et al., 1998), and the Japanese Arc (Togashi et al., 2000). We attribute these differences to local heterogeneities associated with the Canadian Shield. Specifically, repeated glaciations during the Pliocene-Pleistocene may have generated more than 120 meters of erosion in this region, leaving primarily crystalline basement rocks exposed (Bell and Laine, 1985; Marshak, 2013). Moreover, these crystalline bedrocks contain large proportions of Na-rich granites such as tonalites and trondhjemites (Martin et al., 2005), which likely contributes to the relatively high Na estimates from this region. In addition, because P is an incompatible element that tends to increase in igneous rocks over geological time (Cox et al., 2018), the more ancient rocks of the Canadian Shield may result in lower P concentrations. This, along with potential P loss due to chemical weathering associated with metasedimentary bedrocks in the area (e.g., Shaw et al., 1967; Taylor et al., 1986), could contribute to lower P concentrations in UCC estimates derived from sampling this region (Fig. 1b).

1.4.3. Geological significance

1.4.3.1. Average igneous component in the UCC

The UCC is generally defined as the uppermost 10–20 km of the continental crust. It consists primarily of crystalline bedrocks that are composed of plutonic and metamorphic rocks, along with a relatively thin sedimentary cover (~1–3 km), which mainly includes

sedimentary rocks derived from reworked older sediments and basement, and occasionally volcanic rocks (e.g., Ronov and Yaroshevsky, 1976; Wedepohl, 1995; Mooney et al., 1998; Huang et al., 2013; Laske et al., 2013). Previous UCC estimates obtained from sedimentary rocks provide insights primarily into the composition of the overlying sedimentary cover (e.g., Goldschmidt, 1933; Kamber et al., 2005; Canil and Lacourse, 2011; Bayon et al., 2015; Gaschnig et al., 2016; Xiao et al., 2022). By contrast, estimates derived from other approaches (e.g., averaging igneous rocks, large-scale sampling, lithology model calculation) are more focused on the crystalline basement, sometimes combining the sedimentary layer with the crystalline bedrock into a single UCC compositional model (e.g., Clarke, 1889; Shaw et al., 1967; Taylor and McLennan, 1985; Wedepohl, 1995; Gao et al., 1998; Rudnick and Gao, 2003).

The new estimate of the average major element composition of the UCC presented here is distinct in that it is derived directly or indirectly from igneous rock data. This provides essentially an average of the igneous UCC. If the crystalline bedrock is assumed to be primarily of igneous origin, these estimates can even be taken to represent the crystalline bedrock. However, some sedimentary rocks may have been metamorphosed and turned into crystalline rocks, and are therefore incorporated into the crystalline bedrock. The incorporation of (meta)sedimentary rocks could introduce the following trends, which can be gleaned from element behavior in sedimentary rocks:

(1) Less soluble elements like SiO_2, Al_2O_3, FeO_T, and TiO_2 tend to be relatively enriched compared to soluble elements like CaO, MgO, Na_2O, K_2O, MnO, and P_2O_5 in siliciclastic sediments.

(2) Mineral sorting associated with grain size (coarse- versus fine-grained) and density can affect the concentrations of elements such as SiO_2, K_2O, and TiO_2 in sediments.

(3) Incorporation of carbonates would enhance concentrations of CaO, MgO, and MnO in sediments.

(4) LOI values, along with carbonate, influence the absolute concentrations of elements in sedimentary rocks. LOI, in particular, can be influenced by both chemical weathering and metamorphic dehydration processes.

If we assume that the sediments incorporated into the crystalline bedrock (i.e., transformed into metasedimentary rocks) have an average composition similar to the median values of either the glacial diamictites (carbonates-filtered) reported in Gaschnig et al. (2016) or the shales derived from our collected data (Table S3), bulk mixing between these sediments and our new igneous crust estimate can be used to model the proportion of sedimentary rocks present in previous UCC estimates. Given the preferential removal of Na and Ca from siliciclastic sediments by chemical weathering, elemental ratios CaO/Al_2O_3 and Na_2O/Al_2O_3 appear to be the most useful indicators for this purpose, as shown in Fig. 11b. The results indicate that previous estimates generally follow the mixing trends, although some show relatively higher Na_2O/Al_2O_3 ratios, possibly due to preferential sampling of the Canadian Shield (see discussion above). Additionally, most previous estimates based on large-scale sampling and/or model calculations suggest that the UCC contains less than 40% sedimentary rocks, regardless of whether the glacial diamictites or shale medians are used as endmembers (Fig. 11b). This < 40% sedimentary rock content in previous UCC

compositional models suggests that the UCC retains a predominantly igneous composition, with igneous rocks primarily residing in the crystalline basement, while the sedimentary rocks could either exist in the overlying sedimentary layer or have been incorporated into the basement via metamorphism.

Meanwhile, this relatively small proportion of sediments may not account for all sediments generated throughout geological history, as some may have been recycled into the deep Earth. The recycled sediment may be associated with subducted continental crust and may have been partially incorporated into arc magmas during subduction and later accreted to the continental crust (Plank and Langmuir, 1993), relaminated to the base of the continental crust either physically or via partial melting (Hacker et al., 2011; Kelemen et al., 2025), or even recycled to the deep mantle (Willbold and Stracke, 2006; Jackson et al., 2007).

1.4.3.2. UCC influence on seawater

During continental weathering, crustal material can be physically or chemically removed and transported into the ocean. This process not only provides nutrients to marine organisms but also helps regulate seawater chemistry. When plotting the concentration ratios of (median shale)/UCC against the partition coefficient between seawater and the UCC ($R_{Shale/UCC}$ versus $K_{Seawater/UCC}$, Fig. 12), nearly insoluble elements like Al, Fe, Ti, and Si exhibit $R_{Shale/UCC}$ ratios close to 1, indicating limited removal of these elements from the UCC during chemical weathering. By contrast, other elements show either much lower $R_{Shale/UCC}$ ratios or higher $K_{Seawater/UCC}$ ratios, reflecting their greater solubility during continental weathering. Among these soluble elements, P and Na show a general decreasing trend in $R_{Shale/UCC}$ ratios as

$K_{Seawater/UCC}$ increases (Fig. 12), suggesting that continental weathering serves as a dominant source of these elements in the ocean. By comparison, Mn and Ca exhibit relatively low $K_{Seawater/UCC}$ ratios compared to their reduced $R_{Shale/UCC}$ ratios, likely due to the precipitation of Mn nodules and carbonate from seawater. Conversely, K and Mg display much higher $R_{Shale/UCC}$ ratios than expected from their $K_{Seawater/UCC}$ ratios. This may reflect their absorption onto clays, with K primarily associating with illite and Mg with vermiculite (e.g., Nesbitt et al., 1980; Middelburg et al., 1988; Nesbitt and Young, 1989). Moreover, the potential incorporation of Mg from seawater into seafloor dolomite suggests that Mg could initially have a higher $K_{Seawater/UCC}$ ratio, possibly approaching that of Na and Ca.

Considering all these factors, the solubility of major elements during continental weathering can be ranked as (Ca, Na, Mg) > (K, Mn, P) >> (Si, Ti, Fe, Al), with Ca, Na, and Mg exhibiting the highest solubility, K, Mn, P moderate solubility, and Si, Ti, Fe, and Al being largely insoluble. This trend generally aligns with findings from studies on element behavior in weathering profiles, though their specific order may vary depending on factors such as source lithology, climate conditions, and redox states (e.g., Nesbitt et al., 1980; Middelburg et al., 1988; Nesbitt and Wilson, 1992).

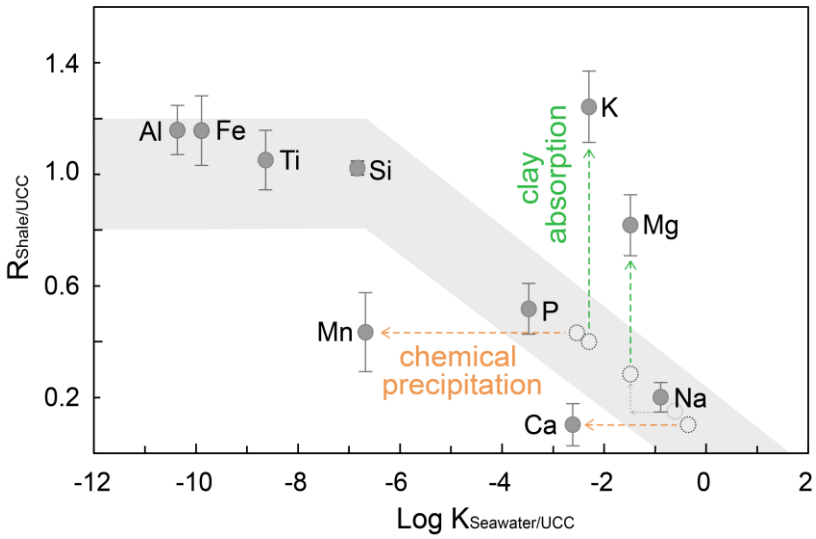

Fig. 12. Concentration ratios of shale relative to the UCC ($R_{Shale/UCC}$) are plotted against the partition coefficient between seawater and the UCC ($K_{Seawater/UCC}$, on a logarithmic scale). The shale concentrations are calculated from the medians of the compiled shale data (Table S3). The UCC estimates are derived from this study, while the seawater composition is from Bruland and Lohan (2003). Errors represent two standard errors for the $R_{Shale/UCC}$ ratios. The gray shaded area represents the inferred trend for elements with varying solubility during continental weathering.

1.5. Conclusions

This work systematically examined the behavior of major elements, including volatile elements via LOI, in crustal igneous and sedimentary rocks (loess, glacial diamictites, and shales). By investigating elemental patterns during magmatic differentiation and sedimentary processes such as chemical weathering and mineral sorting, we propose a new compositional model for the average UCC, with uncertainties of < 5% (two standard errors) for all major elements. These new estimates align well with elemental trends observed in fine-grained sedimentary rocks, particularly in loess, demonstrating efficient mixing in loess relative to shales and glacial diamictites.

The approaches presented here represent a means of addressing the compositional heterogeneity of the continental crust, with advantages in overcoming potential sampling biases that may plague previous attempts, such as averaging igneous rocks, large-scale sampling, and/or analyzing fine-grained sediments. Since our estimates are derived directly or indirectly from igneous datasets, they should represent an average igneous component of the UCC. Our new compositional estimate confirms the evolved, granodioritic composition of the UCC while suggesting relatively higher concentrations of soluble elements, such as CaO, Na_2O, and P_2O_5, compared to previous estimates.

Based on a mixing model and comparisons with previous UCC estimates, we suggest that the UCC retains a predominantly igneous composition, with the amounts of sedimentary rocks at the present surface and/or incorporated into the crystalline bedrocks typically less than 40% by mass. Moreover, the solubility of elements during continental weathering is ranked as (Ca, Na, Mg) > (K, Mn, P) >> (Si, Ti, Fe, Al). However, the final composition of shales and the partition coefficient between seawater and the UCC are further influenced by element adsorption onto clays, as well as the precipitation of chemical sediments such as carbonate and Mn nodules from seawater.

Chapter II. Halogen (F, Cl, Br, and I) Concentrations of the Upper Continental Crust Through Time as Recorded in Ancient Glacial Diamictite Composites

As published in *Geochimica et Cosmochimica Acta* in 2023

With co-authors Roberta L. Rudnick[1], Tao He[2], Michael A.W. Marks[3], Shui-Jiong Wang[4], Richard M. Gaschnig[5], Zhao-Chu Hu[2]

[1]Department of Earth Science and Earth Research Institute, University of California - Santa Barbara, Santa Barbara, CA 93106, USA

[2]State Key Laboratory of Geological Processes and Mineral Resources, China University of Geosciences, Wuhan, 430074, PR China

[3]Eberhard Karls Universität Tübingen, Geo- und Umweltforschungszentrum, Schnarrenbergstraße 94-96, 72076 Tübingen, Germany

[4]State Key Laboratory of Geological Processes and Mineral Resources, China University of Geosciences, Beijing, 100083, PR China

[5]Department of Environmental, Earth and Atmospheric Sciences, University of Massachusetts Lowell, Lowell, MA 01854, USA

Abstract

The continental crust is an important reservoir for incompatible elements, including the halogen elements (F, Cl, Br, and I), but their concentrations remain poorly known, thus hindering better understanding of the role of the crust in Earth's halogen cycle. We present halogen data (F, Cl, Br, and I) for twenty-four well-characterized glacial diamictite composites that derive from the upper continental crust (UCC) and were deposited during discrete glacial events at ~2.9 Ga, ~2.4–2.2 Ga, 0.75–0.58 Ga, and ~0.30 Ga. A good correlation between Cl and the highly soluble Na ($R^2 = 0.70$), together with low and scattered Cl concentrations in the diamictites (2–279 ppm), indicates significant Cl loss during chemical weathering of the continents. The other halogens (F, Br, and I), however, are not strongly affected by chemical weathering as revealed by their correlations with less soluble elements like K, P, Nd, and Lu, which may be due to their retention in secondary minerals and/or organic matter. Increasing concentrations of F in the composites through time may reflect the evolving composition of the UCC. Using the median values of the Neoproterozoic and Paleozoic diamictite composites, halogen concentrations of the present-day weathered UCC are estimated to be: 575 ± 87 ppm F, 29 ± 20 ppm Cl, 0.65 ± 0.14 ppm Br, and 0.05 ± 0.01 ppm I (errors quoted at the median absolute deviation). Linear correlations between halogens and other elements provide estimates for minimum halogen concentrations of the present-day crystalline UCC: 394 ± 67 ppm F, 83 ± 24 ppm Cl, 0.41 ± 0.04 ppm Br, and 0.03 ± 0.01 ppm I (with 2σ uncertainties). These estimates are all lower than normalized concentrations of elements of similar incompatibility during igneous differentiation, which may reflect loss of halogens via magmatic degassing/exsolution and/or chemical weathering during the formation of the continental crust. The distinct behavior of Cl compared to Br and

I during continental weathering leads to a wide range of Br/Cl (2–265 * 10^{-3}) and I/Cl (122–197,952 * 10^{-6}) ratios, and Br/I ratios that are distinctly higher than those of pelagic sediments and marine pore fluids. Similar halogen signals have been reported from the lithospheric mantle and may reflect recycling of terrigenous sediments. The calculated weathering flux of Cl from the continents is quite small compared to the total Cl content of seawater (< 8–34 %), suggesting that Cl in seawater is mainly derived from outgassing of the mantle and/or late volatile accretion. On the other hand, the significantly higher Br and I contents in terrigenous organic-rich sediments compared to those of crystalline bedrocks suggest that significant amounts of Br and I were transported from the oceans to the continents.

2.1. Introduction

Halogen elements—fluorine (F), chlorine (Cl), bromine (Br), iodine (I), and astatine (At)—constitute Group VIIA of the periodic table. With the exception of the short-lived radioactive At (with a half-life of less than 8.1 hours), halogens are stable and concentrated at Earth's surface, with F being enriched in crustal rocks, Cl and Br in seawater, and I (and to a lesser extent, Br) in organic matter. The halogens play a critical role in modulating the habitability of Earth. Specifically, F and Cl in hydrothermal fluids can complex and transport economically important metals and thus facilitate ore deposit formation (Lecumberri-Sanchez and Bodnar, 2018 and references therein); Cl and Br in seawater help regulate ocean salinity (Knauth, 1998; Sharp and Draper, 2013); and the release of halogens to the atmosphere (via volcanic degassing, sea salt aerosols, and/or anthropogenic emissions) can contribute to climatic fluctuations and ozone depletion (Simpson et al., 2007; Kutterolf et al., 2013; Broadley et al., 2018b; Clay, 2021; Cuevas et al., 2022). Halogens can be also recycled into Earth's interior like other volatile elements (e.g., C, H, and N) via subduction, and thus alter the chemical and physical properties of arc-related magmas and the deep mantle (e.g., Straub and Layne, 2003; John et al., 2011; Kendrick et al., 2014; Broadley et al., 2016; Kendrick et al., 2017; Hanyu et al., 2019; Sobolev et al., 2019; Kendrick et al., 2020; Bekaert et al., 2021). Despite their importance, halogen concentrations in the continental crust, an important reservoir for incompatible elements, remain poorly constrained, hindering a better understanding of how halogens behave during continental crust formation and evolution, and the role of the continental crust in Earth's halogen cycle.

The building materials of the continental crust are ultimately derived from mantle melting, which concentrates incompatible elements in the crust (e.g., Taylor and McLennan,

1985; Hofmann, 1988; Rudnick, 1995; Rudnick and Gao, 2003). The halogen elements (F, Cl, Br, and I) are all highly incompatible. However, only F is enriched in crustal rocks, whereas the other halogens (Cl, Br, and I) are relatively depleted. This is mainly due to the much larger radii of Cl^-, Br^-, and I^- compared to that of F^-, which cause them to partition strongly into fluids rather than into the crystal structures of major rock-forming minerals (Bureau et al., 2000; Mi and Pan, 2018). In addition, chemical weathering may enhance halogen depletions, as a large portion of halogens in crustal rocks, especially Cl, Br, and I (up to 70-100%), are water-soluble and leachable if they mainly reside in soluble phases like halides, or in fluid inclusions, and/or absorb to mineral surfaces (Fuge et al., 1978; Hanley et al., 2004; Burisch et al., 2016). However, the degree to which halogens are leached out of crustal rocks is still uncertain, as is the degree to which leached halogens could be later incorporated into crystal lattices of secondary minerals formed during chemical weathering and/or absorbed onto mineral surfaces. The only study to address halogen behavior during chemical weathering directly, to our knowledge, is Kronberg et al. (1987), who documented Cl and I accumulation rather than depletion as weathering advances, likely due to atmospheric additions from rains and/or aerosols; they also observed no significant Br variations in weathering profiles. Without knowing the weathering behavior of halogens, it is hard to determine whether there is a systematic preservation or loss of Cl, Br, and I from the continental crust due to chemical weathering and how this may have affected the composition of the continents. This situation is further complicated by the enrichment of halogens in soil and organic matter on the continental surface, as halogens can be fixed in organic compounds via biotic and/or abiotic processes and/or absorbed onto metal oxides and clay minerals during pedogenesis (e.g., Price and Calvert, 1977; Kabata-Pendias, 2000; Leri

and Ravel, 2015; Yamasaki et al., 2015; Takeda et al., 2018; Roulier et al., 2019; Epp et al., 2020; Epp et al., 2022; Neidhardt et al., 2022).

An essential step in quantifying the behavior of halogens in the continental crust is to have a more accurate estimate of their crustal concentrations. To date, there are only three individual halogen estimates available for the upper continental crust (UCC) (Shaw et al., 1967 and 1976; Wedepohl, 1995; Gao et al., 1998) and a fourth, for I, that can be calculated from the information provided in Muramatsu and Wedepohl (1998). There is, however, disparity among these previous estimates, especially those of Wedepohl (1995), which are significantly higher than the others for all halogens (Table 1 and Fig. 1). The relatively high UCC concentrations of Wedepohl (1995) could partly reflect the many halogen-rich samples like shales and carbonates incorporated into his UCC compositional model. By contrast, estimates from Shaw et al. (1967 and 1976) and Gao et al. (1998) were directly averaged from large-scale sampling of the Canadian shield and eastern China, respectively, with the former mainly comprised of Precambrian igneous and metamorphic rocks and the latter dominated by crystalline basement rocks and sedimentary cover from both Precambrian cratons and Phanerozoic fold belts. In addition, the much lower I estimate (0.218 ppm) updated by Muramatsu and Wedepohl (1998) from the 1.6 ppm of Wedepohl (1995) also raises concerns about the quality of the data used in Wedepohl's 1995 UCC model. In general, previous halogen estimates in the UCC were hampered by the very low and heterogenous halogen concentrations in crustal rocks and the challenges of obtaining precise and accurate halogen concentrations at low abundances (especially for Br and I).

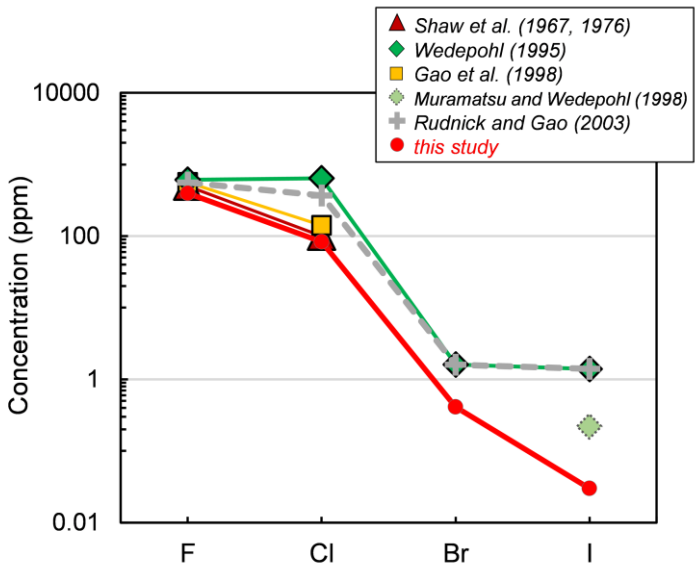

Fig. 1. Halogen (F, Cl, Br, and I) abundance estimates of the UCC from previous studies and this study. Note that the values in Rudnick and Gao (2003) are averaged or compiled from Shaw et al. (1967, 1976), Wedepohl (1995), and Gao et al. (1998).

In this study, we use the fine-grained matrix of ancient glacial diamictite composites to constrain halogen concentrations of the UCC. Glacial diamictite is a poorly-sorted, terrigenous sedimentary rock deposited when glaciers melted after having scrapped across the continental surface. The sediments they carry sample exposed crust that was physically eroded. The glacial diamictite composites analyzed in this study were created from the fine-grained matrix of individual diamictites deposited at ~2.9 Ga, ~2.4–2.2 Ga, 0.75–0.58 Ga, and ~0.30 Ga (Gaschnig et al., 2016). Previous studies revealed that these samples record the secular evolution of the average composition of the UCC, and carry an inherited weathering signature from their source regions (Gaschnig et al., 2014; Chen et al., 2016; Gaschnig et al., 2016; Li et al., 2016; Chen et al., 2020; Greaney et al., 2020). We employ two advanced halogen analytical methods to determine halogen concentrations in the diamictite composites: (1) F, Cl, and Br analyses by combustion ion chromatography (C-IC) of Epp et al. (2019),

and (2) Cl, Br, and I analyses by inductively coupled plasma mass spectrometry (N-ICPMS, in which the *N* represents the digestion of bulk rock samples by NH_4HF_2) of He et al. (2019). X-ray diffraction (XRD) data are used to determine the mineralogy of the diamictite composites. Combined with previously reported whole-rock major and trace element data, we use the new halogen and XRD data to: (1) assess halogen (F, Cl, Br, and I) behavior during continental weathering and the secular change of halogen concentrations in the UCC, (2) estimate halogen concentrations of the present-day crystalline and weathered UCC, and (3) explore relationships between the continental crust and other terrestrial reservoirs in Earth's halogen cycle.

Table 1. Halogen concentrations of the UCC

F (ppm)	Cl (ppm)	Br (ppm)	I (ppm)	References	*Note*
500	100	-	-	Shaw et al (1967,1976)	*large-scale sampling from the Canadian shield*
561	142	-	-	Gao et al (1998)	*large-scale sampling from Eastern China*
611	640	1.6	1.4	Wedepohl (1995)	*model-calculation based on various UCC lithologies*
-	-	-	0.218*	Muramatsu and Wedepohl (1998)	*model-calculation based on various UCC lithologies*
557	370	1.6	1.4	Rudnick and Gao (2003)	*averaged or compiled from previous studies*[#]
394 ± 67	*83 ± 24*	*0.41 ± 0.04*	*0.03 ± 0.01*	This study[§]	*ancient glacial diamictites (regression approach)*

***** The UCC iodine abundance (0.218 ppm) was not directly reported by Muramatsu and Wedepohl (1998) but is calculated based on their UCC lithologic model and the reported I concentrations of different types of crustal rocks.

[#] Rudnick and Gao overlooked the work of Muramatsu and Wedepohl (1998) in their compilation, which is why their value only reflects that of Wedepohl, (1995).

[§] Estimates from this study represent minimum halogen concentrations in the present-day crystalline UCC (see discussion in the text).

2.2. Samples

The 24 glacial diamictite composites investigated here were created from 122 individual samples, with each composite sample representing one stratigraphic unit (Gaschnig et al., 2016). In generating these composites, the fine-grained matrix was isolated from clasts (larger than ~5 mm) by visual inspection and then pulverized, and equal weight aliquots of samples from multiple outcrops or drill cores of a particular formation were combined. The depositional ages of the samples cover four geological periods: Mesoarchean (~2.9 Ga), Paleoproterozoic (~2.4–2.2 Ga), Neoproterozoic (0.75–0.58 Ga), and Paleozoic (~0.30 Ga). Details of the sampling localities, stratigraphic units, sample preparation procedures, and whole-rock geochemical data can be found in Gaschnig et al. (2014, 2016). A number of studies have been conducted on the same suite of composites to track the elemental and isotopic composition of the UCC through time, including Re-Os isotopes and platinum-group element contents (Chen et al., 2016), Li and Pb isotopes (Li et al., 2016), N content and isotopes (Johnson and Goldblatt, 2017), Ba isotopes (Nan et al., 2018), ^{182}W isotopes (Mundl et al., 2018), Ni isotopes and S content (Wang et al., 2019), Cu and Ag contents (Chen et al., 2020), Mo content in sulfides (Li et al., 2020), Mo isotopes (Greaney et al., 2020), Fe isotopes (Liu et al., 2022), and Si isotopes (Murphy et al., 2022). These studies demonstrate that the glacial diamictites are generally reliable proxies for the evolving composition of the UCC and record interaction between the continental surface and Earth's atmosphere and hydrosphere.

2.3. Analytical methods

2.3.1. Mineralogical analyses

Petrography and XRD analyses were carried out to determine the mineralogy of the diamictites. The former was performed on polished thin sections of individual samples (Fig. S1), while the latter was conducted on the powder of the diamictite composites. XRD was performed at the Mineralogy Facility at the Indiana University in Bloomington, IN. X-ray diffraction patterns were recorded with a Bruker D8 Advance X-Ray Powder Diffractometer, using CuK_{α} radiation and a Sol-X energy dispersive point detector. Powdered samples were scanned from 2 to 70° 2θ with a step size of 0.02° and a count time of 2 seconds. The patterns were analyzed by Rietveld refinement (Rietveld, 1969; Bish and Post, 1993) with TOpas (Bruker AXS) software to quantitatively determine mineral abundances, with uncertainties determined by the variance of the least squared fit. The XRD results are reported in Table S1 and shown in Fig. S2.

2.3.2. Halogen analyses

Halogen concentrations (Table 2) were analyzed using two different methods: (1) Combustion ion chromatography analysis (C-IC) for F, Cl, and Br (Fachbereich Geowissenschaften, Universität Tübingen) and (2) NH_4HF_2 digestion and ICPMS analysis (N-ICPMS) for Cl, Br, and I (State Key Laboratory of Geological Processes and Mineral Resources, China University of Geosciences, Wuhan).

Table 2. Halogen concentrations of the glacial diamictite composites

Samples	Locality (country)	Age (Ga)	F ± 2σ (ppm)*		Cl ± 2σ (ppm)*		Br ± 2σ (ppm)*		I ± 2σ (ppm)*	
			C-IC	*N-ICPMS*	*C-IC*	*N-ICPMS*	*C-IC*	*N-ICPMS*	*C-IC*	*N-ICPMS*
Mozaan	S Africa	2.9	91 ± 8	-	8 ± 9	3 ± 2	0.3 ± 0.7	0.19 ± 0.10	-	0.01 ± 0.03
Afrikander	S Africa	2.9	36 ± 13	-	12 ± 4	16 ± 4	0.2 ± 0.5	0.18 ± 0.05	-	0.01 ± 0.01
Coronation	S Africa	2.9	219 ± 8	-	5 ± 3	6 ± 3	0.2 ± 0.3	0.40 ± 0.24	-	0.03 ± 0.07
Promise	S Africa	2.9	148 ± 10	-	13 ± 5	15 ± 8	0.2 ± 0.0	0.28 ± 0.13	-	0.02 ± 0.05
Ramsay Lake	Canada	2.4	343 ± 52	-	49 ± 2	68 ± 17	0.6 ± 0.4	0.22 ± 0.05	-	0.01 ± 0.01
Gowganda	Canada	2.4	297 ± 40	-	62 ± 27	90 ± 22	0.4 ± 0.6	0.48 ± 0.12	-	0.02 ± 0.01
Bottle Creek	USA	2.4	263 ± 32	-	110 ± 14	137 ± 34	0.1 ± 0.4	0.24 ± 0.06	-	0.02 ± 0.01
Bruce	Canada	2.4	365 ± 45	-	68 ± 11	113 ± 29	0.3 ± 0.2	0.54 ± 0.14	-	0.04 ± 0.01
Makganyene	S Africa	2.3	386 ± 25	-	27 ± 6	38 ± 10	0.2 ± 0.4	0.21 ± 0.05	-	0.03 ± 0.01
Timeball	S Africa	2.2	384 ± 103	-	13 ± 2	7 ± 4	0.1 ± 0.0	0.29 ± 0.01	-	0.01 ± 0.01
Duitschland	S Africa	2.4	830 ± 90	-	38 ± 12	37 ± 9	0.1 ± 0.1	0.36 ± 0.22	-	0.01 ± 0.01
Konnarock	USA	0.7	725 ± 72	-	29 ± 12	65 ± 16	0.3 ± 0.6	0.74 ± 0.03	-	0.01 ± 0.01
Gaskiers	Canada	0.58	384 ± 44	-	80 ± 15	137 ± 34	0.3 ± 0.1	0.78 ± 0.19	-	0.04 ± 0.01
Pocatello	USA	0.7	1051 ± 10	-	15 ± 5	14 ± 7	0.1 ± 0.1	0.68 ± 0.17	-	0.08 ± 0.02
Nantuo	China	0.64	497 ± 16	-	18 ± 4	15 ± 8	0.1 ± 0.1	0.51 ± 0.13	-	0.05 ± 0.01
Gucheng	China	0.7	475 ± 67	-	14 ± 6	8 ± 4	0.3 ± 0.3	0.48 ± 0.03	-	0.06 ± 0.02
Blaubeker	Namibia	0.7	384 ± 20	-	17 ± 6	48 ± 12	0.4 ± 1.0	0.63 ± 0.16	-	0.21 ± 0.05
Kaigas	Namibia	0.75	895 ± 43	-	52 ± 8	64 ± 16	0.2 ± 0.2	0.51 ± 0.13	-	0.32 ± 0.08
Chuos	Namibia	0.7	775 ± 70	-	14 ± 5	2 ± 1	0.3 ± 0.0	0.53 ± 0.10	-	0.39 ± 0.01
Numees	Namibia	0.6	558 ± 122	-	154 ± 24	279 ± 70	0.1 ± 0.3	0.61 ± 0.15	-	0.26 ± 0.06
Ghaub	Namibia	0.64	612 ± 134	-	41 ± 9	56 ± 2	0.3 ± 0.6	0.36 ± 0.02	-	0.75 ± 0.08
Bolivia	Bolivia	0.3	404 ± 26	-	24 ± 7	23 ± 6	0.4 ± 1.0	0.46 ± 0.09	-	0.01 ± 0.01
Dwyka East	S Africa	0.3	506 ± 13	-	20 ± 5	16 ± 4	0.1 ± 0.0	0.43 ± 0.11	-	0.06 ± 0.01
Dwyka West	S Africa	0.3	349 ± 101	-	55 ± 5	57 ± 14	0.4 ± 0.1	0.51 ± 0.13	-	0.06 ± 0.02

*Fluorine, Cl, Br, and I concentrations of the diamictites are obtained by C-IC and/or N-ICPMS. The reported uncertainties are 2σ of repeated analyses. However, when repeated analysis is not available for the N-ICPMS data, the uncertainties (underlined) are estimated at 25% of the measured concentrations, according to uncertainty levels revealed by the analyzed reference materials (see Table S2). Moreover, for samples Cl and I content close to detection limits (i.e., < 15 ppm, and < 15 ppb, respectively), their uncertainties (also underlined) are estimated at 50%.

2.3.2.1. Combustion ion chromatography analysis (C-IC) for F, Cl, and Br

The C-IC is an automated combination of combustion digestion (or pyrohydrolysis) and ion chromatography. For combustion, a mixture of 5-15 mg sample powder mixed with the same amount of WO_3 powder was placed into a quartz vial that was capped on both sides with quartz wool. The vial was placed into a quartz vessel where the sample was combusted at 1050°C for 12 min in a flow of Ar (100 mL/min) and O_2 (300 mL/min), while a constant water flow (0.2 mL/min) was maintained to collect the released halogens. The loaded steam was collected in an absorber module containing 4 ml of 500 ppm H_2O_2 solution. After matrix elimination (using a Metrosep A PCC 2 HC/4.0 column), the solutions were injected into the ion chromatograph (for more details see Epp et al. (2019)). The effective detection limits are about 10 ppm for F and Cl, and about 0.2 ppm for Br. All samples were analyzed at least twice and accuracy was monitored through analysis of international reference material GS-N (granite). In order to cross-check the C-IC results with the Cl and Br results from the N-ICPMS analysis, reference materials BE-N (basalt), BHVO-2 (basalt), AGV-2 (andesite), GSR-2 (andesite), and GSP-2 (granodiorite) were also analyzed (Table S2). Based on replicate analyses of reference materials, the precision of the measurements is better than 10% for F, 20% for Cl, but much higher (up to 250%) for Br (2 RSD), as Br concentrations in the reference materials and diamictite samples are close to the detection limit (around 0.2 ppm, see above).

2.3.2.2. NH_4HF_2 digestion and ICPMS analysis (N-ICPMS) for Cl, Br, and I

For the N-ICPMS analyses, 100 mg of whole rock powder was mixed with 400 mg of NH_4HF_2 in a 15 ml screw-top Teflon vessel and then placed in an oven at 220°C for 2h.

Upon cooling, the digested cake was transferred to a polyethylene bottle and then diluted to 25 g via 5% v/v NH_4OH solution. Ten µl of an internal standard solution of Te (10 µg/ml) was added to 1 ml of supernatant solution of the digested sample in a new polyethylene tube. The supernatant was then analyzed using an ELEMENT XR inductively coupled plasma sector field mass spectrometer. More details of the method can be found in He et al. (2019). Detection limits for this method are 5 ppm for Cl, 15 ppb for Br, and 5 ppb for I (He et al., 2019). The same reference materials measured by C-IC (i.e., BE-N, BHVO-2, AGV-2, GSR-2, GSP-2, and GS-N) were also analyzed as unknowns by N-ICPMS (Table S2). Precision of the method is typically better than 25% (2 RSD). However, the precision for I is much poorer (with 2 RSD > 45%) when the measured I content is lower than 15 ppb (i.e., close to the detection limit).

2.3.2.3. Inter-laboratory comparison of halogen results

The six reference materials and the 24 glacial diamictite composites analyzed in this study by both C-IC and N-ICPMS can be used to cross-check the results from the two analytical methods. In Fig. S3, the F-Cl-Br data for the reference materials obtained by C-IC and the Cl-Br-I data from N-ICPMS are plotted together with GeoReM data (Jochum et al., 2005) compiled from previous studies (Table S2). The F contents determined by C-IC show good agreement with the GeoReM values, demonstrating their accuracy. Analyses of Cl and Br by C-IC and N-ICPMS are generally in agreement with their GeoReM values within uncertainties, except for Cl and Br in GSP-2. In fact, the halogen concentrations of GSP-2 remain poorly constrained due to limited analyses (Table S2), and the discrepant Cl and Br

estimates for GSP-2 may be due to sample heterogeneity or to variable recovery yields for the different methods.

The Cl and Br concentrations determined by C-IC are often lower (by 25–50%) than those determined by N-ICPMS in both the reference materials and the diamictites (Fig. S4), which is consistent with previous reports of incomplete halogen recovery by pyrohydrolysis (e.g., Marks et al., 2017; Kendrick et al., 2018a). At the same time, a few samples with very low N-ICPMS Cl (< 15 ppm) and Br (< 0.3 ppm) contents have comparatively high C-IC Cl and Br contents (Fig. S4), which is likely due to the large analytical uncertainties of the C-IC analysis when sample concentrations are close to detection limits. The I concentrations in the analyzed reference materials are not well-constrained (as one can see from the large error bars in Fig. S3d), which makes it difficult to assess the accuracy of the I analysis of the N-ICPMS method. Despite this, all of the measured I contents in the reference materials by N-ICPMS are located within the range of previously reported values (Fig. S3d). In addition, He et al. (2019) assessed the long-term stability of N-ICPMS I analyses by repeat analyses of the reference material BHVO-2 (n = 7) over a one-year period, and found it was constant at 0.046 ± 0.010 ppm (2σ). These data demonstrate the reliability of I analyses by N-ICPMS. Based on the above results for international reference materials and inter-laboratory comparisons, we use the F data from C-IC and the Cl, Br, and I data from N-ICPMS (Table 2) to investigate the behavior of halogens in the glacial diamictite composites.

2.4. Results

2.4.1. Mineralogy

The XRD mineral abundances of the diamictite composites (Table S1 and Fig. S2) are consistent with thin section examination of individual samples (Fig. S1), with most comprised mainly of quartz, plagioclase, K-feldspar, mica, chlorite, and sometimes carbonate. Quartz is the most abundant mineral, which makes up 17–62% of the matrix of each sample. Plagioclase is generally sericitized (Fig. S1d), and the XRD results show that > 70% of plagioclase is now albite. Illite and muscovite are difficult to distinguish based on the XRD spectra, so they are grouped together in this study. A few samples contain significant carbonate (calcite/dolomite/siderite), amphibole, hematite, magnetite, and corundum, which is probably related to their distinct provenances. Accessory phases like apatite, titanite, epidote, and zircon are also observed in thin section, but not detected by XRD, which is likely due to their overall low abundances.

2.4.2. Halogen concentrations

Halogen concentrations in the diamictite composites are summarized in Table 2 and plotted in Fig. 2. Fluorine concentrations range from 36 to 1051 ppm, with most composites centering around 300–600 ppm (Fig. 2). In general, the Paleozoic and Neoproterozoic diamictites contain higher F (349–1051 ppm) compared to Mesoarchean and Paleoproterozoic diamictites (36–830 ppm). Chlorine concentrations are more variable, ranging over two orders of magnitude from 2 to 279 ppm, which are all lower than the reported UCC Cl abundance (370 ppm) (Rudnick and Gao, 2003). In contrast to Cl, Br concentrations show a narrower range, varying from 0.18 to 0.78 ppm. These values are

much lower than the previous UCC Br estimate (1.6 ppm) from Wedepohl (1995). As for the I concentrations, the 24 diamictite composites can be divided into two groups: (1) the five Neoproterozoic composites from Namibia (Blaubeker, Kaigas, Chuos, Numees, and Ghaub formations) have distinctively high I contents (0.21–0.75 ppm); and (2) the rest of the diamictite composites show significantly lower I concentrations, ranging from 0.01 to 0.08 ppm.

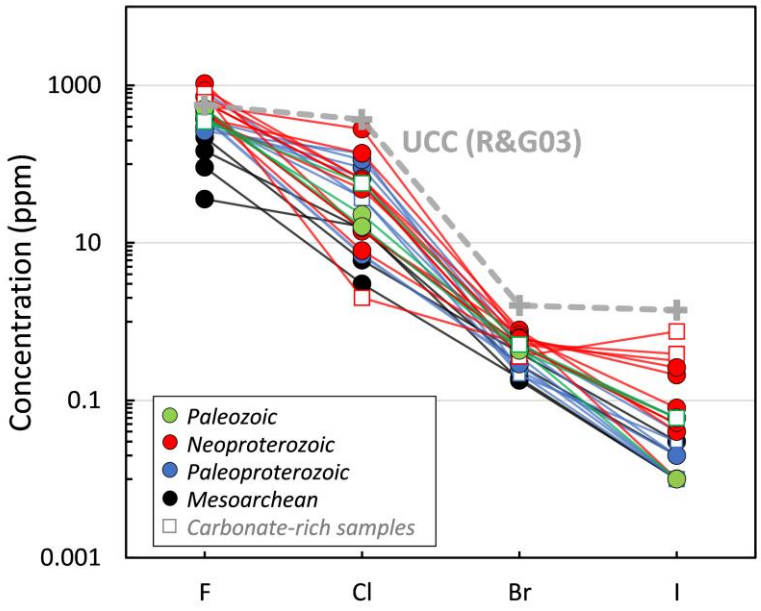

Fig. 2. Halogen concentrations of the glacial diamictite composites. Here and elsewhere, the F data are from C-IC analyses, while Cl, Br, and I data are from N-ICPMS analyses. Samples with different depositional ages are shown in solid circles of different colors. Open squares show carbonate-rich samples (i.e., Duitschland, Makganyene, Chuos, Ghaub, and Dwyka West). The gray dashed line ("R&G03") represents the average UCC halogen abundances from Rudnick and Gao (2003).

2.5. Discussion

2.5.1. Processes controlling the mineralogy of the diamictites

The diamictites are mainly composed of quartz, plagioclase, K-feldspar, clay/mica and chlorite, as well as variable amounts of carbonate. Of these minerals, quartz is the most abundant, consistent with its resistant nature during chemical weathering and transport (Nesbitt and Young, 1989). By contrast, plagioclase content decreases with increasing chemical index of alteration values (CIA = molar Al_2O_3 / (Al_2O_3 + CaO*+ K_2O + Na_2O, where CaO* is corrected for carbonate and apatite (Nesbitt and Young, 1982) and the carbonate correction is based on the approach of McLennan (1993)), especially when CIA values are higher than ~60 (Fig. 3a). This is consistent with the susceptibility of plagioclase to chemical weathering (Nesbitt and Young, 1989). When CIA values are < 60, different samples have, however, variable plagioclase contents, which probably reflects their provenances. Plagioclase contents also correlate well with whole-rock Na_2O concentrations (Fig. 3b), a correlation consistent with the composition of a pure albite (Na-plagioclase, $NaAlSi_3O_8$), which not only supports the XRD result that plagioclase is dominantly albite (Table S1), but also indicates that Na in the diamictites is mainly hosted in plagioclase. Albite in sedimentary rocks can be produced by two processes: (1) preferential loss of the anorthite component from plagioclase during chemical weathering (Clayton, 1986; Vázquez et al., 2016), and/or (2) albitization of Ca-rich plagioclase and/or K-feldspar during diagenesis (e.g., Boles, 1982; Saigal et al., 1988; Aagaard et al., 1990; Morad et al., 1990; González-Acebrón et al., 2010). Though it is difficult to distinguish between these two processes based on our data, the dominance of albite in all of the diamictite composites,

irrespective of the extent of chemical weathering they record, suggests that most albites are of diagenetic origin.

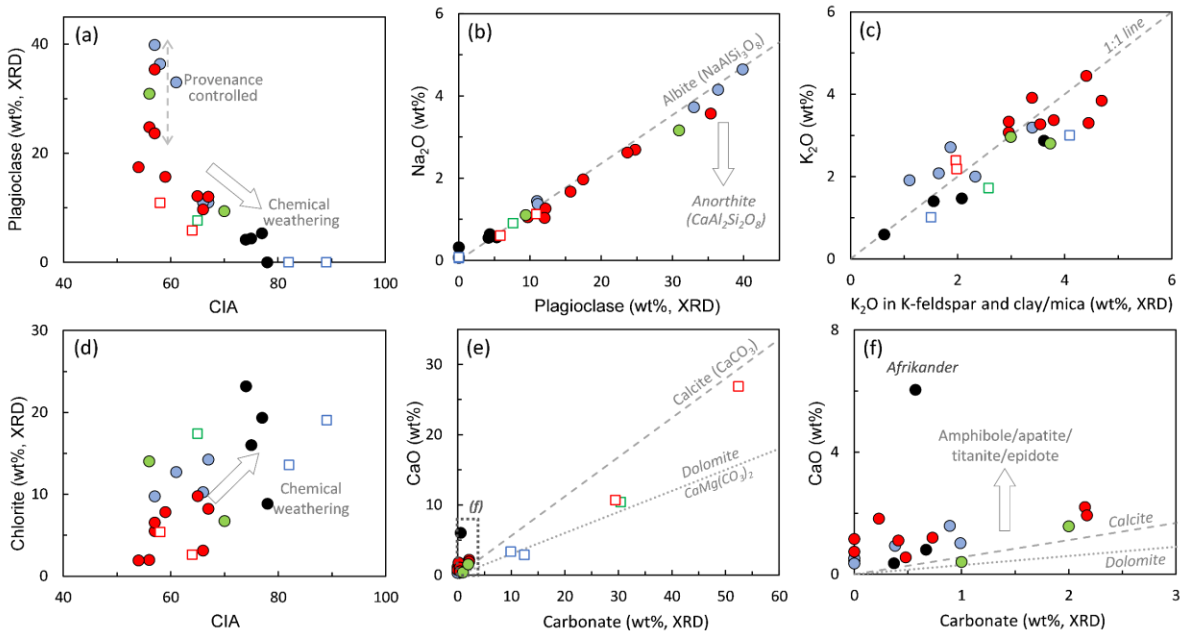

Fig. 3. Mineral modes from X-ray diffraction (provided in Table S1) compared to major element concentrations of the diamictite composites (Gaschnig et al., 2016). Symbols as in Fig. 2. CIA in (a) and (d) stands for chemical index of alteration, a measure of chemical weathering intensity (see text for calculation). The x-axis of plot (c) is the sum of K_2O content that is hosted by K-feldspar and clay/mica (a combination of illite-muscovite and biotite), which is calculated from the XRD K-feldspar and clay/mica contents and their K_2O proportions in chemical formula (i.e., 17% *K-feldspar + 12% clay/mica).

Albitization of plagioclase and/or K-feldspar often occurs during the middle to late stages of diagenesis, when temperatures reach 75–160°C during deep burial of sediments (e.g., Boles, 1982; Ramseyer et al., 1992; Schrank and De Ros, 2015). At similar or slightly higher temperatures (80–200°C), clay minerals like kaolinite, smectite, and vermiculite can be gradually transformed to illite, muscovite, and chlorite (e.g., Segonzac, 1970; Árkai, 2002). Small euhedral muscovite and chlorite grains are common in the diamictites (Fig. S1e-f).

Combined with the lack of kaolinite and smectite from the XRD analyses, it is likely that most of the original clay minerals were recrystallized to illite-muscovite and chlorite during diagenesis. In a few samples, euhedral biotite and actinolite are also observed (Fig. S1e and S1h). As these two phases are usually formed at ~350°C, near the biotite isograd of pelitic rocks (McDowell and Elders, 1980), it seems that a few of the diamictites were subjected to greenschist facies metamorphism. The summed K_2O content of clay/mica (i.e., illite-muscovite and biotite) and K-feldspar correlates well with whole rock K_2O (Fig. 3c). Based on the typically higher modal abundances of clay/mica compared to K-feldspar (Table S1), we conclude that K is mainly hosted in clay/mica. Chlorite is instead more concentrated in Mg-Fe rich samples, and a scattered, positive correlation is also observed between chlorite and CIA values (Fig. 3d). Therefore, the abundance of chlorite could be controlled by not only the whole-rock Mg and Fe contents, but also the extent of weathering.

Five diamictite composites (Duitschland, Makganyene, Chuos, Ghaub and Dwyka West) have XRD carbonate content near or above 10 wt.% (Table S1 and Fig. S2). In these samples, angular carbonate clasts are observed in thin sections (Fig. S1b-c), indicating a detrital origin. The distribution between the XRD carbonate content and whole-rock CaO concentration supports the XRD result that the carbonate in these samples is not pure calcite, but also contains significant dolomite-ankerite (Fig. 3e). As carbonates may contain more halogens than silicate phases (Rude and Aller, 1991; Lu et al., 2010; Wang et al., 2020), the five diamictites enriched in carbonate are designated as “carbonate-rich” in the following discussion and are plotted as open squares in the figures. By contrast, the other samples are grouped as “carbonate-poor.” In the carbonate-poor diamictites, whole rock CaO concentrations are generally higher than that can be accounted for by carbonate (Fig. 3f).

Based on thin section examination, the excess Ca is likely hosted in amphibole (note that there is 28 wt.% amphibole in the Afrikander diamictite, which also has the highest CaO content), apatite, titanite, and epidote.

2.5.2. Halogen behavior in the diamictites

2.5.2.1. Fluorine

Except for a few carbonate-rich samples, F correlates well with the concentrations of incompatible elements such as K_2O ($R^2 = 0.64$), P_2O_5 ($R^2 = 0.84$), and Nd ($R^2 = 0.89$) (Fig. 4a-c). As K, P, and Nd are not typically lost during chemical weathering (Gaschnig et al., 2016), F could be similarly retained in the diamictites. This is consistent with the reported low mobility of F during chemical weathering (Kronberg et al., 1987; Sallet et al., 2019). Despite this, F depletion, as measured by its normalized abundance relative to elements of similar incompatibility during igneous differentiation ($F/F^* = F_n/(Pr_n/Nd_n)^{0.5}$, in which the concentrations of F, Pr, and Nd are normalized to the primitive mantle, McDonough and Sun (1995)), negatively correlates with the CIA values (Fig. 5a), suggesting that some F may be lost during chemical weathering. This is consistent with the observation that fluorides are commonly found in groundwater, rivers, and seawater (e.g., Bruland and Lohan, 2003; Berger et al., 2016).

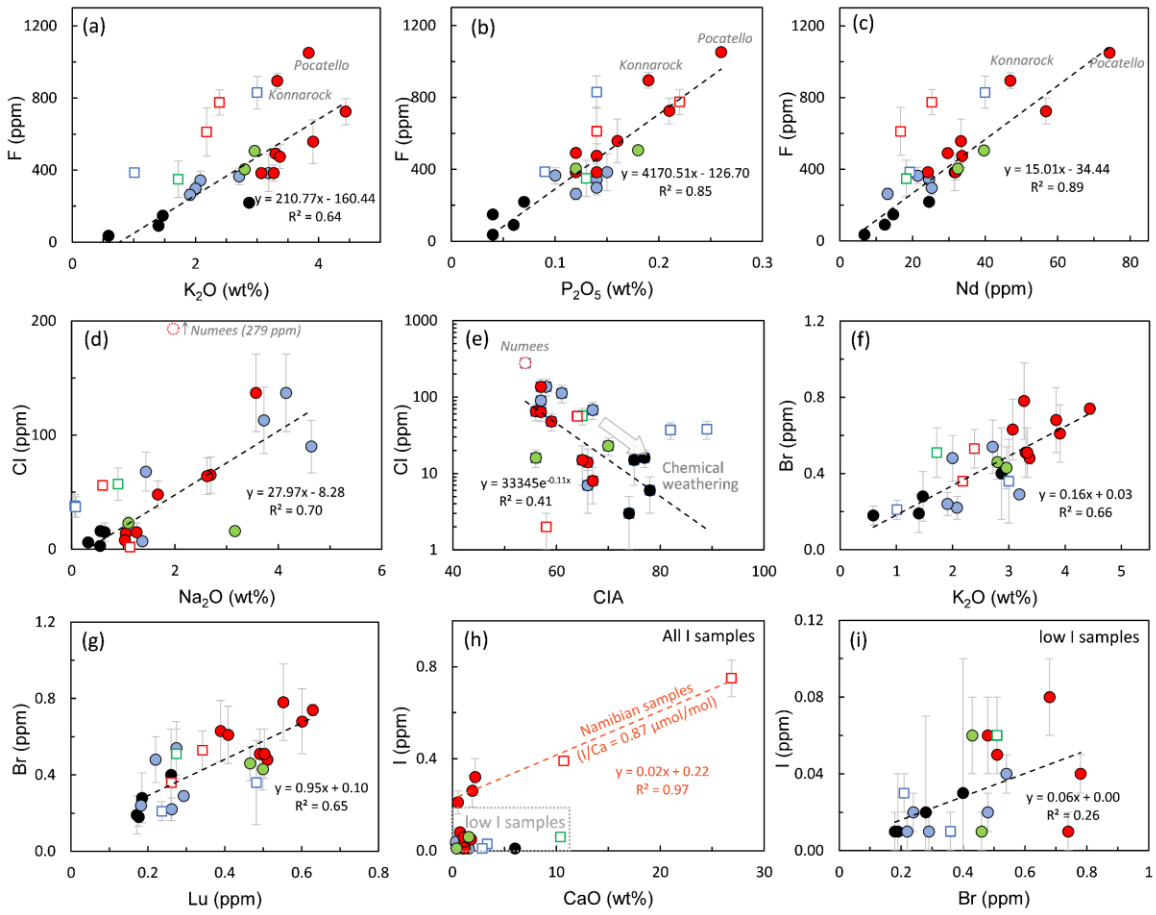

Fig. 4. Correlations between halogen (F, Cl, Br, and I) and other elements (or CIA values) in the diamictites. Symbols as in Fig. 2. Error bars of halogen concentrations are shown as 2σ. The regression lines are mainly calculated from samples shown as solid circles, i.e., excluding carbonate-rich samples (open squares) and the Numees for Cl (dotted open circle); the exception is the regression line in (h) that is calculated from all five Namibian samples (Blaubeker, Kaigas, Chuos, Numees, and Ghaub), which include carbonate-rich samples.

The correlations between F, K and P suggest that clay/mica and apatite are the two main hosts of F. Most carbonate-rich diamictites lie above the regression line defined by others (Fig. 4a-c), revealing that carbonate may be an additional host of F. High F content (up to ~1600 ppm) has been observed in marine carbonate (Rude and Aller, 1991), which is suggested to be due to the substitution of two F^- for the $[CO_3]^{2-}$ group (Feng et al., 2021). In

addition, the Neoproterozoic Pocatello and Konnarock composites have unusually high F contents (1051 and 725 ppm, respectively), as well as K, P, Ti, Nb, and Ta, which reflects the dominance of A-type granites in their provenances (Gaschnig et al., 2016), as A-type granites commonly have relatively high F contents (0.05–1.7 wt.%) (Whalen et al., 1987; Eby, 1990).

2.5.2.2. Chlorine

Chlorine correlates with the highly soluble element Na ($R^2 = 0.70$), except for the Numees composite, which has an anomalously high Cl content of 279 ppm (Fig. 4d). Two hypotheses could explain the observed Na-Cl correlation: (1) the presence of halite (NaCl) in the diamictites, and/or (2) Na and Cl were similarly leached from source rocks during chemical weathering. No halite (NaCl) was detected by XRD, and because halite is not typically found in open shallow marine environments in which many of the glacial diamictites were deposited, the presence of halite is unlikely. Instead, the very low and scattered Cl concentrations in the diamictites compared to the average UCC (Fig. 2) indicate that Cl, like Na, was lost during chemical weathering. This explanation is supported by the negative correlations between Cl concentrations and CIA values (Fig. 4e). In addition, clay fractions from rivers, a highly weathered product, generally have < 45 ppm Cl (Sallet et al., 2019), similar to that of the diamictites with CIA values > 65. Overall, the above observations favor the hypothesis that Cl was removed during chemical weathering. The reason for the anomalously high Cl content (279 ppm) of the Numees composite is unclear, but could be related to a provenance with distinctly high Cl.

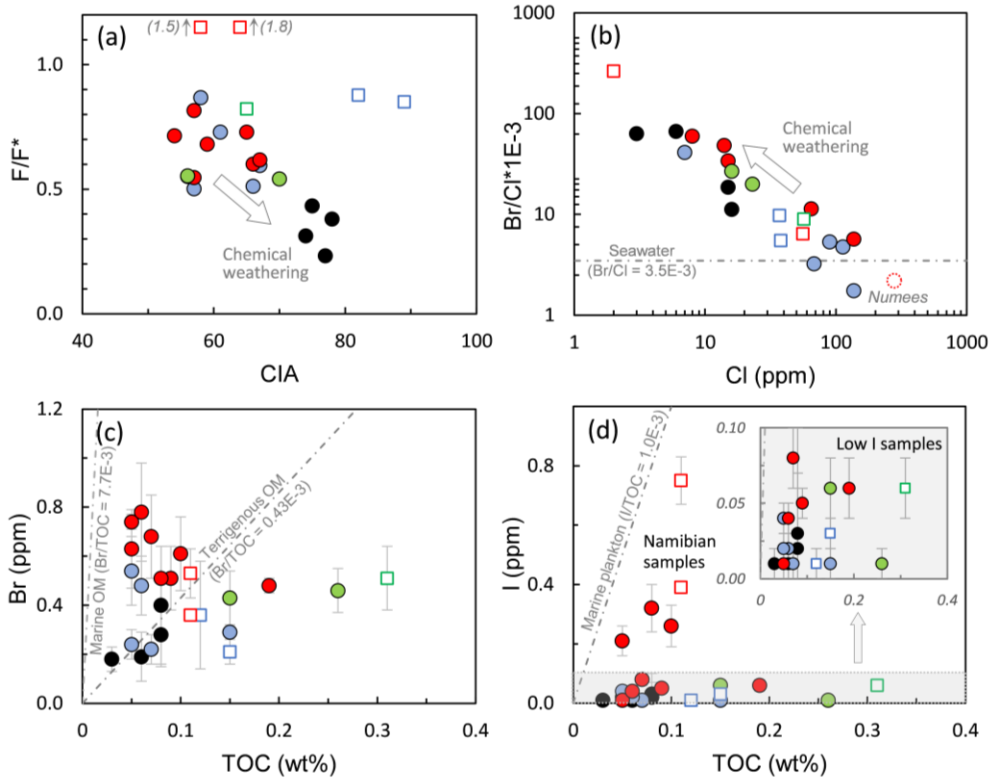

Fig. 5. (a) F/F* (the relative F depletion, defined as $F_n/(Pr_n/Nd_n)^{0.5}$, in which the concentrations of F, Pr, and Nd are normalized to the primitive mantle, McDonough and Sun (1995)) versus CIA values. The carbonate-poor diamictites show a decreasing trend with CIA values. **(b)** Br/Cl ratio versus the Cl content. Br/Cl ratios are elevated when the Cl content decreases, and most of them are higher than that of seawater (~$3.5*10^{-3}$, gray dash-dotted line). The decreasing Cl content may result from chemical weathering of source rocks (see text). **(c)** Br versus total organic carbon (TOC) content (TOC values from Greaney et al. (2020)). Br/TOC ratios for organic matter (OM) of terrestrial and marine sources ($0.43*10^{-3}$ and $7.7*10^{-3}$, respectively, from Mayer et al. (2007)) are plotted for comparison. **(d)** I versus TOC content; "low I samples" are shown in the inset. I/TOC ratio ($1.0*10^{-3}$, graded dash-dotted line) of typical marine organic matter, marine plankton, is plotted for comparison (Elderfield and Truesdale, 1980). Symbols as in Fig. 2.

Regarding the mineral host(s) of Cl, unlike Na, which is mainly hosted in plagioclase, Cl is likely hosted in carbonate and hydrous silicate phases such as apatite and clay/mica, like other halogens (F, Br, and I) (Mangler et al., 2014; Teiber et al., 2014). In addition, previous

crushing-heating analyses (Chavrit et al., 2016) and leaching experiments (Burisch et al., 2016) on typical crustal rocks like gabbro, granite, and sandstone showed that Cl, Br, and I can also be preserved in non-structural sites such as grain boundaries or melt/fluid inclusions. Though such data are not available for the diamictites, the general low compatibilities of these elements in crystal lattices suggest that some amount of Cl, Br, and I in the diamictites may also be contained in non-structural sites.

2.5.2.3. Bromine

The less scattered Br concentrations (Fig. 2), and correlations between Br and K_2O (R^2 = 0.66) and heavy rare earth elements like Lu (R^2 = 0.65) (Fig. 4f-g), suggest that Br behaves differently from Cl and has been preferentially retained in the diamictites. Their distinct behavior is also reflected in the elevated Br/Cl ratios, which largely reflects Cl depletion relative to Br (Fig. 5b). The "preservation" of Br in the diamictites can be explained by the following hypotheses: (1) leaching of Br from parent rocks is not as strong as Cl; or (2) Br is leached the same amount as Cl, but it was later retained by secondary minerals/organic matter contained within the weathered regolith. Because Br has a larger anionic radius (1.95 Å) than Cl (1.81 Å), making it harder to fit into the crystal lattice compared to Cl, the first hypothesis seems unlikely. So next we will focus on evaluating the second possibility, i.e., the retention of Br by secondary minerals and/or organic matter.

Bromine contents in organic-rich sediments and soils can be up to tens of ppm, which is generally 2–3 orders of magnitude higher than Br concentrations in most igneous and metamorphic rocks, which typically have < 1 ppm Br (Hanley and Koga, 2018). Such significantly elevated Br contents have received growing interest, as they suggest that Br in

natural ecosystems is more reactive than previously thought. Studies on organic-rich sediments and/or soils have shown that Br can be fixed in organic compounds via biotic and/or abiotic processes and absorbed onto metal oxides (Fe, Al oxides) and clay minerals during pedogenesis (e.g., Price and Calvert, 1977; Kabata-Pendias, 2000; Goldberg and J. Kabengi, 2010; Leri and Ravel, 2015; Yamasaki et al., 2015; Takeda et al., 2018; Epp et al., 2020; Epp et al., 2022; Neidhardt et al., 2022). Organic matter, Fe or Al oxides, and clay minerals all occur in the diamictite composites, though clays are much more abundant than the others. Organic matter content, based on total organic carbon (TOC) analyses, ranges from 0.03 to 0.26 wt.% (Greaney et al., 2020) and oxides such as hematite, magnetite, and corundum are only detected by XRD in a few of the composites, with scattered abundances from 0.8 to 11.5 wt.% (Table S1). By contrast, the sum of the clay content, including illite-muscovite, biotite, and chlorite, is higher than 18 wt.% in each diamictite composite and can even be up to 45 wt.% (Table S1 and Fig. S2). Combined with the good correlation between Br and K (Fig. 4f), we conclude that Br is mainly hosted by K-rich phases like clay/mica in the diamictites. However, the possibility of Br being hosted in organic matter still can not be completely ruled out, despite the poor correlation observed between Br and TOC (Fig. 5c), because Br has a strong biophile affinity and the Br content in natural organic matter can be affected by factors such as the types of organic matter (e.g., marine verus terrigneous origin, Mayer et al., 2007), abiotic processes (Leri and Ravel, 2015), and even the age of the organic matter (Cortizas et al., 2016).

If the “preservation” of Br in the diamictites is indeed mainly caused by K-rich clay/mica as suggested above, what specific phase(s) selectively incorporate and/or absorb Br over Cl and thus fractionate Br/Cl ratios? This remains is difficult to answer due to limited high-

quality Cl and Br data for terrigenous sediments. Based on the observation of decreased Br/Cl ratios of pore water extracted from highly altered volcaniclastic sediments from the New Hebrides trench, Martin (1999) concluded that Br/Cl ratios in altered volcaniclastic sediments are elevated due to hydrous alteration of the sediments to clay and zeolite. However, elevated Br/Cl ratios are not observed in altered oceanic crust. Rather, the Br/Cl ratios in these clay-bearing products are very close to, or even a little lower than, the seawater value (Kendrick, 2019a; Kendrick, 2019b). The reason for the contrasting behaviors of halogens in these two different alteration settings remains unclear, but could be related to the different secondary minerals that are, in turn, associated with the different compositions of the altered rocks. In fact, secondary minerals related to continental weathering are commonly Al- or K- rich (e.g., kaolinite and illite) due to the more felsic or evolved composition of the parental rocks, while those produced from mafic rocks of the oceanic crust are typically more Fe- or Mg- rich (e.g., chlorite, talc, and serpentine). This may explain why fractionated Br/Cl ratios are only observed during in continental weathering environments, or during hydrous alteration of volcaniclastic trench sediments, but not during alteration of the oceanic crust. Thus, it is possible that K-rich clay/mica and organic matter in the diamictites have both helped retain Br during continental weathering, though it is hard to tell which process plays a dominant role due to the limited data.

2.5.2.4. Iodine

All five Neoproterozoic diamictite composites from Namibia (Blaubeker, Kaigas, Chuos, Numees, and Ghaub formations) are characterized by high I contents and show a robust correlation with CaO ($R^2 = 0.97$) (Fig. 4h), indicating that carbonate is an important host of I

in some of these samples. In addition to I hosted by carbonate, the Namibian samples have a uniformly high I background concentration (around 0.25 ppm), as seen in the Blaubeker sample that contains little carbonate (0.48 wt.%) but has 0.25 ppm I. One possible cause of the high I background is addition of modern marine aerosols that can transport I from the oceans to continents (Muramatsu and Wedepohl, 1998). However, no other samples located close to the coast (e.g., Gaskiers, Dwyka east, and Mozaan, Fig. S5) have similarly high I contents, and neither the I nor $I_{decarbonated}$ (calculated by deducting the potential I hosted in carbonate from the total I content) concentrations of the Namibian samples show any correlations with proximity to the coast (Fig. S6). Therefore, it seems that aerosol contamination, if it exists, is not very significant in the Namibian diamictite composites.

On the other hand, the limited paleogeographic distribution of the Namibian samples may suggest that their elevated I contents result from I-rich sedimentary rocks/organic matter in their provenances. Indeed, the high I content of the Namibian diamictites is similar to those of sedimentary rocks/organic matter rather than igneous and metamorphic rocks (Fig. 6). Moreover, the relatively low I/TOC ratios of these samples (from $0.3*10^{-3}$ to $0.7*10^{-3}$) compared to those of marine sediments/organic matter (> ~$1.0*10^{-3}$) (Elderfield and Truesdale, 1980) (Fig. 5d) suggests that the I-rich sedimentary/organic inputs to the Namibian samples were largely sourced from a terrestrial and/or reducing environment, in which I/TOC ratios are affected by the low I concentrations and/or limited free O_2 of the depositional settings (Price and Calvert, 1977; Muramatsu and Wedepohl, 1998). The latter inference is supported by the very low I/Ca ratio (0.87 μmol/mol) calculated from the I-Ca correlation of the Namibian composites (Fig. 4h), which is significantly lower than the ~2.5 μmol/mol I/Ca for carbonate formed in well-oxygenated water (Lu et al., 2016).

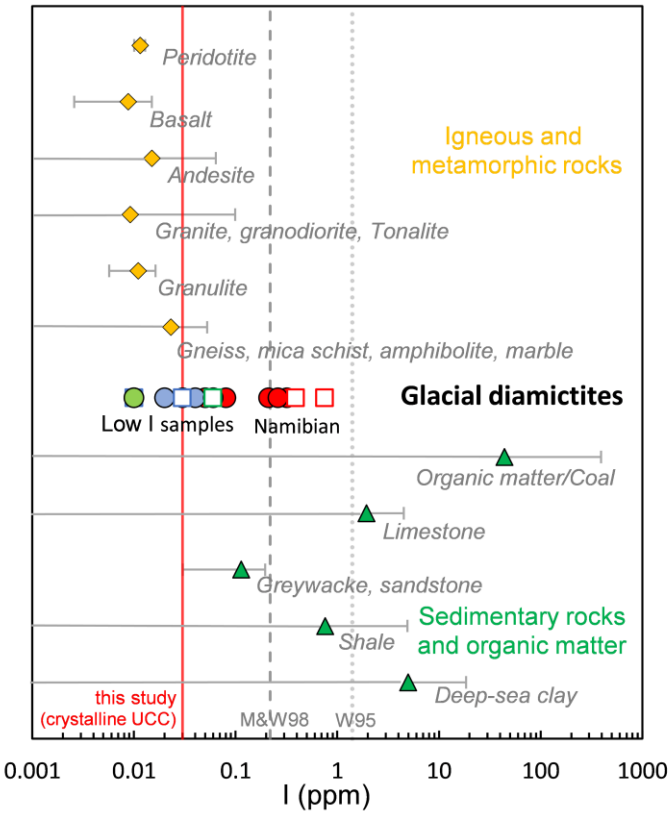

Fig. 6. Iodine concentration ranges of the glacial diamictites composites (symbols as in Fig. 2), and other types of terrestrial rocks that are divided to two groups: (1) igneous and metamorphic rocks, and (2) sedimentary rocks and organic matter (data from Muramatsu and Wedepohl (1998) and references therein). The orange diamonds and green triangles represent the median concentrations, with 2σ uncertainties, of groups (1) and (2), respectively. The three vertical lines represent different estimates for the I abundance of the UCC, in which 1.4 ppm (gray dotted, "*W95*") is from Wedepohl (1995), 0.218 ppm (gray dashed, "*M&W98*") from Muramatsu and Wedepohl (1998), and 0.03 ppm (red) that is for the present-day crystalline UCC from this study.

The remaining diamictite composites have much lower I concentrations, overlapping those of igneous and metamorphic rocks (Fig. 6). No correlation is observed between I and CaO in these samples, but there is a very weak, positive trend with Br ($R^2 = 0.27$) despite the large uncertainty of the I concentrations (Fig. 4i). Thus, it seems that I is similar to Br, being retained during chemical weathering. The specific mechanism responsible for the retention of

I remains unclear, but like Br, could be due to incorporation into and/or absorption onto clay/mica and organic matter during chemical weathering (see above) (Whitehead, 1984; Assemi and Erten, 1994; Kaplan et al., 2000; Hong et al., 2012; Epp et al., 2022).

2.5.3. Secular changes in halogen concentrations in the diamictites

The diamictites were deposited during four different time intervals (~2.9 Ga, ~2.4–2.2 Ga, 0.75–0.58 Ga, and ~0.30 Ga) and compositional changes over these time intervals reflect the evolving composition of the UCC (Gaschnig et al., 2016; Chen et al., 2020), including for the halogens. To remove the effect of dilution by quartz and other minerals during sedimentation (e.g., Fe oxides in the case of samples that incorporated BIF; Gaschnig et al., 2016), the halogen concentrations of the diamictites need to be normalized to an insoluble element whose concentration in the UCC is well documented. For this, we use the Al_2O_3 content of the diamictites and normalize them to the Al_2O_3 abundance of the UCC (15.26 wt.%, Rudnick and Gao, 2003). The normalized halogen concentrations (F_{Al}, Cl_{Al}, Br_{Al}, and I_{Al}) in the diamictites is shown in Fig. 7 as a function of depositional ages.

Excluding the carbonate-rich samples, F_{Al} concentrations of the diamictites gradually increase from ~2.9 Ga to ~0.3 Ga, and the Student's t-test shows that F_{Al} contents of the Neoproterozoic and Paleozoic composites are statistically different from those of the Mesoarchean and Paleoproterozoic composites ($P < 0.05$, Table S3). As F is not strongly affected by chemical weathering (see above), the increasing F_{Al} may reflect the evolving composition of the UCC and is generally consistent with the UCC changing from a more mafic composition in the Archean to a more differentiated composition with time (e.g., Taylor and McLennan, 1985; Condie, 1993; Gaschnig et al., 2016; Tang et al., 2016; Smit

and Mezger, 2017). Alternatively, other processes could also contribute to the varied F_{Al} concentrations of the diamictite composites as a function of age, such as the evolving composition of the mantle due to increased halogen recycling through time, and greater degrees of F loss by magmatic degassing/exsolution and chemical weathering in Earth's history. Further detailed discussion of the temporal evolution of the F concentrations of the diamictite composites can be found in section 2.5.5.1.

By contrast, Cl_{Al} concentrations in the diamictites are variable and show no clear trend with time, which is likely due to the high solubility of Cl during chemical weathering. Br_{Al} and I_{Al} (excluding the I-enriched Namibian samples) also show slightly increasing concentrations with time (Fig. 7), but no statistically significant trends are observed for them (Table S3) due to the large analytical errors.

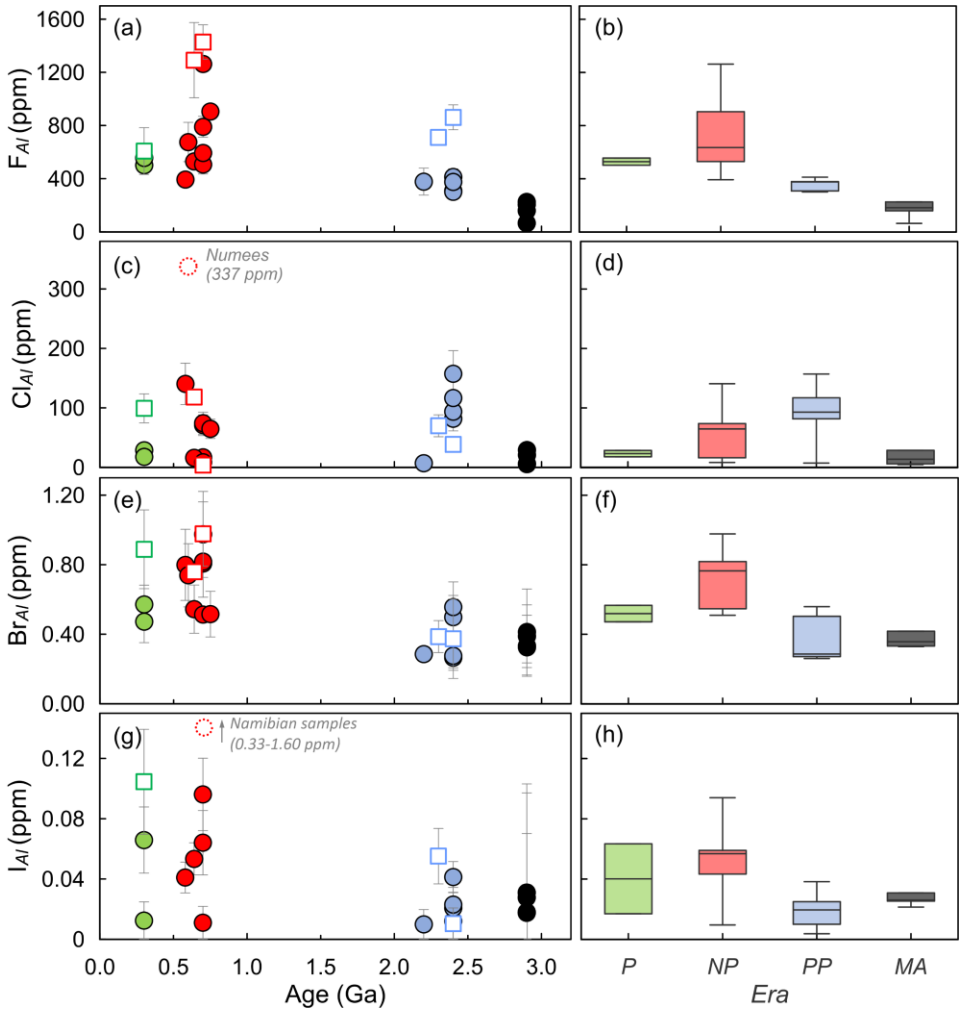

Fig. 7. Secular evolution of halogen concentrations in the glacial diamictites. **(a)**, **(c)**, **(e)**, and **(g)** represent the Al-normalized F, Cl, Br, and I concentrations of the diamictites, respectively (with 2σ uncertainties). Al-normalization is adopted to eliminate the effects of concentration dilution by the addition of quartz and Fe-oxides. Symbols as in Fig. 2. **(b)**, **(d)**, **(f)**, and **(h)** show the corresponding box-and-whisker plots for F_{Al}, Cl_{Al}, Br_{Al}, and I_{Al}, respectively. In the x-axis, *MA* is Mesoarchean, *PP* is Paleoproterozoic, *NP* is Neoproterozoic, and *P* is Paleozoic. The carbonate-rich samples, the Cl-rich Numees sample, and all the Namibian samples with high I content, are excluded from the box-and-whisker calculation.

2.5.4. Halogen concentrations of the present-day UCC

As fine-grained terrigenous sediments like shale, loess, and diamictite matrix are typically derived from widespread continental areas, they have been used to estimate the composition of the average UCC (Taylor et al., 1983; Taylor and McLennan, 1985; Rudnick and Gao, 2003; Hu and Gao, 2008; Gaschnig et al., 2016). There are two approaches to make such estimates. One is to adopt the median or averaged concentrations of the investigated element(s) in fine-grained sediments (Taylor and McLennan, 1985; Rudnick and Gao, 2003; Gaschnig et al., 2016), and the other is based on regression between the element of interest and another element whose concentration is well constrained in the UCC (McLennan, 2001; Rudnick and Gao, 2003; Hu and Gao, 2008). Below we use the diamictite data and the above two approaches to investigate halogen concentrations of the UCC.

2.5.4.1. Median approach

The first method is typically used to obtain the abundances of insoluble elements of the UCC, as they are not easily fractionated or affected by weathering and sedimentary processing. However, because the halogens are likely differently affected by chemical weathering (see discussion above), this method will surely not produce the original halogen abundances of the UCC, but it could instead provide valuable insights into halogen composition of the weathered UCC. In the following discussion, we use the median rather than the arithmetic mean of Al-normalized halogen concentrations of the diamictites to represent the weathered UCC, as the former is less influenced by outliers (Gaschnig et al., 2016).

Table 3. Estimated halogen concentrations of the UCC based on the glacial diamictite composites of different time periods.

Carbonate-poor diamictite composites used in the calculation (sample numbers)	Estimated UCC halogen concentration ± uncertainty*			
	F (ppm)	Cl (ppm)[#]	Br (ppm)	I (ppm)[#]
Median approach				
Mesoarchean and Paleoproterozoic (n = 9)	302 ± 76	29 ± 24	0.33 ± 0.06	0.02 ± 0.01
Neoproterozoic and Paleozoic (n = 10)	575 ± 87	29 ± 20	0.65 ± 0.14	0.05 ± 0.01
Present-day weathered UCC	**575 ± 87**	**29 ± 20**	**0.65 ± 0.14**	**0.05 ± 0.01**
Regression approach				
Mesoarchean, Paleoproterozoic, Neoproterozoic, and Paleozoic (n = 19)	363 ± 61	83 ± 24	0.41 ± 0.04	0.03 ± 0.01
Paleoproterozoic, Neoproterozoic, and Paleozoic (n = 15)	395 ± 67	84 ± 25	0.42 ± 0.04	0.07 ± 0.09
Neoproterozoic and Paleozoic (n = 10)	376 ± 137	81 ± 49	0.45 ± 0.10	0.07 ± 0.09
Present-day crystalline UCC	**395 ± 67**	**83 ± 24**	**0.41 ± 0.04**	**0.03 ± 0.01**

* The uncertainties provided for the results from the Median approach are quoted at median absolute deviations (MAD) and are calculated from the median of the absolute deviations from the dataset's median, while those from the Regression approach are 2σ.

[#] The anomalous Cl in the Numees diamictite composite and high I in the Namibian samples are excluded from the calculation.

Table 3 compares the median and the median absolute deviation (MAD, which is used to qualify the uncertainty of the median) of the "Mesoarchean + Paleoproterozoic" and "Neoproterozoic + Paleozoic" diamictites. Carbonate-rich diamictites, the anomalous Cl in the Numees composite, and the high I in the Namibian samples are excluded from the calculations in order to limit the influence of localized or non-representative provenances. Except for Cl, the estimated F, Br, and I concentrations from the "Mesoarchean + Paleoproterozoic" composites are systematically lower than those of the "Neoproterozoic + Paleozoic" composites (Table 3), which is likely related to the evolving composition of the UCC, as discussed above. Therefore, we use the median values of the "Neoproterozoic + Paleozoic" diamictites (i.e., 575 ± 87 ppm F, 29 ± 20 ppm Cl, 0.65 ± 0.14 ppm Br, and 0.05 ± 0.01 ppm I, errors quoted at MAD) to represent halogen concentrations of the present-day weathered UCC.

2.5.4.2. Regression approach

Unlike the first method, the correlation-based strategy using regression approach enables one to calculate halogen concentrations of their source rocks that have been subjected limited chemical weathering and/or organic enrichment. Thus, this method provides an estimate of the halogen composition of the UCC crystalline bedrocks. The underlying assumption is that correlations between elements can help reveal their similarities in behaviors during crustal processes like partial melting and/or chemical weathering, and by projecting the recommended UCC value of one element to the regression line, the UCC concentration of the element of interest can be then determined. We use the following procedure to determine halogen concentrations of the present-day crystalline UCC: (1) analyze the correlations

between each halogen and 55 other elements (including both major and trace elements) in the carbonate-poor diamictites (Fig. S7), (2) project the recommended concentrations of the 55 other elements in the UCC (Rudnick and Gao, 2003) to the regression lines with halogen elements, providing up to 55 independent estimates for each halogen (see the appendix for details on determining the uncertainties of the new estimates), and (3) average the results derived from elements that correlate well with the halogens (i.e., having an R^2 *value* > 0.5 for F, Cl, and Br, and > 0.3 for I) and are also well-constrained in the UCC (i.e., their reported RSD values from Rudnick and Gao (2003) are ≤ 10% for major elements and ≤ 20% for trace elements) (Fig. 8).

We next compare how the final halogen estimates are influenced by either including or excluding the Mesoarchean and/or Paleoproterozoic samples to see if a changing UCC composition could influence these estimates. The estimates with and without the older samples generally agree well with each other, although there are larger uncertainties when the Mesoarchean and/or Paleoproterozoic samples are excluded (Table 3). The one exception to this generality is for F. The F estimate using all samples (i.e., 363 ± 63 ppm, 2σ) is lower than 394 ± 67 ppm, the result when the Mesoarchean samples are excluded (Table 3). This is probably due to a marked depletion of F in the Mesoarchean diamictite composites (discussed below). Thus, to constrain the composition of the present-day UCC, we adopted the latter value for F.

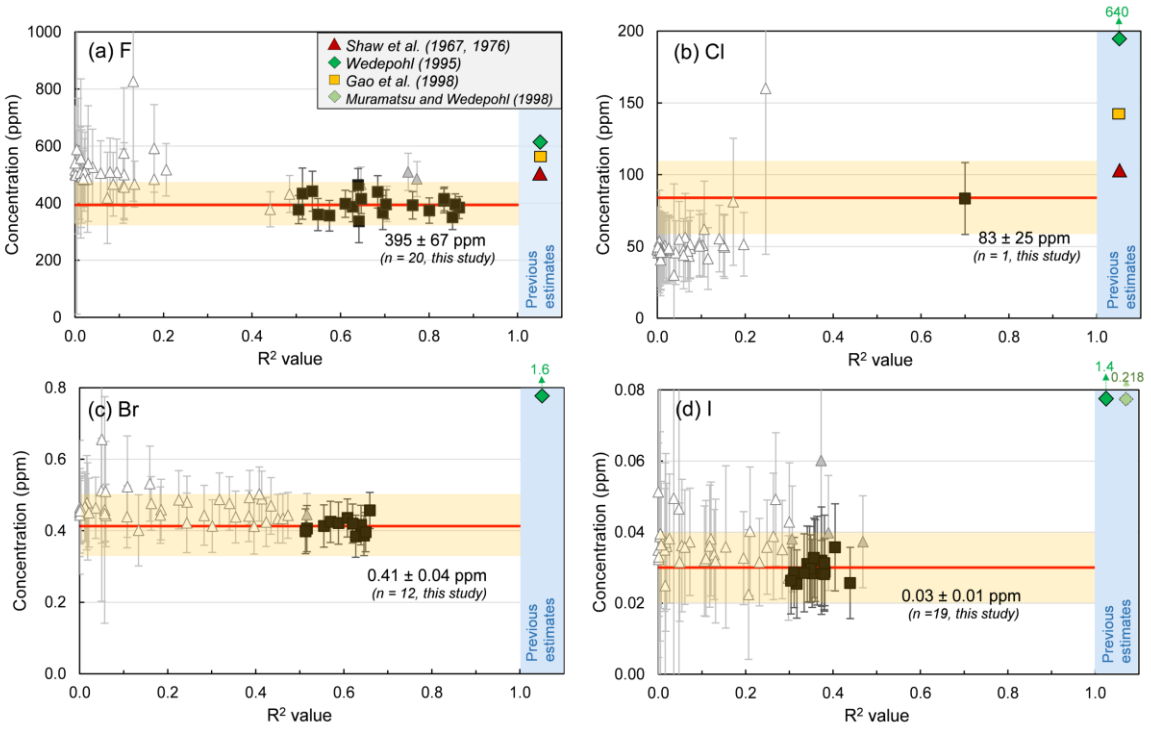

Fig. 8. Halogen abundance estimates in the present-day crystalline UCC. These new estimates are calculated by projecting the published UCC abundance of the element of interest (Rudnick and Gao, 2003) to its regression line with the halogen element (F, Cl, Br, or I) in the diamictites. The y axis shows halogen concentration estimates calculated from other elements. Each other element has a different correlation coefficient (R^2 value, x axis), when plotted against the halogen element. The final F, Cl, and Br abundances (errors are 2σ) are averaged from the estimates from R^2 values > 0.5, and the I abundance from R^2 values > 0.3, which are shown as black squares. Estimates that are not used in the above calculations are shown as either gray triangles (calculated from elements that are not well constrained in the UCC like TiO_2, P_2O_5, Sn, and Be) or white triangles (R^2 values < 0.5 for F, Cl, and Br, and R^2 values < 0.3 for I). The uncertainty on each estimate is given as 2σ and the reference elements used to calculate the above estimates can be found in Fig. S7. Details about the calculations can be found in the text and *Appendix-3* in the supplementary document. Previous UCC halogen estimates (in ppm) are shown as colored symbols within the blue vertical bars on the right side of each diagram.

The new estimates for F, Cl, Br, and I concentrations in the present-day crystalline UCC are: 395 ± 67 ppm F, 83 ± 24 ppm Cl, 0.41 ± 0.04 ppm Br, and 0.03 ± 0.01 ppm I (2σ

uncertainties). However, because halogens could be differently affected by chemical weathering, even the regression approach adopted here may not correct the systematic weathering losses of halogens relative to other elements and hence the calculated results would be unavoidably low. Thus, these estimates should be considered lower bounds on halogen concentrations in the crystalline UCC. Comparing the halogen estimates of the present-day weathered and crystalline UCC, it is obvious that, except for Cl, the estimated F, Br, and I concentrations in the weathered UCC are all higher than those in the crystalline UCC by a factor from 1.5 to 1.7 (Table 3), which probably results both from their retention by secondary minerals and/or organic matter, and the preferential loss of other soluble elements like Ca and Na during chemical weathering.

2.5.4.3. Comparison with previous estimates

Unlike this study, which provides two individual estimates of halogen concentrations for the present-day weathered and crystalline UCC, respectively, previous estimates for halogens in the UCC (Shaw et al., 1967 and 1976; Wedepohl, 1995; Gao et al., 1998; Muramatsu and Wedepohl, 1998) were all aimed at the averaged composition of the whole upper portion of the continental crust that includes not only the crystalline bedrocks but also the sedimentary cover and even the organic-rich layer. Shaw et al. (1967 and 1976) and Gao et al. (1998) based on their estimates on large-scale sampling in the Canadian shield and eastern China, respectively, and both reported average F and Cl estimates. The other strategy is based on measuring halogen concentrations in various crustal rocks and assuming a lithologic model for the UCC. Wedepohl (1995) obtained estimates for the four halogen elements (F, Cl, Br,

and I) using this approach, with the I estimate being later updated by Muramatsu and Wedepohl (1998).

Compared to these previous estimates, F and Cl estimates of this study (395 ± 67 ppm F and 83 ± 24 ppm Cl) are relatively low, but close to those of Shaw et al. (1967 and 1976) (500 ppm F and 100 ppm Cl) and Gao et al. (1998) (561 ppm F and 142 ppm Cl), though no uncertainties were given in the two latter studies (Fig. 9). By contrast, our estimates are much lower than those of Wedepohl (1995), especially for Cl, Br, and I (Fig. 8). The very high estimates of Wedepohl (1995) could result partly from the inclusion of many halogen-rich samples like shale and carbonate in his UCC model, and partly from the poor quality of halogen data he compiled from studies from the early 1970s or earlier. Regarding the first possibility, the similar I contents in most diamictite composites (except the Namibian samples) to those in igneous and metamorphic rocks (Fig. 6) suggest that our estimates mainly reflect crystalline bedrocks, without incorporating the sedimentary cover and/or organic-rich layer that are often halogen enriched. The second concern regarding the data quality in Wedepohl (1995) is supported by the revised I estimate from 1.4 ppm in Wedepohl (1995) to 0.218 ppm in Muramatsu and Wedepohl (1998) in which a more precise pyrohydrolysis ICP-MS method of analysis was used. Another possible reason for the systematically lower halogen concentration estimates from this study is that halogens in the diamictites experienced different degrees of weathering loss, and future analyses of continental magmatic and metamorphic rocks, or less-weathered clastic sediments, would be useful to constrain halogen concentrations in the crystalline UCC more precisely.

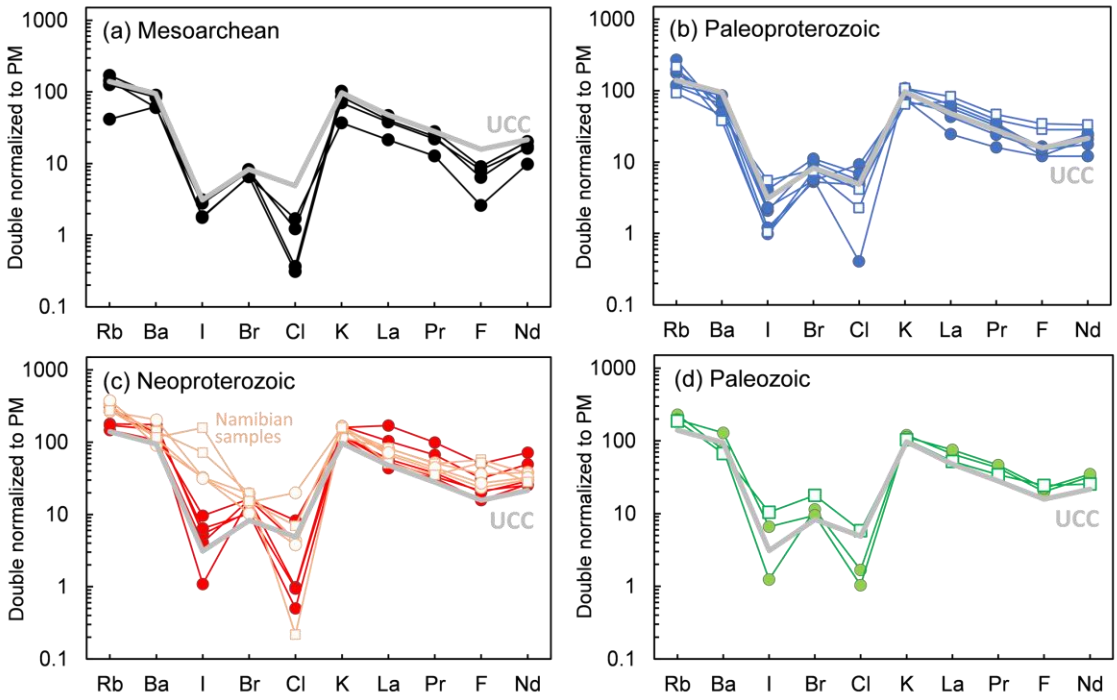

Fig. 9. Multielement plots of halogen (F, Cl, Br, and I, this study) concentrations together with other incompatible elements in the glacial diamictite composites. Concentrations are double-normalized, with the aluminum-normalization (normalizing the Al_2O_3 content of each sample to 15.26 wt%, the UCC Al_2O_3 value from Rudnick and Gao (2003)) to remove the dilution effects of quartz and oxides, and then normalizing each trace element to the primitive mantle (PM, McDonough and Sun (1995)). The diamictites are grouped by depositional periods: **(a)** Mesoarchean, **(b)** Paleoproterozoic, **(c)** Neoproterozoic, and **(d)** Paleozoic. Symbols as in Fig. 2. The element order follows their decreasing incompatibilities during mantle melting (Kendrick et al., 2017). The gray line labelled UCC represents the average composition of the UCC using the halogen estimates from this study: F = 394 ppm, Cl = 83 ppm, Br = 0.41 ppm, and I = 0.03 ppm, while the other elements are from Rudnick and Gao (2003).

2.5.5. Geological implications

Except for F in the carbonate-rich samples, and I in the Namibian samples, halogens in the diamictites are depleted compared to other incompatible elements of similar incompatibility (Fig. 9). Such depletions could represent an inherent feature of the UCC. In

this section we discuss the potential processes that could lead to the UCC halogen depletions, how the halogen concentrations in the UCC are related to those of other geochemical reservoirs such as Earth's mantle and oceans, and the overall halogen cycle within Earth.

2.5.5.1. Fluorine in the UCC

2.5.5.1.1. Fluorine depletion from magmatic degassing and chemical weathering

Of the four halogens, F is the least depleted in the UCC relative to elements of similar incompatibility, with the F/F* value ranging from 0.50 to 0.87 in post-Archean (Paleoproterozoic, Neoproterozoic, and Paleozoic) carbonate-poor diamictite composites and from 0.23 to 0.43 in the Mesoarchean composites (Fig. 9). The depletion of F can also be seen in the significantly lower F/Nd ratios of the diamictites compared to those of undegassed mid-ocean ridge and/or ocean island basalts (MORB/OIB, Kendrick et al. (2017)) and arc/backarc lavas (Kendrick et al., 2020) (Fig. 10). F/Nd ratios in MORB/OIB are similar to the bulk silicate Earth (BSE) ratio (~20, McDonough and Sun (1995)), while undegassed arc/backarc lavas have much higher F/Nd ratios (with a median value of ~28.7), which could reflect addition of F from subducted sediments and/or slabs to subduction zone magmas (Straub and Layne, 2003; Kendrick et al., 2020). Because the continental crust is thought to be dominantly generated at convergent margins (i.e., subduction settings) (Rudnick and Gao, 2003), the relatively low F/Nd ratio observed in the diamictites requires that significant F is lost during continental crust formation either by (1) partitioning of F from silicate melts to hydrothermal fluids and/or associated volcanic degassing during magmatic differentiation and/or (2) chemical weathering of the continents.

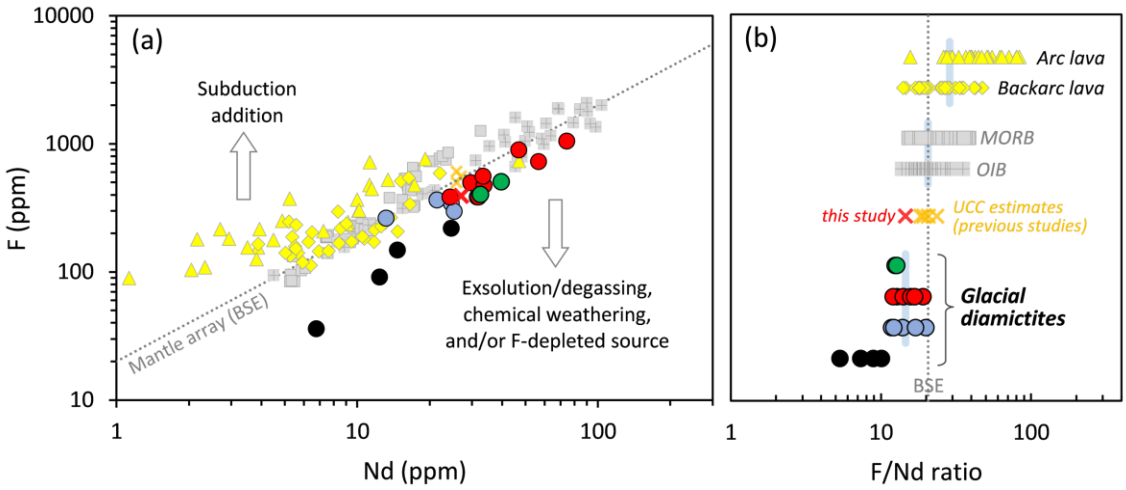

Fig. 10. Fluorine versus Nd contents of various terrestrial samples. **(a)** Concentrations of F and Nd in the glacial diamictite composites (this study, symbols as in Fig. 2, but note that carbonate-rich samples are not plotted here for simplicity) and undegassed arc/backarc lavas (yellow triangles, yellow diamonds, respectively) (Kendrick et al., 2020), mid-ocean ridge basalts (MORB, gray squares), and ocean island basalts (OIB, gray cross-centered squares) (Kendrick et al. (2017) and references therein). MORB and OIB samples generally follow the dashed line, at F/Nd ratio (~20) of bulk silicate Earth (BSE, from McDonough and Sun (1995)). Previous F and Nd estimates of the UCC from Shaw et al. (1967, 1976), Wedepohl (1995), Gao et al. (1998), and Rudnick and Gao (2003) are shown as orange crosses, and the red cross is crystalline UCC from this study. **(b)** F/Nd ratio (log-scale) distributions of the samples in **(a)**. Median values of the undegassed arc/backarc lavas, MORB/OIB, and post-Archean (i.e., Paleoproterozoic, Neoproterozoic, and Paleozoic) glacial diamictites are 28.7, 20.6, and 14.1, respectively, as marked by blue vertical bars. The four Mesoarchean diamictites, however, have much lower F/Nd ratios, ranging from 5.3 to 10.1. F/Nd ratios of previous UCC estimates range from 18.5 to 23.6, higher than the value (14.6) reported in this study.

Although F is highly soluble in melts and is generally retained in magmas during magmatic differentiation, F can partition into fluids under certain conditions such as in slowly-cooled plutonic systems and/or in alkaline phonolitic melts (Dolejš and Baker, 2007; Aiuppa et al., 2009). Indeed, F can be enriched in late-stage magmatic-hydrothermal fluids

(Webster et al., 2004; Thomas et al., 2005; Chevychelov et al., 2008), which often leads to the formation of fluorite-rich veins or greisen systems (hydrothermally altered granitic rocks with variable F- or B-rich minerals) associated with granitic complexes (Pirajno, 2018). In addition, gaseous forms of F (mainly HF, but also other fluoride species) are also commonly found in volcanic gases (Pyle and Mather, 2009). Estimates for the volcanic output of F suggest that there is 0.06–8.6 Tg yr^{-1} of F emitted to the atmosphere, with the dominant output coming from arc volcanoes (Aiuppa et al., 2009; Pyle and Mather, 2009).

In addition to hydrothermal fluid exsolution and volcanic degassing, chemical weathering could also contribute to F loss from the UCC, as suggested by the anticorrelation between F/F* and CIA values of the carbonate-free diamictite composites (Fig. 5a). This is probably also the reason why the F/Nd ratio (~14.6) reported in this study is much lower than those from previous studies, which range from 19.3 to 23.6 (Shaw et al., 1967 and 1976; Wedepohl, 1995; Gao et al., 1998; Rudnick and Gao, 2003) (Fig. 10). In this regard, a related question is: how representative is the F/Nd ratio reported in this study for the average UCC if the glacial diamictites were affected by chemical weathering? This question is hard to answer until more work is conducted to assess the weathering flux of F from the continental surface. Given that the F estimate from this study (395 ± 67 ppm for the present-day crystalline UCC) represents a lower-bound on the average UCC, it could very well be that the F depletion in the UCC is not as extreme as suggested here. A worthy endeavor for better constraining the F concentration and F/Nd ratio of the UCC is to determine the F content in loess, which is another proxy for average UCC composition but generally has a weaker weathering signature (Taylor et al., 1983; Sauzéat et al., 2015).

2.5.5.1.2. More depleted F in the Mesoarchean UCC

The Mesoarchean diamictites show greater F depletions and lower F/Nd ratios compared to younger samples (Figs. 9 and 10). Based on the difference of F/F* values from 0.50–0.87 in the post-Archean carbonate-free composites to 0.23–0.43 in the Mesoarchean composites, the Archean UCC has > ~30% F depletion compared to younger samples. The more depleted F in the Mesoarchean samples could result from greater magmatic degassing/exsolution and/or chemical weathering in the Archean, as discussed above. Greater degassing of Archean volcanic rocks is consistent with the proposed higher outgassing rates from the mantle before the end of the Archean based on evidence from Xe isotopes; indeed the mantle degassing rate at the end of the Archean has been suggested to be an order of magnitude higher than today (Avice et al., 2017; Marty et al., 2019). However, the stronger weathering signatures (i.e., higher CIA values) of the Archean-Paleoproterozoic UCC compared with post-Paleoproterozoic UCC (Li et al., 2016) lend support to more intense F loss by weathering in the Mesoarchean. Currently we cannot distinguish between these two hypotheses based on our limited dataset, and they are not mutually exclusive.

In addition, the very depleted F in the Mesoarchean composites could be inherited from a volatile-depleted mantle at that time. Consistent with this idea, Korenaga (2011) suggested that a drier mantle existed in the Hadean and Archean because of the continuous degassing from the mantle to the surface related to a putative magma ocean and a stagnant-lid tectonic regime, with limited recycling of surficial volatiles into the mantle in the early Earth. An Archean net degassing regime that changed to net regassing ~2.5 Ga was suggested by Parai and Mukhopadhyay (2018) based on Xe isotopes. If this hypothesis is correct, the relative increase of F/F* values from the Mesoarchean to the Paleoproterozoic diamictite composites

(Fig. 10) could mark the onset of global plate tectonics between 2.9–2.4 Ga, whereby F concentrated at Earth's surface (e.g., sediments and seawater) is recycled into the mantle thereby increasing the F concentration. This idea is consistent with previous studies that suggest that plate tectonics may not have become the dominant tectonic regime until the late Archean (e.g., Dhuime et al., 2015; Tang et al., 2016; Smit and Mezger, 2017; Johnson et al., 2019; Chen et al., 2020; Hawkesworth et al., 2020). However, it should be noted that no similar Cl, Br, and I depletion trend is found in the Mesoarchean diamictite composites (Fig. 9), which may be due to: (1) Cl, Br, and I are not as efficiently recycled to the mantle by subducted slabs as F (Straub and Layne, 2003; John et al., 2011; Pagé et al., 2016; Kendrick et al., 2017); (2) Cl, Br, and I in the glacial diamictites are more easily altered than F by many geological processes like magmatic degassing and chemcial weathering; and (3) their depleted signatures may be obscued by the larger analytical uncertainties.

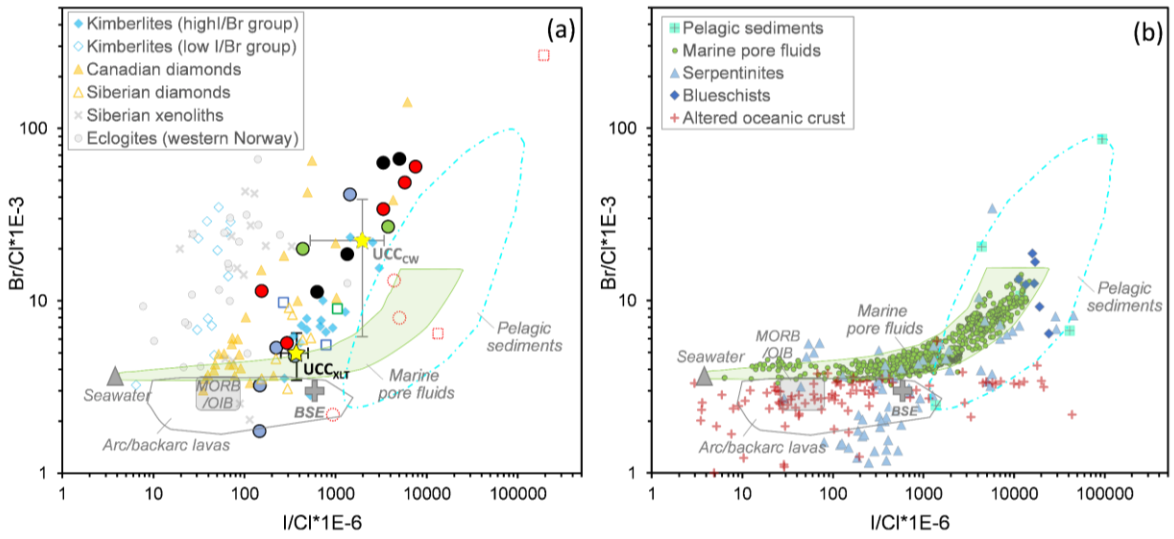

Fig. 11. (a) Br/Cl versus I/Cl ratios of glacial diamictite composites (symbols as in Fig. 2, except that the five Namibian samples: Blaubeker, Kaigas, Chuos, Numees, and Ghaub, are shown with open dashed circles/squares to distinguish their anomalously high I content), kimberlites of both high and low I/Br groups (Toyama et al., 2021), fluid inclusions from Canadian and Siberian diamonds (Johnson et al., 2000; Burgess et al., 2009; Broadley et al., 2018a), lithospheric mantle xenoliths from Siberia (Broadley et al., 2018b), and eclogites from western Norway (Svensen et al., 2001; Hughes et al., 2021). **(b)** Br/Cl and I/Cl ratios from pelagic sediments (John et al., 2011) and marine pore fluids (Fehn et al., 2000; Muramatsu et al., 2001; Fehn et al., 2003; Fehn et al., 2006; Fehn et al., 2007; Muramatsu et al., 2007; Tomaru et al., 2007; Lu et al., 2008; Tomaru et al., 2009), serpentinites (John et al., 2011; Kendrick et al., 2013; Pagé and Hattori, 2017), blueschists (Pagé et al., 2016), and altered oceanic crust (Chavrit et al., 2016; Kendrick, 2019a; Kendrick, 2019b). The yellow star in **(a)** represents the estimated present-day crystalline UCC (UCC_{XLT}), while the dashed yellow star (UCC_{CW}) is for the present-day weathered UCC (see text). Errors for the UCC_{XLT} and UCC_{CW} halogen ratios are 2σ. Br/Cl and I/Cl ratios from other terrestrial reservoirs are plotted for comparison: pelagic sediments (cyan dashed circle), sedimentary pore fluids (green-filled field), seawater (large gray triangle, Bruland and Lohan (2003)), bulk silicate Earth (BSE, gray plus sign) (McDonough and Sun, 1995), MORB/OIB (gray rectangle) (Kendrick et al. (2017) and references therein), and arc/backarc lavas (gray outline) (Kendrick et al., 2020).

2.5.5.2. Chlorine, Br, and I in the UCC

2.5.5.2.1. Insights from Br/Cl and I/Cl ratios

In contrast to F, the other three halogen elements (Cl, Br, and I) in the diamictites exhibit much stronger depletions relative to their neighboring incompatible elements like Ba and K, except for I in the Namibian samples (Fig. 9). In our new estimate of halogen concentrations in the present-day crystalline UCC, the relative depletion value (i.e., X/X* values ($X/X^* = X_n/(Ba_n/K_n)^{0.5}$, in which X represents Cl, Br, and I, and the subscript "n" represents being normalized to the primitive mantle values from McDonough and Sun (1995)) is about 0.05 for Cl, 0.09 for Br, and 0.03 for I, indicating that more than 90% of Cl, Br, and I were lost during formation of the UCC. The halogen loss could be even higher if we take arc lavas as the initial building blocks of the continental crust, as Cl, Br, and I are greatly enriched in these lavas due to halogen additions from subducted slabs and sediments (Kendrick et al., 2020). Such strong depletions in the crystalline UCC could reflect preferential partitioning of Cl, Br, and I into fluids during magmatic differentiation (Bureau et al., 2000) and loss from the continental crust via fluid exsolution and/or volcanic degassing. The Br/Cl and I/Cl ratios calculated from estimates of the present-day crystalline UCC in this study (Fig. 11a, yellow star) are similar to those of the BSE and arc/backarc lavas, though the Br/Cl ratio is slightly elevated, likely reflecting the large uncertainties on our estimates.

The Br/Cl and I/Cl ratios of individual diamictite composites are much higher, and except for the Namibian samples, the other diamictites show a distinct trend that is characterized by the endmember Br/Cl ($22*10^{-3}$) and I/Cl ($1{,}966*10^{-6}$) ratios of the present-day weathered UCC proposed in this study (Fig. 11a, yellow star with dashed outline). As we infer that Cl is subject to strong weathering loss, while Br and I are retained by clay/mica and/or organic

matter (see above), this trend could generally reflect continental weathering of crystalline bedrocks of the UCC. In addition, it is interesting that most of the diamictites, except for the Namibian samples, have relatively higher Br/Cl and lower I/Cl ratios than those of pelagic sediments and sedimentary pore fluids associated with marine organic matter (Muramatsu et al., 2001; Muramatsu et al., 2007; John et al., 2011) (Fig. 11b). Thus, if Br and I in the diamictite composites are indeed retained in organic matter, it may suggest that terrigenous organic matter has distinct halogen ratios compared to those marine equivalents; more data for terrigenous organic-bearing sediments would be helpful in evaluating this hypothesis.

In addiiton, the elevated Br/Cl and I/Cl ratios in the diamictites are similar to those observed in fluid inclusions in diamonds from Canada and Siberia (Johnson et al., 2000; Burgess et al., 2009; Broadley et al., 2018a) and in the high I/Br group kimberlites from south Africa, Greenland, Brazil, and Canada (Toyama et al., 2021) (Fig. 11a). Because the diamonds and high I/Br group kimberlites all originated in and/or ascended through the lithospheric mantle, their halogen ratios might represent those of the continental lithospheric mantle. Indeed, similar ratios are observed in lithospheric mantle xenoliths from Siberia (Broadley et al., 2018b) (Fig. 11a). The origin of the highly fractionated halogen ratios in the lithospheric mantle remains unclear, but has been proposed to reflect either (1) crystallization of apatite from mantle fluids (Johnson et al., 2000), (2) phase separation of immiscible Cl-rich fluids (Burgess et al., 2009), or (3) mixing with fluids derived from altered oceanic crust (Chavrit et al., 2016; Broadley et al., 2018a). An alternative explanation, based on the diamictite results, is that it reflects recycling of terrigenous sediments to the mantle. Such recycled halogens are distinguished from those of seawater, marine sedimentary pore fluids, pelagic sediments, serpentinites, blueschists, and altered oceanic crust as the latter have

either much higher I/Cl ratios or lower Br/Cl ratios relative to the diamictites (Fig. 11b) (Muramatsu et al., 2001; Muramatsu et al., 2007; John et al., 2011; Kendrick et al., 2013; Chavrit et al., 2016; Pagé et al., 2016; Pagé and Hattori, 2017; Kendrick, 2019a; Kendrick, 2019b). In addition, Hughes et al. (2021) suggested recycling of continental halogens to great depths, based on the highly fractionated halogen ratios observed in continental-origin ultra-high-pressure (UHP) eclogites from western Norway, which are very similar to those of the low I/Br group kimberlites and the Siberian lithospheric mantle xenoliths (Fig. 11a). However, instead of interpreting the fractionated halogen ratios in the eclogites to be inherited from continental weathering, they suggested preferential removal of Cl over Br and I during UHP metamorphism (Hughes et al., 2021), though the behavior of Cl, Br, and I during metamorphism remain poorly constrained because of limited high-quality data available for crustal metamorphic rocks (Stepanov, 2021). To sum up, it is possible that Br/Cl and I/Cl ratios of continental rocks can be strongly fractionated during chemical weathering, organic enrichment, or high-grade metamorphism, and such halogen signals could be recycled to the mantle, thus representing a vital part of Earth's halogen cycle.

2.5.5.2.2. Cycling of Cl, Br, and I at Earth's surface

Chlorine weathered from the continents ultimately ends up in the oceans, but our data suggest that the amount of Cl transported to the oceans by continental weathering is too small to account for the present mass of Cl in the oceans. The total weathering inputs of Cl from the continents to the oceans over Earth's history can be calculated if we assume that the Cl content of the UCC decreased from 83–142 ppm (the present-day crystalline UCC from this study and Gao et al. (1998)) to ~29 ppm (the present-day weathered UCC from this study)

and that 2–4 times the present mass of the continental crust ($20.6*10^{21}$ Kg) has been lost to weathering and recycled into the mantle (Liu and Rudnick, 2011). In this scenario, ~2.2–$9.1*10^{18}$ Kg of Cl was removed from the continents due to chemical weathering over Earth's history. This amounts to only 8–34% of the total Cl mass in modern seawater and would be even lower if the recycled seawater into the mantle is considered (Holland and Ballentine, 2006). These estimates support previous suggestions that Cl in the ocean is not dominantly sourced from continental weathering, but instead is mainly contributed by processes such as volcanic outgassing from Earth's mantle and/or late-accretion of volatile-rich materials (Rubey, 1951; Schilling et al., 1978; Holland et al., 2009; Clay et al., 2017) (Fig. 12).

Bromine and I in the oceans should behave similarly to Cl and are also mainly sourced from outgassing of the mantle and/or late volatile accretion, especially when considering their more limited losses relative to Cl during continental weathering (see above). In addition, the significantly higher Br and I contents of terrigenous sediments/organic matter compared to those of igneous and metamorphic rocks (Muramatsu and Wedepohl, 1998; Hanley and Koga, 2018) suggest that crystalline bedrock of the continental crust is not the main supplier of these two elements to terrigenous sediments/organic matter. This is consistent with the I crustal distribution calculated by Muramatsu and Wedepohl (1998), who suggested that $2.4 *10^{12}$ t of I exists in sedimentary rocks of the UCC, which is about 20 times higher than that contained in metamorphic and magmatic rocks ($1.2*10^{11}$ t of I) of the UCC. Therefore, Br and I from other sources are required to be transported and later concentrated on the continental surface. This source could be the oceans, as seawater and associated marine sediments constitute a dominant reservoir for Br and I in and above Earth's crust (Muramatsu and Wedepohl, 1998; Hanley and Koga, 2018). Transport of Br and I, as

well as some Cl, could be achieved either by tectonic emplacement of halogen-rich sediments formed via interaction with seawater, or by atmospheric deposition that is, in turn, derived from volcanic degassing or marine aerosols (Fig. 12). Atmospheric deposition of halogens derived from marine aerosols is supported by the higher Br and I contents of soils and/or plants in coastal areas compared to those of inland sediments (Yuita, 1983; Fuge and Johnson, 1986). Moreover, the increased Br/Cl and I/Cl ratios of wet deposition or surface run-off in inland areas compared to coastal areas (Fuge, 1988; Short et al., 2017) also demonstrates more efficient transportation of Br and I over Cl from the marine to continental environments via the hydrological cycle.

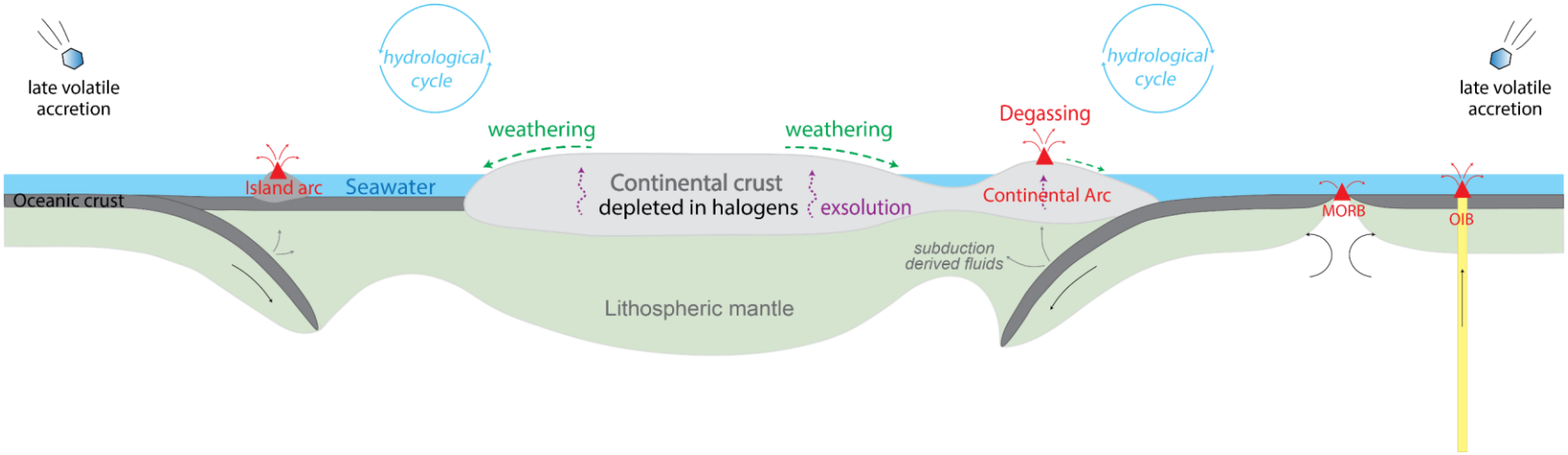

Fig. 12. Schematic summary of important processes controlling halogen distributions in Earth's major geochemical reservoirs.

2.6. Conclusions

The main conclusions derived from our study of halogens in ancient glacial diamictite composites are as follows:

(1) Chlorine is strongly depleted by chemical weathering of the UCC, compared to F, Br, and I. Fluorine in the glacial diamictite composites shows a secular increase in the UCC from ~2.9 Ga to the Phanerozoic, which likely reflects the evolving composition of the UCC as it became more felsic and differentiated with time.

(2) Two sets of estimated halogen concentrations of the present-day UCC are derived from the diamictite data. One is for the present-day weathered UCC: 575 ± 87 ppm F, 29 ± 20 ppm Cl, 0.65 ± 0.14 ppm Br, and 0.05 ± 0.01 ppm I (errors quoted at MAD), and the other is for the present-day crystalline UCC: 394 ± 67 ppm F, 83 ± 24 ppm Cl, 0.41 ± 0.04 ppm Br, and 0.03 ± 0.01 ppm I (with 2σ uncertainties). Higher concentrations of F, Br, and I in the weathered UCC reflect their retention within and adsorption onto clay/mica and/or organic matter.

(3) Halogens are depleted in the UCC relative to elements of similar incompatibility during igneous differentiation. This depletion likely reflects magmatic degassing/exsolution and chemical weathering during the formation of the continental crust. More significant F depletions in the Mesoarchean diamictites may indicate a more volatile-depleted mantle existed prior to the onset of global plate tectonics and widespread recycling of volatile elements.

(4) Distinct weathering behavior of Cl relative to Br and I leads to a wide range of Br/Cl (2–265 * 10^{-3}) and I/Cl (122–197,952 * 10^{-6}) ratios, and Br/I ratios that are distinctly

higher than those of pelagic sediments and marine pore fluids. Similar halogen ratios are observed in samples from the lithospheric mantle, which may reflect recycling of terrigenous sediments into the mantle.

(5) The calculated weathering loss of Cl from the continents over Earth's history is too low to supply the amount of Cl currently in the oceans, suggesting that significant Cl (and also Br and I) in seawater is derived from outgassing of the mantle and/or late volatile accretion rather than continental weathering. In addition, Br and I enrichment in terrigenous sediments/organic matter relative to crystalline bedrocks require transport of significant amounts of Br and I the oceans to the continents.

Chapter III. Halogen Enrichment on the Continental Surface: A Perspective from Loess

As published in *Geochemical Perspective Letters* in 2024

With co-authors Roberta L. Rudnick[1], Zhao-Chu Hu[2], Tao He[2],

Michael A.W. Marks[3], Kang Chen[2]

[1]Department of Earth Science and Earth Research Institute, University of California - Santa Barbara, Santa Barbara, CA 93106, USA

[2]State Key Laboratory of Geological Processes and Mineral Resources, China University of Geosciences, Wuhan, 430074, PR China

[3]Eberhard Karls Universität Tübingen, Geo- und Umweltforschungszentrum, Schnarrenbergstraße 94-96, 72076 Tübingen, Germany

Abstract

Halogen (F, Cl, Br, and I) concentrations for 129 loess samples from worldwide localities yield geometric means of 517 ± 53 μg/g F, 150 ± 20 μg/g Cl, 1.58 ± 0.16 μg/g Br, 1.16 ± 0.11 μg/g I (2 standard errors). These concentrations, notably for Br and I, are substantially higher than previous estimates for the average upper continental crystalline bedrocks, with enrichment factors of $1.3^{+0.7}_{-0.4}$ (F), $1.8^{+2.4}_{-0.8}$ (Cl), $3.8^{+1.3}_{-1.0}$ (Br), and 39^{+71}_{-16} (I) (95% confidence), documenting enrichment of halogens on the continental surface. These surface halogens are likely sourced from the oceans and may be influenced by climate fluctuations. Halogen ratios (Br/Cl, I/Cl, and Br/I) in loess are similar to those of organic-rich soils/sediments from both terrigenous and marine settings, suggesting that terrigenous and marine organic matter have indistinguishable halogen ratios. The Br/I ratios differ from those in the fine-grained matrix of glacial diamictites, indicating that another process (beyond biological influence) is responsible for fractionating halogens in the upper continental crust. Using a mixing model, we calculate that over 80–90% of loess originates from crystalline bedrocks, while the remainder (<10–20%) derives from the halogen- and organic-rich sedimentary cover or other sources (*e.g.,* marine aerosols).

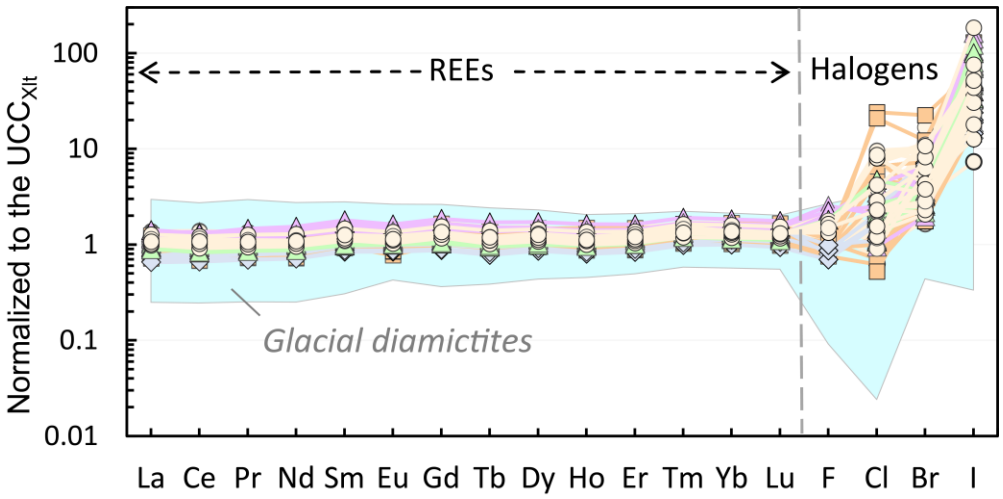

(Graphical Abstract)

3.1. Introduction

Halogens (F, Cl, Br, and I), an important group of lithophile and volatile elements, are primarily concentrated in Earth's surface reservoirs (*e.g.,* crust, seawater, and sediments) and play a critical role in modulating Earth's habitability (Kendrick, 2024 and references therein). To quantify the halogen cycle operating on Earth, it is necessary to have an accurate estimate of halogen distributions in different terrestrial reservoirs. However, such estimates are still lacking for much of the continental crust. This lack of knowledge regarding the geochemical behaviour of halogens during terrestrial geological processes, such as chemical weathering, metamorphic dehydration, and geobiological activity, limits our understanding of the role of the continental crust in the global halogen cycle, and also hinders our ability to utilise halogen concentrations and elemental ratios to trace geologic processes (Hanley and Koga, 2018).

To date, there are only five independent estimates of halogen concentrations in the upper continental crust (UCC), and these estimates can differ by up to a factor of ~50 (Shaw et al., 1967; Wedepohl, 1995; Gao et al., 1998; Muramatsu and Wedepohl, 1998; Han et al., 2023). Poorly constrained halogen concentrations in continental rocks are partly due to heterogeneous halogen distributions, and partly due to the analytical challenges of obtaining precise and accurate halogen concentrations at low abundances, especially for Br and I. With recent advances in analytical techniques, Han et al. (2023) reported a comprehensive set of high-quality F-Cl-Br-I data for 24 composite samples of the fine-grained matrix of ancient glacial diamictites, considered a proxy for upper continental crust (Gaschnig et al., 2016), and used these data to derive halogen estimates for the crystalline and weathered UCC. However, because the diamictites record chemical weathering in their provenance, the new

estimates may represent minima for the crystalline UCC (Han et al., 2023). Moreover, significant fractionation of Br/Cl and I/Cl ratios is observed in the glacial diamictites relative to pelagic sediments, and the reasons for this are unknown. These differences may reflect organic matter enrichment in the sea floor sediments relative to the UCC, chemical weathering of the UCC, or the effects of diagenesis/metamorphism on the diamictites (Han et al., 2023). To better constrain the average halogen composition of the continental surface and to explore the mechanism(s) responsible for the fractionation of halogen ratios in sediments, we analysed 129 loess samples from worldwide localities.

Loess is a silt-sized, terrestrial aeolian sediment that covers about 10% of the continental surface (Pye, 1995). Previous studies have used loess as a proxy for the average composition of the UCC because of its wide-scale sampling of the continental surface, limited chemical weathering (compared to shales) and minor mineralogical and elemental fractionation during sedimentary transportation and deposition (e.g., Taylor et al., 1983; Gallet et al., 1998; Chauvel et al., 2014; Sauzéat et al., 2015). However, previous research on loess mainly focused on insoluble elements like rare earth elements, with little attention paid to halogens. Only two previous studies have reported halogen concentrations in loess, but only for one or two halogens (F and Cl by Liu et al., 1981; I by Fan et al., 2021) in loess-paleosol profiles to track paleoclimate. Thus, there have been no systematic studies of the behaviour of halogens in loess. Here, we report F-Cl-Br-I concentrations, along with major and rare earth element abundances, for 129 loess samples from Germany, Switzerland, the United States, Argentina, Kazakhstan, and China (Table S-1 and Fig. S-1), and discuss the behaviour of halogens on the continental surface and implications for global halogen recycling.

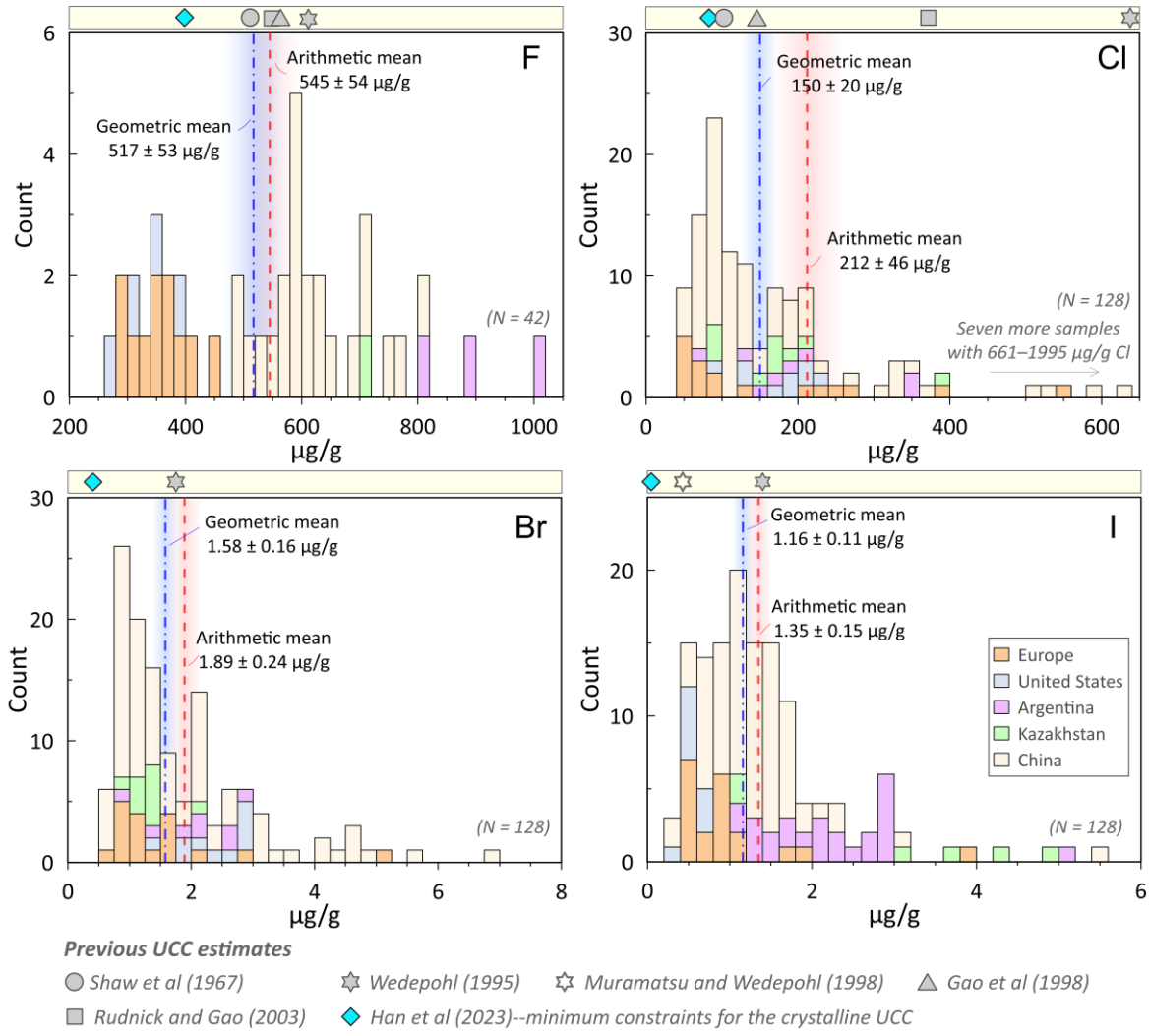

Fig. 1. Halogen (F, Cl, Br, and I) concentrations of loess samples. The blue dash-dotted and the red dashed lines represent the geometric and arithmetic means of the loess dataset, respectively, along with uncertainties of 2 standard errors (SE, light-shaded bars, see Fig. S-5 for more details on the calculation). Symbols above each histogram represent previous estimates of halogen abundances in the UCC.

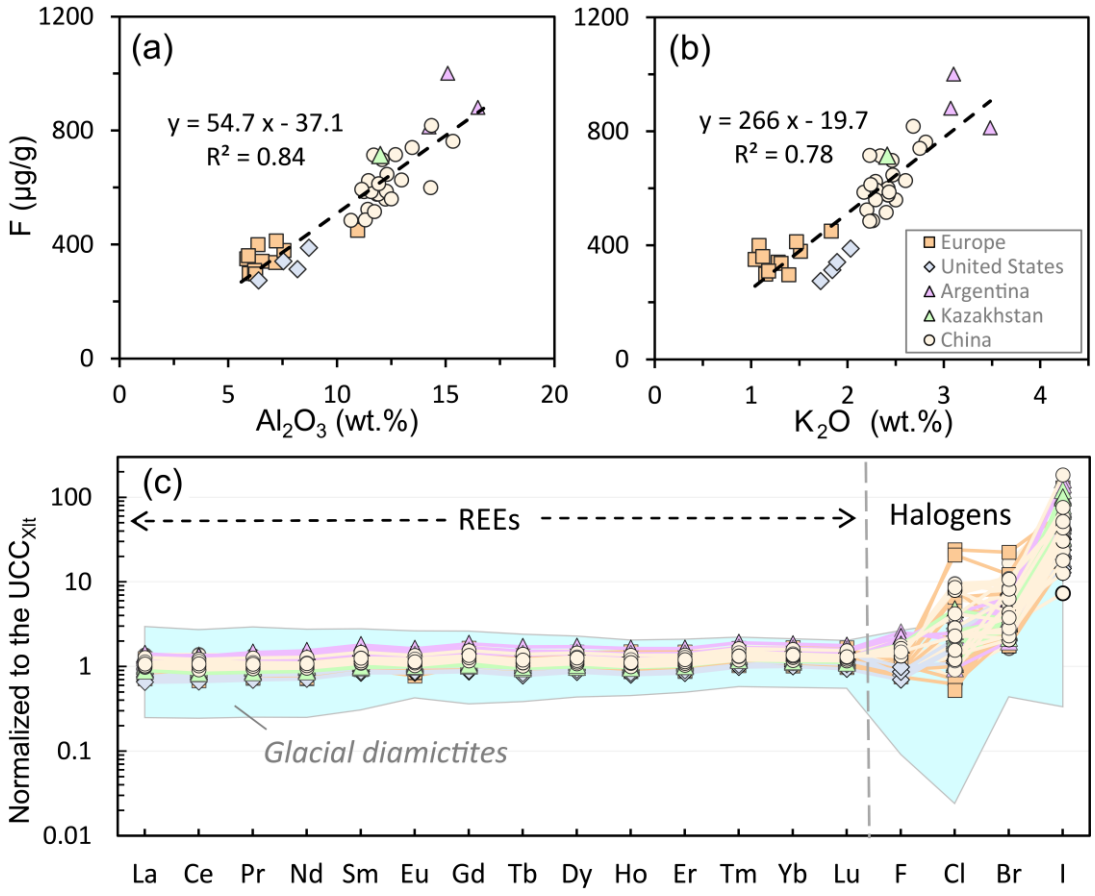

Fig. 2. Fluorine versus Al_2O_3 **(a)** and K_2O **(b)** contents of loess. **(c)** Normalised rare earth element (REE) and halogen concentrations of loess samples relative to the composition of the crystalline UCC (UCC_{Xlt}): REE estimates for UCC are from Rudnick and Gao (2003) and halogens are from Han et al. (2023). The cyan-shaded area shows the compositional field of glacial diamictite composites.

3.2. Halogen concentrations and mineralogical hosts in loess

Halogen concentrations were analysed by two methods: (1) combustion ion chromatography analysis (C-IC) for F and (2) NH_4HF_2 digestion and ICPMS analysis (N-ICPMS) for Cl, Br, and I (supplementary information). Halogen concentrations of loess are reported in Table S-1 and plotted in Figure 1. Each halogen has distinctive geochemical properties, making each likely to be controlled by different phases in loess. Loess is mainly

composed of quartz, feldspar, and various amounts of phyllosilicates and carbonates (Pye, 1995). Fluorine, with the smallest anionic radius of the group, may readily replace the hydroxyl anion and be incorporated into phyllosilicates. This is supported by a good correlation between F and Al_2O_3 ($R^2 = 0.84$) and K_2O ($R^2 = 0.78$) in loess, the latter two elements being enriched in phyllosilicates (Fig. 2a-b). Another mineral in loess capable of hosting F is carbonate, as two F^- can substitute for CO_3^{2-} (Feng et al., 2021). However, F and CaO show a slight negative correlation (Fig. S-3), suggesting that F in loess is mainly controlled by phyllosilicates, rather than carbonates. The anti-correlation between F and CaO contrasts with the relatively high F content observed in some marine carbonates (Rude and Aller, 1991). The reason for a lack of carbonate control on F in the loess is unclear but may indicate that F substitution within carbonate occurs only in certain geological environments, which, in turn, might relate to the salinity, pCO_2, and/or temperature of the water body from which the carbonates precipitate (e.g., Rude and Aller, 1991; Ramos et al., 2005; Feng et al., 2021).

The increasing anionic radii of Cl, Br, and I compared to F make them less likely to be incorporated into the crystal lattices of silicate minerals, particularly for Br and I. Instead, they may be absorbed on mineral surfaces or concentrated in fluid inclusions, evaporite minerals, and/or organic matter. We conducted a leaching experiment with MilliQ water on 14 samples to determine the location of these elements in loess (Table S-1 and Fig. S-4). The water-soluble component of halogens in loess gradually decreases from Cl (as high as ~85%) to Br (~50%), to I (~25%) (Fig. S-4), suggesting that most of the Cl in loess exists in soluble form, while Br and I are mainly present in water insoluble phases. The soluble halogens in loess (Cl and Br) may originate from a range of sources: (1) soluble inorganic halogens

incorporated or absorbed onto the silicate phases within loess source materials; (2) soluble halogens in organic matter, (3) evaporite minerals like halite; and (4) post-depositional contamination from either anthropogenic sources and/or meteoric/ground water. The first three sources may reflect halogen distributions on the continental surface when loess deposits formed, while the fourth suggests potential disturbances of halogen contents after deposition. Since no significant regional differences are observed in the Cl and Br contents of samples from different areas (Fig. 1), and considering that their concentrations in meteoric water and groundwater are typically 10–100 times lower than those of loess (Worden, 2018), any enrichment from localised post-depositional processes, if they occurred, is likely minimal.

The concentrations of residual Br and I (after leaching) in loess are significantly higher than their averages in glacial diamictites (Fig. S-4). Because both elements have a strongly biophilic affinity, they may primarily be hosted in organic matter. Loess contains a significantly greater amount of organic matter than crystalline bedrocks, which are the main source of glacial diamictites (Han et al., 2023). A possible reason for this difference might be the colder environment prevailing during the formation of glacial diamictites, leading to lower biomass on land surfaces and consequently less enrichment of halogens in the diamictites. This explanation also aligns with the proposition put forward by Fan et al. (2021) regarding climate fluctuations and I content in loess: in warmer periods, more halogens will be transported from the ocean to land and retained by surface biota, while during colder periods, both halogen transport efficiency and retention on land will decrease. In other words, halogen concentrations in terrigenous sediments, particularly for the less soluble Br and I, may be used as a proxy to monitor past temperature changes and to trace patterns of halogen movement between land and sea.

As a whole, the geometric and arithmetic means calculated from the dataset are systematically higher than the recent estimates for crystalline UCC derived from data for ancient glacial diamictite composites (Han et al., 2023). Using a bootstrap approach, we estimate the degree of halogen enrichment in loess relative to crystalline UCC to be $1.3^{+0.7}_{-0.4}$ times for F, $1.8^{+2.4}_{-0.8}$ times for Cl, $3.8^{+1.3}_{-1.0}$ times for Br, and 39^{+71}_{-16} times for I (95% confidence, see Fig. S-6), with an exponential increase in enrichment from F to I (*i.e.* F < Cl < Br << I, Fig. 2c and Fig. S-7). There are two non-mutually exclusive factors that could explain the higher halogen contents in loess relative to glacial diamictites: (1) a lower degree of chemical weathering in the provenance of loess compared to that of glacial diamictites, and (2) greater potential for incorporation and preservation of organic matter in loess than in glacial diamictites (Fig. S-8). On the other hand, the mean halogen concentrations in loess are comparable to previous estimates of halogens in the UCC based on either large-scale sampling (Shaw et al., 1967; Gao et al., 1998) or models based on lithologies (Wedepohl, 1995; Muramatsu and Wedepohl, 1998) (Fig. 1), both of which incorporate data not only for crystalline bedrocks, but also for many halogen-rich lithologies such as shales, carbonates, and evaporites from the overlying sedimentary cover. The similarity between mean halogen concentrations in loess and these previous estimates suggests that halogens in loess may provide a useful average of halogen concentrations across various types of rocks and sediments at the continental surface. Halogen enrichment on the continental surface may derive from the oceans, a major halogen reservoir (Hanley and Koga, 2018), with halogen fluxes from oceans to continents potentially regulated by climate fluctuations, as suggested by Fan et al. (2021).

3.3. Halogen ratios in loess

The Br/Cl and I/Cl ratios of loess, as well as the leached residues of loess samples, are significantly fractionated relative to those in igneous rocks like MORB/OIB and arc/backarc lavas, closely tracking the compositional range seen in pelagic sediments, whose halogen concentrations are primarily controlled by marine organic matter (John et al., 2011) (Fig. 3). This supports the inference above, based on leaching experiments (Fig. S-4), that Br and I primarily reside in water-insoluble organic matter in loess. It also suggests that both terrigenous and marine organic matter have indistinguishable halogen ratios. This notion is further supported by the consistently narrow range of the Br/I ratio observed in organic-rich soils and sediments from Japan (Yamasaki et al., 2015) and China (He et al., 2018) (Fig. S-9). However, no correlation is observed between Br (or I) and TOC in either the loess or Japanese soil samples (Fig. S-10), which is somewhat counterintuitive and may result from varying Br/TOC (or I/TOC) ratios in different types of organic matter (Muramatsu and Wedepohl, 1998; Mayer et al., 2007). Therefore, great caution should be exercised when using the correlation of Br and I with TOC to infer the presence of organohalogens in sediments.

The halogen ratios observed in loess are also similar to those found in blueschists and serpentinites from subduction zone settings (Fig. 3), indicating that the halogens in these metamorphic rocks may be overprinted by fluids derived from subducted terrigenous organic-bearing sediments, not just marine sediments (e.g., John et al., 2011; Kendrick et al., 2013; Pagé et al., 2016). Most glacial diamictite composites (excluding five carbonate- and terrigenous sediment-rich samples from Namibia), however, have significantly higher Br/I ratios (7–74) compared to loess (0.25–6.3) (Fig. 3). This difference suggests that halogen

ratios are significantly fractionated within the upper continental crust by an additional process, such as continental weathering and/or diagenesis/metamorphism. We note that the diamictites generally carry a stronger chemical weathering signature than loess (Fig. S-8), and most experienced greenschist-facies metamorphism (Han et al., 2023).

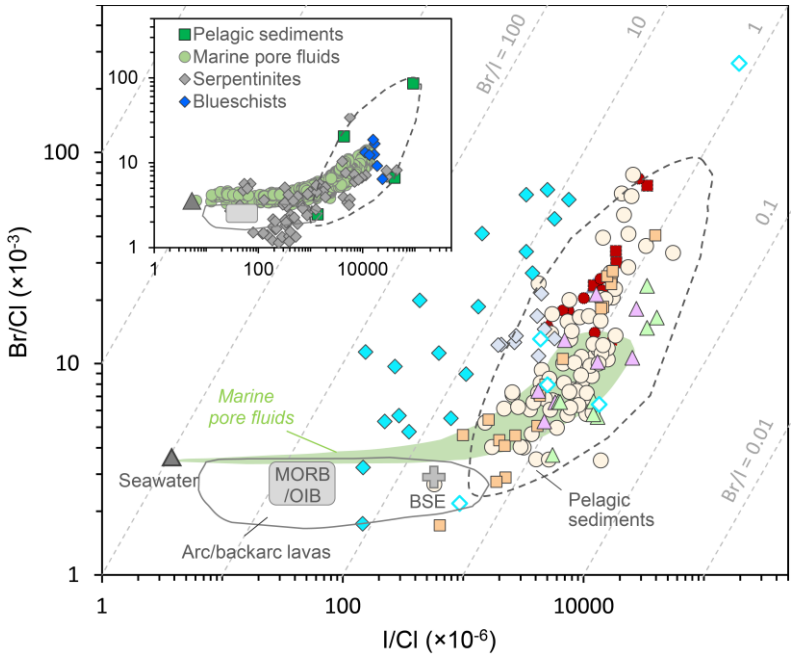

Fig. 3. Br/Cl versus I/Cl ratios of loess (symbols as in Fig. 2, this study) and glacial diamictite composites (cyan diamonds, Han et al., 2023). Note that (1) the leached loess residues are plotted as deep-red dashed symbols and (2) five carbonate-rich and terrigenous sediment-rich glacial diamictites from Namibia have notably elevated I content and relatively low Br/I ratios and are shown with open diamonds (see Han et al. (2023) for discussion). Halogen ratios of seawater (grey triangle), bulk silicate Earth (BSE, grey plus sign), mid-ocean ridge and ocean island basalts (MORB/OIB, grey rectangle, Kendrick et al., 2017), arc/backarc lavas (grey outline, Kendrick et al., 2020), pelagic sediments (grey dashed outline, John et al., 2011), and marine pore fluids (green field, Fehn et al., 2006; Muramatsu et al., 2007) are plotted for comparison. Thin grey dashed lines are constant Br/I ratio contours, ranging from 0.01 to 10,000. The inset shows samples from the subduction zone setting: pelagic sediments, marine pore fluids, serpentinites (John et al., 2011; Kendrick et al., 2013), and blueschists (Pagé et al., 2016).

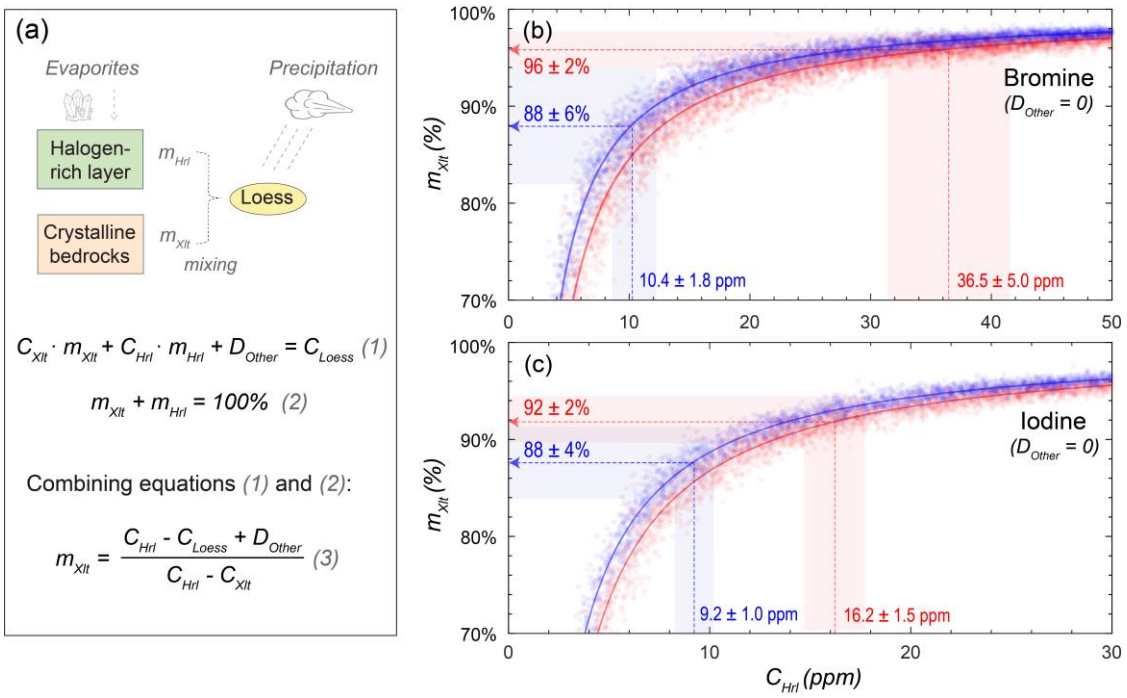

Fig. 4. **(a)** Mixing model for the source of halogens in loess. In the equations, C_{Xlt}, C_{Hrl}, and C_{Loess} represent halogen concentrations of the UCC crystalline bedrocks, halogen-rich sedimentary layer, and loess, respectively; D_{Other} represents other potential inputs from precipitation and/or evaporites that could contribute significant halogens without substantially affecting the system's mass; m_{Xlt} and m_{Hrl} are assumed mass proportions of the UCC crystalline bedrocks and the sedimentary halogen-rich component in loess. **(b)** and **(c)** show the simulated relationship between m_{Xlt} and C_{Hrl} from equation (3) in **(a)** when D_{Other} = 0, for mixing of Br and I, respectively. The red and blue curves are calculated using either the geometric (blue) or arithmetic (red) means of the loess samples and the adjacent pale red/blue circles represent related errors (modelled from Monte Carlo resampling, 10,000 times). The vertical dashed lines are geometric (in blue, 2 SE) and arithmetic (in red, 2 SE) means of Japanese soils. The calculated mass proportion of crystalline rocks in loess is shown as horizontal dashed lines (with 2σ uncertainties), which are obtained when projecting the geometric or arithmetic mean of Japanese soils (Fig. S-10) to the red or blue curves.

3.4. Implications for loess provenance

Previous studies suggested that loess derives from rocks that have generally experienced moderate chemical weathering during multiple cycles of sedimentation (Gallet et al., 1998; Sauzéat et al., 2015). Based on the Li isotopic composition of loess, Sauzéat et al. (2015) estimated that the proportion of chemically weathered material at Earth's surface was $37^{+17}_{-10}\%$. However, because Li isotopes are not sensitive to the presence of organic matter, it remains unclear what proportion of material within loess is derived from pulverized unweathered crystalline bedrocks versus mature sediments that have extensively interacted with the biosphere. As Br and I are strongly enriched in organic-bearing sediments and their concentrations will be sensitive to the amount of such sediment in the loess provenance, we used a mixing model to calculate the proportions of the above sources in loess. In this calculation, the Br and I contents in loess are assumed to result from a mixture of (1) clastic sediments derived from glacially pulverized unweathered crystalline bedrocks, (2) an overlying halogen-rich sedimentary cover, and (3) inputs from other sources, such as precipitation (marine aerosols) and evaporite minerals (Fig. 4). Although the composition of the third end member is difficult to define and may vary between samples and locations, we assume that the first end member is well represented by the glacial diamictites (Han et al., 2023), and the second by the Japanese soil samples (Yamasaki et al., 2015). When projecting the geometric or arithmetic mean of Japanese soils (Fig. S-11) onto the mixing line for either Br or I, assuming no other inputs, the calculated mass proportions of the UCC crystalline bedrocks in loess are consistently >80–90% (Fig. 4). This proportion would be even higher if other inputs were considered. Overall, this suggests that the sediments that have extensively interacted with the biosphere in the loess provenance is <10–20%, which is somewhat lower

than the sum proportion of chemically weathered components, $37^{+17}_{-10}\%$, at the continental surface as estimated by Sauzéat et al. (2015). Thus, it can be concluded that the primary source of loess material is the crystalline bedrocks of the UCC, which validates its use to infer the average composition of the present-day UCC (Taylor et al., 1983; Gallet et al., 1998; Chauvel et al., 2014).

Chapter IV. Halogen Behavior During High-Grade Metamorphism and Partial Melting in the Deep Continental Crust (Ivrea Zone, NW Italy)

In Preparation for *Earth and Planetary Science Letters*

With co-authors Madison Huising[2], Roberta L. Rudnick[1], Jaime D. Barnes[3], Michael A.W. Marks[4], Tao He[5], Fernando Bea[6], Zhaochu Hu[5]

[1]Department of Earth Science and Earth Research Institute, University of California - Santa Barbara, Santa Barbara, CA 93106, USA

[2]Department of Earth and Environmental Sciences, University of Michigan, 1100 North University Avenue, Ann Arbor, Michigan 48109, USA

[3]Department of Earth and Planetary Sciences, University of Texas at Austin, Austin, TX 78712-0254, USA

[4]Eberhard Karls Universität Tübingen, Geo- und Umweltforschungszentrum, Schnarrenbergstraße 94-96, 72076 Tübingen, Germany

[5]State Key Laboratory of Geological Processes and Mineral Resources, China University of Geosciences, Wuhan, 430074, PR China

[6]Department of Mineralogy and Petrology, University of Granada, Campus Fuentenueva, 18002 Granada, Spain

Abstract

The concentrations of F, Cl, Br, I, and Cl isotopes in a suite of amphibolite- to granulite-facies metapelites, metabasites and associated leucosomes from the Ivrea Zone, Northwest Italy, reveal halogen behavior during high-grade metamorphism and partial melting in the deep continental crust. Fluorine, Br, and I concentrations in metapelites decrease from amphibolite- to granulite- metamorphic facies, documenting progressive dehydration with increasing metamorphic grade. Fluorine decreases from 764 ± 255 to 347 ± 195 ppm, Br from 0.78 ± 0.11 to 0.61 ± 0.30 ppm, and I from 0.09 ± 0.08 to 0.02 ± 0.01 ppm, all with 1σ uncertainties. By contrast, Cl concentrations increase with metamorphic grade, changing from 49 ± 9 to 87 ± 36 ppm (1σ), thereby lowering Br/Cl and I/Cl ratios in the samples. Metabasites also experienced >50% F loss during granulite-facies metamorphism, as indicated by the decrease in F/Nd ratio from around 20 to 10, although no significant trends were observed for the other halogens. Leucosomes, mainly formed by partial melting, yield similar trends to the metapelites for F (169 to 18 ppm) and Cl (67 to 98 ppm), but contrasting relationships for Br and I, where Br increases (0.56 to 1.12 ppm) with metamorphic grade and I instead remains constant (at ~0.08 ppm). These results suggest that (1) F, I, and possibly Br are lost during metamorphic dehydration, and (2) an external, Cl-rich fluid source may have been present in the lower continental crust during granulite-facies metamorphism, possibly introduced by underplating magmas. This latter observation aligns with the Cl-rich fluid inclusions and minerals commonly found in other granulite terrains, suggesting the widespread presence of Cl-rich fluids during granulite-facies metamorphism. Halogens released by metamorphic dehydration and introduced through underplating magmas in the lower continental crust may have played a crucial role in facilitating partial

melting, promoting granitic magma generation, and contributing to the chemical differentiation of the continental crust. All measured samples (metapelites, metabasites, and leucosomes) exhibit scattered but narrow $\delta^{37}Cl$ values, ranging from -1.26 ‰ to +0.65 ‰, overlapping previously reported values for terrigenous and marine sediments. This suggests that no Cl isotope fractionation occurs during metamorphic dehydration, partial melting, and fluid infiltration processes in the deep continental crust.

4.1. Introduction

The continental crust is a primary feature of Earth, characterized by an evolved igneous composition (Taylor and McLennan, 1985; Rudnick and Gao, 2003). Over Earth's history, it has undergone extensive interactions with other reservoirs (atmosphere, oceans, and mantle), resulting in significant elemental exchanges (e.g., Kay and Kay, 1993; Rudnick, 1995; Plank and Langmuir, 1998; Gaschnig et al., 2014). At the same time, ongoing tectonic processes and magmas intruding from the mantle continuously alter the thermal state of the continental crust, leading to widespread metamorphism and partial melting of the rocks within it (e.g., Clemens and Vielzeuf, 1987; Sawyer et al., 2011; Brown, 2013; Aranovich et al., 2014; Weinberg and Hasalová, 2015). These processes result in substantial redistribution of elements, particularly volatile and incompatible ones, in crustal rocks, contributing to the differentiation of the crust. One of the main goals of geologists is to decipher these processes to better understand the differentiation history of the continental crust.

Halogens (F, Cl, Br, and I) are an important group of volatile elements, comprising Group IIA of the period table. Due to their high volatility and incompatibility during magmatic differentiation, halogens are enriched on Earth's surface and play a critical role in modulating Earth's habitability (e.g., Aiuppa et al., 2009; Sharp and Draper, 2013; Broadley et al., 2018b). The similar yet distinct properties of each element also make their ratios (e.g., F/Cl, Br/Cl, and I/Cl, and Br/I), as well as Cl isotopes, valuable tracers of geological fluids and melts (e.g., Barnes and Sharp, 2017; Kendrick and Barnes, 2022; Kendrick, 2024). Over the past decade, halogens have been widely used to investigate the fluid/melt interactions between crust and mantle, particularly in oceanic and subduction settings, because seawater and associated marine sediments are major halogen reservoirs at Earth's surface and their

subduction can significantly alter the chemical and physical properties of arc-related magmas and the deep mantle (e.g., John et al., 2011; Pagé et al., 2016; Kendrick et al., 2017; Beaudoin et al., 2022; Segee-Wright et al., 2023). By comparison, the distribution of halogens in the continental crust, a major reservoir for incompatible and lithophile elements, remains poorly constrained, as does their behavior during intra-crustal processes (Hanley and Koga, 2018; Han et al., 2023).

Previous efforts to investigate halogen behavior in crustal rocks have primarily focused on analyzing halogens in mineral separates (e.g., apatite, biotite, amphibole, and zircon) (Webster et al., 2009; Zhang et al., 2012; Finch and Tomkins, 2017; Tang et al., 2019; Kendall-Langley et al., 2021) and/or in fluid and melt inclusions (Svensen et al., 2001; Webster et al., 2004; Ferrero et al., 2021). These analyses typically target only F and Cl, rather than all four halogens. Moreover, because they are primarily conducted at the mineral scale, the measured halogen compositions can be influenced by the equilibrium mineral assemblage. As a result, they often carry substantial uncertainties and offer limited insights into halogen distributions at the whole-rock scale. Direct whole-rock halogen analyses of crustal rocks remain scare, partly due to their very low concentrations in such rocks (particularly for Br and I, which are often present at sub-ppm levels) and partly due to the unconventional analytical methods required for their accurate measurement.

Using two advanced halogen analysis methods, Han et al., (2023) updated halogen estimates for crystalline bedrocks of the UCC and documented their behavior during chemical weathering, based on the results from a suite of world-wide glacial diamictite composites. A subsequent study on global loess samples (Han et al., 2024) also found

that halogens can become highly concentrated on the continental surface, potentially transported from the ocean via atmospheric deposition and fixed by biological activity. Together, these two studies show that significant halogen fractionation can occur in the upper continental crust, leading to a wide range of Br/Cl (1 to $265*10^{-3}$), I/Cl (122 to $197{,}952*10^{-6}$), and Br/I ratios (0.25 to 74). The mechanism(s) driving this large halogen fractionation remains unclear, but it could be related to chemical weathering, biological enrichment, and/or diagenesis to (sub)greenschist-facies metamorphism associated with glacial diamictites (Han et al., 2023; Han et al., 2024). Moreover, since similar halogen ratios have been found in the lithospheric mantle (e.g., Johnson et al., 2000; Svensen et al., 2001; Burgess et al., 2009; Broadley et al., 2018b; Hughes et al., 2021; Toyama et al., 2021), it has been suggested that subducting terrigenous sediments eroded from the continental surface can transport these signals to the deep Earth (Han et al., 2023). However, this hypothesis assumes that halogen signatures in recycled terrigenous sediments remain largely unmodified during metamorphism under elevated pressure and temperature conditions—an assumption supported for rocks that have undergone blueschist- to eclogite- facies metamorphism (e.g., John et al., 2011; Kendrick et al., 2013; Pagé et al., 2018), but not yet been tested in rocks subject to regional Barrovian-Style (greenschist-, amphibolite-, and granulite-facies) metamorphism in continental settings.

Here we investigate halogen behavior during metamorphic dehydration and partial melting in the deep continental crust. We determined halogen concentrations and chlorine isotope composition for well-characterized amphibolite- to granulite-facies rocks of the Ivrea Zone (South Alps, Northwest Italy) (Bea and Montero, 1999). The samples include metapelites and metabasites, along with some leucosomes generated from partial melting.

With prograde metamorphism from amphibolite facies and granulite facies, and minimal modifications of these samples after exhumation, the Ivrea zone provides a natural laboratory to study halogen composition and fractionation in the middle and lower continental crust.

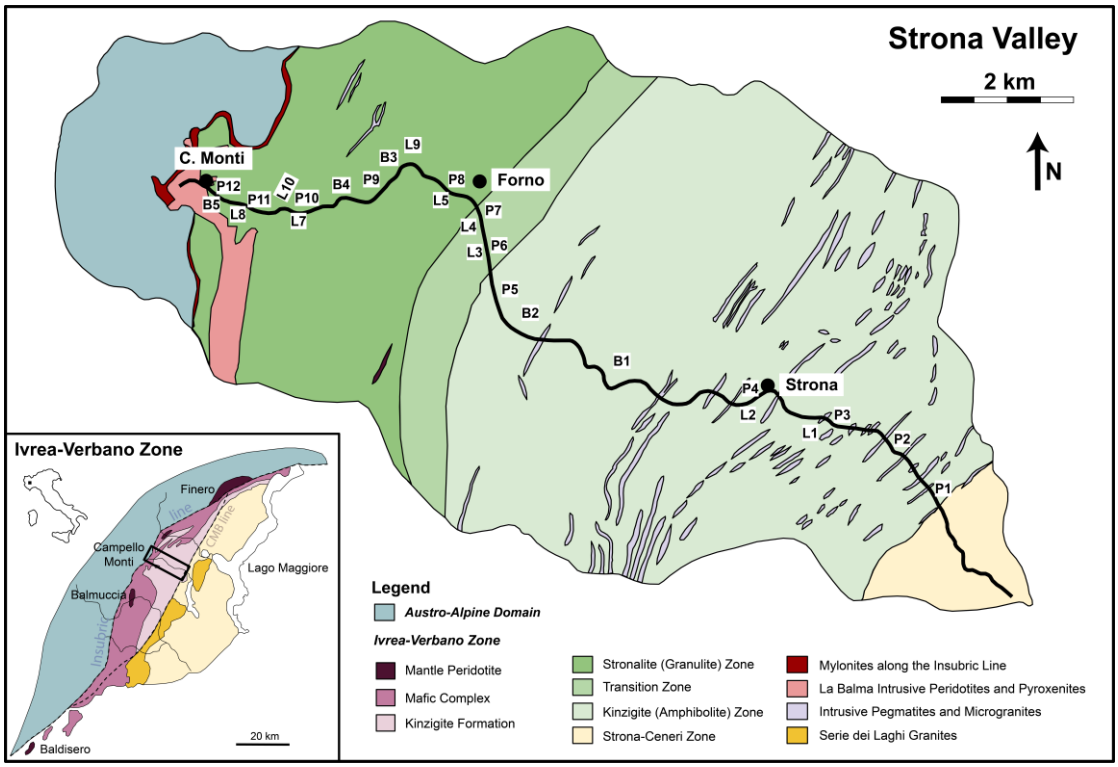

Fig. 1. Geologic sketch map of the Strona Valley in the Ivrea-Verbano Zone (modified from Bea and Montero, 1999). CMB line, Cossato-Mergozzo-Brissago line. Rocks of different lithologies (e.g., metasediments, metacarbonates, and metabasites) along the metamorphic zone are not shown for simplicity. Labels indicate the locations of the collected samples, with the initial letter representing the lithology: “B” for metabasites, “P” for metapelites, “L” for leucosomes.

4.2. Geologic background

The Ivrea Zone (also known as the Ivrea-Verbano Zone) is an exposed middle to lower crustal section of the Permian Southern Alpine crust. These rocks were initially deformed and metamorphosed during regional metamorphism associated with the Variscan orogeny (~370–290 Ma), followed by crustal attenuation, cooling, and uplift during the late Paleozoic and early Mesozoic (~290–160 Ma). The section was ultimately emplaced as a relatively rigid body during the Alpine orogeny (~50–20 Ma) (e.g., Zingg et al., 1990; Henk et al., 1997; Handy et al., 1999; Ewing et al., 2015).

The Ivrea Zone is bounded by the Insubric line to the west and by the Cossato-Mergozzo-Brissago line to the east, and consists of two main units: the Mafic Complex and the Kinzigite Formation, along with minor ultramafic rocks conventionally interpreted as mantle tectonites (Fig. 1). The Mafic Complex consists of gabbros to diorites that intruded the Kinzigite Formation. Intrusion mainly occurred between 286 and 282 Ma (Peressini et al., 2007; Karakas et al., 2019), although some individual mafic intrusions may date back to 314 ± 4 Ma (Klötzli et al., 2014). The Kinzigite Formation consist of interlayered metapelites and metabasites, along with subordinate quartzites and marbles, all of which have undergone metamorphism from amphibolite to granulite facies. Regional peak metamorphism (700–770 °C, 0.65–0.75 GPa) occurred around 320–310 Ma (Peressini et al., 2007; Redler et al., 2012; Ewing et al., 2013) and may have followed an extended period of high-temperature (> 650 °C) for more than 50 Ma (Klötzli et al., 2014; Kunz et al., 2018; Wyatt et al., 2022; Connop et al., 2024). The Kinzigite Formation is the focus of this study.

Metapelites of the Kinzigite Formation gradually change from mica schist to banded granoblastic migmatitic gneiss, reflecting a decrease in muscovite and biotite and a

corresponding increase in K-feldspar and garnet with rising metamorphic grade from southeast to northwest (Bea and Montero, 1999; Redler et al., 2012). Traditionally, this formation has been subdivided into three zones: the Kinzigite Zone, the Transition Zone, and the Stronalite Zone (Schnetger, 1994; Bea and Montero, 1999). The Kinzigite Zone corresponds to amphibolite facies, the Stronalite Zone to granulite facies, and the Transition Zone represents an intermediate grade between the two. Results from conventional thermobarometry indicate P-T conditions of 0.4–0.6 GPa and 550–650°C for the Kinzigite Zone, 0.6–0.7 GPa and 670–700°C for the Transition Zone, and 0.65–0.75 GPa and 700–770°C for the Stronalite Zone (Redler et al., 2012 and references therein). However, Zr-in-rutile thermometry and detailed phase equilibria modelling suggest higher P-T conditions of 850–930°C and 0.9–1.2 GPa for the Stronalite Zone (Luvizotto and Zack, 2009; Redler et al., 2012; Kunz and White, 2019). Stronalite rocks are mainly residuum in composition, with an estimated 20–40% melt having been extracted from the Kinzigite precursors (Schnetger, 1994; Redler et al., 2013).

The interlayered metabasites in the Kinzigite Formation share a similar metamorphic history (prograde, peak, and retrograde) to the metapelites and exhibit increasing amounts of clinopyroxene and orthopyroxene at the expense of hornblende and plagioclase with increasing metamorphic grade (Kunz et al., 2014; Kunz and White, 2019). The textures also transition from granoblastic in the Kinzigite Zone to metatexitic and diatexitic in the Stronalite Zone (Kunz and White, 2019). Leucosomes, the light-colored portions of migmatites formed by partial melting, are widespread in the Kinzigite Formation and occur in both metapelites and metabasites. In the Kinzigite and Transition Zones, leucosomes are less abundant and typically smaller in size, mostly ranging from 0.5 to 2

cm. By contrast, in the Stronalite Zone, they commonly exceed 15 vol.% and can reach sizes of 50–80 cm (Redler et al., 2012).

4.3. Samples

We analyzed a total of 24 samples, including 12 metapelites, 5 metabasites, and 9 leucosomes (7 hosted in metapelites and 2 hosted in metabasites). All these samples were originally described by Bea and Montero (1999), who provided bulk-rock major and trace element compositions, along with petrographic descriptions. This same suite of samples has also been analyzed for Li concentration and Li isotopes (Qiu et al., 2011), Mg isotopes (Wang et al., 2015), and N concentration and N isotopes (Halama et al., 2021).

The metapelites investigated in this study generally contain biotite + garnet + sillimanite + quartz + k-feldspar + plagioclase ± cordierite ± orthopyroxene, with accessory phases such as apatite, monazite, xenotime, and zircon. Biotite content decreases gradually from the Kinzigite Zone to the Stronalite Zone, accompanied by an increase in garnet (Bea and Montero, 1999). Based on modal biotite/garnet ratios, samples P1–P5 were assigned to the Kinzigite Zone (modal biotite/garnet ratio > 2), samples P6–P7 to the Transition Zone (2 > modal biotite/garnet ratio > 0.2), and samples P8–P12 to the Stronalite Zone (modal biotite/garnet ratio < 0.2) (Bea and Montero, 1999).

The metabasites are mainly composed of hornblende + plagioclase + clinopyroxene + orthopyroxene + garnet + biotite + quartz + ilmenite, with minor amounts of titanite, apatite, and zircon (Mazzucchelli and Siena, 1986; Kunz et al., 2014; Kunz and White, 2019). Clinopyroxene, orthopyroxene, and garnet typically do not appear until the Transition and Stronalite Zones, in which they are accompanied by a decrease in biotite and the

transformation of green hornblende to brown. Of the five metabasites analyzed in this study, two samples (B1 and B2) are from the Kinzigite Zone, while the remaining three (B3, B4, and B5) are from the Stronalite Zone.

In the Kinzigite and Transition Zones, leucosomes are primarily composed of quartz and plagioclase, with quartz comprising up to 90 vol.%. In the Stronalite zone, leucosomes typically consist of K-feldspar + quartz + plagioclase, and may also contain garnet, clinopyroxene (in metabasites), and/or orthopyroxene (in metapelites) (Redler et al., 2013; Kunz and White, 2019). Here we analyzed a total of nine leucosomes: two hosted in the metapelites from the Kinzigite Zone (L1, L2), two in metapelites from the Transition Zone (L3, L4), three in metapelites from the Stronalite Zone (L5, L7, L8), and two in metabasites from the Stronalite Zone (L9, L10).

4.3. Methods

4.3.1. Halogen concentration analyses

Halogen concentrations were analyzed using two different methods: (1) F-Cl ± Br concentrations were measured by pyrohydrolysis coupled with ion chromatography analysis at the University of Texas at Austin and Universität Tübingen; and (2) Cl-Br-I concentrations were analyzed using NH_4HF_2 digestion followed by ICPMS analysis (N-ICPMS) at the State Key Laboratory of Geological Processes and Mineral Resources, China University of Geosciences, Wuhan.

4.3.1.1. Pyrohydrolysis analysis of F-Cl ± Br concentrations

Pyrohydrolysis extracts volatile like halogens and sulfur from solid rock samples at high temperatures. The extracted volatiles, initially in gas form, are trapped in aqueous solutions (typically NaOH or H_2O_2) and subsequently analyzed by ion chromatography (Shimizu et al., 2015; Mishra and Jeyakumar, 2018). The pyrohydrolysis procedures used in the two laboratories involved in our study (University of Texas at Austin and Universität Tübingen) differ and are briefly summarized below. More detailed descriptions of the procedures can be found in Segee-Wright et al. (2023) and Epp et al. (2019), respectively.

Pyrohydrolysis at University of Texas, Austin: About 0.5 g dried sample powder is mixed with 0.25 g of pure V_2O_5 powder, which aids in combustion and/or fusion. The mixed powder is then placed within a quartz tube, both ends of which are capped with quartz wool. The quartz tube is manually heated with a gas-oxygen torch to a temperature near or exceeding the melting point of the quartz tube (~1700 °C). The released volatiles are carried by a constant water vapor stream, pass through a condenser, and are finally concentrated in a 20 mM NaOH solution. The pyrohydrolysis solutions are then analyzed using a Dionex ICS 2000 Ion Chromatograph for F and Cl concentrations. Detection limits for both F and Cl are 5 ppm (Beaudoin et al., 2024). Reference materials analyzed include NKT-1 (Nephelinite), RGM-2 (rhyolite), SyMP-1 (syenite), and AGV-1 (andesite), with results provided in Table 1. Long-term reproducibility (based on repeat analyses of reference materials and samples) is typically better than 20% (1 SD).

Pyrohydrolysis at Universität Tübingen: An automated combination of combustion digestion (or pyrohydrolysis) and ion chromatography was used at the Universität Tübingen. For combustion, a mixture of 5–15 mg sample powder, mixed with an equal amount of WO_3

powder, was placed into a quartz vial, which was capped on both sides with quartz wool. The vial was placed into a quartz vessel, where the sample was combusted at 1050°C for 12 minutes in a flow of Ar and O_2, while a constant water vapor flow was maintained to collect the released halogens. The loaded steam was collected in an absorber module containing 4 mL of 500 ppm H_2O_2 solution. After matrix elimination, the solutions were injected into the ion chromatograph. The effective detection limits are about 10 ppm for F and Cl, and about 0.2 ppm for Br (Epp et al., 2019). Accuracy was monitored through the analysis of international reference material GS-N (granite), which generally showed consistency within the uncertainty of the previously reported values by Govindaraju (1994) and Wang et al. (2018) (Table 1). All samples were analyzed at least twice, with the calculated 2 SD typically better than 40% for F and Cl (Table 1).

4.3.1.2. N-ICPMS analysis of Cl-Br-I concentrations

For the N-ICPMS analyses, 100 mg of whole rock powder was mixed with 400 mg of NH_4HF_2 in a 15 mL screw-top Teflon vessel and placed in an oven at 220°C for 2 hours. After cooling, the digested cake was transferred to a polyethylene bottle and diluted to 25 g via 5 % v/v NH_4OH solution. Ten µl of an internal standard solution of Te (10 µg/ml) was added to 1 mL of supernatant solution of the digested sample in a new polyethylene tube. The supernatant was then analyzed using an ELEMENT XR inductively coupled plasma sector field mass spectrometer. Detection limits for this method are 5 ppm for Cl, 15 ppb for Br, and 5 ppb for I (He et al., 2019). Reference materials (i.e., BE-N, BHVO-2, GSS-8, GSS-25) were analyzed during the course of this study, with results generally

agreeing with previously reported values from Han et al. (2023) and He et al. (2019) (Table 1). Precision of the method is typically better than 25% (2 RSD).

4.3.2. Chlorine isotope analyses

Chlorine stable isotope analysis was conducted at University of Texas, Austin and the procedures are based on Eggenkamp et al. (1995). After the Cl was extracted from the sample via pyrohydrolysis into an aqueous solution, it was reacted with $AgNO_3$ to precipitate AgCl. The AgCl was then reacted with methyl iodide (CH_3I) to form methyl chloride (CH_3Cl). CH_3Cl was then purified from excess CH_3I using a gas chromatography column, with continuous helium flow. Measurements are conducted on a ThermoElectron MAT 253. Data are reported in standard per mil notation versus standard mean ocean chloride (‰ vs SMOC). The reproducibility is typically ± 0.2 ‰ (1SD) based on long-term reproducibility of seawater standard measurements.

Table 1. Halogen analyses of reference materials.

Labs	Analytical method	Sample Name	Rock type	Repeats (N)	Measured values (ppm)*								Reference values (ppm)				
					F	1σ	Cl	1σ	Br	1σ	I	1σ	F	Cl	Br	I	Sources
UT Austin	Pyrohydrolysis	NKT-1	Nephelinite	2	667	59	46	0.3	-	-	-	-	900	75	-	-	Webb et al. (2011)
		RGM-2	Rhyolite	1	467	93	383	77	-	-	-	-	350	510	-	-	Cullen et al. (2019)
		SyMP-1	Syenite	2	3610	71	145	11	-	-	-	-	3400	146	-	-	Webb et al. (2016)
		AGV-1	Andesite	1	404	81	103	21	-	-	-	-	425	133	-	-	Jochum et al. (2016)
Universität Tübingen	Pyrohydrolysis	GSN	Granite	22	1068	99	417	19	2.0	0.4	-	-	1050	450	2.3		Govindaraju (1994) Wang et al. (2018)
China Uni. Geosciences, Wuhan	N-ICPMS	BEN	Basalt	9	-	-	166	6	0.33	0.02	0.01	0.002	-	218	0.27	0.02	Han et al. (2023)
		BHVO-2	Basalt	1	-	-	86	17	0.22	0.04	0.04	0.01	-	87	0.28	0.05	He et al. (2019)
		GSS-8	Soil/loess	1	-	-	65	13	1.86	0.37	1.68	0.34	-	63.5	2.19	1.91	He et al. (2019)
		GSS-25	Soil/loess	1	-	-	62	12	2.20	0.44	1.22	0.24	-	63	2.52	1.5	He et al. (2019)

* The reported uncertainty is 1σ of repeated analysis. However, when repeated analyses are not available, the uncertainty (underlined) is estimated as 20% of the measured concentrations, based on the reproductivity of repeat analyses from reference materials and samples.

4.4. Results

4.4.1. Inter-laboratory comparison of halogen concentrations

F and Cl analysis of the same samples from different labs allow for inter-laboratory comparison. Fluorine concentrations measured at the Universität Tübingen and the University of Texas at Austin agree well, generally within 10% uncertainty (Fig. 2a). This consistency suggests efficiency recovery of F by both pyrohydrolysis methods, despite differences in experimental procedures (see above). By contrast, systematic differences are observed in Cl concentrations among different labs. The Austin lab reports the highest Cl values, followed by the Wuhan lab, and finally the Tübingen lab, with discrepancies exceeding 50% in some cases (Fig. 2b). Chlorine concentrations in metabasites show the greatest consistency across labs (within ~25%), whereas greater variability is observed for metapelites and leucosomes. These lithology-dependent differences may be due to more refractory Cl hosting phases, compared to F, in metapelites and leucosomes than in metabasites, which can significantly affect the efficiency of Cl extraction (see discussion below). For Br and I analysis, results are available only from the Wuhan lab by N-ICPMS, so no inter-lab comparison is possible.

In the following discussion, we use the averaged F concentrations obtained from the two pyrohydrolysis methods, and the Cl-Br-I data from the Wuhan lab (Table 2). With the exception of B1 and B2 (which were analyzed only at the Austin lab), data from Wuhan is used for consistency in the Cl-Br-I results (as Br and I were not analyzed by the other two labs), however, it is noted that the Cl concentrations might be systematically underestimated, as indicated above.

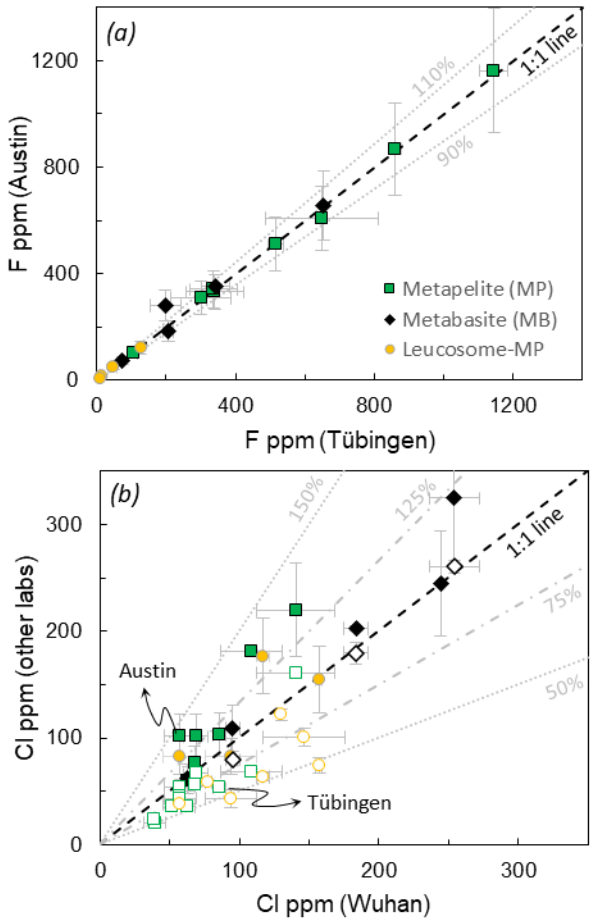

Fig. 2. Interlaboratory comparison of F and Cl analyses: **(a)** F concentrations from the Tübingen lab (x axis) versus the results from the Austin lab (y axis). **(b)** Cl concentrations from the Austin lab (solid symbols) and the Tübingen lab (open symbols), compared to results from the Wuhan lab. Error bars are 1σ.

4.4.2. Halogen concentrations and Cl isotopic composition

Halogen concentrations and Cl isotopic composition of samples with different lithologies (metapelites, metabasites, and leucosomes) are presented in Table 2. Trends in halogen concentrations with metamorphic grade are shown in Fig. 3a-d. Metapelites contain 103–1154 ppm F, 39–140 ppm Cl, 0.12–0.92 ppm Br, and 0.01–0.22 ppm I (n = 12). Fluorine and I exhibit a significant decreasing trend from amphibolite-facies to

granulite-facies, while Br shows only a slight decrease and Cl exhibits an increasing trend. The five metabasite samples contain 74–654 ppm F, 95–254 ppm Cl, 0.21–0.49 ppm Br, and 0.03–0.16 ppm I, and show no obvious trend with metamorphic grade, although Br and I concentrations for samples B1 and B2 are still pending results from the Wuhan lab (Table 2).

Leucosomes (associated with both metapelites and metabasites) have halogen concentrations ranging from 7-1478 ppm F, 57–157 ppm Cl, 0.38–2.35 ppm Br, 0.01–0.17 ppm I. With the exception of one sample (L-7, with 1478 ppm F), F concentrations in leucosomes are systematically lower than those in metapelites and metabasites of the same metamorphic grade (Fig. 3a). By contrast, the concentrations of Cl, Br, and I in leucosomes are generally higher than those in metapelites and metabasites of comparable metamorphic grade (Fig. 3b and 3d).

Chlorine isotopes were analyzed in fifteen samples: six metapelites, five metabasites, and four leucosomes (Fig. 3e). Samples from different lithologies display a similar range of $\delta^{37}Cl$ values, from -1.0‰ to +0.5‰, consistent with the range of -3.4‰ and +2.4‰ reported for metasedimentary rocks (Barnes and Sharp, 2017 and reference therein). No significant trend in $\delta^{37}Cl$ values is observed with increasing metamorphic grade (Fig. 3e).

Table 2. Halogen concentrations and Cl isotope composition of the Ivrea Zone samples.

Samples	Lithology	Metamorphic facies	F*		Cl#		Br#		I#		Cl isotopes	
			ppm	1σ	ppm	1σ	ppm	1σ	ppm	1σ	δ^{37}Cl ‰	1σ
P1	Metapelite	Amphibolite facies	643	128	57	11	0.76	0.15	0.10	0.02	-	-
P2	Metapelite	Amphibolite facies	602	20	39	8	0.92	0.18	0.09	0.02	-	-
P3	Metapelite	Amphibolite facies	513	3	57	1	0.61	0.04	0.02	0.01	-0.72	0.27
P4	Metapelite	Amphibolite facies	1116	6	39	1	0.81	0.03	0.22	0.01	-	-
P5	Metapelite	Amphibolite facies	945	7	51	2	0.78	0.06	0.02	0.01	-	-
P6	Metapelite	Transition Zone	864	6	69	8	0.52	0.00	0.03	0.003	-0.96	0.33
P7	Metapelite	Transition Zone	1154	12	86	5	0.63	0.06	0.02	0.001	-0.68	0.33
P8	Metapelite	Granulite facies	305	6	140	28	0.74	0.15	0.02	0.004	0.65	0.26
P9	Metapelite	Granulite facies	628	30	58	12	0.51	0.10	0.01	0.003	-	-
P10	Metapelite	Granulite facies	336	7	63	5	0.79	0.03	0.02	0.001	-	-
P11	Metapelite	Granulite facies	339	3	68	4	0.12	0.06	0.02	0.003	0.29	0.26
P12	Metapelite	Granulite facies	103	2	109	22	0.86	0.17	0.02	0.005	-0.79	0.27
B1	Metabasite	Amphibolite facies	*654*	*131*	*244*	*49*	*pending*		*pending*		0.50	0.27
B2	Metabasite	Amphibolite facies	*74*	*15*	*62*	*12*	*pending*		*pending*		0.30	0.27
B3	Metabasite	Granulite facies	239	59	95	5	0.21	0.07	0.04	0.01	-0.15	0.27
B4	Metabasite	Granulite facies	347	6	184	9	0.44	0.06	0.16	0.01	-0.20	0.27
B5	Metabasite	Granulite facies	196	15	254	18	0.49	0.21	0.03	0.001	-0.55	0.27
L1	Leucosome in metapelite	Amphibolite facies	210	21	78	2	0.74	0.01	0.03	0.02	-	-
L2	Leucosome in metapelite	Amphibolite facies	124	3	57	11	0.38	0.08	0.12	0.02	-0.71	0.33
L3	Leucosome in metapelite	Transition Zone	16	1	94	19	1.60	0.32	0.01	0.002	-0.38	0.33
L4	Leucosome in metapelite	Transition Zone	47	1	157	2	2.35	0.02	0.01	0.000	0.11	0.26
L5	Leucosome in metapelite	Granulite facies	42	4	130	1	2.02	0.01	0.17	0.03	-	-
L7	Leucosome in metapelite	Granulite facies	1478	170	147	29	1.02	0.20	0.03	0.01	-	-
L8	Leucosomein metapelite	Granulite facies	7	5	117	4	1.43	0.004	0.10	0.01	-1.26	0.27
L9	Leucosome in metabasite	Granulite facies	*pending*		159	32	0.88	0.18	0.04	0.01	-	-
L10	Leucosome in metabasite	Granulite facies	*pending*		221	44	0.81	0.16	0.10	0.02	-	-

*Fluorine content is averaged from pyrohydrolysis analyses conducted at both Universität Tübingen and the University of Texas at Austin, except for B1 and B2, which were analyzed only at the Austin lab (complete data are provided in the supplement). Fluorine and Cl analyses from Tübingen for B1, B2, L9, and L10, as well as Cl-Br-I analyses for B1 and B2 from Wuhan, are still pending.

#Cl, Br, and I concentrations are taken from N-ICPMS results provided by the China University of Geosciences, Wuhan, except for B1 and B2, for which Cl data are available only from the UT Austin analysis. The uncertainty represents one standard deviation of duplicate analysis, if available. Otherwise, it is estimated as 20% of the measured concentrations.

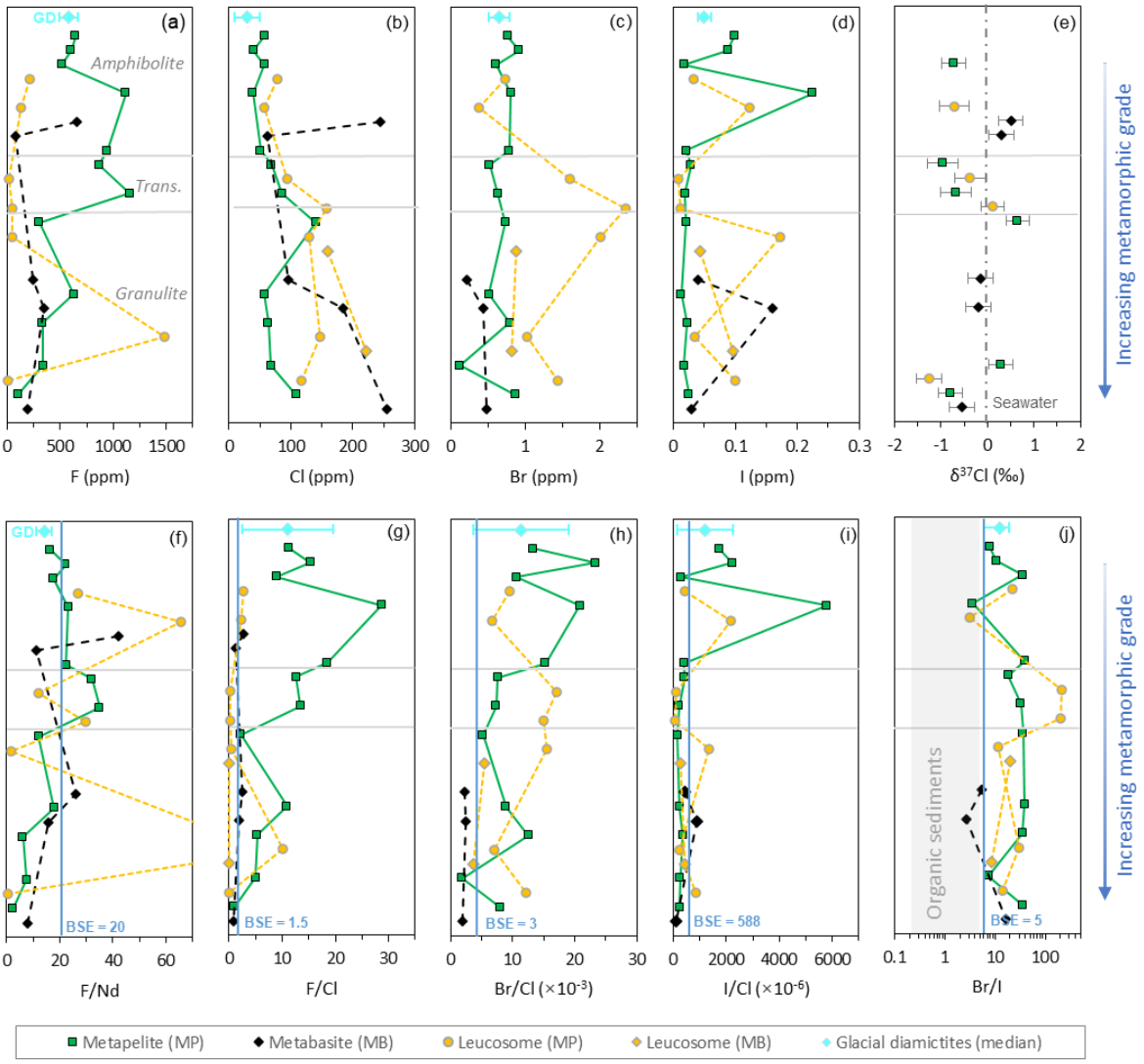

Fig. 3. (a-d) Halogen concentrations and **(e)** Cl isotopic compositions ($\delta^{37}Cl$) as a function of metamorphic grade. **(f-j)** are for halogen ratios (F/Nd, F/Cl, Br/Cl, I/Cl, and Br/I). The light blue lines in (f-j) represent Bulk Silicate Earth (BSE) values from McDonough and Sun (1995). The cyan diamond on every plot represents the median value of ancient glacial diamictite composites (GD, from Han et al. (2023)), with error bars representing median absolute deviations. In plot (j), the shaded area indicates Br/I ratios of organic-rich sediments like marine sediments and loess (see Han et al. (2024) for further discussion).

4.5. Discussion

4.5.1. Halogen concentration changes during metamorphism

4.5.1.1. Fluorine (F)

4.5.1.1.1. Fluorine in metapelites

Metapelites from the amphibolite-facies and Transition Zone contain 500–1200 ppm F, which contrasts sharply with the significantly lower F contents in granulite-facies rocks (103–600 ppm). Most amphibolite-facies and Transition Zone metapelites have F concentrations comparable or higher than the median value of ancient glacial diamictite composites reported by Han et al. (2023) (575 ± 187 ppm, Fig. 3a). These glacial diamictite samples are clastic sediments eroded from the continental surface during glacial periods and have only undergone diagenesis to (sub-)greenschist facies metamorphism (Gaschnig et al., 2014; Han et al., 2023). Their consistency with the amphibolite-facies samples studied here suggests metamorphic dehydration of F was minimal, both prior to and during amphibolite facies metamorphism. This interpretation is supported by petrographic observations and bulk-rock geochemical modelling results (Schnetger, 1994; Redler et al., 2012; Redler et al., 2013). By contrast, the systematically lower F concentrations in granulite-facies rocks likely reflect substantial F loss from metamorphic dehydration and partial melting. The decreased F content also correlate with modal abundances of biotite and apatite (Fig. 4a and 4b), suggesting that the loss of F may be associated with the breakdown of biotite and apatite. Assuming the median value of glacial diamictites approximates the protolith's F concentration for the Ivrea Zone metapelites, the granulite samples have lost 40–80% of their original F (Table 2).

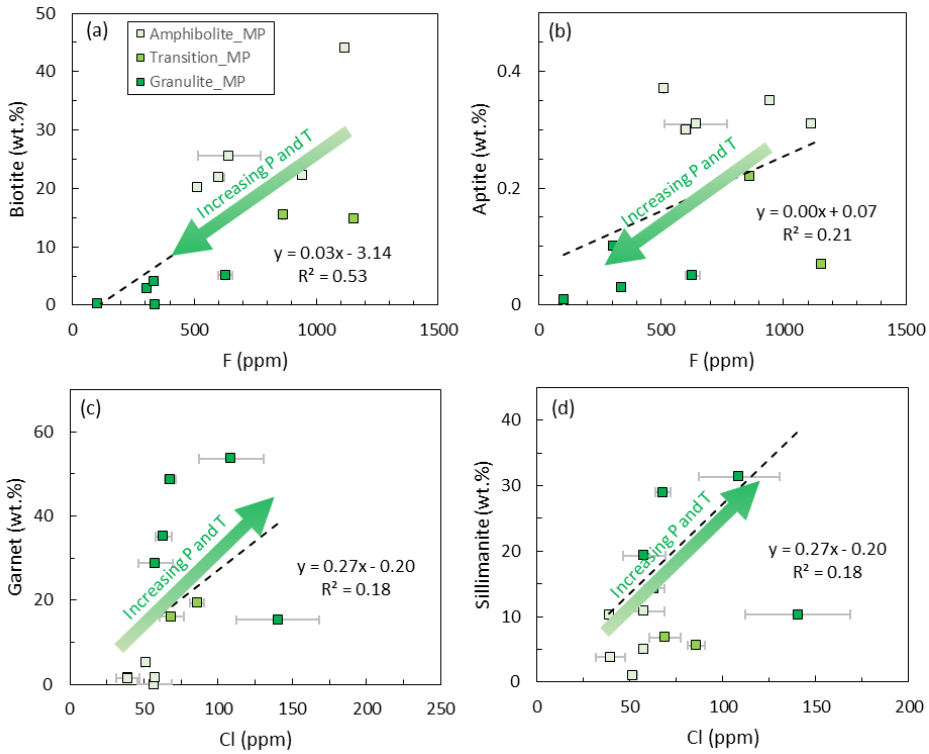

Fig. 4. (a-b) Correlations of F with modal abundance of biotite and apatite in metapelites, and **(c-d)** correlations of Cl with garnet and sillimanite. The green arrow represents the trend of increasing pressure and temperature from amphibolite-facies to granulite-facies. The modal abundances of the above minerals were obtained by Bea and Montero (1999) based on point counting. The dashed line is a linear regression of the data with associated statistics.

Despite the general trend of decreasing modal abundance of apatite in the samples, apatite in granulite-facies rocks exhibit a slightly but significantly higher F content (5.84–6.47 wt.%) compared to those in amphibolite-facies rocks (3.03–5.01 wt.%) (Bea and Montero, 1999). A similar pattern is observed for monazite, in which F changes from 0.47 wt.% to 0.65 wt.% in amphibolite-facies rocks to 0.65 to 2.54 wt.% in granulite-facies rocks. These results may suggest greater stability of F-rich endmembers of these minerals under high-grade metamorphic conditions, possibly due to the preferential loss

of Cl from these phases during metamorphism (Bea and Montero, 1999; Spear and Pyle, 2002).

4.5.1.1.2. Fluorine in metabasites

No significant trend is observed for F concentrations in metabasites, which may be related to the complex geological history of these rocks, including heterogeneity in magmatic sources, varying degrees of crystal fractionation, and interactions with country rocks during prograde metamorphism (Kunz et al., 2014). To further evaluate whether significant F loss occurred during prograde metamorphism, we examined the ratio of F to Nd, an element with similar incompatibility during mantle melting (McDonough and Sun, 1995). The ratio shows a gradual decrease from ~20 to ~10 (Fig. 3f), demonstrating preferential loss of F over Nd during metamorphism and partial melting. Although no careful mineralogical study was conducted on these samples by Bea and Montero (1999), we suspect that this F loss may be related to the transformation of green hornblende (characteristic of amphibolite-facies) into brown hornblende and, eventually, pyroxenes during prograde metamorphism (Sills and Tarney, 1984).

4.5.1.1.3. Fluorine in leucosomes

Except for one sample (L7), F content of leucosomes is significantly lower than that of metapelites (possibly also metabasites, but still awaiting F analysis from Tübingen for L9 and L10, see Table 2), which is consistent with their primary quartzofeldspathic mineralogy and lack of hydrous phases such as biotite and amphibole. The L-7 sample, however, has a very high F content (1478 ppm), with no other significant elemental anomalies observed in this

sample. We suspect this elevated F may result from the incorporation of F-rich accessory minerals, such as apatite or fluorite. The systematically lower F concentrations in leucosomes suggest that most of the F released from metamorphic dehydration and partial melting was not retained within the residual melts. Instead, much of it may have been transported to upper crustal levels, either in the form of melts or hydrothermal fluids.

4.5.1.2. Chlorine (Cl)

4.5.1.2.1. Chlorine in metapelites

Chlorine concentrations in the amphibolite-facies metapelites (39–57 ppm) generally fall within uncertainty of the median values reported for glacial diamictites (29 ± 20 ppm) (Han et al., 2023). However, Transition Zone and granulite-facies metapelites tend to have significantly higher Cl contents, ranging from 58 to 140 ppm (Fig. 3b and Table 2). The elevated Cl concentrations in granulite-facies rocks could be due to: (1) secondary contamination, (2) source heterogeneity, and (3) the presence of Cl-rich fluids associated with granulite metamorphism. We explore each of these possibilities next.

Although soluble Cl is ubiquitous in near-surface environments, Cl concentrations in meteoric and river water typically range from 4 to 7 ppm (Worden, 2018), which is much lower than those measured in the Ivrea Zone metapelites. Therefore, secondary contamination is unlikely to account for the elevated Cl content in granulite-facies samples, as supported by the similar Cl concentrations observed between the median of the glacial diamictites and the Ivrea amphibolite-facies metapelites (Fig. 3b). Another possible explanation is that the granulite-facies rocks may have a different provenance compared to the amphibolite-facies rocks, possibly incorporating more Cl-rich phases

such as evaporites (e.g., halite—NaCl and sylvite—KCl). However, this is at odds with the generally accepted view that the amphibolite- and granulite- facies rocks share the same protolith, based on field observations and other geochemical characteristics (Schnetger, 1994; Redler et al., 2012). Moreover, even if Cl-rich phases were present in the protoliths of granulite-facies samples, it is unclear how such signals could have been preserved through high-grade metamorphism and partial melting, considering the high solubility of Cl in partial melts and fluids (Carroll and Webster, 1994). Therefore, protolith heterogeneity is also considered an unlikely explanation.

This leaves the third explanation as the most likely: infiltration of Cl-rich fluids during granulite-facies metamorphism (see Section 4.5.3.1 for a discussion of potential sources). This is supported by the presence of salt crystals in fluid inclusions within quartz from granulite-facies metapelites (De Negri and Touret, 1979), as well as the $CaCl_2$ crystals found in metasomatically induced K-feldspar veins (Harlov and Wirth, 2000), both of which have been interpreted to reflect the presence of Cl-rich fluids under granulite-facies conditions. In addition, our data show a positive trend between Cl content and the modal abundance of garnet and sillimanite (Fig. 4c and 4d). Given that these are nominally anhydrous minerals, it is inferred that any Cl present is primarily hosted in fluid and melt inclusions. If the above explanation is correct, the encapsulation of Cl in various silicate phases could also pose a challenge to its complete extraction from rock samples during analyses, potentially explaining the discrepancies in Cl yields observed across the different analytical methods used in this study (Fig. 2b).

4.5.1.2.2. Chlorine in metabasites

No clear trend is observed in Cl concentrations of metabasites of different metamorphic grades, nor in their Cl/Nb ratios (Cl data for the amphibolite-facies rocks are currently only available from the Austin lab, while Br and I results from the Wuhan lab are still pending; see Table 2). Nb is considered to have similar partitioning behavior as Cl during mantle melting (McDonough and Sun, 1995), and so the Cl/Nb ratio can be used to assess non-magmatic influences on Cl concentrations. The metabasite Cl/Nb ratios are also within the range of other mantle-derived rocks (Fig. 5b), making it difficult to assess whether there is a net increase or decrease in Cl content related to prograde metamorphism. This stands in stark contrast to the clearly elevated Cl concentrations observed in granulite-facies metapelites. To further assess the response of metabasites to the inferred Cl-rich fluids during high-grade metamorphism, more systematic sampling and/or petrographic analysis may be needed in the future.

4.5.1.2.3. Chlorine in leucosomes

In leucosomes, Cl content follows a similar pattern to that of metapelites, with concentrations in granulite-facies rocks significantly higher than in amphibolite-facies leucosomes (Fig. 3b). Additionally, leucosomes exhibit much higher Cl/Nb (22–605) and Ba/Nb (65–3,884) ratios compared to those of metapelites (1.8–7.8 and 9–55, respectively), suggesting that the Cl in leucosomes may have originated from metamorphic dehydration and/or externally derived fluids (Fig. 5b). Together with the elevated Cl content in metapelites, these observations suggest that external fluid input likely played a dominant role in controlling the Cl budget of granulite-facies rocks.

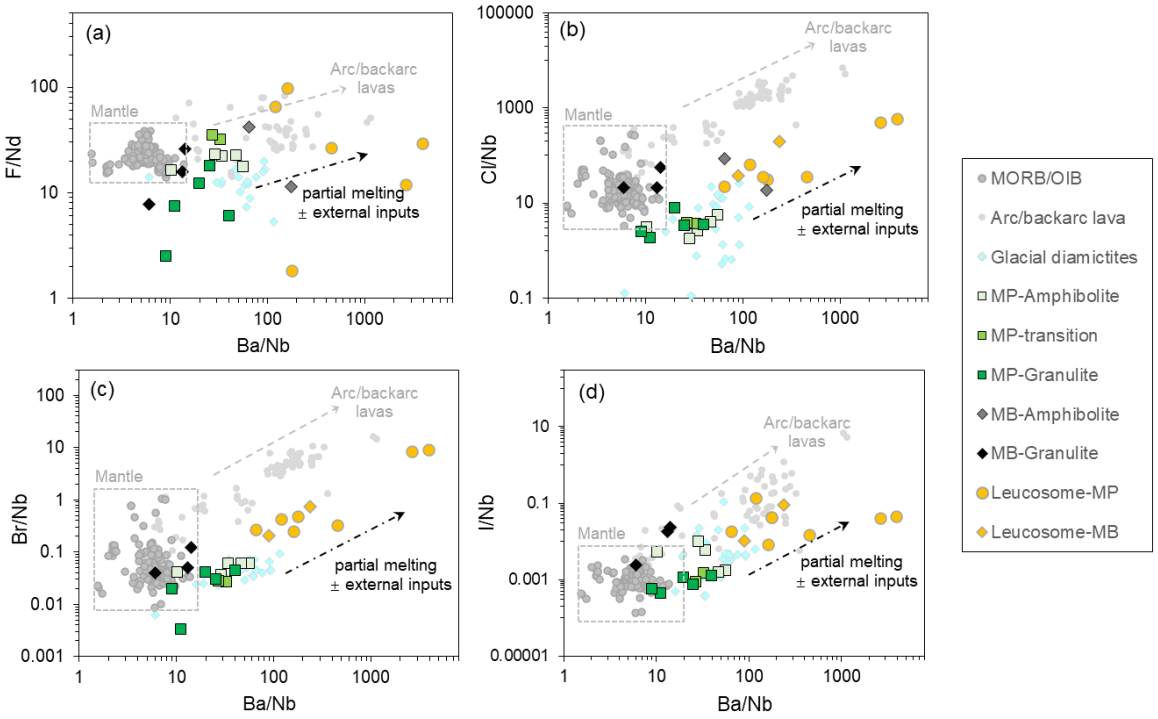

Fig. 5. Halogens and Ba relative to fluid-immobile lithophile elements of similar compatibility. **(a)** F/Nd versus Ba/Nb, **(b)** Cl/Nb versus Ba/Nb, **(c)** Br/Nd versus Ba/Nb, and **(d)** I/Nb versus Ba/Nb. Leucosomes typically exhibit elevated halogen and Ba contents compared to their source rocks (i.e., metapelites and metabasites), likely due to partitioning of these elements into the leucosome melt with or without external fluid inputs. Data for mantle-derived igneous rocks (mid-ocean ridge and ocean island basalts) are sourced from Kendrick et al. (2017 and references therein). Data for island arc/backarc lavas are from Kendrick et al. (2020); their elevated halogens and Ba likely reflect subduction additions.

4.5.1.3. Bromine (Br) and Iodine (I)

Like Cl, the Br (0.61–0.92 ppm) and I (0.02–0.22 ppm) content of the amphibolite-facies metapelites are also similar to the median values of glacial diamictites (0.65 ± 0.14 ppm, and 0.05 ± 0.01 ppm, respectively; Fig. 3c and 3d). However, unlike I, which shows a significant loss in granulite-facies rocks (all values <0.02 ppm), Br exhibits only a weak decreasing trend, from 0.78 ± 0.11 ppm (1σ) in amphibolite-facies rocks to 0.61 ± 0.30 ppm in granulite-

facies rocks. Combined with the analysis of F and Cl behavior in metapelites, it is inferred that I, like F, is primarily hosted in hydrous phases such as biotite and is therefore significantly affected by metamorphic dehydration. The less pronounced trend observed for Br may indicate that it is not predominantly controlled by hydrous phases; instead, part of it may behave similar to Cl, being hosted in fluid and/or melt inclusions. Moreover, given the extensive metamorphism of these rocks have experienced, the weak decreasing trend with metamorphic grade observed for Br concentrations in metapelites (Fig. 3c) may reflect a balance between metamorphic dehydration and an input of Br from external fluids, although the latter appears to be less significant than for Cl (see discussion above).

The metabasites (Br and I data for amphibolite-facies are not yet available) show highly scattered values and no significant trends. The leucosome samples, however, display markedly higher Br and I content (Fig. 3c and 3d), as well as elevated Br/Nb and I/Nb ratios (Fig. 5c and 5d), compared to metapelites and/or metabasites of the same metamorphic grade. This suggests that Br and I were significantly concentrated in the melts during partial melting, consistent with their high solubility in silicate melts (Dolejš and Zajacz, 2018). These halogens could have been derived from both metamorphic dehydration and/or external fluid inputs, though our current data does not allow for a definitive assessment of their relative contributions.

4.5.2. Halogen fractionations

4.5.2.1. Halogen ratios

The similar yet distinct behavior of each halogen makes halogen ratios (e.g., F/Cl, Br/Cl, I/Cl, and Br/I) valuable tracers for geological fluids and melts (e.g., Svensen et al., 2001; Burgess et al., 2002; John et al., 2011; Pagé et al., 2016; Kendrick et al., 2018b). The Br/Cl and I/Cl ratios of the Ivrea Zone samples are shown in Fig. 6a. Among these, metabasites plot exclusively within the arc-backarc lava field, as defined by Kendrick et al. (2020). By contrast, metapelites and leucosomes exhibit a much wider range of Br/Cl ratios (1.8 to $23.4*10^{-3}$) and I/Cl ratios (75 to $5{,}786*10^{-6}$), closely resembling those reported for most glacial diamictite composites by Han et al. (2023). Most of the glacial diamictite composites contain little to no organo-halogens, based on their low total organic carbon contents and their high Br/I ratios (7–74), in comparison to much lower Br/I values observed in organic-rich pelagic sediments, loess, and soils (Br/I = 0.25–6.3) (Han et al., 2024). Since Br/I ratios in the metapelites do not vary significantly with metamorphic grade (Fig. 3j and Fig. 6a), it suggests that metamorphic dehydration does not fractionate them. Therefore, they can be used to infer the potential sources of these sediments. In this regard, the high Br/I values observed in the Ivrea metapelites (3.6–39.4), similar to those found in most glacial diamictites, suggest that these metasedimentary rocks, like the glacial diamictites, contained little to no organic halogens at the time of deposition.

A careful examination of metapelites across different metamorphic grade reveals that F/Cl, Br/Cl, and I/Cl gradually decrease with increasing grade, approaching bulk silicate Earth (BSE) values in the highest-grade samples (Fig. 3g-i). These decreasing trends in halogen ratios could be due to a combination of (1) the loss of F, I, and possibly Br during

metamorphic dehydration, and (2) ingress of Cl-rich fluids during granulite facies metamorphism. These processes contrast with the explanations for similarly fractionated halogen ratios observed in glacial diamictites by Han et al. (2023), where preferential loss of Cl was invoked to explain elevated Br/Cl and I/Cl ratios in the residual sediments. In this context, granulite-facies metamorphism may impose a reverse trend on Br/Cl and I/Cl ratios compared to chemical weathering (Fig. 6a). In other words, the highly fractionated halogen signatures generated during continental weathering could be mitigated—or even overprinted—by metamorphic dehydration and the influx of external Cl-bearing fluids during deep crustal metamorphism. Moreover, the overall similarity in Br/Cl and I/Cl ratios among the Ivrea Zone metapelites, glacial diamictite composites, and lithospheric mantle samples (e.g., eclogites, diamonds, kimberlites, and peridotite xenoliths; Fig. 6b) supports the hypothesis that recycled sediments were transported to great depths, introducing distinct halogen signatures into the lithospheric mantle (Han et al., 2023).

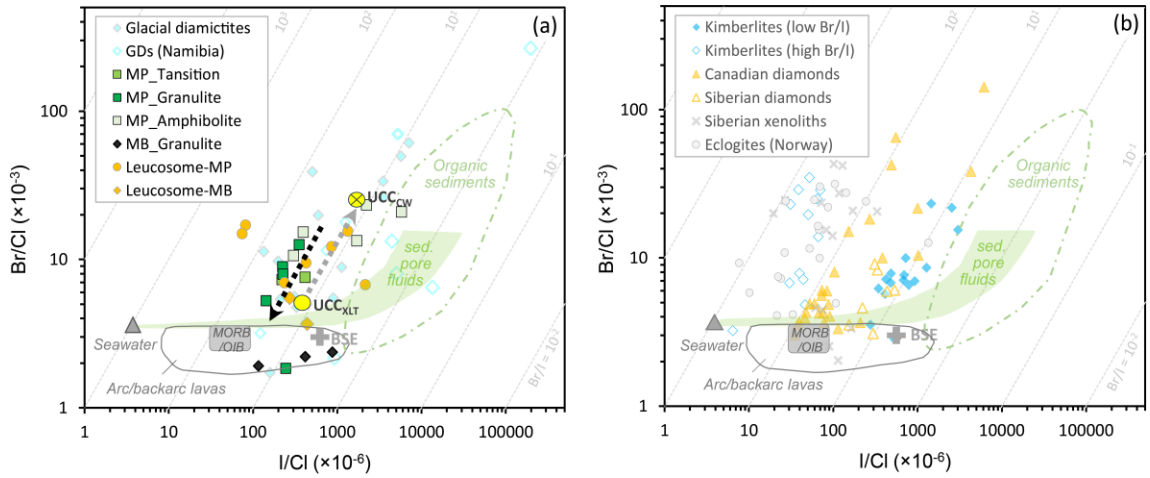

Fig. 6. (a) Br/Cl versus I/Cl ratios of the Ivrea Zone samples (this study) and glacial diamictite composites (Han et al., 2023). Note that five glacial diamictite composites from Namibia, which exhibit relatively high I contents potentially due to the involvement of organic matter, are shown as open diamonds (see Han et al. (2023) for discussion). The open and crossed yellow circles represent the estimated crystalline upper continental crust (UCC_{Xlt}) and the weathered UCC (UCC_{CW}), respectively, as deduced by Han et al. (2023). The difference between UCC_{Xlt} and UCC_{CW} likely reflects preferential loss of Cl during continental weathering, as indicated by the gray dotted arrow. The black arrow shows the trend due to granulite-facies metamorphism (this study, see text). **(b)** Br/Cl and I/Cl ratios from kimberlites of both high and low Br/I groups (Toyama et al., 2021), fluid inclusions from Canadian and Siberian diamonds (Johnson et al., 2000; Burgess et al., 2009; Broadley et al., 2018a), lithospheric mantle xenoliths from Siberia (Broadley et al., 2018b), and eclogites from Norway (Svensen et al., 2001; Hughes et al., 2021). In both (a) and (b), halogen ratios of seawater (grey triangle), bulk silicate Earth (BSE, grey plus sign), mid-ocean ridge and ocean island basalts (MORB/OIB, grey rectangle, Kendrick et al., 2017), arc/backarc lavas (grey outline, Kendrick et al., 2020), organic-rich sediments (green dot-dashed outline, John et al., 2011; Han et al., 2024), and sedimentary pore fluids (green field, Fehn et al., 2006; Muramatsu et al., 2007) are plotted for comparison. Thin grey dashed lines are constant Br/I ratios, ranging from 0.01 to 10,000.

4.5.2.2. Chlorine isotopes

Chlorine has two stable isotopes (^{35}Cl and ^{37}Cl), and their relative proportions in samples provide additional means to examine halogen fractionation (Barnes and Sharp, 2017, and references therein). Previous studies of metasedimentary rocks have shown a wide range of $\delta^{37}Cl$ values (from -3.4 to +2.4‰), but systematic investigations of Cl isotope behavior with metamorphic grade remain limited.

The higher-grade metamorphism (from amphibolite-facies to granulite-facies) and partial melting experienced by the Ivrea Zone samples offer a unique opportunity to examine Cl isotope behavior in the deep continental crust. The $\delta^{37}Cl$ values range from -0.96 to +0.29‰ in metapelites, -0.55 to +0.50‰ in metabasites, and -1.26 to +0.11‰ in leucosomes (Table 2). Except for a slight decreasing trend in $\delta^{37}Cl$ values in the metabasites with increasing metamorphic grade, no clear trends are observed in other lithologies (Fig. 3e). The cause of the decreasing trend in metabasites in unclear and may not be significant, as there is no correlation between Cl concentrations and $\delta^{37}Cl$ values, as well as between Cl/Nb and $\delta^{37}Cl$ values—similar to observations in other lithologies (Fig. 7). Taken together, these results suggest that no significant Cl isotope fractionation occurs during amphibolite- to granulite-facies metamorphism and partial melting in the lower continental crust, consistent with findings from metamorphosed sediments subject to blueschist-eclogite and greenschist-amphibolite facies metamorphism (John et al., 2010; Selverstone and Sharp, 2015; Barnes et al., 2019).

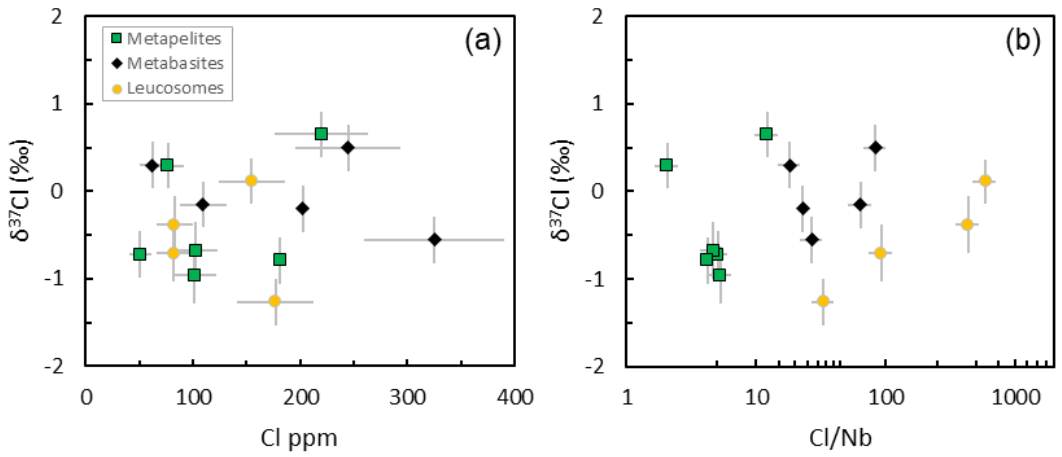

Fig. 7. Chlorine isotopes versus **(a)** Cl concentrations and **(b)** Cl/Nb ratios of the Ivrea Zone samples. Uncertainties represent 1σ.

4.5.3. Geological implications

4.5.3.1. Fluids in the lower continental crust

Based on halogen concentrations and ratios, we infer that a Cl-rich fluid might have percolated through the granulite-facies rocks. If this inference is correct, it raises several key questions: when and how did these fluids enter the system? What were the physical and chemical properties of the fluids?

The distinct pattern of Cl concentration within the amphibolite-facies and granulite-facies rocks, as well as the elevated halogens in leucosomes, suggests that the presence of Cl-rich fluids may be closely linked to granulite-facies metamorphism. Regional metamorphism is suggested to have begun around 316 ± 3 Ma, as determined from metamorphic zircon U-Pb dates in amphibolite-facies metapelites (Ewing et al., 2013). Additional zircon and monazite U-Pb data reveal younger dates, with ages ranging from ~316 Ma in the amphibolite-facies to ~260 Ma in the granulite-facies (e.g., Henk et al., 1997; Ewing et al., 2013; Kunz et al., 2018;

Wyatt et al., 2022). Combined with the 264–287 Ma interval inferred for the garnet growth, based on either garnet U-Pb or Lu-Hf ages by Bartoli et al. (2024) and Connop et al. (2024), it has been suggested that the Ivrea Zone lower continental crust may have been subjected to protracted heating, with temperatures exceeding 650°C for over 50 million years (from ~310 Ma to ~260 Ma). During this period, multiple magmatic intrusions were emplaced, possibly starting with minor intrusions as early as ~314 ± 5 Ma, continuing up to the main intrusion phase of the Mafic Complex between 282–286 Ma (Peressini et al., 2007; Klötzli et al., 2014; Karakas et al., 2019). These intrusions may have provided the necessary heat and possibly Cl-rich fluids, which could have been released during the crystallization of the intruding magmas. Together, these factors may have contributed to the metamorphism and partial melting of the overlying crustal rocks (Fig. 8). Some studies also suggested that anatexis and contact metamorphism associated with emplacement of the Mafic Complex postdate the regional metamorphism and are spatially limited to only a few kilometers (Barboza et al., 1999; Barboza and Bergantz, 2000; Redler et al., 2012), therefore concluding that the contribution of Mafic Complex intrusions to the regional granulite metamorphism is rather limited. If this explanation is correct, the incorporation of Cl-rich fluids into the granulite rocks may have occurred prior to the intrusion of the Mafic Complex (likely before 282–286 Ma).

The proposed Cl-rich fluid is consistent with the hypotheses of Franz and Harlov (1998) and Harlov and Förster (2002a, b), who suggested the presence of pervasive, high-temperature, low-H_2O-activity brines during granulite facies metamorphism that may be enriched in alkaline elements and possibly Cl and F. These brines are thought to have played an essential role in metamorphic dehydration, facilitating the transformation of the

hydrous mineral-bearing zone (muscovite-biotite-hornblende) into an H_2O-poor, garnet- and pyroxene- rich granulite zone. This interpretation is further supported by reports of abundant CO_2 and NaCl observed within fluid inclusions in quartz from granulite rocks (De Negri and Touret, 1979), as well as $CaCl_2$ crystals found in metasomatic K-feldspar veins (Harlov and Wirth, 2000). Therefore, the fluid percolating through the lower continental crust during granulite-facies metamorphism can be summarized to be a high-salinity fluid enriched in Cl, alkaline elements, and CO_2.

The characteristics of the above described fluids are very similar to those that are released from mantle magmas during underplating at the base of the crust (Newton and Manning, 2010; Newton et al., 2019; Touret et al., 2022). Franz and Harlov (1998) also linked the metamorphic fluids in the Ivrea Zone to intrusions of mantle-derived magmas associated with the Mafic Complex. However, this explanation contrasts with that of Baker (1988), who argued for limited fluid infiltration from the mantle into the Ivrea Zone crustal rocks based on the general lack of carbon and oxygen isotopic homogenization observed in mineral separates (e.g., calcite and graphite) and some bulk rock samples. Building on Baker's conclusion, Carvalho et al. (2019) proposed that the variable proportions of CO_2, CH_4, and N_2 hosted in fluid inclusions within garnet reflect a COHN fluid that is immiscible with partial melts and primarily derived from the dehydration of metapelites, rather than from underplated mantle magmas. Further discussion of this issue is beyond the scope of this paper, but the halogen data presented here clearly indicate an external input of Cl-rich fluid into the lower continental crust. The exact composition of the fluids, their origins, the timing of their ingress, and the scale of their impact remain open questions that require further investigation and analysis.

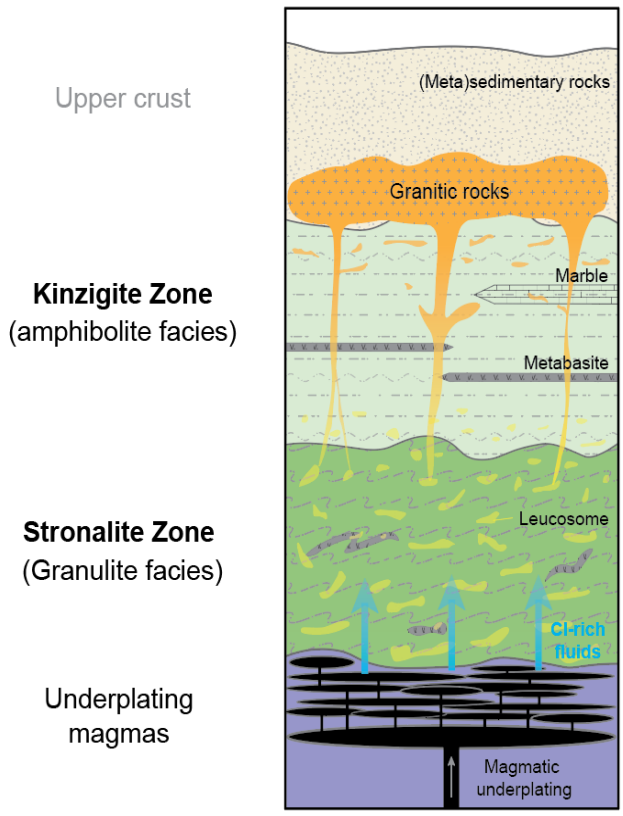

Fig. 8. Suggested model for the high-grade metamorphism and partial melting of the deep crust sampled in the Ivrea Zone, modified from Franz and Harlov (1998). With multiple intrusions of mafic magmas from mantle underplating at the base of the continental crust, heat and Cl-rich fluids will be released as the intruding magmas crystallize. Fluorine, I, and possibly Br may also be released from the metasedimentary rocks through metamorphic dehydration, further facilitating the generation of granitic magmas. These melts subsequently migrated to the upper levels of the crust to form granitic magmas.

4.5.3.2. Implication for crust differentiation

High-grade metamorphism and partial melting play a critical role in the reworking and differentiation of the continental crust. The unexpectedly elevated Cl contents in the Ivrea Zone granulite-facies metapelites documented here points to the involvement of Cl-rich fluids during granulite-facies metamorphism. Assuming that the Cl was released

from mantle-derived magmas underplating the base of the crust (as discussed above), this highlights the important interaction between the crust and mantle during granulite-facies metamorphism. Furthermore, this finding, together with previous reports of Cl-rich fluids in granulite-facies rocks—either preserved as fluid inclusions (e.g., Touret, 1985; Crawford and Hollister, 1986; Touret and Huizenga, 1999; Van den Berg and Huizenga, 2001; Bushmin et al., 2020), mineral salts (De Negri and Touret, 1979; Markl and Bucher, 1998), or inferred from Cl-rich minerals such as biotite or apatite (e.g., Harlov and Förster, 2002; Higashino et al., 2013; Kawakami et al., 2017; Samuel et al., 2021)—suggest that Cl-rich fluids may be a widespread and essential component of high-grade metamorphism. In this context, fluid-present partial melting might be more common than previously thought, contributing to the ongoing debate over the fluid regime (fluid-present versus fluid-absent) in deep-crustal metamorphism and anatexis (for more discussions, see: Clemens and Vielzeuf, 1987; Brown, 2013; Aranovich et al., 2014; Weinberg and Hasalová, 2015).

In addition to externally introduced Cl, our study also reveals that F, I, and possibly Br undergo metamorphic loss during granulite-facies metamorphism. These halogens, once released, may become concentrated in immiscible Cl-rich fluids and/or partial melt due to their relatively high solubility in these liquids (Aiuppa et al., 2009; Dolejš and Zajacz, 2018). Moreover, because of their strong capacity to reduce melt viscosity, lower the solidus of crustal rocks, and complex with other elements in solution (e.g., Manning, 1981; Dingwell et al., 1985; Agangi et al., 2010; Baasner et al., 2013; Feisel et al., 2022), halogens can facilitate the formation and migration of granitic magma, thus contributing to the chemical differentiation of the crust.

Assuming the amphibolite-facies rocks represent the protoliths of granulite-facies rocks prior to high-grade metamorphism and partial melting, the differences between these two rock types provide an opportunity to investigate the effect of these processes, as demonstrated by Schnetger (1994) and Redler et al. (2013). A comparison of the elemental distribution between granulite-facies and amphibolite-facies metapelites from the Ivrea Zone shows that many strongly incompatible elements (e.g., N, Cs, Li, Be, Rb, U, Tl, U, Pb) are strongly depleted in the granulite-facies rocks (Fig. 9). Light rare elements (LREEs) and other incompatible elements (e.g., Ba, Sr, Ta, Th, Nb, Zr) show only moderate loss, while compatible elements (e.g., Zn, Ni, V, Sc, Cr) and heavy REEs (which may be compatible in garnet-bearing residues) are largely preserved. Many of elements depleted in the granulite-facies rocks are also absent in the residual partial melts (the leucosomes), suggesting that these elements may have migrated to the upper crust via partial melts and/or hydrothermal fluids. Interestingly, many of the elements depleted in granulites (e.g., Rb, Sr, Pb, Ba, La, Ce, U) are known to have enhanced solubility in Cl-bearing aqueous fluids based on experimental data (Keppler and Wyllie, 1991; Keppler, 1996; Tropper et al., 2011; Kawamoto et al., 2014; Keppler, 2017), as well as studies of melt inclusions from arc basalts (Cervantes and Wallace, 2003; Portnyagin et al., 2007). A careful examination of elemental behavior in leucosomes from the Ivrea Zone also reveals higher mobility of Rb, Pb, U, and Ba relative to elements of similar compatibility with increasing Cl concentrations (Fig. 10). This pattern is distinct from that observed in arc/backarc lavas, which typically form through hydrous fluid-induced mantle melting at subduction zones. These findings further support the hypothesis that

Cl-rich fluids may have played a critical role in mobilizing those elements during granulite-facies metamorphism, thereby contributing to intracrustal differentiation.

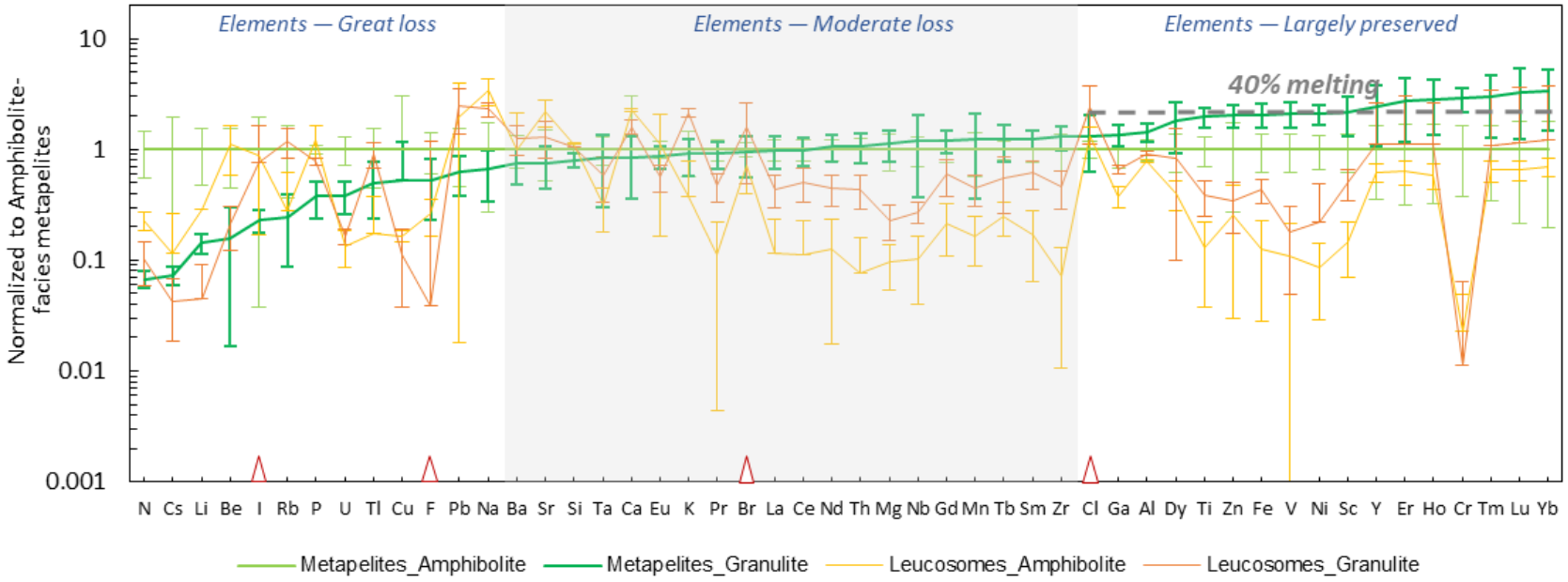

Fig. 9. Median composition of granulite-facies metapelites, normalized to that of amphibolite-facies metapelites. The elemental order is determined by the degree of loss in granulite-facies rocks relative to amphibolite-facies ones, assuming the latter represents the protoliths of granulite rocks prior to high-grade metamorphism and partial melting. The error bars represent 1σ. Leucosomes from both amphibolite-facies and granulite-facies are also plotted for comparison, after the same normalization. The elements are broadly divided into three categories: "great loss" with normalized values < 0.7, "moderate loss" with normalized values >0.7 and <1.3, "largely preserved" with normalized values > 1.3. The gray dashed line represents the predicted composition of granulite rocks after 40% partial melting based on mass balance, with 40% being the highest melting degree inferred by Schnetger (1994) and Redler et al. (2013).

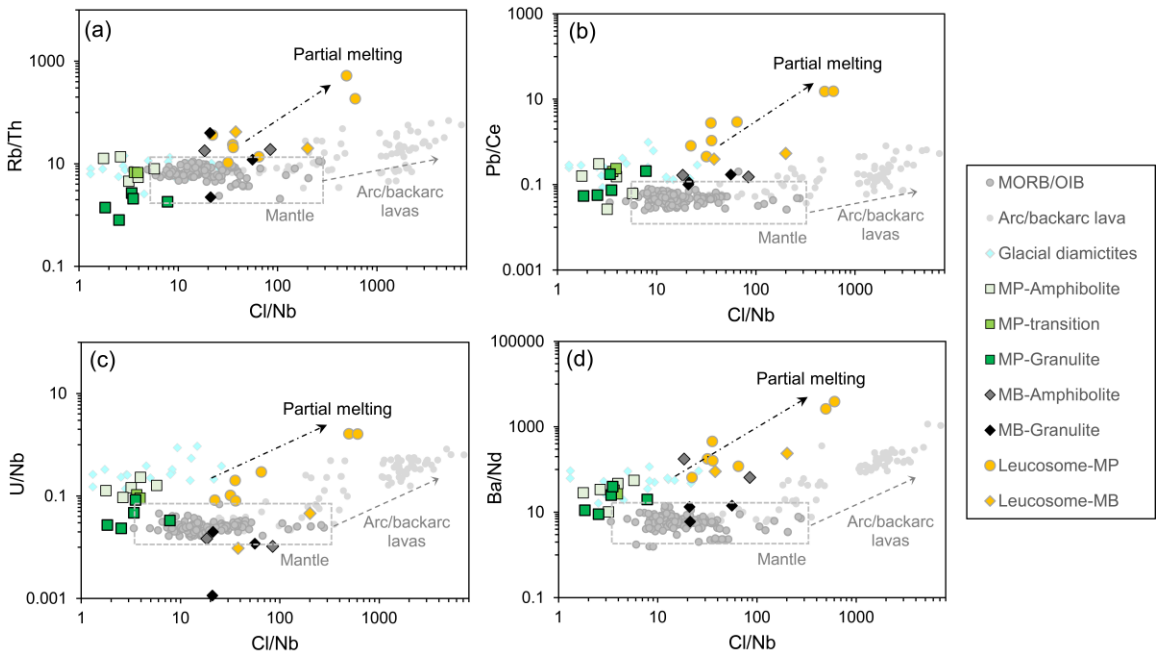

Fig. 10. Mobility of incompatible elements: **(a)** Rb, **(b)** Pb, **(c)** U, and **(d)** Ba relative to elements of similar compatibility with increasing Cl/Nb ratios. Leucosome samples generally show elevated concentrations of these elements and Cl, likely due to Cl-rich fluid-assisted partial melting (see discussion in text). Glacial diamictite data are from Han et al. (2023). Data for mantle-derived igneous rocks (mid-ocean ridge and ocean island basalts), and arc/backarc lavas are sourced from Kendrick et al. (2017) and Kendrick et al. (2020), respectively.

4.6. Conclusions

(1) This study reveals the behavior of halogens across the metamorphic sequence of the middle to lower continental crust, demonstrating that F, I, and possibly Br are significantly depleted during progressive metamorphic dehydration, while Cl concentrations increase with metamorphic grade.

(2) Elevated Cl concentrations in granulite rocks suggest the presence of Cl-rich fluid in the lower continental crust, potentially sourced from mantle-derived magmas underplating the crust.

(3) No significant fractionations occur in Cl isotope composition during metamorphic dehydration, partial melting, and fluid infiltration processes in the deep continental crust.

(4) Halogens released during metamorphic dehydration, along with those introduced by magmas underplating the crust, may have been instrumental in triggering partial melting, aiding the formation of granitic magmas, and driving the chemical evolution of the continental crust.

Summary and Outlook

With a primary focus on the chemical composition of the continental crust, this dissertation systematically examines the concentrations and distributions of major elements and halogens (F, Cl, Br, I) in crustal rocks and explores their implications for crust formation, differentiation, and evolution.

Chapter I focuses on the major elements in the UCC. Despite longstanding efforts to characterize the distribution of these elements, significant uncertainties persist in existing estimates (Rudnick and Gao, 2003 and references therein). These uncertainties are compounded by ambiguity in the definition of the UCC—specifically, whether it refers solely to the igneous crust formed through magmatic differentiation or also includes variable proportions of (meta)sedimentary rocks. Based on a new set of world-wide loess samples, along with a compiled dataset of igneous and sedimentary rocks (including glacial diamictites, shales, and loess) from previous studies, we systematically examined elemental concentrations and ratios across these datasets. From this analysis, we propose a new compositional model, with less than 5% uncertainty (2 standard errors), for the average igneous component of the UCC. The methodology developed in this study introduces a new framework for estimating UCC composition, with the advantage of avoiding potential sampling biases that plague previous attempts, such as oversampling mafic rocks by averaging igneous rocks, and influences of weathering signals in large-scale sampling and/or analyses of fine-grained sedimentary rocks. This new method also provides a foundation for estimating the abundance of other trace elements in the UCC (related work in preparation).

The revised UCC major element composition provides a baseline for evaluating the extent and effects of magmatic differentiation and chemical weathering on the continental crust. With an estimated average granodioritic composition, this study demonstrates the evolved nature of the UCC. By comparing the new model with previous estimates obtained from large-scale sampling and model-based calculations, and by examining partition coefficients between the UCC and seawater, it is found that (1) (meta)sedimentary rocks constitute less than 40% of the exposed continental crust, suggesting that the UCC has largely preserved a dominantly igneous composition despite modifications over geological history; and (2) continental weathering exerts significant control on seawater chemistry for many elements. Despite these advances, important questions remain. Further work will be needed to explore how the revised UCC compositional model relates to climate changes and/or biological evolution, how deeply it extends and relates to the composition of the middle and lower continental crust, and how chemical weathering may have shaped the long-term evolution of the continental crust.

Chapter II and Chapter III present halogen (F, Cl, Br, and I) concentration analyses on globally collected glacial diamictite composites and loess samples, respectively, to characterize halogen abundances in the UCC. While these two find-grained sample types have traditionally served as alternative proxies for investigating elemental abundances in the UCC (e.g., Gallet et al., 1998; Gaschnig et al., 2016), their halogen concentrations differ markedly. Glacial diamictite composites display significantly lower halogen concentrations than loess samples, particularly for Br and I (Han et al., 2023; Han et al., 2024). The halogen composition of most glacial diamictite composites, despite significant weathering signatures, closely resembles that of crustal crystalline rocks (i.e., igneous and metamorphic), suggesting

that these samples primarily reflect the composition of crystalline bedrock component of the UCC. By contrast, loess appears to incorporate substantial halogen contributions from the overlying sedimentary cover on the continental surface, which has been significantly enriched in halogens through biological activity, with halogens likely transported from the oceans to the continents via atmospheric deposition. Accordingly, two sets of halogen abundances are proposed for the UCC: one representing the crystalline basement and another reflecting the more general UCC that averages not only the crystalline bedrocks but also the halogen-enriched sedimentary cover. In addition, the contrast between these two sample sets also provides a key insight that elements can undergo significant fractionation during sedimentary processes, and thus even the most commonly analyzed sedimentary samples—such as fine-grained sediments used in previous studies—may not accurately represent the composition of the crystalline bedrock component of the UCC. This realization also motivated us to compile and analyze igneous rock datasets, along with various types of sedimentary rocks (loess, glacial diamictites, and shales), in order to better estimate the abundances and distribution of other elements in the UCC, as undertaken in Chapter I.

Further analysis of the glacial diamictites suggests that Cl could be preferentially lost relative to Br and I during continental weathering. However, the contribution of Cl from the continents to the oceanic reservoir is minimal (<8–34 %), indicating that most Cl in seawater is sourced from mantle degassing and/or late volatile-accretion. By contrast, enriched halogens in loess samples appear to follow an exponential trend from F to I, with their enrichment factors estimated to be $1.3^{+0.7}_{-0.4}$ (F), $1.8^{+2.4}_{-0.8}$ (Cl), $3.8^{+1.3}_{-1.0}$ (Br), and 39^{+71}_{-16} (I). Together, these observations reveal significant fractionation of halogen ratios (Br/Cl, and I/Cl, and Br/I) on the continental surface, thereby providing additional constraints on using

halogen ratios in tracing geological fluids and melts (Kendrick and Barnes, 2022). Moreover, a mixing model based on organic-sensitive elements such as Br and I suggests that loess is predominantly derived from crystalline bedrock, with less than 10–20% of its composition originating from halogen- and organic-rich sedimentary cover. This finding further supports that loess is a reliable proxy for estimating the average composition of the crystalline UCC, particularly for elements not highly sensitive to biological enrichment, chemical weathering, and mineral sorting (as demonstrated in Chapter I). Finally, halogen concentrations in loess are highly variable, a pattern hypothesized in Chapter III to reflect climate fluctuations during loess formation. This hypothesis is based on the assumption that climate variability could influence both the transport of halogens from the oceans to the continents and their biological fixation into organic matter. To test this, future studies should focus on high-resolution halogen profiles along well-dated loess sequences.

While the first three chapters focus on elemental behavior in upper continental crustal settings, Chapter IV shifts the perspective to geochemical processes within the deep continental crust. The amphibolite- to granulite-facies metamorphism recorded in the Ivrea Zone rocks provides a unique opportunity to examine the behavior of halogens (F, Cl, Br, I, and Cl isotopes) under high-grade metamorphism and partial melting. The results indicate that F, I, and possibly Br are lost through metamorphic dehydration during progressive metamorphism, while Cl appears to be enhanced by input from externally-derived Cl-rich fluids, potentially sourced from underplating magmas. These processes result in significant fractionation of halogen ratios (F/Cl, Br/Cl, and I/Cl), with trends opposite to those observed during continental weathering in glacial diamictites (Chapter II). As no significant fractionation of Cl isotopes was observed across different lithologies (metapelites,

metabasites, and leucosomes) and metamorphic grades (amphibolite- versus granulite-facies), this study shows that Cl isotopes undergo little to no fractionation in the deep continental crust.

Combined with the presence of Cl-rich fluid inclusions and minerals reported in the Ivrea Zone metamorphic rocks (De Negri and Touret, 1979; Harlov and Wirth, 2000), as well as in other granulite terranes (e.g., Touret, 1985; Markl and Bucher, 1998; Kawakami et al., 2017; Ferrero et al., 2021; Samuel et al., 2021), it is suggested that Cl-rich fluids were widespread during granulite-facies metamorphism. Moreover, the pervasive halogens present in the lower continental crust, sourced either from metamorphic dehydration (F, I, and possibly Br) and/or magma underplating (Cl), may have played an essential role in the generation of granitic magma, thereby contributing to the differentiation of the continental crust. However, to further constrain the properties of fluids in the lower continental crust, including their origins, exact halogen concentrations, partition coefficients with lower-crustal mineral phases (such as garnet, pyroxene, and amphibole), and interactions with other elements and metals, future studies should include more systematic halogen analyses of samples from other high-grade terranes, fluid/melt inclusions, and related experimental work.

REFERENCES

Aagaard, P., Egeberg, P., Saigal, G., Morad, S. and Bjorlykke, K. (1990) Diagenetic albitization of detrital K-feldspars in Jurassic, Lower Cretaceous and Tertiary clastic reservoir rocks from offshore Norway; II, Formation water chemistry and kinetic considerations. J. Sediment. Res. 60, 575-581.

Aarons, S.M., Dauphas, N., Greber, N.D., Roskosz, M., Bouchez, J., Carley, T., Liu, X.-M., Rudnick, R.L. and Gaillardet, J. (2023) Titanium transport and isotopic fractionation in the Critical Zone. Geochim. Cosmochim. Acta 352, 175-193.

Agangi, A., Kamenetsky, V.S. and McPhie, J. (2010) The role of fluorine in the concentration and transport of lithophile trace elements in felsic magmas: insights from the Gawler Range Volcanics, South Australia. Chem. Geol. 273, 314-325.

Aiuppa, A., Baker, D. and Webster, J. (2009) Halogens in volcanic systems. Chem. Geol. 263, 1-18.

Amiotte Suchet, P., Probst, J.L. and Ludwig, W. (2003) Worldwide distribution of continental rock lithology: Implications for the atmospheric/soil CO2 uptake by continental weathering and alkalinity river transport to the oceans. Glob. Biogeochem. Cycle 17.

An, Z., Kukla, G.J., Porter, S.C. and Xiao, J. (1991) Magnetic susceptibility evidence of monsoon variation on the Loess Plateau of central China during the last 130,000 years. Quaternary Research 36, 29-36.

Annen, C. and Burgisser, A. (2021) Modeling water exsolution from a growing and solidifying felsic magma body. Lithos 402, 105799.

Antoine, P., Rousseau, D.-D., Moine, O., Kunesch, S., Hatté, C., Lang, A., Tissoux, H. and Zöller, L. (2009) Rapid and cyclic aeolian deposition during the Last Glacial in European loess: a high-resolution record from Nussloch, Germany. Quaternary Science Reviews 28, 2955-2973.

Aranovich, L.Y., Makhluf, A.R., Manning, C.E. and Newton, R.C. (2014) Dehydration melting and the relationship between granites and granulites. Precambrian Res. 253, 26-37.

Árkai, P. (2002) Phyllosilicates in very low-grade metamorphism: transformation to micas. Rev. Mineral. Geochem. 46, 463-478.

Assemi, S. and Erten, H. (1994) Sorption of radioiodine on organic rich soil, clay minerals and alumina. J. Radioanal. Nucl. Chem. 178, 193-204.

Avice, G., Marty, B. and Burgess, R. (2017) The origin and degassing history of the Earth's atmosphere revealed by Archean xenon. Nat. Commun. 8, 1-9.

Baasner, A., Schmidt, B. and Webb, S.L. (2013) The effect of chlorine, fluorine and water on the viscosity of aluminosilicate melts. Chem. Geol. 357, 134-149.

Baker, A. (1988) Stable isotope evidence for limited fluid infiltration of deep crustal rocks from the Ivrea Zone, Italy. Geology 16, 492-495.

Balcone-Boissard, H., Villemant, B. and Boudon, G. (2010) Behavior of halogens during the degassing of felsic magmas. Geochem. Geophys. Geosyst. 11.

Barboza, S.A. and Bergantz, G.W. (2000) Metamorphism and anatexis in the mafic complex contact aureole, Ivrea Zone, Northern Italy. J. Petrol. 41, 1307-1327.

Barboza, S.A., Bergantz, G.W. and Brown, M. (1999) Regional granulite facies metamorphism in the Ivrea zone: Is the Mafic Complex the smoking gun or a red herring? Geology 27, 447-450.

Barnes, J.D., Penniston-Dorland, S.C., Bebout, G.E., Hoover, W., Beaudoin, G.M. and Agard, P. (2019) Chlorine and lithium behavior in metasedimentary rocks during prograde metamorphism: A comparative study of exhumed subduction complexes (Catalina Schist and Schistes Lustrés). Lithos 336, 40-53.

Barnes, J.D. and Sharp, Z.D. (2017) Chlorine isotope geochemistry. Rev. Mineral. Geochem. 82, 345-378.

Barth, M.G., McDonough, W.F. and Rudnick, R.L. (2000) Tracking the budget of Nb and Ta in the continental crust. Chem. Geol. 165, 197-213.

Bartoli, O., Millonig, L.J., Carvalho, B.B., Marschall, H.R. and Gerdes, A. (2024) The Age of Granulite-Facies Metamorphism in the Ivrea–Verbano Zone (NW Italy) Determined Through In Situ U–Pb Dating of Garnet. J. Petrol. 65, egae083.

Bayon, G., Delvigne, C., Ponzevera, E., Borges, A., Darchambeau, F., De Deckker, P., Lambert, T., Monin, L., Toucanne, S. and André, L. (2018) The silicon isotopic composition of fine-grained river sediments and its relation to climate and lithology. Geochim. Cosmochim. Acta 229, 147-161.

Bayon, G., Toucanne, S., Skonieczny, C., André, L., Bermell, S., Cheron, S., Dennielou, B., Etoubleau, J., Freslon, N., Gauchery, T., Germain, Y., Jorry, S.J., Ménot, G., Monin, L., Ponzevera, E., Rouget, M.L., Tachikawa, K. and Barrat, J.A. (2015) Rare earth elements and neodymium isotopes in world river sediments revisited. Geochim. Cosmochim. Acta 170, 17-38.

Bea, F. and Montero, P. (1999) Behavior of accessory phases and redistribution of Zr, REE, Y, Th, and U during metamorphism and partial melting of metapelites in the lower crust: an example from the Kinzigite Formation of Ivrea-Verbano, NW Italy. Geochim. Cosmochim. Acta 63, 1133-1153.

Beard, B.L. and Johnson, C.M. (2004) Fe isotope variations in the modern and ancient earth and other planetary bodies. Rev. Mineral. Geochem. 55, 319-357.

Beaudoin, G., Barnes, J., Orlandini, O., Chatterjee, R., Stockli, D. and John, T. (2024) Halogen (F, Cl, Br, and I) devolatilization during prograde subduction: Insights from Western Alps ophiolites. Geochem. Geophys. Geosyst. 25, e2023GC011295.

Beaudoin, G.M., Barnes, J.D., John, T., Hoffmann, J.E., Chatterjee, R. and Stockli, D.F. (2022) Global halogen flux of subducting oceanic crust. Earth Planet. Sci. Lett. 594, 117750.

Bekaert, D., Turner, S., Broadley, M., Barnes, J., Halldórsson, S., Labidi, J., Wade, J., Walowski, K. and Barry, P. (2021) Subduction-driven volatile recycling: a global mass balance. Annu. Rev. Earth Planet. Sci. 49, 37-70.

Bell, M. and Laine, E. (1985) Erosion of the Laurentide region of North America by glacial and glaciofluvial processes. Quaternary Research 23, 154-174.

Berger, T., Mathurin, F.A., Drake, H. and Åström, M.E. (2016) Fluoride abundance and controls in fresh groundwater in Quaternary deposits and bedrock fractures in an area with fluorine-rich granitoid rocks. Sci. Total Environ. 569, 948-960.

Berner, R.A. and Berner, E.K. (1997) Silicate weathering and climate, Tectonic uplift and climate change. Springer, pp. 353-365.

Bettis III, E.A., Muhs, D.R., Roberts, H.M. and Wintle, A.G. (2003) Last glacial loess in the conterminous USA. Quaternary Science Reviews 22, 1907-1946.

Bish, D.L. and Post, J.E. (1993) Quantitative mineralogical analysis using the Rietveld full-pattern fitting method. Am. Mineral. 78, 932-940.

Boles, J.R. (1982) Active albitization of plagioclase, gulf coast Tertiary. Am. J. Sci. 282, 165-180.

Borodin, L. (1999) Estimated chemical composition and petrochemical evolution of the upper continental crust. Geochemistry International 37, 723-734.

Bowring, S.A. and Williams, I.S. (1999) Priscoan (4.00–4.03 Ga) orthogneisses from northwestern Canada. Contrib. Mineral. Petrol. 134, 3-16.

Bradley, D.C. (2011) Secular trends in the geologic record and the supercontinent cycle. Earth-Sci. Rev. 108, 16-33.

Broadley, M., Kagi, H., Burgess, R., Zedgenizov, D., Mikhail, S., Almayrac, M., Ragozin, A., Pomazansky, B. and Sumino, H. (2018a) Plume-lithosphere interaction, and the formation of fibrous diamonds. Geochem. Perspect. Lett. 8.

Broadley, M.W., Ballentine, C.J., Chavrit, D., Dallai, L. and Burgess, R. (2016) Sedimentary halogens and noble gases within Western Antarctic xenoliths: Implications of extensive volatile recycling to the sub continental lithospheric mantle. Geochim. Cosmochim. Acta 176, 139-156.

Broadley, M.W., Barry, P.H., Ballentine, C.J., Taylor, L.A. and Burgess, R. (2018b) End-Permian extinction amplified by plume-induced release of recycled lithospheric volatiles. Nat. Geosci. 11, 682-687.

Brown, M. (2013) Granite: From genesis to emplacement. GSA bulletin 125, 1079-1113.

Bruland, K.W. and Lohan, M.C. (2003) Controls of Trace Metals in Seawater. Treatise on Geochemistry 6.02, 23-47.

Bureau, H., Keppler, H. and Métrich, N. (2000) Volcanic degassing of bromine and iodine: experimental fluid/melt partitioning data and applications to stratospheric chemistry. Earth Planet. Sci. Lett. 183, 51-60.

Burgess, R., Cartigny, P., Harrison, D., Hobson, E. and Harris, J. (2009) Volatile composition of microinclusions in diamonds from the Panda kimberlite, Canada: Implications for chemical and isotopic heterogeneity in the mantle. Geochim. Cosmochim. Acta 73, 1779-1794.

Burgess, R., Layzelle, E., Turner, G. and Harris, J. (2002) Constraints on the age and halogen composition of mantle fluids in Siberian coated diamonds. Earth Planet. Sci. Lett. 197, 193-203.

Burisch, M., Marks, M.A., Nowak, M. and Markl, G. (2016) The effect of temperature and cataclastic deformation on the composition of upper crustal fluids—An experimental approach. Chem. Geol. 433, 24-35.

Bushmin, S., Vapnik, Y.A., Ivanov, M., Lebedeva, Y.M. and Savva, E. (2020) Fluids in high-pressure granulites. Petrology 28, 17-46.

Canfield, D.E., Erik, K. and Bo, T. (2005) The Iron and Manganese Cycles, in: Canfield, D.E., Kristensen, E., Thamdrup, B. (Eds.), Advances in Marine Biology. Academic Press, pp. 269-312.

Canil, D. and Lacourse, T. (2011) An estimate for the bulk composition of juvenile upper continental crust derived from glacial till in the North American Cordillera. Chem. Geol. 284, 229-239.

Carpentier, M., Weis, D. and Chauvel, C. (2013) Large U loss during weathering of upper continental crust: the sedimentary record. Chem. Geol. 340, 91-104.

Carroll, M.R. and Webster, J.D. (1994) Solubilities of sulfur, noble gases, nitrogen, chlorine, and fluorine in magmas. Reviews in Mineralogy 30, 231-231.

Carvalho, B.B., Bartoli, O., Ferri, F., Cesare, B., Ferrero, S., Remusat, L., Capizzi, L.S. and Poli, S. (2019) Anatexis and fluid regime of the deep continental crust: New clues from melt and fluid inclusions in metapelitic migmatites from Ivrea Zone (NW Italy). J. Metamorph. Geol. 37, 951-975.

Cawood, P.A., Hawkesworth, C. and Dhuime, B. (2013) The continental record and the generation of continental crust. Bulletin 125, 14-32.

Cervantes, P. and Wallace, P.J. (2003) Role of H2O in subduction-zone magmatism: new insights from melt inclusions in high-Mg basalts from central Mexico. Geology 31, 235-238.

Chauvel, C., Garçon, M., Bureau, S., Besnault, A., Jahn, B.-m. and Ding, Z. (2014) Constraints from loess on the Hf–Nd isotopic composition of the upper continental crust. Earth Planet. Sci. Lett. 388, 48-58.

Chavrit, D., Burgess, R., Sumino, H., Teagle, D.A., Droop, G., Shimizu, A. and Ballentine, C.J. (2016) The contribution of hydrothermally altered ocean crust to the mantle halogen and noble gas cycles. Geochim. Cosmochim. Acta 183, 106-124.

Che, X. and Li, G. (2013) Binary sources of loess on the Chinese Loess Plateau revealed by U–Pb ages of zircon. Quaternary Research 80, 545-551.

Chen, K., Rudnick, R.L., Wang, Z., Tang, M., Gaschnig, R.M., Zou, Z., He, T., Hu, Z. and Liu, Y. (2020) How mafic was the Archean upper continental crust? Insights from Cu and Ag in ancient glacial diamictites. Geochim. Cosmochim. Acta 278, 16-29.

Chen, K., Walker, R.J., Rudnick, R.L., Gao, S., Gaschnig, R.M., Puchtel, I.S., Tang, M. and Hu, Z.C. (2016) Platinum-group element abundances and Re-Os isotopic systematics of the upper continental crust through time: evidence from glacial diamictites. Geochim. Cosmochim. Acta 191, 1-16.

Chevychelov, V.Y., Botcharnikov, R.E. and Holtz, F. (2008) Partitioning of Cl and F between fluid and hydrous phonolitic melt of Mt. Vesuvius at~ 850–1000 C and 200 MPa. Chem. Geol. 256, 172-184.

Clarke, F.W. (1889) The relative abundance of the chemical elements. Bulletin of the Philosophical Society of Washington 11, 135-143.

Clarke, F.W. and Washington, H.S. (1924) The composition of the earth's crust. US Government Printing Office.

Clay, P. (2021) Halogen Abundances and Isotopes, Encyclopedia of Geology: Geochemistry, Geochemical Proxies. Elsevier, pp. 81-99.

Clay, P.L., Burgess, R., Busemann, H., Ruzié-Hamilton, L., Joachim, B., Day, J.M. and Ballentine, C.J. (2017) Halogens in chondritic meteorites and terrestrial accretion. Nature 551, 614-618.

Clayton, J.L. (1986) An estimate of plagioclase weathering rate in the Idaho batholith based upon geochemical transport rates. Rates of Chemical Weathering of rocks and minerals, 453-466.

Clemens, J. and Vielzeuf, D. (1987) Constraints on melting and magma production in the crust. Earth Planet. Sci. Lett. 86, 287-306.

Condie, K.C. (1993) Chemical composition and evolution of the upper continental crust: Contrasting results from surface samples and shales. Chem. Geol. 104, 1-37.

Condie, K.C. (2008) Did the character of subduction change at the end of the Archean? Constraints from convergent-margin granitoids. Geology 36, 611-614.

Condie, K.C. and O'Neill, C. (2010) The Archean-Proterozoic boundary: 500 my of tectonic transition in Earth history. Am. J. Sci. 310, 775-790.

Connop, C.H., Smye, A.J., Garber, J.M., Moser, A.C., Caddick, M.J. and Vervoort, J.D. (2024) Assembly of lower continental crust: a garnet Lu-Hf petrochronological investigation of the Ivrea-Verbano zone, Italy. Earth Planet. Sci. Lett. 634, 118677.

Cortizas, A.M., Vázquez, C.F., Kaal, J., Biester, H., Casais, M.C., Rodríguez, T.T. and Lado, L.R. (2016) Bromine accumulation in acidic black colluvial soils. Geochim. Cosmochim. Acta 174, 143-155.

Cox, G.M., Lyons, T.W., Mitchell, R.N., Hasterok, D. and Gard, M. (2018) Linking the rise of atmospheric oxygen to growth in the continental phosphorus inventory. Earth Planet. Sci. Lett. 489, 28-36.

Crawford, M. and Hollister, L. (1986) Metamorphic fluids: the evidence from fluid inclusions, Fluid—Rock Interactions during Metamorphism. Springer, pp. 1-35.

Cuevas, C.A., Fernandez, R.P., Kinnison, D.E., Li, Q., Lamarque, J.-F., Trabelsi, T., Francisco, J.S., Solomon, S. and Saiz-Lopez, A. (2022) The influence of iodine on the Antarctic stratospheric ozone hole. Proc. Natl. Acad. Sci. 119, e2110864119.

Cullen, J.T., Hurwitz, S., Barnes, J.D., Lassiter, J.C., Penniston-Dorland, S., Kasemann, S.A. and Thordsen, J.J. (2019) Temperature-dependent variations in mineralogy, major element chemistry and the stable isotopes of boron, lithium and chlorine resulting from hydration of rhyolite: Constraints from hydrothermal experiments at 150 to 350 C and 25 MPa. Geochim. Cosmochim. Acta 261, 269-287.

Dauphas, N., Roskosz, M., Alp, E.E., Neuville, D.R., Hu, M.Y., Sio, C., Tissot, F., Zhao, J., Tissandier, L. and Médard, E. (2014) Magma redox and structural controls on iron isotope variations in Earth's mantle and crust. Earth Planet. Sci. Lett. 398, 127-140.

De Negri, G. and Touret, J. (1979) Fluid inclusions in metapelites from Valle Strona, province of Novara. Memorie degli Istituti di Geologia e Mineralogia dell' Universita di Padova 33, 87-94.

Deer, W.A., Howie, R.A. and Zussman, J. (2013) An introduction to the rock-forming minerals. Mineralogical Society of Great Britain and Ireland.

Deng, Z., Chaussidon, M., Savage, P., Robert, F., Pik, R. and Moynier, F. (2019) Titanium isotopes as a tracer for the plume or island arc affinity of felsic rocks. Proc. Natl. Acad. Sci. 116, 1132-1135.

Derbyshire, E., Meng, X. and Kemp, R.A. (1998) Provenance, transport and characteristics of modern aeolian dust in western Gansu Province, China, and interpretation of the Quaternary loess record. Journal of arid environments 39, 497-516.

Dhuime, B., Wuestefeld, A. and Hawkesworth, C.J. (2015) Emergence of modern continental crust about 3 billion years ago. Nat. Geosci. 8, 552-555.

Ding, Z., Ren, J., Yang, S. and Liu, T. (1999) Climate instability during the penultimate glaciation: Evidence from two high-resolution loess records, China. J. Geophys. Res.: Solid Earth 104, 20123-20132.

Dingwell, D.B., Scarfe, C.M. and Cronin, D.J. (1985) The effect of fluorine on viscosities in the system Na2O–Al2O3–SiO2: implications for phonolites, trachytes and rhyolites. Am. Mineral. 70, 80-87.

Dolejš, D. and Baker, D.R. (2007) Liquidus equilibria in the system K2O–Na2O–Al2O3–SiO2–F2O− 1–H2O to 100 MPa: I. Silicate–fluoride liquid immiscibility in anhydrous systems. J. Petrol. 48, 785-806.

Dolejš, D. and Zajacz, Z. (2018) Halogens in silicic magmas and their hydrothermal systems. The role of halogens in terrestrial and extraterrestrial geochemical processes: surface, crust, and mantle, 431-543.

Eby, G.N. (1990) The A-type granitoids: a review of their occurrence and chemical characteristics and speculations on their petrogenesis. Lithos 26, 115-134.

Eggenkamp, H., Kreulen, R. and Van Groos, A.K. (1995) Chlorine stable isotope fractionation in evaporites. Geochim. Cosmochim. Acta 59, 5169-5175.

Elderfield, H. and Truesdale, V.W. (1980) On the biophilic nature of iodine in seawater. Earth Planet. Sci. Lett. 50, 105-114.

Epp, T., Marks, M.A., Ludwig, T., Kendrick, M.A., Eby, N., Neidhardt, H., Oelmann, Y. and Markl, G. (2019) Crystallographic and fluid compositional effects on the halogen (Cl, F, Br, I) incorporation in pyromorphite-group minerals. Am. Mineral. 104, 1673-1688.

Epp, T., Marks, M.A.W., Neidhardt, H., Oelmann, Y. and Markl, G. (2022) Halogen (F, Cl, Br, I) contents in silt and clay fractions of a Cambisol from a temperate forest. Am. Mineral. 107, 946-954.

Epp, T., Neidhardt, H., Pagano, N., Marks, M.A., Markl, G. and Oelmann, Y. (2020) Vegetation canopy effects on total and dissolved Cl, Br, F and I concentrations in soil and their fate along the hydrological flow path. Sci. Total Environ. 712, 135473.

Ewing, T.A., Hermann, J. and Rubatto, D. (2013) The robustness of the Zr-in-rutile and Ti-in-zircon thermometers during high-temperature metamorphism (Ivrea-Verbano Zone, northern Italy). Contrib. Mineral. Petrol. 165, 757-779.

Ewing, T.A., Rubatto, D., Beltrando, M. and Hermann, J. (2015) Constraints on the thermal evolution of the Adriatic margin during Jurassic continental break-up: U–Pb dating of rutile from the Ivrea–Verbano Zone, Italy. Contrib. Mineral. Petrol. 169, 1-22.

Fahrig, W. and Eade, K. (1968) The chemical evolution of the Canadian Shield. Can. J. Earth Sci. 5, 1247-1252.

Fan, Y., Zhou, W., Hou, X., Kong, X., Chen, N. and Burr, G.S. (2021) Indication of new climatic proxy by loess iodine variation. Quaternary Science Reviews 251, 106720.

Favero, G. and Jobstraibizer, P. (1996) The distribution of aluminium in the earth: from cosmogenesis to Sial evolution. Coordination chemistry reviews 149, 367-400.

Fedo, C.M., Wayne Nesbitt, H. and Young, G.M. (1995) Unraveling the effects of potassium metasomatism in sedimentary rocks and paleosols, with implications for paleoweathering conditions and provenance. Geology 23, 921-924.

Fehn, U., Lu, Z. and Tomaru, H. (2006) Data report: 129I/I ratios and halogen concentrations in pore water of Hydrate Ridge and their relevance for the origin of gas hydrates: A

progress report, Proceedings of the Ocean Drilling Program: Scientific Results. Texas A & M University, pp. 1-25.

Fehn, U., Snyder, G. and Egeberg, P.K. (2000) Dating of pore waters with 129I: relevance for the origin of marine gas hydrates. Science 289, 2332-2335.

Fehn, U., Snyder, G. and Muramatsu, Y. (2007) Iodine as a tracer of organic material: 129I results from gas hydrate systems and fore arc fluids. J. Geochem. Explor. 95, 66-80.

Fehn, U., Snyder, G.T., Matsumoto, R., Muramatsu, Y. and Tomaru, H. (2003) Iodine dating of pore waters associated with gas hydrates in the Nankai area, Japan. Geology 31, 521-524.

Feisel, Y., Castro, J.M., Helo, C. and Dingwell, D.B. (2022) The effect of halogens (F, Cl) on the near-liquidus crystallinity of a hydrous trachyte melt. American Mineralogist: Journal of Earth and Planetary Materials 107, 1007-1017.

Feng, X., Steiner, Z. and Redfern, S.A. (2021) Fluorine incorporation into calcite, aragonite and vaterite CaCO3: Computational chemistry insights and geochemistry implications. Geochim. Cosmochim. Acta 308, 384-392.

Feng, Z.-D., Ran, M., Yang, Q., Zhai, X., Wang, W., Zhang, X. and Huang, C. (2011) Stratigraphies and chronologies of late Quaternary loess–paleosol sequences in the core area of the central Asian arid zone. Quaternary International 240, 156-166.

Ferrero, S., Ague, J.J., O'Brien, P.J., Wunder, B., Remusat, L., Ziemann, M.A. and Axler, J. (2021) High-pressure, halogen-bearing melt preserved in ultrahigh-temperature felsic granulites of the Central Maine Terrane, Connecticut (USA). Am. Mineral. 106, 1225-1236.

Filippelli, G.M. (2008) The global phosphorus cycle: past, present, and future. Elements 4, 89-95.

Finch, E. and Tomkins, A. (2017) Fluorine and chlorine behaviour during progressive dehydration melting: Consequences for granite geochemistry and metallogeny. J. Metamorph. Geol. 35, 739-757.

Force, E.R. (1976) Titanium contents and titanium partitioning in rocks. Geological Survey Professional Paper 959, A1-A10.

Franz, L. and Harlov, D.E. (1998) High-grade K-feldspar veining in granulites from the Ivrea-Verbano Zone, northern Italy: fluid flow in the lower crust and implications for granulite facies genesis. J. Geol. 106, 455-472.

Fuge, R. (1988) Sources of halogens in the environment, influences on human and animal health. Environ. Geochem. Health 10, 51-61.

Fuge, R., Johnson, C. and Phillips, W. (1978) Iodine in granitic and associated rocks. Chem. Geol. 22, 347-352.

Fuge, R. and Johnson, C.C. (1986) The geochemistry of iodine—a review. Environ. Geochem. Health 8, 31-54.

Gallet, S., Jahn, B.-m., Lanoë, B.V.V., Dia, A. and Rossello, E. (1998) Loess geochemistry and its implications for particle origin and composition of the upper continental crust. Earth Planet. Sci. Lett. 156, 157-172.

Gao, S. (2010) Chemical composition of the continental crust: a perspective from China. Geochemical News 143.

Gao, S., Luo, T.C., Zhang, B.R., Zhang, H.F., Han, Y.W., Zhao, Z.D. and Hu, Y.K. (1998) Chemical composition of the continental crust as revealed by studies in East China. Geochim. Cosmochim. Acta 62, 1959-1975.

Gaschnig, R.M., Horan, M.F., Rudnick, R.L., Vervoort, J.D. and Fisher, C.M. (2022) History of crustal growth in Africa and the Americas from detrital zircon and Nd isotopes in glacial diamictites. Precambrian Res. 373, 106641.

Gaschnig, R.M., Rudnick, R.L., McDonough, W.F., Kaufman, A.J., Hu, Z. and Gao, S. (2014) Onset of oxidative weathering of continents recorded in the geochemistry of ancient glacial diamictites. Earth Planet. Sci. Lett. 408, 87-99.

Gaschnig, R.M., Rudnick, R.L., McDonough, W.F., Kaufman, A.J., Valley, J.W., Hu, Z., Gao, S. and Beck, M.L. (2016) Compositional evolution of the upper continental crust through time, as constrained by ancient glacial diamictites. Geochim. Cosmochim. Acta 186, 316-343.

Goldberg, S. and J. Kabengi, N. (2010) Bromide adsorption by reference minerals and soils. Vadose Zone Journal 9, 780-786.

Goldschmidt, V. (1933) Grundlagen der quantitativen Geochemie. Fortschr. Mienral. Kirst. Petrogr 17, 112.

Gong, Y., Xia, Y., Huang, F. and Yu, H. (2017) Average iron isotopic compositions of the upper continental crust: constrained by loess from the Chinese Loess Plateau. Acta Geochimica 36, 125-131.

González-Acebrón, L., Arribas, J. and Mas, R. (2010) Role of sandstone provenance in the diagenetic albitization of feldspars: A case study of the Jurassic Tera Group sandstones (Cameros Basin, NE Spain). Sediment. Geol. 229, 53-63.

Govindaraju, K. (1994) 1994 compilation of working values and sample description for 383 geostandards. Geostan. Newsl. 18, 1-158.

Greaney, A.T., Rudnick, R.L., Romaniello, S.J., Johnson, A.C., Gaschnig, R.M. and Anbar, A.D. (2020) Molybdenum isotope fractionation in glacial diamictites tracks the onset of oxidative weathering of the continental crust. Earth Planet. Sci. Lett. 534, 116083.

Gromet, L.P., Haskin, L.A., Korotev, R.L. and Dymek, R.F. (1984) The "North American shale composite": Its compilation, major and trace element characteristics. Geochim. Cosmochim. Acta 48, 2469-2482.

Guan, Q., Pan, B., Gao, H., Li, N., Zhang, H. and Wang, J. (2008) Geochemical evidence of the Chinese loess provenance during the Late Pleistocene. Palaeogeogr. Palaeoclimatol. Palaeoecol. 270, 53-58.

Guo, Z., Biscaye, P., Wei, L., Chen, X., Peng, S. and Liu, T. (2000) Summer monsoon variations over the last 1.2 Ma from the weathering of loess-soil sequences in China. Geophys. Res. Lett. 27, 1751-1754.

Guo, Z., Liu, T. and An, Z. (1994) Paleosols of the last 0.15 Ma in the Weinan loess section and their paleoclimatic significance. Quaternary Sciences 14, 256-269.

Hacker, B.R., Kelemen, P.B. and Behn, M.D. (2011) Differentiation of the continental crust by relamination. Earth Planet. Sci. Lett. 307, 501-516.

Halama, R., Bebout, G.E. and Bea, F. (2021) Nitrogen loss and isotopic fractionation during granulite-facies metamorphism in the lower crust (Ivrea Zone, NW Italy). Chem. Geol. 584, 120475.

Han, P.-Y., Rudnick, R.L., He, T., Marks, M.A., Wang, S.-J., Gaschnig, R.M. and Hu, Z.-C. (2023) Halogen (F, Cl, Br, and I) concentrations of the upper continental crust

through time as recorded in ancient glacial diamictite composites. Geochim. Cosmochim. Acta 341, 28-45.

Han, P.Y., Rudnick, R.L., Hu, Z.C., He, T., Marks, M.A.W. and Chen, K. (2024) Halogen enrichment on the continental surface: a perspective from loess. Geochem. Perspect. Lett. 32, 52-57.

Handy, M., Franz, L., Heller, F., Janott, B. and Zurbriggen, R. (1999) Multistage accretion and exhumation of the continental crust (Ivrea crustal section, Italy and Switzerland). Tectonics 18, 1154-1177.

Hanley, J.J. and Koga, K.T. (2018) Halogens in terrestrial and cosmic geochemical systems: abundances, geochemical behaviors, and analytical methods, The role of halogens in terrestrial and extraterrestrial geochemical processes. Springer, pp. 21-121.

Hanley, J.J., Mungall, J.E., Bray, C.J. and Gorton, M.P. (2004) The origin of bulk and water-soluble Cl and Br enrichments in ore-hosting Sudbury Breccia in the Fraser Copper Zone, Strathcona Embayment, Sudbury, Ontario, Canada. Can. Mineral. 42, 1777-1798.

Hanyu, T., Shimizu, K., Ushikubo, T., Kimura, J.-I., Chang, Q., Hamada, M., Ito, M., Iwamori, H. and Ishikawa, T. (2019) Tiny droplets of ocean island basalts unveil Earth's deep chlorine cycle. Nat. Commun. 10, 1-7.

Hao, J., Knoll, A.H., Huang, F., Hazen, R.M. and Daniel, I. (2020) Cycling phosphorus on the Archean Earth: Part I. Continental weathering and riverine transport of phosphorus. Geochim. Cosmochim. Acta 273, 70-84.

Harlov, D.E. and Förster, H.-J. (2002) High-grade fluid metasomatism on both a local and a regional scale: the Seward peninsula, Alaska, and the Val Strona di Omegna, Ivrea–

Verbano Zone, Northern Italy. Part I: petrography and silicate mineral chemistry. J. Petrol. 43, 769-799.

Harlov, D.E. and Wirth, R. (2000) K-feldspar–quartz and K-feldspar–plagioclase phase boundary interactions in garnet–orthopyroxene gneiss's from the Val Strona di Omegna, Ivrea–Verbano Zone, northern Italy. Contrib. Mineral. Petrol. 140, 148-162.

Hawkesworth, C., Cawood, P.A. and Dhuime, B. (2020) The evolution of the continental crust and the onset of plate tectonics. Frontiers in earth science 8.

Hawkesworth, C., Dhuime, B., Pietranik, A., Cawood, P., Kemp, A. and Storey, C. (2010) The generation and evolution of the continental crust. J. Geol. Soc. 167, 229-248.

He, T., Hu, Z., Zhang, W., Chen, H., Liu, Y., Wang, Z. and Hu, S. (2019) Determination of Cl, Br, and I in geological materials by sector field inductively coupled plasma mass spectrometry. Anal. Chem. 91, 8109-8114.

He, T., Liu, L., Chen, Y., Sheng, X. and Ji, J. (2016) Plagioclase sub-species in Chinese loess deposits: Implications for dust source migration and past climate change. Quaternary Research 85, 17-24.

He, T., Xie, J., Hu, Z., Liu, T., Zhang, W., Chen, H., Liu, Y., Zong, K. and Li, M. (2018) A rapid acid digestion technique for the simultaneous determination of bromine and iodine in fifty-three Chinese soils and sediments by ICP-MS. Geostand. Geoanal. Res. 42, 309-318.

Henk, A., Franz, L., Teufel, S. and Oncken, O. (1997) Magmatic underplating, extension, and crustal reequilibration: Insights from a cross-section through the Ivrea Zone and Strona-Ceneri Zone, northern Italy. J. Geol. 105, 367-378.

Higashino, F., Kawakami, T., Satish-Kumar, M., Ishikawa, M., Maki, K., Tsuchiya, N., Grantham, G.H. and Hirata, T. (2013) Chlorine-rich fluid or melt activity during granulite facies metamorphism in the Late Proterozoic to Cambrian continental collision zone—an example from the Sør Rondane Mountains, East Antarctica. Precambrian Res. 234, 229-246.

Hofmann, A.W. (1988) Chemical differentiation of the Earth: the relationship between mantle, continental crust, and oceanic crust. Earth Planet. Sci. Lett. 90, 297-314.

Holland, G. and Ballentine, C.J. (2006) Seawater subduction controls the heavy noble gas composition of the mantle. Nature 441, 186-191.

Holland, G., Cassidy, M. and Ballentine, C.J. (2009) Meteorite Kr in Earth's mantle suggests a late accretionary source for the atmosphere. Science 326, 1522-1525.

Hong, C., Weng, H., Jilani, G., Yan, A., Liu, H. and Xue, Z. (2012) Evaluation of iodide and iodate for adsorption–desorption characteristics and bioavailability in three types of soil. Biol. Trace Elem. Res. 146, 262-271.

Hu, Z.C. and Gao, S. (2008) Upper crustal abundances of trace elements: A revision and update. Chem. Geol. 253, 205-221.

Huang, T.-Y., Teng, F.-Z., Rudnick, R.L., Chen, X.-Y., Hu, Y., Liu, Y.-S. and Wu, F.-Y. (2020) Heterogeneous potassium isotopic composition of the upper continental crust. Geochim. Cosmochim. Acta 278, 122-136.

Huang, Y., Chubakov, V., Mantovani, F., Rudnick, R.L. and Mcdonough, W.F. (2013) A reference Earth model for the heat-producing elements and associated geoneutrino flux. Geochem. Geophys. Geosyst. 14, 2003–2029.

Hughes, L., Cuthbert, S., Quas-Cohen, A., Ruzié-Hamilton, L., Pawley, A., Droop, G., Lyon, I., Tartèse, R. and Burgess, R. (2021) Halogens in Eclogite Facies Minerals from the Western Gneiss Region, Norway. Minerals 11, 760.

Jackson, M.G., Hart, S.R., Koppers, A.A., Staudigel, H., Konter, J., Blusztajn, J., Kurz, M. and Russell, J.A. (2007) The return of subducted continental crust in Samoan lavas. Nature 448, 684-687.

Jahn, B.-m., Gallet, S. and Han, J. (2001) Geochemistry of the Xining, Xifeng and Jixian sections, Loess Plateau of China: eolian dust provenance and paleosol evolution during the last 140 ka. Chem. Geol. 178, 71-94.

Jeong, G.Y., Hillier, S. and Kemp, R.A. (2008) Quantitative bulk and single-particle mineralogy of a thick Chinese loess–paleosol section: implications for loess provenance and weathering. Quaternary Science Reviews 27, 1271-1287.

Jochum, K.P., Nohl, U., Herwig, K., Lammel, E., Stoll, B. and Hofmann, A.W. (2005) GeoReM: a new geochemical database for reference materials and isotopic standards. Geostand. Geoanal. Res. 29, 333-338.

Jochum, K.P., Weis, U., Schwager, B., Stoll, B., Wilson, S.A., Haug, G.H., Andreae, M.O. and Enzweiler, J. (2016) Reference values following ISO guidelines for frequently requested rock reference materials. Geostand. Geoanal. Res. 40, 333-350.

John, T., Layne, G.D., Haase, K.M. and Barnes, J.D. (2010) Chlorine isotope evidence for crustal recycling into the Earth's mantle. Earth Planet. Sci. Lett. 298, 175-182.

John, T., Scambelluri, M., Frische, M., Barnes, J.D. and Bach, W. (2011) Dehydration of subducting serpentinite: implications for halogen mobility in subduction zones and the deep halogen cycle. Earth Planet. Sci. Lett. 308, 65-76.

Johnson, B.W. and Goldblatt, C. (2017) A secular increase in continental crust nitrogen during the Precambrian. Geochem. Perspect. Lett. 4, 24-28.

Johnson, L., Burgess, R., Turner, G., Milledge, H. and Harris, J. (2000) Noble gas and halogen geochemistry of mantle fluids: comparison of African and Canadian diamonds. Geochim. Cosmochim. Acta 64, 717-732.

Johnson, T.E., Kirkland, C.L., Gardiner, N.J., Brown, M., Smithies, R.H. and Santosh, M. (2019) Secular change in TTG compositions: Implications for the evolution of Archaean geodynamics. Earth Planet. Sci. Lett. 505, 65-75.

Jovanovič, M., Gaudenyi, T., O'Hara-Dhand, K. and Smalley, I. (2014) Karl Caesar von Leonhard (1779–1862), and the beginnings of loess research in the Rhine valley. Quaternary International 334, 4-9.

Kabata-Pendias, A. (2000) Trace elements in soils and plants, 3rd ed. CRC press.

Kamber, B.S., Greig, A. and Collerson, K.D. (2005) A new estimate for the composition of weathered young upper continental crust from alluvial sediments, Queensland, Australia. Geochim. Cosmochim. Acta 69, 1041-1058.

Kaplan, D.I., Serne, R.J., Parker, K.E. and Kutnyakov, I.V. (2000) Iodide sorption to subsurface sediments and illitic minerals. Environ. Sci. Technol. 34, 399-405.

Karakas, O., Wotzlaw, J.-F., Guillong, M., Ulmer, P., Brack, P., Economos, R., Bergantz, G.W., Sinigoi, S. and Bachmann, O. (2019) The pace of crustal-scale magma accretion and differentiation beneath silicic caldera volcanoes. Geology 47, 719-723.

Kawakami, T., Higashino, F., Skrzypek, E., Satish-Kumar, M., Grantham, G., Tsuchiya, N., Ishikawa, M., Sakata, S. and Hirata, T. (2017) Prograde infiltration of Cl-rich fluid

into the granulitic continental crust from a collision zone in East Antarctica (Perlebandet, Sør Rondane Mountains). Lithos 274, 73-92.

Kawamoto, T., Mibe, K., Bureau, H., Reguer, S., Mocuta, C., Kubsky, S., Thiaudière, D., Ono, S. and Kogiso, T. (2014) Large-ion lithophile elements delivered by saline fluids to the sub-arc mantle. Earth, Planets and Space 66, 1-11.

Kay, R.W. and Kay, S.M. (1993) Delamination and delamination magmatism. Tectonophysics, 177-189.

Kelemen, P.B., Behn, M.D. and Hacker, B.R. (2025) Average composition and genesis of the lower continental crust.

Keller, C.B. and Schoene, B. (2012) Statistical geochemistry reveals disruption in secular lithospheric evolution about 2.5 Gyr ago. Nature 485, 490-493.

Keller, C.B., Schoene, B., Barboni, M., Samperton, K.M. and Husson, J.M. (2015) Volcanic-plutonic parity and the differentiation of the continental crust. Nature 523, 301-307.

Kendall-Langley, L.A., Kemp, A.I., Hawkesworth, C.J. and Roberts, M.P. (2021) Quantifying F and Cl concentrations in granitic melts from apatite inclusions in zircon. Contrib. Mineral. Petrol. 176, 1-19.

Kendrick, M. (2019a) Halogens in altered ocean crust from the East Pacific Rise (ODP/IODP Hole 1256D). Geochim. Cosmochim. Acta, 93-112.

Kendrick, M., Hémond, C., Kamenetsky, V., Danyushevsky, L., Devey, C.W., Rodemann, T., Jackson, M. and Perfit, M. (2017) Seawater cycled throughout Earth's mantle in partially serpentinized lithosphere. Nat. Geosci. 10, 222-228.

Kendrick, M.A. (2019b) Halogens in Atlantis Bank gabbros, SW Indian Ridge: Implications for styles of seafloor alteration. Earth Planet. Sci. Lett. 514, 96-107.

Kendrick, M.A. (2024) Halogen Cycling in the Solid Earth. Annu. Rev. Earth Planet. Sci. 52, 195–220.

Kendrick, M.A. and Barnes, J.D. (2022) Sediments, serpentinites, and subduction: halogen recycling from the surface to the deep Earth. Elements 18, 21-26.

Kendrick, M.A., D'Andres, J., Holden, P. and Ireland, T. (2018a) Halogens (F, Cl, Br, I) in thirteen USGS, GSJ and NIST international rock and glass reference materials. Geostand. Geoanal. Res. 42, 499-511.

Kendrick, M.A., Danyushevsky, L.V., Falloon, T.J., Woodhead, J.D., Arculus, R.J. and Ireland, T. (2020) SW Pacific arc and backarc lavas and the role of slab-bend serpentinites in the global halogen cycle. Earth Planet. Sci. Lett. 530, 115921.

Kendrick, M.A., Honda, M., Pettke, T., Scambelluri, M., Phillips, D. and Giuliani, A. (2013) Subduction zone fluxes of halogens and noble gases in seafloor and forearc serpentinites. Earth Planet. Sci. Lett. 365, 86-96.

Kendrick, M.A., Jackson, M.G., Kent, A.J., Hauri, E.H., Wallace, P.J. and Woodhead, J. (2014) Contrasting behaviours of CO2, S, H2O and halogens (F, Cl, Br, and I) in enriched-mantle melts from Pitcairn and Society seamounts. Chem. Geol. 370, 69-81.

Kendrick, M.A., Scambelluri, M., Hermann, J. and Padrón-Navarta, J.A. (2018b) Halogens and noble gases in serpentinites and secondary peridotites: Implications for seawater subduction and the origin of mantle neon. Geochim. Cosmochim. Acta 235, 285-304.

Keppler, H. (1996) Constraints from partitioning experiments on the composition of subduction-zone fluids. Nature 380, 237-240.

Keppler, H. (2017) Fluids and trace element transport in subduction zones. Am. Mineral. 102, 5-20.

Keppler, H. and Wyllie, P.J. (1991) Partitioning of Cu, Sn, Mo, W, U, and Th between melt and aqueous fluid in the systems haplogranite-H2O− HCl and haplogranite-H2O− HF. Contrib. Mineral. Petrol. 109, 139-150.

Klaver, M., MacLennan, S.A., Ibañez-Mejia, M., Tissot, F.L., Vroon, P.Z. and Millet, M.-A. (2021) Reliability of detrital marine sediments as proxy for continental crust composition: The effects of hydrodynamic sorting on Ti and Zr isotope systematics. Geochim. Cosmochim. Acta 310, 221-239.

Klötzli, U.S., Sinigoi, S., Quick, J.E., Demarchi, G., Tassinari, C.C., Sato, K. and Günes, Z. (2014) Duration of igneous activity in the Sesia Magmatic System and implications for high-temperature metamorphism in the Ivrea–Verbano deep crust. Lithos 206, 19-33.

Knauth, L.P. (1998) Salinity history of the Earth's early ocean. Nature 395, 554-555.

Korenaga, J. (2011) Thermal evolution with a hydrating mantle and the initiation of plate tectonics in the early Earth. J. Geophys. Res.: Solid Earth 116.

Kronberg, B., Nesbitt, H. and Fyfe, W. (1987) Mobilities of alkalis, alkaline earths and halogens during weathering. Chem. Geol. 60, 41-49.

Kühn, P., Techmer, A. and Weidenfeller, M. (2013) Lower to middle Weichselian pedogenesis and palaeoclimate in Central Europe using combined micromorphology and geochemistry: the loess-paleosol sequence of Alsheim (Mainz Basin, Germany). Quaternary Science Reviews 75, 43-58.

Kunz, B.E., Johnson, T.E., White, R.W. and Redler, C. (2014) Partial melting of metabasic rocks in Val Strona di Omegna, Ivrea Zone, northern Italy. Lithos 190, 1-12.

Kunz, B.E., Regis, D. and Engi, M. (2018) Zircon ages in granulite facies rocks: decoupling from geochemistry above 850° C? Contrib. Mineral. Petrol. 173, 1-21.

Kunz, B.E. and White, R.W. (2019) Phase equilibrium modelling of the amphibolite to granulite facies transition in metabasic rocks (Ivrea Zone, NW Italy). J. Metamorph. Geol. 37, 935-950.

Kutterolf, S., Hansteen, T.H., Appel, K., Freundt, A., Krüger, K., Perez, W. and Wehrmann, H. (2013) Combined bromine and chlorine release from large explosive volcanic eruptions: A threat to stratospheric ozone? Geology 41, 707-710.

Laske, G., Masters, G., Ma, Z. and Pasyanos, M. (2013) Update on CRUST1. 0—A 1-degree global model of Earth's crust, Geophysical research abstracts, p. 2658.

Lechler, P. and Desilets, M. (1987) A review of the use of loss on ignition as a measurement of total volatiles in whole-rock analysis. Chem. Geol. 63, 341-344.

Lecumberri-Sanchez, P. and Bodnar, R.J. (2018) Halogen geochemistry of ore deposits: contributions towards understanding sources and processes, The role of halogens in terrestrial and extraterrestrial geochemical processes, pp. 261-305.

Lee, C.T., Luffi, P., Le Roux, V., Dasgupta, R., Albarede, F. and Leeman, W.P. (2010) The redox state of arc mantle using Zn/Fe systematics. Nature 468, 681-685.

Lehmkuhl, F., Nett, J.J., Pötter, S., Schulte, P., Sprafke, T., Jary, Z., Antoine, P., Wacha, L., Wolf, D. and Zerboni, A. (2021) Loess landscapes of Europe–Mapping, geomorphology, and zonal differentiation. Earth-Sci. Rev. 215, 103496.

Leri, A.C. and Ravel, B. (2015) Abiotic bromination of soil organic matter. Environ. Sci. Technol. 49, 13350-13359.

Li, G., Chen, J. and Chen, Y. (2013) Primary and secondary carbonate in Chinese loess discriminated by trace element composition. Geochim. Cosmochim. Acta 103, 26-35.

Li, S., Gaschnig, R.M. and Rudnick, R.L. (2016) Insights into chemical weathering of the upper continental crust from the geochemistry of ancient glacial diamictites. Geochimica et Cosmochimica Acta 176, 96-117.

Li, S., Junkin, W.D., Gaschnig, R.M., Ash, R.D., Piccoli, P.M., Candela, P.A. and Rudnick, R.L. (2020) Molybdenum contents of sulfides in ancient glacial diamictites: Implications for molybdenum delivery to the oceans prior to the Great Oxidation Event. Geochim. Cosmochim. Acta 278, 30-50.

Li, S., Li, W., Beard, B.L., Raymo, M.E., Wang, X., Chen, Y. and Chen, J. (2019) K isotopes as a tracer for continental weathering and geological K cycling. Proc. Natl. Acad. Sci. 116, 8740-8745.

Li, W., Liu, X.-M., Hu, Y., Teng, F.-Z. and Hu, Y. (2021) Potassium isotopic fractionation during clay adsorption. Geochim. Cosmochim. Acta 304, 160-177.

Li, Y., Song, Y., Yan, L., Chen, T. and An, Z. (2015) Timing and spatial distribution of loess in Xinjiang, NW China. PLoS One 10, e0125492.

Liang, L., Sun, Y., Beets, C.J., Prins, M.A., Wu, F. and Vandenberghe, J. (2013) Impacts of grain size sorting and chemical weathering on the geochemistry of Jingyuan loess in the northwestern Chinese Loess Plateau. J Asian Earth Sci. 69, 177-184.

Liu, X.-M., Gaschnig, R.M., Rudnick, R.L., Hazen, R.M. and Shahar, A. (2022) Constant iron isotope composition of the upper continental crust over the past 3 Ga. Geochem. Perspect. Lett. 22, 16-19.

Liu, X. and Rudnick, R.L. (2011) Constraints on continental crustal mass loss via chemical weathering using lithium and its isotopes. Proc. Natl. Acad. Sci. 108, 20873-20880.

Liu, Y., Wen, Q. and Chen, Q. (1981) F/Cl ratio in Luochuan loess section, Shaanxi province—A geochemical index for paleoclimatic fluctuation Geochimica, 388-391.

Lu, Z., Hensen, C., Fehn, U. and Wallmann, K. (2008) Halogen and ^{129}I systematics in gas hydrate fields at the northern Cascadia margin (IODP Expedition 311): Insights from numerical modeling. Geochem. Geophys. Geosyst. 9, 1-18.

Lu, Z., Hoogakker, B.A., Hillenbrand, C.-D., Zhou, X., Thomas, E., Gutchess, K.M., Lu, W., Jones, L. and Rickaby, R.E. (2016) Oxygen depletion recorded in upper waters of the glacial Southern Ocean. Nat. Commun. 7, 1-9.

Lu, Z., Jenkyns, H.C., Rickaby, R.E. and Rickaby, R.E. (2010) Iodine to calcium ratios in marine carbonate as a paleo-redox proxy during oceanic anoxic events. Geology 38, 1107-1110.

Luvizotto, G. and Zack, T. (2009) Nb and Zr behavior in rutile during high-grade metamorphism and retrogression: an example from the Ivrea–Verbano Zone. Chem. Geol. 261, 303-317.

Ma, J.-L., Wei, G.-J., Xu, Y.-G., Long, W.-G. and Sun, W.-D. (2007) Mobilization and re-distribution of major and trace elements during extreme weathering of basalt in Hainan Island, South China. Geochim. Cosmochim. Acta 71, 3223-3237.

Macdonald, F.A., Swanson-Hysell, N.L., Park, Y., Lisiecki, L. and Jagoutz, O. (2019) Arc-continent collisions in the tropics set Earth's climate state. Science 364, 181-184.

Mangler, M.F., Marks, M.A.W., Zaitzev, A.N., Eby, G.N. and Markl, G. (2014) Halogens (F, Cl and Br) at Oldoinyo Lengai volcano (Tanzania): Effects of magmatic

differentiation, silicate–natrocarbonatite melt separation and surface alteration of natrocarbonatite. Chem. Geol. 365, 43-53.

Manning, D. (1981) The effect of fluorine on liquidus phase relationships in the system Qz-Ab-Or with excess water at 1 kb. Contrib. Mineral. Petrol. 76, 206-215.

Markl, G. and Bucher, K. (1998) Composition of fluids in the lower crust inferred from metamorphic salt in lower crustal rocks. Nature 391, 781-783.

Marks, M.A., Kendrick, M.A., Eby, G.N., Zack, T. and Wenzel, T. (2017) The F, Cl, Br and I Contents of Reference Glasses BHVO-2G, BIR-1G, BCR-2G, GSD-1G, GSE-1G, NIST SRM 610 and NIST SRM 612. Geostand. Geoanal. Res. 41, 107-122.

Marshak, S. (2013) Essentials of Geology (Fourth Edition), United States of America.

Martignier, L., Nussbaumer, M., Adatte, T., Gobat, J.-M. and Verrecchia, E.P. (2015) Assessment of a locally-sourced loess system in Europe: The Swiss Jura Mountains. Aeolian Research 18, 11-21.

Martin, H., Smithies, R.H., Rapp, R., Moyen, J.F. and Champion, D. (2005) An overview of adakite, tonalite–trondhjemite–granodiorite (TTG), and sanukitoid: relationships and some implications for crustal evolution. Lithos 79, 1-24.

Martin, J.B. (1999) Nonconservative behavior of Br−/Cl− ratios during alteration of volcaniclastic sediments. Geochim. Cosmochim. Acta 63, 383-391.

Marty, B., Bekaert, D.V., Broadley, M.W. and Jaupart, C. (2019) Geochemical evidence for high volatile fluxes from the mantle at the end of the Archaean. Nature 575, 485-488.

Mayer, L.M., Schick, L.L., Allison, M.A., Ruttenberg, K.C. and Bentley, S.J. (2007) Marine vs. terrigenous organic matter in Louisiana coastal sediments: The uses of bromine: organic carbon ratios. Mar. Chem. 107, 244-254.

Mazzucchelli, M. and Siena, F. (1986) Geotectonic significance of the metabasites of the kinzigitic series, Ivrea-Verbano zone (Western Italian Alps). Mineralogy and Petrology 35, 99-116.

McDonough, W.F. and Sun, S.s. (1995) The composition of the Earth. Chem. Geol. 120, 223-253.

McDowell, S.D. and Elders, W.A. (1980) Authigenic layer silicate minerals in borehole Elmore 1, Salton Sea geothermal field, California, USA. Contrib. Mineral. Petrol. 74, 293-310.

McLennan, S.M. (1993) Weathering and Global Denudation. J. Geol. 101, 295-303.

McLennan, S.M. (2001) Relationships between the trace element composition of sedimentary rocks and upper continental crust. Geochem. Geophys. Geosyst. 2, 2000GC000109.

Mi, J.-X. and Pan, Y. (2018) Halogen-rich minerals: crystal chemistry and geological significances, The Role of Halogens in Terrestrial and Extraterrestrial Geochemical Processes, pp. 123-184.

Middelburg, J.J., van der Weijden, C.H. and Woittiez, J.R. (1988) Chemical processes affecting the mobility of major, minor and trace elements during weathering of granitic rocks. Chem. Geol. 68, 253-273.

Middlemost, E.A. (1994) Naming materials in the magma/igneous rock system. Earth-Sci. Rev. 37, 215-224.

Mishra, V. and Jeyakumar, S. (2018) Pyrohydrolysis, a clean separation method for separating non-metals directly from solid matrix. Open Access J Sci 2, 389-393.

Mooney, W.D., Laske, G. and Masters, T.G. (1998) CRUST 5.1: A global crustal model at 5× 5. J. Geophys. Res.: Solid Earth 103, 727-747.

Morad, S., Bergan, M., Knarud, R. and Nystuen, J.P. (1990) Albitization of detrital plagioclase in Triassic reservoir sandstones from the Snorre Field, Norwegian North Sea. J. Sediment. Res. 60, 411-425.

Morgan, J.J. (2005) Kinetics of reaction between O2 and Mn(II) species in aqueous solutions. Geochim. Cosmochim. Acta 69, 35-48.

Moyen, J.-F. (2011) The composite Archaean grey gneisses: petrological significance, and evidence for a non-unique tectonic setting for Archaean crustal growth. Lithos 123, 21-36.

Muhs, D.R. and Bettis, A.E. (2003) Quaternary loess-paleosol sequences as examples of climate-driven sedimentary extremes. 53–74.

Muhs, D.R., Bettis III, E.A., Aleinikoff, J.N., McGeehin, J.P., Beann, J., Skipp, G., Marshall, B.D., Roberts, H.M., Johnson, W.C. and Benton, R. (2008) Origin and paleoclimatic significance of late Quaternary loess in Nebraska: evidence from stratigraphy, chronology, sedimentology, and geochemistry. Geol. Soc. Am. Bull. 120, 1378-1407.

Muhs, D.R., Bettis III, E.A., Roberts, H.M., Harlan, S.S., Paces, J.B. and Reynolds, R.L. (2013) Chronology and provenance of last-glacial (Peoria) loess in western Iowa and paleoclimatic implications. Quaternary Research 80, 468-481.

Muhs, D.R., Bettis III, E.A. and Skipp, G.L. (2018) Geochemistry and mineralogy of late Quaternary loess in the upper Mississippi River valley, USA: Provenance and correlation with Laurentide Ice Sheet history. Quaternary Science Reviews 187, 235-269.

Mundl, A., Walker, R., Reimink, J., Rudnick, R. and Gaschnig, R. (2018) Tungsten-182 in the upper continental crust: evidence from glacial diamictites. Chem. Geol. 494, 144-152.

Muramatsu, Y., Doi, T., Tomaru, H., Fehn, U., Takeuchi, R. and Matsumoto, R. (2007) Halogen concentrations in pore waters and sediments of the Nankai Trough, Japan: Implications for the origin of gas hydrates. Appl. Geochem. 22, 534-556.

Muramatsu, Y., Fehn, U. and Yoshida, S. (2001) Recycling of iodine in fore-arc areas: evidence from the iodine brines in Chiba, Japan. Earth Planet. Sci. Lett. 192, 583-593.

Muramatsu, Y. and Wedepohl, K.H. (1998) The distribution of iodine in the earth's crust. Chem. Geol. 147, 201-216.

Murphy, M.E., Savage, P.S., Gardiner, N.J., Prave, A.R., Gaschnig, R.M. and Rudnick, R.L. (2022) Homogenising the upper continental crust: the Si isotope evolution of the crust recorded by ancient glacial diamictites. Earth Planet. Sci. Lett. 591, 117620.

Nan, X.-Y., Yu, H.-M., Rudnick, R.L., Gaschnig, R.M., Xu, J., Li, W.-Y., Zhang, Q., Jin, Z.-D., Li, X.-H. and Huang, F. (2018) Barium isotopic composition of the upper continental crust. Geochim. Cosmochim. Acta 233, 33-49.

Nance, W.B. and Taylor, S. (1976) Rare earth element patterns and crustal evolution—I. Australian post-Archean sedimentary rocks. Geochim. Cosmochim. Acta 40, 1539-1551.

Neidhardt, H., Lemke, E., Epp, T., Marks, M.A., Markl, G. and Oelmann, Y. (2022) Impact of abiotic and biogeochemical processes on halogen concentrations (Cl, Br, F, I) in mineral soil along a climatic gradient. Environ. Sci.: Process. Impacts 24, 1330-1342.

Nesbitt, H. and Wilson, R. (1992) Recent chemical weathering of basalts. Am. J. Sci. 292, 740-777.

Nesbitt, H. and Young, G. (1982) Early Proterozoic climates and plate motions inferred from major element chemistry of lutites. Nature 299, 715-717.

Nesbitt, H., Young, G., McLennan, S. and Keays, R. (1996) Effects of chemical weathering and sorting on the petrogenesis of siliciclastic sediments, with implications for provenance studies. J. Geol. 104, 525-542.

Nesbitt, H. and Young, G.M. (1989) Formation and diagenesis of weathering profiles. J. Geol. 97, 129-147.

Nesbitt, H.W. (1979) Mobility and fractionation of rare earth elements during weathering of a granodiorite. Nature 279, 206-210.

Nesbitt, H.W., Markovics, G. and Price, R.C. (1980) Chemical processes affecting alkalis and alkaline earths during continental weathering. Geochim. Cosmochim. Acta 44, 1659-1666.

Nesbitt, H.W. and Young, G.M. (1984) Prediction of some weathering trends of plutonic and volcanic rocks based on thermodynamic and kinetic considerations. Geochim. Cosmochim. Acta 48, 1523-1534.

Newton, R. and Manning, C. (2010) Role of saline fluids in deep-crustal and upper-mantle metasomatism: insights from experimental studies. Geofluids 10, 58-72.

Newton, R.C., Aranovich, L.Y. and Touret, J.L. (2019) Streaming of saline fluids through Archean crust: Another view of charnockite-granite relations in southern India. Lithos 346, 105157.

Okita, P.M. (1992) Manganese carbonate mineralization in the Molango District, Mexico. Econ. Geol. 87, 1345-1366.

Pagé, L. and Hattori, K. (2017) Tracing halogen and B cycling in subduction zones based on obducted, subducted and forearc serpentinites of the Dominican Republic. Sci. Repor. 7, 1-9.

Pagé, L., Hattori, K., de Hoog, J.C. and Okay, A.I. (2016) Halogen (F, Cl, Br, I) behaviour in subducting slabs: A study of lawsonite blueschists in western Turkey. Earth Planet. Sci. Lett. 442, 133-142.

Pagé, L., Hattori, K. and Guillot, S. (2018) Mantle wedge serpentinites: A transient reservoir of halogens, boron, and nitrogen for the deeper mantle. Geology 46, 883-886.

Parai, R. and Mukhopadhyay, S. (2018) Xenon isotopic constraints on the history of volatile recycling into the mantle. Nature 560, 223-227.

Park, J.-W., Hu, Z., Gao, S., Campbell, I.H. and Gong, H. (2012) Platinum group element abundances in the upper continental crust revisited–New constraints from analyses of Chinese loess. Geochim. Cosmochim. Acta 93, 63-76.

Pease, G., Gelb, A., Lee, Y. and Keller, B. (2023) A Bayesian Formulation for Estimating the Composition of Earth's Crust. J. Geophys. Res.: Solid Earth 128, e2023JB026353.

Pedersen, T. and Price, N. (1982) The geochemistry of manganese carbonate in Panama Basin sediments. Geochim. Cosmochim. Acta 46, 59-68.

Peressini, G., Quick, J., Sinigoi, S., Hofmann, A.W. and Fanning, M. (2007) Duration of a large mafic intrusion and heat transfer in the lower crust: a SHRIMP U–Pb zircon study in the Ivrea–Verbano Zone (Western Alps, Italy). J. Petrol. 48, 1185-1218.

Pirajno, F. (2018) Halogens in hydrothermal fluids and their role in the formation and evolution of hydrothermal mineral systems, The Role of Halogens in Terrestrial and Extraterrestrial Geochemical Processes, pp. 759-804.

Plank, T. (2014) The Chemical Composition of Subducting Sediments. Treatise on Geochemistry 4, 607-629.

Plank, T., Kelley, K.A., Zimmer, M.M., Hauri, E.H. and Wallace, P.J. (2013) Why do mafic arc magmas contain ~ 4 wt% water on average? Earth Planet. Sci. Lett. 364, 168-179.

Plank, T. and Langmuir, C.H. (1993) Tracing trace elements from sediment input to volcanic output at subduction zones. Nature 362, 739-743.

Plank, T. and Langmuir, C.H. (1998) The chemical composition of subducting sediment and its consequences for the crust and mantle. Chem. Geol. 145, 325-394.

Portnyagin, M., Hoernle, K., Plechov, P., Mironov, N. and Khubunaya, S. (2007) Constraints on mantle melting and composition and nature of slab components in volcanic arcs from volatiles (H2O, S, Cl, F) and trace elements in melt inclusions from the Kamchatka Arc. Earth Planet. Sci. Lett. 255, 53-69.

Post, J.E. (1999) Manganese oxide minerals: Crystal structures and economic and environmental significance. Proc. Natl. Acad. Sci. 96, 3447-3454.

Price, N. and Calvert, S. (1977) The contrasting geochemical behaviours of iodine and bromine in recent sediments from the Namibian shelf. Geochim. Cosmochim. Acta 41, 1769-1775.

Pye, K. (1995) The nature, origin and accumulation of loess. Quaternary Science Reviews 14, 653-667.

Pyle, D. and Mather, T. (2009) Halogens in igneous processes and their fluxes to the atmosphere and oceans from volcanic activity: a review. Chem. Geol. 263, 110-121.

Qin, L. and Humayun, M. (2008) The Fe/Mn ratio in MORB and OIB determined by ICP-MS. Geochim. Cosmochim. Acta 72, 1660-1677.

Qiu, L., Rudnick, R.L., McDonough, W.F. and Bea, F. (2011) The behavior of lithium in amphibolite-to granulite-facies rocks of the Ivrea–Verbano Zone, NW Italy. Chem. Geol. 289, 76-85.

Qiu, L., Rudnick, R.L., McDonough, W.F. and Merriman, R.J. (2009) Li and δ7Li in mudrocks from the British Caledonides: Metamorphism and source influences. Geochim. Cosmochim. Acta 73, 7325-7340.

Rainbird, R., Nesbitt, H. and Donaldson, J. (1990) Formation and diagenesis of a sub-Huronian saprolith: comparison with a modern weathering profile. J. Geol. 98, 801-822.

Ramos, A., Ohde, S., Hossain, M., Ozaki, H., Sirirattanachai, S. and Apurado, J. (2005) Determination of fluorine in coral skeletons by instrumental neutron activation analysis. J. Radioanal. Nucl. Chem. 266, 19-29.

Ramseyer, K., Boles, J.R. and Lichtner, P.C. (1992) Mechanism of plagioclase albitization. J. Sediment. Res. 62, 349-356.

Redler, C., Johnson, T., White, R. and Kunz, B. (2012) Phase equilibrium constraints on a deep crustal metamorphic field gradient: metapelitic rocks from the Ivrea Zone (NW Italy). J. Metamorph. Geol. 30, 235-254.

Redler, C., White, R.W. and Johnson, T.E. (2013) Migmatites in the Ivrea Zone (NW Italy): Constraints on partial melting and melt loss in metasedimentary rocks from Val Strona di Omegna. Lithos 175, 40-53.

Reinhard, C.T., Planavsky, N.J., Gill, B.C., Ozaki, K., Robbins, L.J., Lyons, T.W., Fischer, W.W., Wang, C., Cole, D.B. and Konhauser, K.O. (2017) Evolution of the global phosphorus cycle. Nature 541, 386-389.

Rietveld, H.M. (1969) A profile refinement method for nuclear and magnetic structures. J. Appl. Crystallogr. 2, 65-71.

Rodbell, D.T., Forman, S.L., Pierson, J. and Lynn, W.C. (1997) Stratigraphy and chronology of Mississippi Valley loess in western Tennessee. Geol. Soc. Am. Bull. 109, 1134-1148.

Ronov, A., Yaroshevskiy, A. and Migdisov, A. (1991) Chemical constitution of the Earth's crust and geochemical balance of the major elements. International Geology Review 33, 941-1048.

Ronov, A.B. and Migdisov, A. (1970) Evolution of the chemical composition of the rocks of the shields and of the sedimentary cover of the Russian and North American platforms. Geokhimiya 4, 403-438.

Ronov, A.B. and Yaroshevsky, A.A. (1976) A new model for the chemical structure of the Earth's crust. Geokkimiya 12, 1761-1795.

Roulier, M., Coppin, F., Bueno, M., Nicolas, M., Thiry, Y., Della Vedova, C., Fevrier, L., Pannier, F. and Le Hécho, I. (2019) Iodine budget in forest soils: influence of environmental conditions and soil physicochemical properties. Chemosphere 224, 20-28.

Rousseau, D.D., Chauvel, C., Sima, A., Hatté, C., Lagroix, F., Antoine, P., Balkanski, Y., Fuchs, M., Mellett, C. and Kageyama, M. (2014) European glacial dust deposits: Geochemical constraints on atmospheric dust cycle modeling. Geophys. Res. Lett. 41, 7666-7674.

Rubey, W.W. (1951) Geologic history of sea water: an attempt to state the problem. Geol. Soc. Am. Bull. 62, 1111-1148.

Rude, P.D. and Aller, R.C. (1991) Fluorine mobility during early diagenesis of carbonate sediment: An indicator of mineral transformations. Geochim. Cosmochim. Acta 55, 2491-2509.

Rudnick, R.L. (1995) Making Continental Crust. Nature 378, 571-578.

Rudnick, R.L. and Fountain, D.M. (1995) Nature and composition of the continental crust: A lower crustal perspective. Rev. Geophys. 33, 267-309.

Rudnick, R.L. and Gao, S. (2003) Composition of the Continental Crust, Treatise on Geochemistry, pp. 1-64.

Ruttenberg, K.C. (2003) The Global Phosphorus Cycle. Treatise on Geochemistry 8.13, 585-643.

Saigal, G.C., Morad, S., Bjorlykke, K., Egeberg, P.K. and Aagaard, P. (1988) Diagenetic albitization of detrital K-feldspar in Jurassic, Lower Cretaceous, and Tertiary clastic reservoir rocks from offshore Norway; I, Textures and origin. J. Sediment. Res. 58, 1003-1013.

Sallet, R., Vital, H., Price, J.D. and Moritz, R. (2019) The geochemical behavior of F and Cl during the weathering–diagenesis–metamorphism–anatexis cycle. Insights from the

clay fraction of fine sands from the Amazon River mouth and metapelititic rocks from the Seridó Belt, Brazil. Chem. Geol. 525, 260-267.

Sammon, L.G. and McDonough, W.F. (2021) A geochemical review of amphibolite, granulite, and eclogite facies lithologies: Perspectives on the deep continental crust. J. Geophys. Res.: Solid Earth 126, e2021JB022791.

Samuel, V.O., Santosh, M., Jang, Y. and Kwon, S. (2021) Acidic fluids in the Earth's lower crust. Sci. Repor. 11, 1-8.

Sauzéat, L., Rudnick, R.L., Chauvel, C., Garçon, M. and Tang, M. (2015) New perspectives on the Li isotopic composition of the upper continental crust and its weathering signature. Earth Planet. Sci. Lett. 428, 181-192.

Savage, P.S., Georg, R.B., Williams, H.M. and Halliday, A.N. (2013) The silicon isotope composition of the upper continental crust. Geochim. Cosmochim. Acta 109, 384-399.

Savage, P.S., Georg, R.B., Williams, H.M., Turner, S., Halliday, A.N. and Chappell, B.W. (2012) The silicon isotope composition of granites. Geochim. Cosmochim. Acta 92, 184-202.

Sawyer, E.W., Cesare, B. and Brown, M. (2011) When the continental crust melts. Elements 7, 229-234.

Sayago, J.M. (1995) The Argentine neotropical loess: an overview. Quaternary Science Reviews 14, 755-766.

Schellenberger, A. and Veit, H. (2006) Pedostratigraphy and pedological and geochemical characterization of Las Carreras loess–paleosol sequence, Valle de Tafí, NW-Argentina. Quaternary Science Reviews 25, 811-831.

Schilling, J.-G., Unni, C. and Bender, M. (1978) Origin of chlorine and bromine in the oceans. Nature 273, 631-636.

Schnetger, B. (1994) Partial melting during the evolution of the amphibolite-to granulite-facies gneisses of the Ivrea Zone, northern Italy. Chem. Geol. 113, 71-101.

Schrank, A. and De Ros, L. (2015) Diagenetic processes in cretaceous sandstones from occidental Brazilian Equatorial Margin. J. S. Am. Earth Sci. 63, 1-19.

Schulze, T., Schwahn, L., Fülling, A., Zeeden, C., Preusser, F. and Sprafke, T. (2022) Investigating the loess–palaeosol sequence of Bahlingen-Schönenberg (Kaiserstuhl), southwestern Germany, using a multi-methodological approach. E&G Quaternary Science Journal 71, 145-162.

Segee-Wright, G., Barnes, J.D., Lassiter, J.C., Holmes, D.J., Beaudoin, G.M., Chatterjee, R., Stockli, D.F., Hoffmann, J.E. and John, T. (2023) Halogen enrichment in the North American lithospheric mantle from the dehydration of the Farallon plate. Geochim. Cosmochim. Acta 348, 187-205.

Segonzac, G.D. (1970) The transformation of clay minerals during diagenesis and low-grade metamorphism: a review. Sedimentology 15, 281-346.

Selverstone, J. and Sharp, Z.D. (2015) Chlorine isotope behavior during prograde metamorphism of sedimentary rocks. Earth Planet. Sci. Lett. 417, 120-131.

Sharp, Z. and Draper, D. (2013) The chlorine abundance of Earth: implications for a habitable planet. Earth Planet. Sci. Lett. 369, 71-77.

Shaw, D., Reilly, G., Muysson, J., Pattenden, G. and Campbell, F. (1967) An Estimate of the Composition of the Canadian Precambrian shield. Can. J. Earth Sci. 4, 829-853.

Shaw, D.B. and Weaver, C.E. (1965) The mineralogical composition of shales. J. Sediment. Res. 35, 213-222.

Shaw, D.M., Dostal, J. and Keays, R.R. (1976) Additional estimates of continental surface Precambrian shield composition in Canada. Geochim. Cosmochim. Acta 40, 73-83.

Shimizu, K., Suzuki, K., Saitoh, M., Konno, U., Kawagucci, S. and Ueno, Y. (2015) Simultaneous determinations of fluorine, chlorine, and sulfur in rock samples by ion chromatography combined with pyrohydrolysis. Geochem. J. 49, 113-124.

Short, M.A., de Caritat, P. and McPhail, D.C. (2017) Continental-scale variation in chloride/bromide ratios of wet deposition. Sci. Total Environ. 574, 1533-1543.

Sills, J.D. and Tarney, J. (1984) Petrogenesis and tectonic significance of amphibolites interlayered with metasedimentary gneisses in the Ivrea Zone, Southern Alps, Northwest Italy. Tectonophysics 107, 187-206.

Simpson, W.R., Glasow, R.v., Riedel, K., Anderson, P., Ariya, P., Bottenheim, J., Burrows, J., Carpenter, L., Frieß, U. and Goodsite, M.E. (2007) Halogens and their role in polar boundary-layer ozone depletion. Atmos. Chem. Phys. 7, 4375-4418.

Smalley, I. (1995) Making the material: The formation of silt sized primary mineral particles for loess deposits. Quaternary Science Reviews 14, 645-651.

Smit, M.A. and Mezger, K. (2017) Earth's early O2 cycle suppressed by primitive continents. Nat. Geosci. 10, 788-792.

Sobolev, A.V., Asafov, E.V., Gurenko, A.A., Arndt, N.T., Batanova, V.G., Portnyagin, M.V., Garbe-Schönberg, D., Wilson, A.H. and Byerly, G.R. (2019) Deep hydrous mantle reservoir provides evidence for crustal recycling before 3.3 billion years ago. Nature 571, 555-559.

Spear, F.S. and Pyle, J.M. (2002) Apatite, monatite, and xenotime in metamorphic rocks. Rev. Mineral. Geochem. 48, 293-336.

Stepanov, A.S. (2021) A review of the geochemical changes occurring during metamorphic devolatilization of metasedimentary rocks. Chem. Geol., 120080.

Straub, S.M. and Layne, G.D. (2003) The systematics of chlorine, fluorine, and water in Izu arc front volcanic rocks: implications for volatile recycling in subduction zones. Geochim. Cosmochim. Acta 67, 4179-4203.

Sun, D., Liu, D., Chen, M., An, Z. and John, S. (1997) Magnetostratigraphy and palaeoclimate of red clay sequences from Chinese Loess Plateau. Science in China Series D: Earth Sciences 40, 337-343.

Sun, D., Shaw, J., An, Z., Cheng, M. and Yue, L. (1998) Magnetostratigraphy and paleoclimatic interpretation of a continuous 7.2 Ma Late Cenozoic eolian sediments from the Chinese Loess Plateau. Geophys. Res. Lett. 25, 85-88.

Sun, J. (2002) Provenance of loess material and formation of loess deposits on the Chinese Loess Plateau. Earth Planet. Sci. Lett. 203, 845-859.

Sun, J., Ding, Z., Xiao, W. and Windley, B.F. (2022) Coupling between uplift of the Central Asian Orogenic Belt-NE Tibetan Plateau and accumulation of aeolian Red Clay in the inner Asia began at~ 7 Ma. Earth-Sci. Rev. 226, 103919.

Sun, Y., Lu, H. and An, Z. (2006) Grain size of loess, palaeosol and Red Clay deposits on the Chinese Loess Plateau: Significance for understanding pedogenic alteration and palaeomonsoon evolution. Palaeogeogr. Palaeoclimatol. Palaeoecol. 241, 129-138.

Svensen, H., Jamtveit, B., Banks, D.A. and Austrheim, H. (2001) Halogen contents of eclogite facies fluid inclusions and minerals: Caledonides, western Norway. J. Metamorph. Geol. 19, 165-178.

Taboada, T., Cortizas, A.M., García, C. and García-Rodeja, E. (2006) Particle-size fractionation of titanium and zirconium during weathering and pedogenesis of granitic rocks in NW Spain. Geoderma 131, 218-236.

Takeda, A., Nakao, A., Yamasaki, S.-i. and Tsuchiya, N. (2018) Distribution and speciation of bromine and iodine in volcanic ash soil profiles. Soil Sci. Soc. Am. J. 82, 815-825.

Tang, H., Trail, D., Bell, E. and Harrison, T. (2019) Zircon halogen geochemistry: Insights into Hadean-Archean fluids. Geochem. Perspect. Lett. 9, 49-53.

Tang, M., Chen, K. and Rudnick, R.L. (2016) Archean upper crust transition from mafic to felsic marks the onset of plate tectonics. Science 351, 372-375.

Taylor, S.R. and McLennan, S.M. (1985) The continental crust: its composition and evolution.

Taylor, S.R., Mclennan, S.M. and McCulloch, M.T. (1983) Geochemistry of loess, continental crustal composition and crustal model ages. Geochim. Cosmochim. Acta 47, 1897-1905.

Taylor, S.R., Rudnick, R.L., McLennan, S.M. and Eriksson, K.A. (1986) Rare earth element patterns in Archean high-grade metasediments and their tectonic significance. Geochim. Cosmochim. Acta 50, 2267-2279.

Teiber, H., Marks, M.A., Wenzel, T., Siebel, W., Altherr, R. and Markl, G. (2014) The distribution of halogens (F, Cl, Br) in granitoid rocks. Chem. Geol. 374, 92-109.

Teng, F.-Z., Hu, Y., Ma, J.-L., Wei, G.-J. and Rudnick, R.L. (2020) Potassium isotope fractionation during continental weathering and implications for global K isotopic balance. Geochim. Cosmochim. Acta 278, 261-271.

Teng, F.Z., McDonough, W.F., Rudnick, R.L., Dalpé, C., Tomascak, P.B., Chappell, B.W. and Gao, S. (2004) Lithium isotopic composition and concentration of the upper continental crust. Geochim. Cosmochim. Acta 68, 4167-4178.

Thomas, R., Förster, H.-J., Rickers, K. and Webster, J.D. (2005) Formation of extremely F-rich hydrous melt fractions and hydrothermal fluids during differentiation of highly evolved tin-granite magmas: a melt/fluid-inclusion study. Contrib. Mineral. Petrol. 148, 582-601.

Togashi, S., Imai, N., Okuyama-Kusunose, Y., Tanaka, T., Okai, T., Koma, T. and Murata, Y. (2000) Young upper crustal chemical composition of the orogenic Japan Arc. Geochem. Geophys. Geosyst. 1.

Tomaru, H., Fehn, U., Lu, Z., Takeuchi, R., Inagaki, F., Imachi, H., Kotani, R., Matsumoto, R. and Aoike, K. (2009) Dating of dissolved iodine in pore waters from the gas hydrate occurrence offshore Shimokita Peninsula, Japan: 129I results from the D/V Chikyu shakedown cruise. Resource Geology 59, 359-373.

Tomaru, H., Lu, Z., Snyder, G.T., Fehn, U., Hiruta, A. and Matsumoto, R. (2007) Origin and age of pore waters in an actively venting gas hydrate field near Sado Island, Japan Sea: Interpretation of halogen and 129I distributions. Chem. Geol. 236, 350-366.

Touret, J.L. (1985) Fluid regime in southern Norway: the record of fluid inclusions. The deep proterozoic crust in the north Atlantic provinces, 517-549.

Touret, J.L. and Huizenga, J.M. (1999) Precambrian intraplate magmatism: high temperature, low pressure crustal granulites. Journal of African Earth Sciences 28, 367-382.

Touret, J.L., Santosh, M. and Huizenga, J.M. (2022) Composition and evolution of the continental crust: Retrospect and prospect. Geoscience Frontiers, 101428.

Toyama, C., Sumino, H., Okabe, N., Ishikawa, A., Yamamoto, J., Kaneoka, I. and Muramatsu, Y. (2021) Halogen heterogeneity in the subcontinental lithospheric mantle revealed by I/Br ratios in kimberlites and their mantle xenoliths from South Africa, Greenland, China, Siberia, Canada, and Brazil. Am. Mineral. 106, 1890-1899.

Tropper, P., Manning, C.E. and Harlov, D.E. (2011) Solubility of CePO4 monazite and YPO4 xenotime in H2O and H2O–NaCl at 800 C and 1 GPa: Implications for REE and Y transport during high-grade metamorphism. Chem. Geol. 282, 58-66.

Uto, K. (1986) Variation of Al2O3 content in late cenozoic Japanese basalts: A re-examination of Kuno's high-alumina basalt. Journal of Volcanology and Geothermal Research 29, 397-411.

Van den Berg, R. and Huizenga, J. (2001) Fluids in granulites of the Southern Marginal Zone of the Limpopo belt, South Africa. Contrib. Mineral. Petrol. 141, 529-545.

Vázquez, M., Ramírez, S., Morata, D., Reich, M., Braun, J.-J. and Carretier, S. (2016) Regolith production and chemical weathering of granitic rocks in central Chile. Chem. Geol. 446, 87-98.

Wang, H., Follmer, L.R. and Liu, J.C.-l. (2000) Isotope evidence of paleo–El Niño–Southern Oscillation cycles in loess-paleosol record in the central United States. Geology 28, 771-774.

Wang, L.-X., Ma, C.-Q., Zhang, C., Zhu, Y.-X. and Marks, M.A. (2018) Halogen geochemistry of I-and A-type granites from Jiuhuashan region (South China): Insights into the elevated fluorine in A-type granite. Chem. Geol. 478, 164-182.

Wang, L., Hu, W., Wang, X., Cao, J. and Yao, S. (2020) Halogens (Cl, Br, and I) geochemistry in Middle Triassic carbonates: Implications for salinity and diagenetic alteration of I/(Ca+ Mg) ratios. Chem. Geol. 533, 119444.

Wang, S.-J., Rudnick, R.L., Gaschnig, R.M., Wang, H. and Wasylenki, L.E. (2019) Methanogenesis sustained by sulfide weathering during the Great Oxidation Event. Nat. Geosci. 12, 296-300.

Wang, S., Teng, F. and Bea, F. (2015) Magnesium isotopic systematics of metapelite in the deep crust and implications for granite petrogenesis. Geochem. Perspect. Lett. 1, 75-83.

Webb, P.C., Thompson, M., Potts, P.J., Gowing, C.J. and Wilson, S.A. (2016) GeoPT39–An international proficiency test for analytical geochemistry laboratories–Report on round 39 (Syenite, SyMP-1)/July 2016. International Association of Geoanalysts.

Webb, P.C., Thompson, M., Potts, P.J. and Wilson, S. (2011) GeoPT29–an international proficiency test for analytical geochemistry laboratories–report on round 29 (Nephelinite, NKT-1), Int. Assoc. Geoanal. 2011. International Association of Geoanalysts.

Webster, J., Thomas, R., Förster, H.-J., Seltmann, R. and Tappen, C. (2004) Geochemical evolution of halogen-enriched granite magmas and mineralizing fluids of the Zinnwald tin-tungsten mining district, Erzgebirge, Germany. Miner. Depos. 39, 452-472.

Webster, J.D., Tappen, C.M. and Mandeville, C.W. (2009) Partitioning behavior of chlorine and fluorine in the system apatite–melt–fluid. II: Felsic silicate systems at 200 MPa. Geochim. Cosmochim. Acta 73, 559-581.

Wedepohl, K.H. (1995) The composition of the continental crust. Geochim. Cosmochim. Acta 59, 1217-1232.

Weinberg, R.F. and Hasalová, P. (2015) Water-fluxed melting of the continental crust: A review. Lithos 212, 158-188.

Whalen, J.B., Currie, K.L. and Chappell, B.W. (1987) A-type granites: geochemical characteristics, discrimination and petrogenesis. Contrib. Mineral. Petrol. 95, 407-419.

White, W.M. (2018) Encyclopedia of Geochemistry: a comprehensive reference source on the chemistry of the Earth.

Whitehead, D. (1984) The distribution and transformations of iodine in the environment. Environ. Int. 10, 321-339.

Whitney, D.L. and Evans, B.W. (2009) Abbreviations for names of rock-forming minerals. Am. Mineral. 95, 185-187.

Wilde, S.A., Valley, J.W., Peck, W.H. and Graham, C.M. (2001) Evidence from detrital zircons for the existence of continental crust and oceans on the Earth 4.4 Gyr ago. Nature 409, 175-178.

Willbold, M. and Stracke, A. (2006) Trace element composition of mantle end-members: Implications for recycling of oceanic and upper and lower continental crust. Geochem. Geophys. Geosyst. 7.

Wintsch, R.P. and Kvale, C.M. (1994) Differential mobility of elements in burial diagenesis of siliciclastic rocks. J. Sediment. Res. 64, 349-361.

Worden, R.H. (2018) Halogen Elements in Sedimentary Systems and Their Evolution During Diagenesis, The Role of Halogens in Terrestrial and Extraterrestrial Geochemical Processes: Surface, Crust, and Mantle, pp. 185-260.

Wyatt, D.C., Smye, A.J., Garber, J.M. and Hacker, B.R. (2022) Assembly and Tectonic Evolution of Continental Lower Crust: Monazite Petrochronology of the Ivrea-Verbano Zone (Val Strona di Omegna). Tectonics 41, e2021TC006841.

Xiao, G., Dai, G., Tian, S., Peng, S., Li, L., Meng, X. and Yin, Q. (2023) Periodic variations of alpine glaciation and desertification of the NE Tibetan Plateau: Evidence from the loess-paleosol sequences in the Menyuan Basin. Global and Planetary Change 226, 104160.

Xiao, Y., Wu, S., Sui, P., Niu, Y., Sun, W., Wang, G., Kong, J., Shao, F., Wang, X. and Gong, H. (2022) Chemical variations of loess from the Chinese Loess Plateau and its implications. International Geology Review, 1-16.

Yamasaki, S.-i., Takeda, A., Watanabe, T., Tagami, K., Uchida, S., Takata, H., Maejima, Y., Kihou, N. and Tsuchiya, N. (2015) Bromine and iodine in Japanese soils determined with polarizing energy dispersive X-ray fluorescence spectrometry. J. Soil Sci. Plant Nutr. 61, 751-760.

Yang, S., Ding, F. and Ding, Z. (2006) Pleistocene chemical weathering history of Asian arid and semi-arid regions recorded in loess deposits of China and Tajikistan. Geochim. Cosmochim. Acta 70, 1695-1709.

Yaroshevsky, A. (2006) Abundances of chemical elements in the Earth's crust. Geochemistry International 44, 48-55.

Yu, Y., Wang, H. and Liu, X. (2012) Geochemical Characteristics of Loess Deposition since Last Interglacial at Desert Margin and Its Provenance and Climatic Implications. Acta Sedimentologica Sinica 30, 356-365.

Yuita, K. (1983) Iodine, bromine and chlorine contents in soils and plants of Japan: III. Iodine, bromine and chlorine contents in the andosols and in plants of central Honshu. J. Soil Sci. Plant Nutr. 29, 403-428.

Zen, E.-a. (1986) Aluminum Enrichment in Silicate Melts by Fractional Crystallization: Some Mineralogic and Petrographic Constraints. J. Petrol. 27, 1095-1117.

Zhang, C., Holtz, F., Ma, C., Wolff, P.E. and Li, X. (2012) Tracing the evolution and distribution of F and Cl in plutonic systems from volatile-bearing minerals: a case study from the Liujiawa pluton (Dabie orogen, China). Contrib. Mineral. Petrol. 164, 859-879.

Zhang, H., Lu, H., He, J., Xie, W., Wang, H., Zhang, H., Breecker, D., Bird, A., Stevens, T. and Nie, J. (2022) Large-number detrital zircon U-Pb ages reveal global cooling caused the formation of the Chinese Loess Plateau during Late Miocene. Science advances 8, eabq2007.

Zhao, H., Lu, Y., Wang, C., Chen, J., Liu, J. and Mao, H. (2010) ReOSL dating of aeolian and fluvial sediments from Nihewan Basin, northern China and its environmental application. Quaternary Geochronology 5, 159-163.

Zingg, A., Handy, M., Hunziker, J. and Schmid, S. (1990) Tectonometamorphic history of the Ivrea Zone and its relationship to the crustal evolution of the Southern Alps. Tectonophysics 182, 169-192.

Appendix A

Average Major Element Composition of The Upper Continental Crust Derived from An Integrated Study of Sedimentary and Igneous Rocks

– Supplementary Information

Table S1. Major and trace element concentrations of the compiled sedimentary rocks (336 loess, 116 glacial diamictite, and 756 shale samples).

**Data will be available after publication and upon request.*

Table S2. Rock reference material analysis from this study*

	BCR-2 (*n* = 4), basalt			GSR-3 (*n* = 4), basalt			BHVO-2 (n = 5), Basalt			AGV-2 (n = 5), Andesite			SCo-1 (n = 2), Shale		
	Mean	RSD%	Ref.[%]	Mean	RSD%	Ref.[%]	Mean	RSD%	Ref.[%]	Mean	RSD%	Ref.[%]	Mean	RSD%	Ref.[%]
Major element (wt.%)															
SiO2	54.0	0.2	54.1	44.7	0.1	44.6	-	-	-	-	-	-	-	-	-
TiO2	2.24	1.0	2.26	2.37	0.5	2.37	-	-	-	-	-	-	-	-	-
Al2O3	13.4	0.2	13.5	13.8	0.2	13.8	-	-	-	-	-	-	-	-	-
TFe2O3	13.8	0.2	13.8	13.4	0.4	13.4	-	-	-	-	-	-	-	-	-
MnO	0.188	2.7	0.19	0.162	3.9	0.17	-	-	-	-	-	-	-	-	-
MgO	3.69	1.5	3.59	7.75	0.4	7.77	-	-	-	-	-	-	-	-	-
CaO	7.13	0.2	7.12	8.84	0.2	8.81	-	-	-	-	-	-	-	-	-
Na2O	3.22	1.3	3.16	3.40	0.9	3.38	-	-	-	-	-	-	-	-	-
K2O	1.81	0.6	1.79	2.32	0.3	2.32	-	-	-	-	-	-	-	-	-
P2O5	0.348	1.4	0.35	0.943	0.5	0.95	-	-	-	-	-	-	-	-	-
Trace element (ppm)															
Li	8.48	0.8	9	-	-	-	4.36	5.4	4.8	10.25	3.9	11	46.7	0.7	45
Be	1.94	4.1	-	-	-	-	0.98	6.7	1	2.09	4.8	2.3	1.81	6.1	1.84
Sc	32.9	2.7	33	-	-	-	31.6	0.9	32	12.9	1.9	13	11.8	2.0	10.8
V	413	2.0	416	-	-	-	324	0.5	317	120	2.8	122	130	3.2	131
Cr	15.2	4.8	18	-	-	-	285	1.2	280	15.6	6.4	16	68.9	0.7	68
Co	37.5	2.7	37	-	-	-	45.8	0.8	45	15.8	2.0	16	11.0	4.1	10.5
Ni	12.4	4.5	18	-	-	-	122	1.2	119	18.8	1.5	20	26.6	4.8	27
Cu	18.8	3.3	21	-	-	-	133	3.2	127	52.0	2.8	53	28.1	5.6	28.7
Zn	127	1.9	127	-	-	-	101	0.5	103	87.0	1.9	86	98.1	2.9	103
Ga	21.7	2.2	23	-	-	-	21.4	1.6	22	20.4	1.1	20	16.4	3.6	15
Ge	1.53	1.2	-	-	-	-	1.60	6.1	1.6	1.15	7.7	-	1.63	4.1	1
Rb	46.4	4.1	46.9	-	-	-	9.02	3.5	9.11	66.8	4.0	66.3	112	0.7	112
Sr	339	1.4	340	-	-	-	397	0.9	396	659	1.3	661	167	0.5	174
Y	36.8	2.1	37	-	-	-	26.1	1.7	26	19.5	2.4	19	24.9	1.2	26

Zr	182	1.6	184	-	-	-	169	1.0	172	229	1.1	230	167	2.7	160
Nb	12.3	2.9	12.6	-	-	-	18.6	1.9	18.1	14.1	2.7	14.5	11.9	0.7	11
Mo	248	1.6	250	-	-	-	3.91	6.7	4	2.01	6.0	-	1.21	0.9	1.37
Cd	0.15	14	-	-	-	-	0.07	12	0.06	0.063	8.4	-	0.13	22	0.14
Sn	2.17	2.1	-	-	-	-	1.89	6.8	1.7	2.17	6.2	2.3	3.31	4.7	3.7
Cs	1.14	2.5	1.1	-	-	-	0.10	4.9	0.1	1.14	2.6	1.2	7.87	2.7	7.8
Ba	677	1.6	677	-	-	-	128	4.8	131	1123	0.7	1130	585	0.5	570
La	25.0	3.8	24.9	-	-	-	15.2	3.3	15.2	38.8	3.0	37.9	29.2	2.8	29.5
Ce	53.2	0.9	52.9	-	-	-	37.4	1.8	37.5	70.1	3.0	68.6	58.1	2.8	62
Pr	6.76	2.1	6.7	-	-	-	5.27	1.9	5.35	8.05	1.4	7.84	6.85	0.5	6.6
Nd	29.1	1.8	28.7	-	-	-	24.7	2.1	24.5	30.7	1.5	30.5	26.5	1.9	26
Sm	6.71	1.7	6.58	-	-	-	6.13	2.6	6.07	5.56	2.2	5.49	5.16	0.6	5.3
Eu	1.98	1.5	1.96	-	-	-	2.03	1.6	2.07	1.60	2.6	1.53	1.14	1.2	1.19
Gd	6.80	1.6	6.75	-	-	-	6.22	2.2	6.24	4.71	2.0	4.52	4.51	0.1	4.6
Tb	1.09	1.9	1.07	-	-	-	0.95	2.2	0.92	0.66	1.4	0.64	0.72	3.0	0.7
Dy	6.49	1.9	6.41	-	-	-	5.37	2.5	5.31	3.56	2.5	3.47	4.15	0.2	4.2
Ho	1.30	1.9	1.28	-	-	-	0.97	2.6	0.98	0.66	2.7	0.65	0.85	2.1	0.97
Er	3.65	3.0	3.66	-	-	-	2.51	2.8	2.54	1.84	3.3	1.81	2.41	3.3	2.5
Tm	0.53	1.3	0.54	-	-	-	0.33	3.7	0.33	0.26	2.3	0.26	0.38	6.0	0.42
Yb	3.38	2.2	3.38	-	-	-	1.96	2.8	2	1.63	3.2	1.62	2.41	5.3	2.27
Lu	0.51	1.7	0.50	-	-	-	0.27	4.8	0.274	0.25	3.7	0.247	0.37	4.2	0.34
Hf	4.98	2.9	4.9	-	-	-	4.36	2.9	4.36	5.17	1.7	5	4.51	1.7	4.6
Ta	0.79	2.4	0.74	-	-	-	1.18	2.5	1.14	0.84	3.5	0.87	0.88	0.0	0.92
W	0.59	8.3	-	-	-	-	0.28	13	0.21	0.56	11	-	1.58	3.4	1.4
Tl	0.26	5.1	-	-	-	-	0.025	5.6	0.028	0.27	2.9	0.27	0.72	4.9	0.72
Pb	10.8	3.0	11	-	-	-	1.71	6.2	1.6	13.0	3.3	13.2	30.1	2.2	31
Bi	0.063	12	-	-	-	-	0.016	17	-	0.055	12	-	0.42	9.9	0.37
Th	5.90	3.5	5.7	-	-	-	1.20	2.4	1.22	6.13	1.1	6.1	9.58	0.2	9.7
U	1.66	1.5	1.69	-	-	-	0.41	3.3	0.403	1.86	2.0	1.86	3.07	0.3	3

*Note that this data has also been reported by Park et al. (2012) in the study of Platinum-group elements in Chinese loess samples.

%The reference values of BCR-2, GSR-3, BHVO-2, and AGV-2 are taken from the preferred values in the GeoReM database (http://georem.mpch-mainz.gwdg.de/). The reference values of SCo-1 are taken from Govindaraju (1994).

Table S3. Major element concentrations (in wt.%) of the UCC, shale, and seawater, along with the calculated $R_{Shale/UCC}$ and Log $K_{Seawater/UCC}$ ratios.

	SiO_2	TiO_2	Al_2O_3	FeO_T	MnO	MgO	CaO	Na_2O	K_2O	P_2O_5	Total
Shales[#]	65.70	0.79	17.84	6.14	0.04	2.10	0.50	0.68	3.84	0.11	97.73
2 s.e.	0.50	0.02	0.33	0.23	0.01	0.11	0.18	0.09	0.14	0.01	-
UCC*	64.26	0.75	15.41	5.32	0.10	2.57	4.89	3.39	3.09	0.22	100.00
2 s.e.	0.61	0.03	0.51	0.2	0.01	0.1	0.19	0.11	0.11	0.01	-
$R_{Shales/UCC}$	1.02	1.05	1.16	1.16	0.43	0.82	0.10	0.20	1.24	0.52	-
2 s.e.	0.02	0.11	0.09	0.12	0.14	0.11	0.08	0.05	0.13	0.09	-
Seawater[%]	9.45E-06	1.73E-09	6.69E-10	6.83E-10	2.13E-08	8.41E-02	1.19E-02	4.33E-01	1.57E-02	7.42E-05	-
Log $K_{Seawater/UCC}$	-6.83	-8.64	-10.36	-9.89	-6.68	-1.48	-2.61	-0.89	-2.29	-3.48	-

[#]The median values of the compiled shale samples from Table S1 are reported on a loss-on-ignition (LOI)-free basis.

*Results from this study (see Table 3), normalized to LOI free.

[%]Seawater composition, adapted from Bruland and Lohan (2003).

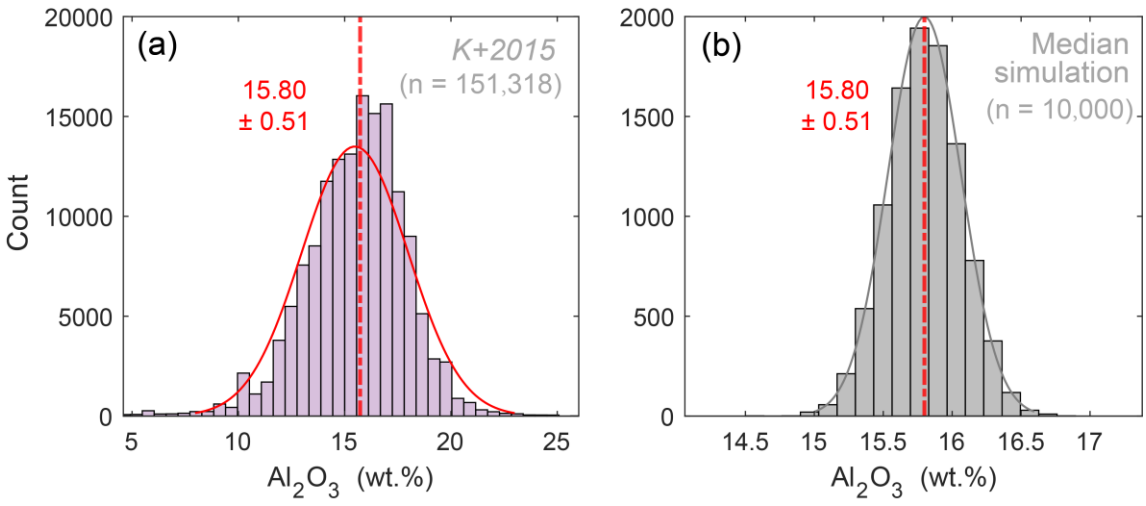

Fig. S1. (**a**) Al_2O_3 concentration distribution in the *K+2015* dataset and (**b**) its median distribution computed using MATLAB bootstrapping. The calculated median of 15.80 ± 0.51 wt.% is consistent with the value of 15.24 ± 0.51 wt.% obtained from the *KS2012* igneous dataset (see Fig.5a-b).

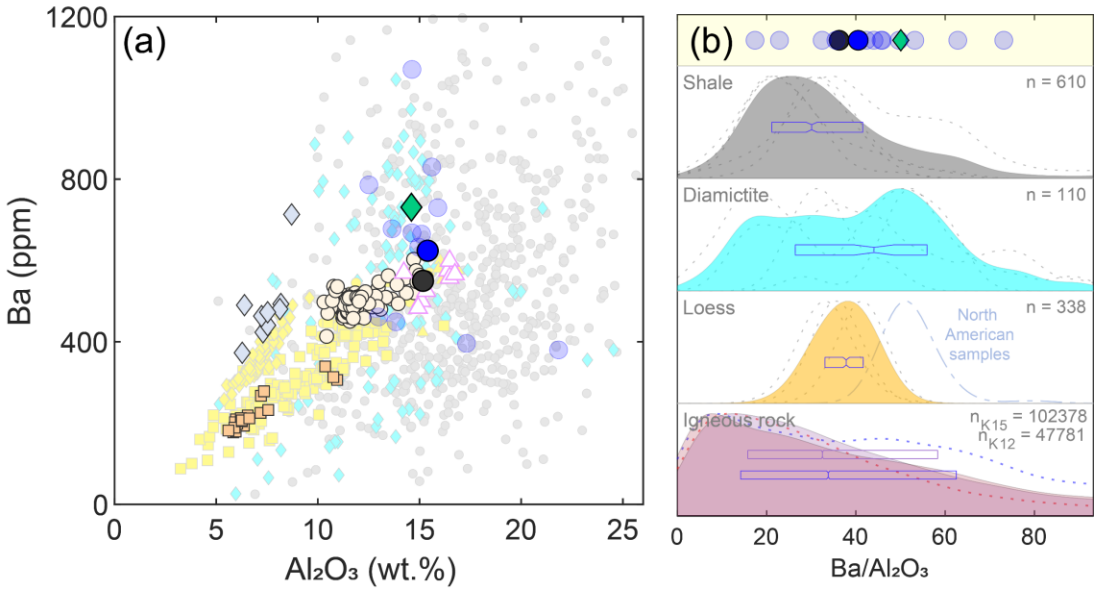

Fig. S2. (**a**) Barium versus Al_2O_3 content in the collected sediments and (**b**) the probability distribution of Ba/Al_2O_3 ratios for different datasets. Symbols as those in Fig. 6 and 7. Note that the loess samples from North America have distinctly higher Ba/Al_2O_3 ratios. Together with the elevated K_2O/Al_2O_3 ratios (Fig. 6e and 7b), this may indicate K-feldspar enrichment in these samples.

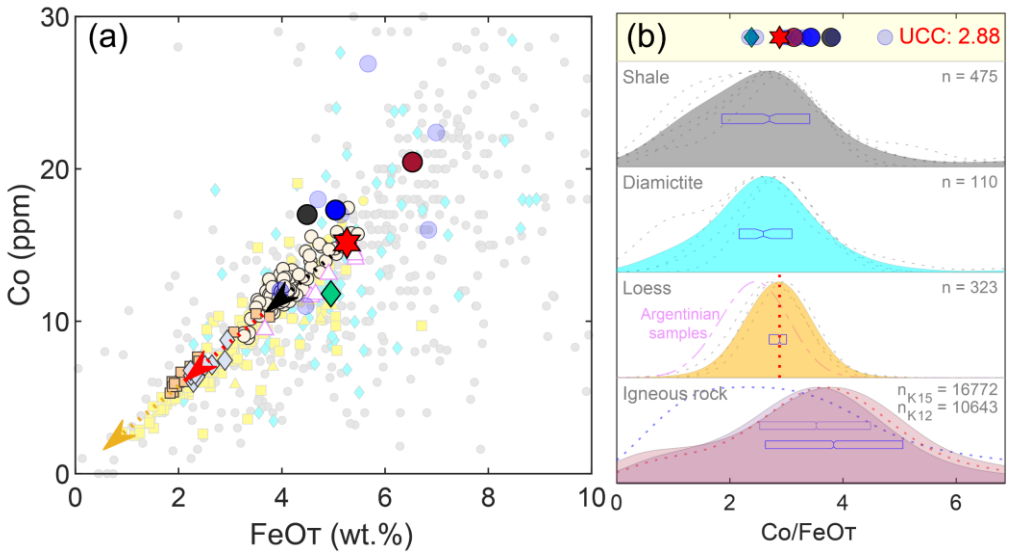

Fig. S3. (**a**) Cobalt versus FeO_T content in the collected sedimentary samples and (**b**) the probability distribution of Co/FeO_T ratios for different datasets. Symbols as those in Fig. 6 and 7. The new Co abundance (15.1 ± 0.6 ppm) in the UCC is determined from the median Co/FeO_T = 2.88 of loess samples (Argentinian samples excluded). The relatively lower median values observed in glacial diamictite and shale samples are unclear but may be related to Co loss during more extensive chemical weathering.

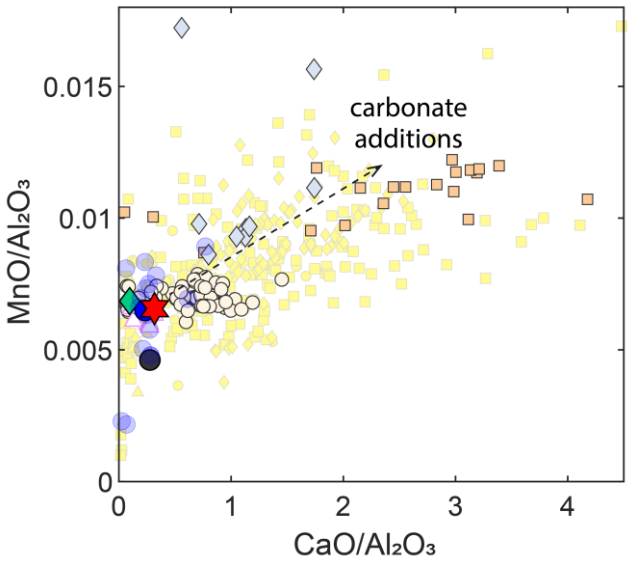

Fig. S4. A positive trend in MnO/Al_2O_3 and CaO/Al_2O_3 is observed in loess samples, likely indicating Mn enrichment in loess due to carbonate.

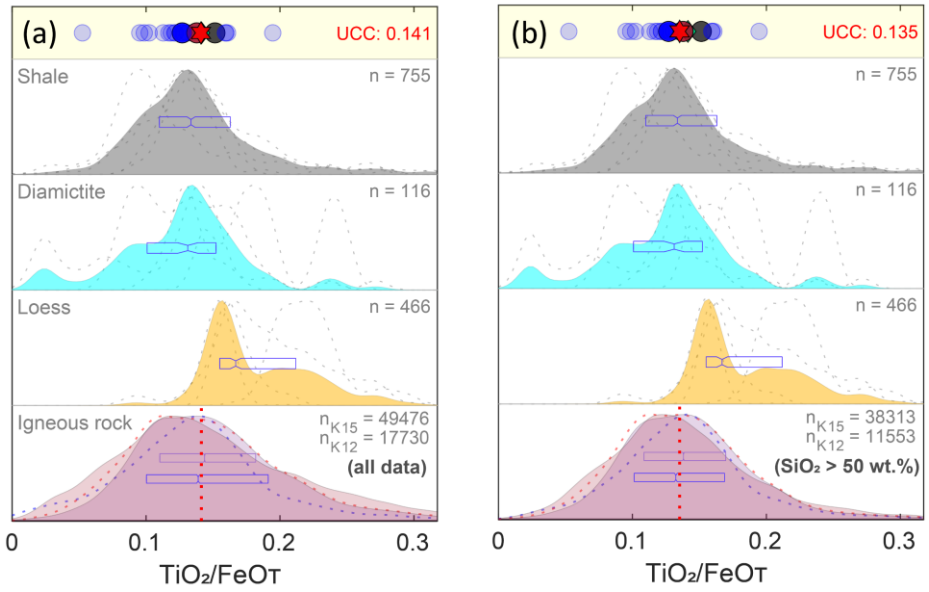

Fig. S5. The probability distribution of TiO_2/FeO_T ratios for different datasets. In (a), the igneous dataset used all data reported in *KS2012* and *K+2015*, while in (b), only SiO_2 > 50 wt.% samples are plotted.

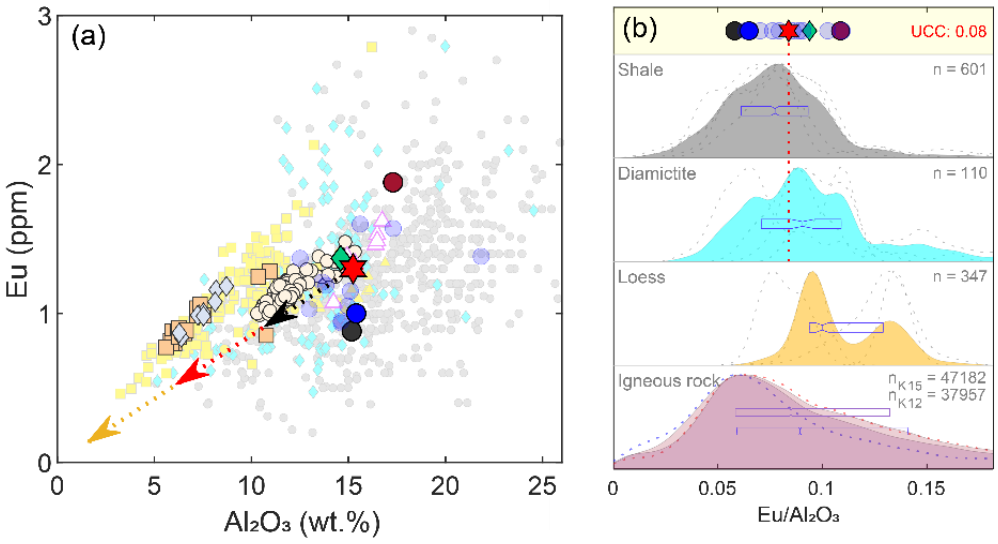

Fig. S6. (**a**) Europium versus Al_2O_3 content in the collected sedimentary samples and (**b**) the probability distribution of Eu/Al_2O_3 ratios for different datasets. Symbols as those in Fig. 6 and 7. The new Eu abundance (1.3 ± 0.1 ppm) in the UCC is determined from the median Eu/Al_2O_3 = 0.08 of the shale and glacial diamictite datasets. The relatively higher values observed in loess could be due to concentrations of accessory phases such as titanite, apatite, and zircons (work in preparation).

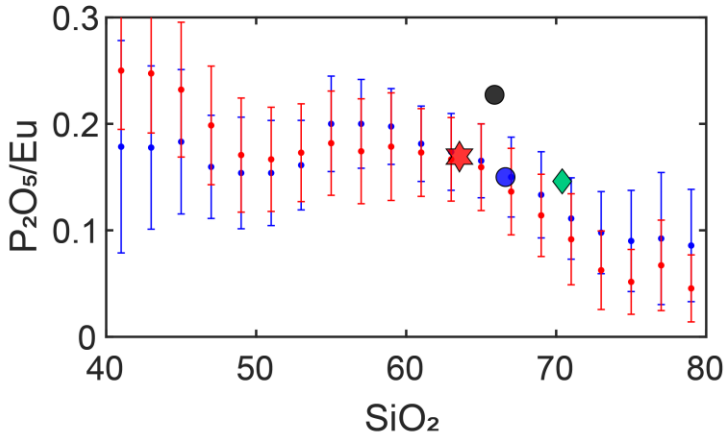

Fig. S7. Trend of P_2O_5/Eu ratio with increasing SiO_2 (in wt.%) in the *K+2015* igneous dataset. Symbols are defined in Fig. 4. The Eu concentration in the UCC is determined as 1.3 ± 0.1 ppm, see Fig. S6.

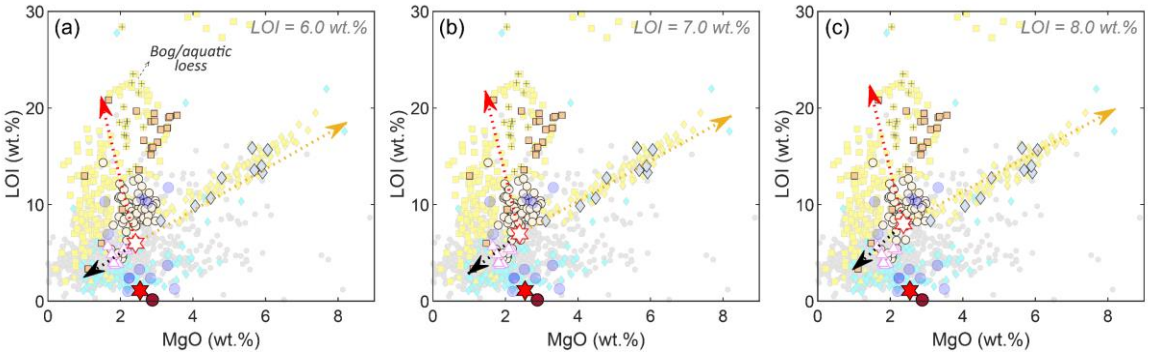

Fig. S8. LOI versus MgO in the compiled sedimentary samples. The trends in loess samples can be modeled by mixing an average siliciclastic source with 6–8 wt.% LOI (**a-c**, open red hexagon) with dolomite and calcite. Symbols as in Fig. 4 and Fig. 9.

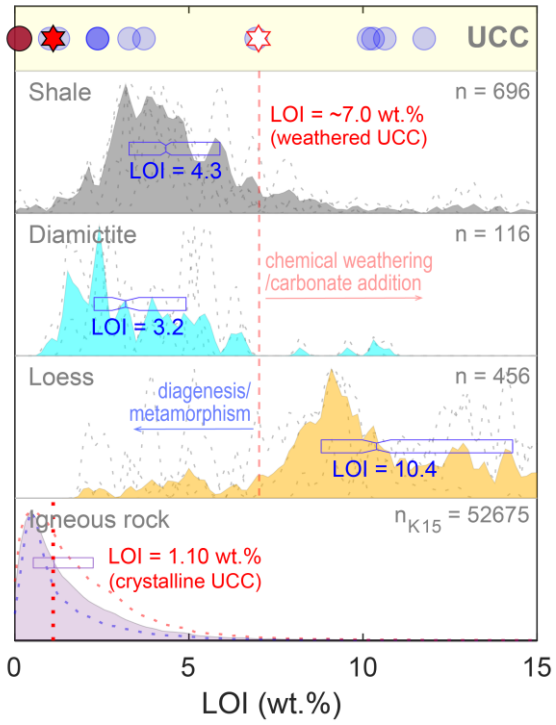

Fig. S9. LOI distribution across different datasets. The solid red hexagon represents the suggested LOI value for the crystalline UCC (1.10 wt.%), while the open red hexagon represents the weathered UCC (LOI = ~7.0 wt.%). Most loess samples have LOI > 7 wt.% due to carbonate influences, whereas shales and glacial diamictites have much lower LOI, potentially related to dehydration caused by diagenesis and metamorphism.

Appendix B

Halogen (F, Cl, Br, and I) concentrations of the upper continental crust through time as recorded in ancient glacial diamictite composites

– Supplementary Information

Table S1. X-ray diffraction (XRD) derived modal abundances (in wt.%) of the glacial diamictite composites.

Samples	Age (Ga)	Qz	Pl (Ab%)	Kfs	Clay/mica		Chl (Mg%)	Carbonate			Amp	Others		
					Ilt-Ms	Bi		Cal	Dol-Ank	Sd		Hem	Mag	Crn
Mozaan	2.9	52.1	4.2 (100%)	9.1	-	4.3	23.2 (47%)	-	-	-	-	-	7.0	-
Afrikander	2.9	42.1	5.4 (91%)	3.7	-	-	19.5 (81%)	-	0.6	-	28.7	-	-	-
Coronation	2.9	60.4	-	-	30.3	-	8.9 (81%)	0.4	-	-	-	-	-	-
Promise	2.9	62.3	4.4 (70%)	2.3	14.3	-	16.1 (62%)	0.7	-	-	-	-	-	-
Ramsay Lake	2.4	51.2	11.9 (93%)	0.9	13.6	5.9	15.4 (72%)	1.1	-	-	-	-	-	-
Gowganda	2.4	28.5	40.1 (100%)	7.5	8.9	2.6	9.8 (75%)	0.4	-	-	2.1	-	-	-
Bottle Creek	2.4	40.9	36.5 (100%)	-	9.2	8.0	5.3 (76%)	-	-	-	-	-	-	-
Bruce	2.4	36.3	35.5 (78%)	5.2	9.4	-	13.7 (74%)	-	-	-	-	-	-	-
Makganyene	2.3	62.2	-	8.9	-	-	19.0 (15%)	-	9.9	-	-	-	-	-
Timeball	2.2	38.4	11.2 (97%)	1.9	25.8	-	10.3 (57%)	0.9	-	-	-	-	-	11.5
Duitschland	2.4	40.5	-	1.6	31.8	-	13.6 (36%)	-	8.9	3.6	-	-	-	-
Konnarock	0.7	37.1	25.0 (100%)	10.2	22.6	-	2.0 (71%)	0.7	-	-	-	2.4	-	-
Gaskiers	0.58	32.1	35.4 (100%)	5.9	21.2	-	5.5 (62%)	-	-	-	-	-	-	-
Pocatello	0.7	47.7	9.7 (100%)	2.6	35.4	-	3.1 (63%)	-	-	-	-	1.6	-	-
Nantuo	0.64	42.8	12.1 (100%)	4.7	30.5	-	9.8 (56%)	0.2	-	-	-	-	-	-
Gucheng	0.7	47.3	12.1 (93%)	-	31.9	-	8.3 (68%)	0.4	-	-	-	-	-	-
Blaubeker	0.7	55.6	15.7 (100%)	10.1	10.3	-	7.8 (60%)	0.5	-	-	-	-	-	-
Kaigas	0.75	35.1	24.5 (92%)	-	25.5	5.9	6.8 (79%)	2.2	-	-	-	-	-	-
Chuos	0.7	30.5	11.0 (100%)	3.3	11.8	8.4	5.4 (46%)	6.8	22.9	-	-	-	-	-
Numees	0.6	46.9	17.4 (100%)	4.5	21.9	5.2	1.9 (67%)	2.2	-	-	-	-	-	-
Ghaub	0.64	17.5	5.8 (100%)	-	16.5	5.1	2.6 (75%)	46.1	6.3	-	-	-	-	-
Bolivia	0.3	55.1	9.4 (100%)	6.5	21.9	-	6.7 (47%)	0.4	-	-	-	-	-	-
Dwyka East	0.3	34.8	30.9 (100%)	11.1	9.2	-	14.0 (61%)	-	-	-	-	-	-	-
Dwyka West	0.3	25.5	7.7 (32%)	9.3	8.5	-	17.5 (71%)	7.7	23.0	-	-	0.8	-	-

* Note that mineral abbreviations are from Whitney and Evans (2009): Qz = quartz, Pl = plagioclase, Ab = albite, Kfs = K-feldspar, Ilt = illite, Ms = muscovite, Bi = biotite, Chl = chlorite, Cal = calcite, Dol = dolomite, Ank = ankerite, Sd = siderite, Amp = amphibole, Hem = hematite, Mag = magnetite, and Crn = corundum.

Table S2. Halogen (F, Cl, Br, and I) concentrations in reference materials

Element	Reference material	C-IC analysis (ppm)			N-ICPMS analysis (ppm)			GeoReM compilation (ppm)		
		mean	2σ	*repeats*	mean	2σ	*repeats*	compiled*	2σ*	*previously reported values*[#]
F	BE-N	1124	6	*n=3*	-	-	-	*1056*	*104*	*1000 (compiled, ref-1), 1000 (compiled, ref-2), 1080 (IC, ref-3), 1100 (compiled, ref-4), 1100 (compiled, ref-5)*
	BHVO-2	387	30	*n=4*	-	-	-	*396*	*39*	*370 (compiled, ref-10), 376 (IC, ref-11), 396 (compiled, ref-5), 402 (IC, ref-3), 409 (IC, ref-12), 420 (SIMS, ref-13)*
	AGV-2	458	7	*n=3*	-	-	-	*408*	*55*	*377 (IC, ref-3), 389 (SIMS, ref-13), 400 (compiled, ref-5), 432 (IC, ref-12), 440 (compiled, ref-10)*
	GSR-2	301	30	*n=4*	-	-	-	*280*	*0*	*280 (compiled, ref-1), 280 (ref-15)*
	GSP-2	4025	108	*n=3*	-	-	-	*3453*	*1150*	*3000 (compiled, ref-16), 3260 (SIMS, ref-13), 4100 (various methods, ref-17)*
	GS-N	1085	33	*n=3*	-	-	-	*954*	*134*	*890 (IC, ref-11), 915 (IC, ref-18), 919 (IC, ref-3), 920 (EPMA, ref-19), 932 (IC, ref-20), 1050 (compiled, ref-1), 1050 (compiled, ref-2)*
Cl	BE-N	154	6	*n=3*	218	137	*n=2*	*196*	*29*	*170 (IC, ref-3), 180 (compiled, ref-5), 200 (compiled, ref-1), 200 (compiled, ref-2), 200 (compiled, ref-4), 216.7 (PIXE, ref-6)*
	BHVO-2	56	8	*n=4*	85	8	*n=9*	*106*	*48*	*81 (IC, ref-11), 89 (IC, ref-12), 102 (NG, ref-13), 104 (RNAA, ref-14), 107 (compiled, ref-5), 150 (IC, ref-3)*
	AGV-2	75	6	*n=4*	84	9	*n=4*	*72*	*16*	*61 (IC, ref-12), 68 (compiled, ref-5), 72.8 (RNAA, ref-14), 75 (IC, ref-3), 83 (NG, ref-13)*
	GSR-2	33	6	*n=4*	37	9	*n=6*	*44*	*6*	*42 (compiled, ref-1), 46 (ref-15)*
	GSP-2	282	3	*n=3*	377	83	*n=7*	*381*	*37*	*363 (RNAA, ref-14), 381 (NG, ref-13), 400 (various methods, ref-17)*
	GS-N	393	27	*n=3*	429	99	*n=2*	*417*	*111*	*346 (IC, ref-11), 349 (IC, ref-3), 378 (IC, ref-18), 407 (LA-ID-ICPMS, ref-21), 450 (compiled, ref-1), 450*

										(compiled, ref-2), 456 (IC, ref-20), 497 (EPMA, ref-19)
Br	BE-N	0.1	0.2	*n=4*	0.27	0.30	*n=2*	*1.02*	*1.44*	*0.32 (INAA, ref-7), 0.6 (ICPMS, ref-3), <1 (INAA, ref-8), 1 (compiled, ref-5), 2.2 (INAA, ref-9)*
	BHVO-2	0.1	0.2	*n=3*	0.28	0.07	*n=7*	*0.27*	*0.04*	*0.24 (RNAA, ref-14), 0.259 (NG, ref-13), 0.269-0.277 (ICPMS, ref-3), 0.29 (ICPMS, ref-11), 0.3 (compiled, ref-5)*
	AGV-2	0.2	0.2	*n=3*	0.27	0.06	*n=4*	*0.15*	*0.12*	*0.101 (RNAA, ref-14), 0.107-0.145 (ICPMS, ref-3), 0.13 (compiled, ref-5), 0.244 (NG, ref-13)*
	GSR-2	0.2	0.3	*n=4*	0.19	0.04	*n=5*	-	-	-
	GSP-2	0.1	0.2	*n=4*	0.60	0.18	*n=7*	*0.097*	*0.06*	*0.077 (NG, ref-13), 0.117 (RNAA, ref-14)*
	GS-N	2.1	1.0	*n=3*	2.03	0.32	*n=2*	*2.33*	*0.82*	*1.6 (ICPMS, ref-11), 1.9 (IC, ref-20), 2.283 (ICPMS, ref-18), 2.4 (XRF, ref-20), 2.5 (INAA, ref-8), 2.517 (ICPMS, ref-3), 2.56 (LA-ID-ICPMS, ref-21), 2.91 (INAA, ref-7)*
I	BE-N	-	-	-	0.02	0.01	*n=2*	*0.018*	*0.006*	*0.016 (ICPMS, ref-3), 0.02 (compiled, ref-5)*
	BHVO-2	-	-	-	0.05	0.01	*n=8*	*0.087*	*0.250*	*0.016 (ICPMS, ref-3), 0.02 (ICPMS, ref-11), 0.02 (compiled, ref-5), 0.07 (NG, ref-13), 0.307 (RNAA, ref-14)*
	AGV-2	-	-	-	0.01	0.01	*n=4*	*0.073*	*0.179*	*0.007 (ICPMS, ref-3), 0.007 (compiled, ref-5), 0.080 (NG, ref-13), 0.197 (RNAA, ref-14)*
	GSR-2	-	-	-	0.00	0.01	*n=2*	*0.140*	-	*0.14 (compiled, ref-15)*
	GSP-2	-	-	-	0.01	0.01	*n=4*	*0.048*	*0.078*	*0.02 (NG, ref-13), 0.075 (RNAA, ref-14)*
	GS-N	-	-	-	0.04	0.01	*n=2*	*0.070*	*0.060*	*0.042 (ICPMS, ref-3), 0.046 (ICPMS, ref-11), 0.092 (ICPMS, ref-18), <0.1 (LA-ID-ICPMS, ref-21)*

* The “compiled” value of every reference material is averaged from all previous reported values that could be found in GeoReM (http://georem.mpch-mainz.gwdg.de/sample_query.asp, June 2022). The associated uncertainty represents two standard deviations from the mean.

[#] Summary of previously reported values for each reference material, with parenthesis indicating their analytical methods and reference sources (see below for the analytical method abbreviation and original references). In addition, although He et al. (2019) also provided Cl, Br, I and estimates for BHVO-2, AGV-2, GSR-2, and GSP-2 based on the N-ICPMS analysis, their results are not taken as previous values here because we used the same method in this study, and some values from He et al. (2019) are updated here.

Abbreviations for analytical methods in Table S2:

IC:	*Ion chromatography*
PIXE	*Proton Induced X-ray Emission*
INAA	*Instrumental neutron activation analysis*
ICPMS	*Inductively coupled plasma mass spectrometry*
SIMS	*Secondary ion mass spectrometer*
NG	*Nobel gas*
RNAA	*Radiochemical neutron activation analysis*
EPMA	*Electron probe microanalysis*
LA-ID-ICPMS	*Laser ablation coupled isotope dilution ICPMS*
XRF	*X-ray fluorescence*
compiled	*compiled from previously reported values and no independent measurement is available*
C-IC	*Combustion ion chromatography analysis (this study)*
N-ICPMS	*NH4HF2 digestion coupled with ICPMS analysis (this study)*

References in Table S2:

1 *Govindaraju, K., 1994. 1994 compilation of working values and sample description for 383 geostandards. Geostandards newsletter, 18, pp.1-158.*

2 *Govindaraju, K., 1995. 1995 working values with confidence limits for twenty-six CRPG, ANRT and IWG-GIT geostandards. Geostandards Newsletter, 19, pp.1-32.*

3 *Michel, A. and Villemant, B., 2003. Determination of halogens (F, Cl, Br, I), sulfur and water in seventeen geological reference materials. Geostandards Newsletter, 27(2), pp.163-171.*

4 *Abbey, S., 1996. Application of the five-mode method to three GIT-IWG rock reference samples. Geostandards Newsletter, 20(1), pp.29-40.*

5 *Jochum, K.P., Weis, U., Schwager, B., Stoll, B., Wilson, S.A., Haug, G.H., Andreae, M.O. and Enzweiler, J., 2016. Reference values following ISO guidelines for frequently requested rock reference materials. Geostandards and Geoanalytical Research, 40(3), pp.333-350.*

6 *Bakraji, E., Ahmad, M., Salman, N., Haloum, D., Boutros, N. and Abboud, R., 2011. Dating and classification of Syrian excavated pottery from Tell Saka Site, by means of thermoluminescence analysis, and multivariate statistical methods, based on PIXE analysis. Journal of Radioanalytical and Nuclear Chemistry, 289(2), pp.423-429.*

7 *Mizera, J. and Řanda, Z., 2010. Instrumental neutron and photon activation analyses of selected geochemical reference materials. Journal of radioanalytical and nuclear chemistry, 284(1), pp.157-163.*
8 *Korotev, R.L., 1996. A self-consistent compilation of elemental concentration data for 93 geochemical reference samples. Geostandards Newsletter, 20(2), pp.217-245.*
9 *El Maghraoui, M., Joron, J.L., Etoubleau, J., Cambon, P. and Treuil, M., 1999. Determination of forty-four major and trace elements in GPMA magmatic rock reference materials using X-ray Fluorescence Spectrometry (XRF) and Instrumental Neutron Activation Analysis (INAA). Geostandards Newsletter, 23(1), pp.59-68.*
10 *Plumlee, G., 1998. USGS Certificate of Analysis Basalt, Hawaiian Volcanic Observatory, BHVO-2.*
11 *Balcone-Boissard, H., Michel, A. and Villemant, B., 2009. Simultaneous determination of fluorine, chlorine, bromine and iodine in six geochemical reference materials using pyrohydrolysis, ion chromatography and inductively coupled plasma-mass spectrometry. Geostandards and Geoanalytical Research, 33(4), pp.477-485.*
12 *Wang, Q., Makishima, A. and Nakamura, E., 2010. Determination of fluorine and chlorine by pyrohydrolysis and ion chromatography: comparison with alkaline fusion digestion and ion chromatography. Geostandards and geoanalytical research, 34(2), pp.175-183.*
13 *Kendrick, M.A., D'Andres, J., Holden, P. and Ireland, T., 2018. Halogens (F, Cl, Br, I) in thirteen USGS, GSJ and NIST international rock and glass reference materials. Geostandards and Geoanalytical Research, 42(4), pp.499-511.*
14 *Sekimoto, S. and Ebihara, M., 2017. Accurate Determination of chlorine, bromine and iodine in US Geological Survey geochemical reference materials by radiochemical neutron activation analysis. Geostandards and Geoanalytical Research, 41(2), pp.213-219.*
15 *Wang, Y., Gu, T.X., Wang, X., Gao, Y., Jochum, K.P. and Müller, W.E.G., 2013. Practical Handbook of Reference Materials for Geoanalysis, (Chinese-English).*
16 *Gunderson, L., 1998. Granodiorite, Silver Plume, Colorado, GSP-2: US Geological Survey Certificate of Analysis. Available from < https://emrlibrary.gov.yk.ca/ygs/open_files/2019/2019-1/Appendix%20C/C4_QAQC/GSP-2_StandardInformation_USGS.pdf>*
17 *Peterman, Z.E. and Cloke, P.L., 2002. Geochemistry of rock units at the potential repository level, Yucca Mountain, Nevada. Applied Geochemistry, 17(6), pp.683-698.*
18 *Wang, L.X., Ma, C.Q., Zhang, C., Zhu, Y.X. and Marks, M.A., 2018. Halogen geochemistry of I-and A-type granites from Jiuhuashan region (South China): Insights into the elevated fluorine in A-type granite. Chemical Geology, 478, pp.164-182.*
19 *Zhang, C., Koepke, J., Wang, L.X., Wolff, P.E., Wilke, S., Stechern, A., Almeev, R. and Holtz, F., 2016. A practical method for accurate measurement of trace level fluorine in Mg-and Fe-bearing minerals and glasses using electron probe microanalysis. Geostandards and Geoanalytical Research, 40(3), pp.351-363.*
20 *Wang, L.X., Marks, M.A., Keller, J. and Markl, G., 2014. Halogen variations in alkaline rocks from the Upper Rhine Graben (SW Germany): Insights into F, Cl and Br behavior during magmatic processes. Chemical Geology, 380, pp.133-144.*
21 *Boulyga, S.F. and Heumann, K.G., 2005. Direct determination of halogens in powdered geological and environmental samples using isotope dilution laser ablation ICP-MS. International Journal of Mass Spectrometry, 242(2-3), pp.291-296.*

Table S3. Student's t-test for the comparison of Aluminum-normalized halogen (F_{Al}, Cl_{Al}, Br_{Al}, and I_{Al}) concentrations of diamictites from different age-groups

F_{Al} (h values)	~2.9 Ga	~2.4–2.2 Ga	0.75–0.58 Ga	~0.30 Ga
~2.9 Ga	0	1	1	1
~2.4-2.2 Ga	1	0	1	1
0.75-0.58 Ga	1	1	0	0
~0.30 Ga	1	1	0	0

Cl_{Al} (h values)	~2.9 Ga	~2.4–2.2 Ga	0.75–0.58 Ga	~0.30 Ga
~2.9 Ga	0	1	0	0
~2.4-2.2 Ga	1	0	0	0
0.75-0.58 Ga	0	0	0	0
~0.30 Ga	0	0	0	0

Br_{Al} (h values)	~2.9 Ga	~2.4–2.2 Ga	0.75–0.58 Ga	~0.30 Ga
~2.9 Ga	0	0	1	1
~2.4-2.2 Ga	0	0	1	0
0.75-0.58 Ga	1	1	0	0
~0.30 Ga	1	0	0	0

I_{Al} (h values)	~2.9 Ga	~2.4–2.2 Ga	0.75–0.58 Ga	~0.30 Ga
~2.9 Ga	0	0	0	0
~2.4-2.2 Ga	0	0	0	0
0.75-0.58 Ga	0	0	0	0
~0.30 Ga	0	0	0	0

Note that h-values from Student's t-test for each halogen are summarized here, in which "0" indicates no significant difference between two tested age-groups in statistics, while "1" represents there is a significant difference between the two age-groups in statistics ($P < 0.05$).

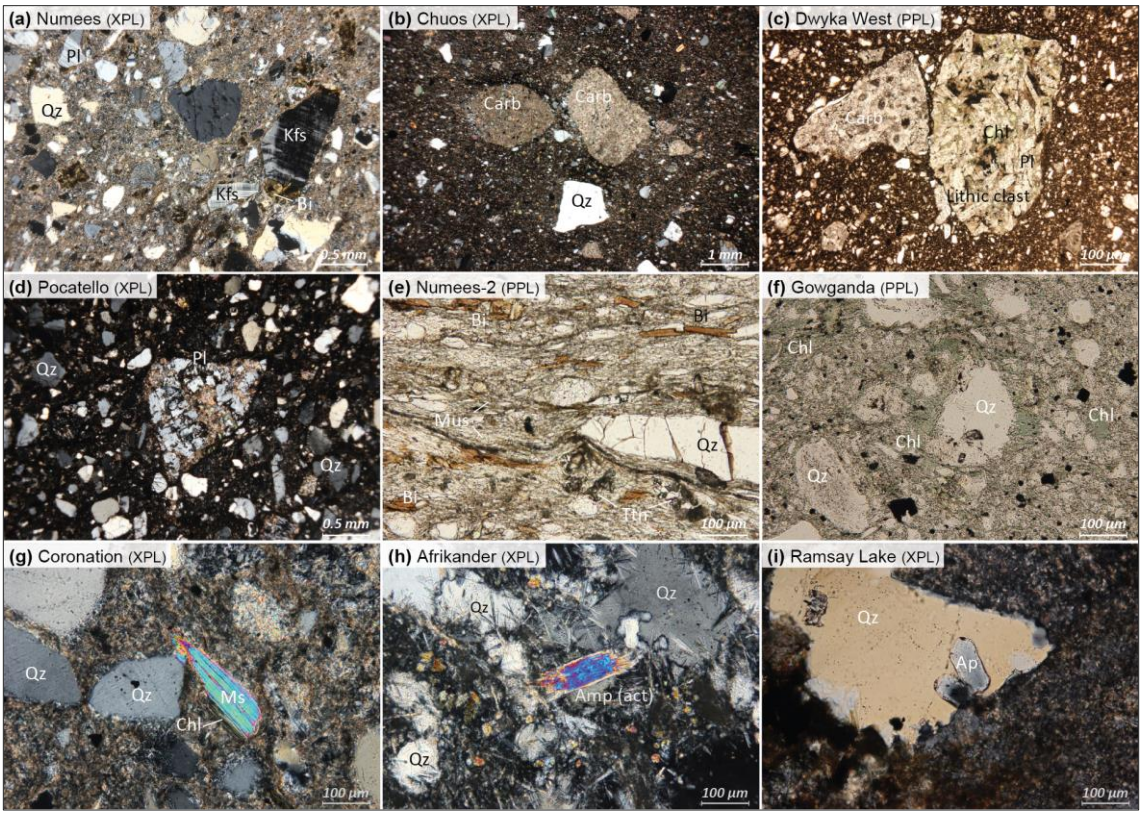

Fig. S1. Photomicrographs of the glacial diamictites. **(a)** Quartz (Qz), plagioclase (Pl), and K-feldspar (Kfs) clasts of the Numees diamictite. Some biotite (Bi) occurs in the rim of plagioclase and K-feldspar grains. **(b)** Carbonate (Carb) and quartz clasts in the Chuos diamictite. **(c)** Carbonate and lithic clasts in the Dwyka West diamictite. Within the lithic clast, plagioclase and chlorite (Chl) are also observed. **(d)** Plagioclase and quartz clasts from the Pocatello diamictite. Note that the plagioclase grain is sericitized. **(e)** Authigenic biotite and muscovite (Ms) observed in the Numees diamictite. **(f)** Authigenic chlorite in the Gowganda diamictite. **(g)** Rounded muscovite clast (likely detrital origin) in the Coronation diamictite; rims have been transformed to chlorite. **(h)** Fibrous amphibole (Amp, maybe actinolite (act), metamorphic origin) in the Afrikander diamictite. **(i)** Apatite (Ap) grains found in detrital quartz clast in the Ramsay Lake diamictite. "XPL" means the picture is taken under cross-polarized light while "PPL" is under plane-polarized light.

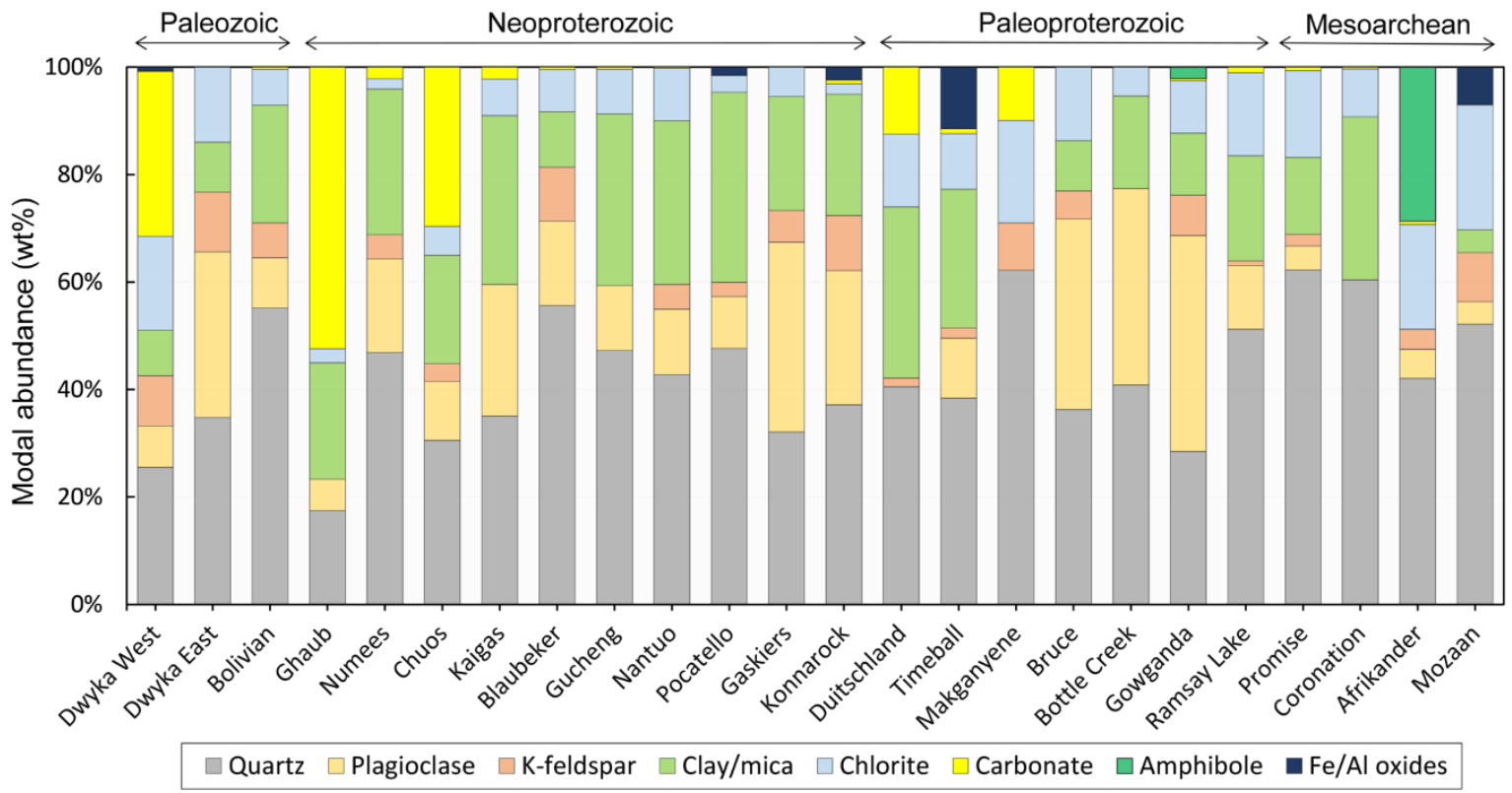

Fig. S2. Mineral modal abundances in the diamictite composites derived from the XRD results (Table S1). Note that "*Clay/mica*" is a combination of illite-muscovite and biotite, "*Carbonate*" represents all carbonate minerals like calcite, dolomite-ankerite, and siderite, and "*Fe/Al oxides*" is the sum of hematite, magnetite, and corundum.

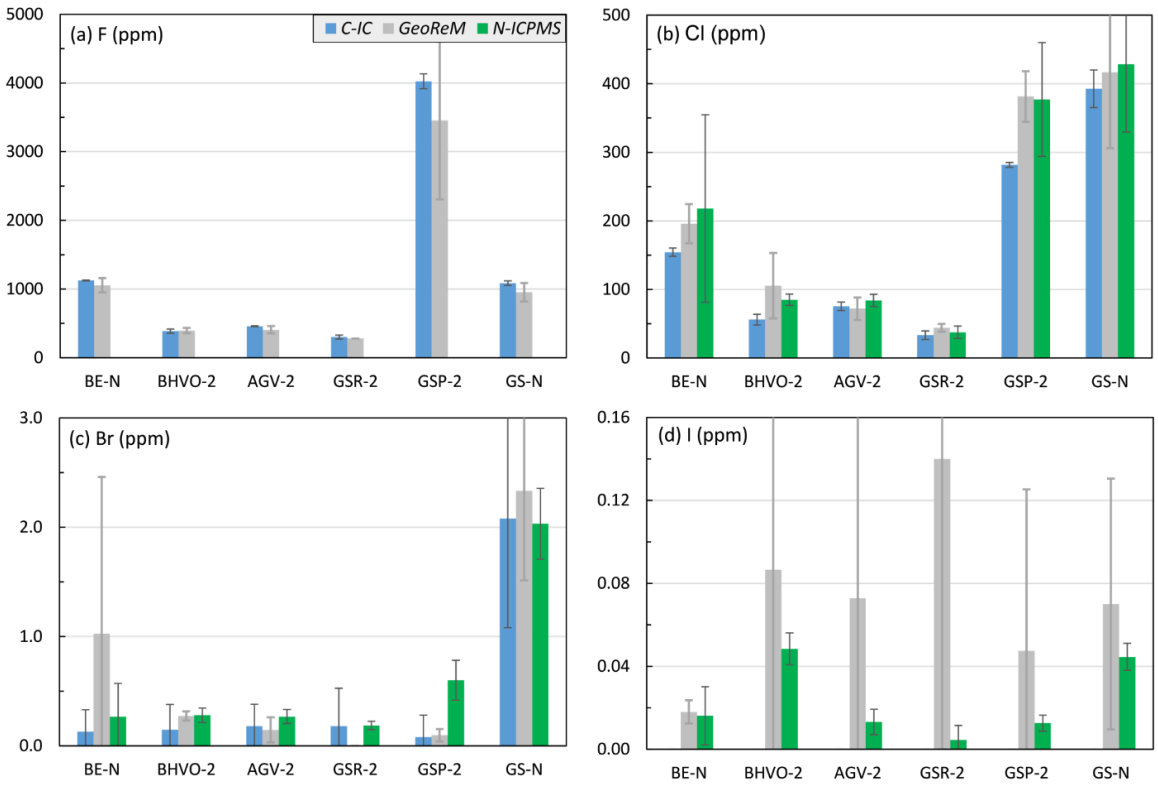

Fig. S3. Comparison of F **(a)**, Cl **(b)**, Br **(c)**, and I **(d)** data of reference materials analyzed by C-IC and N-ICPMS analyses (blue and green bars, respectively) and the GeoReM compilation (gray bar, averaged from all previously reported values, see Table S2). Error bars represent 2σ uncertainty.

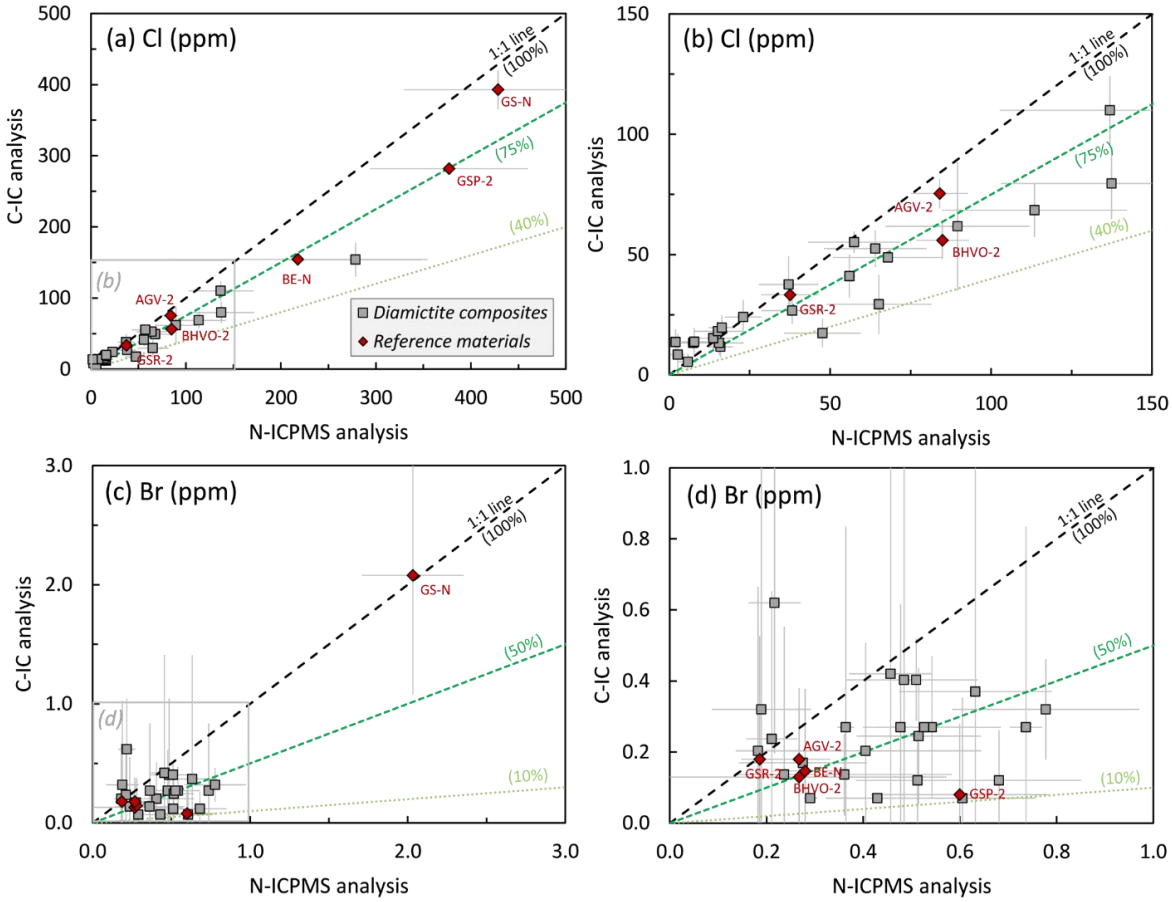

Fig. S4. Comparison of Cl **(a-b)** and Br **(c-d)** data in the reference materials and the diamictite composites analyzed in this study by C-IC and N-ICPMS, respectively. Error bars are in 2σ. The measured Cl and Br contents by C-IC are often lower than the ones obtained by N-ICPMS, except for several samples with very low N-ICPMS Cl (< 15 ppm) and Br (< 0.3 ppm) contents, which probably result from large analytical uncertainties of the C-IC analysis when sample concentrations are close to the detection limits. The different colored dash lines compare the offset of the C-IC data relative to N-ICPMS data.

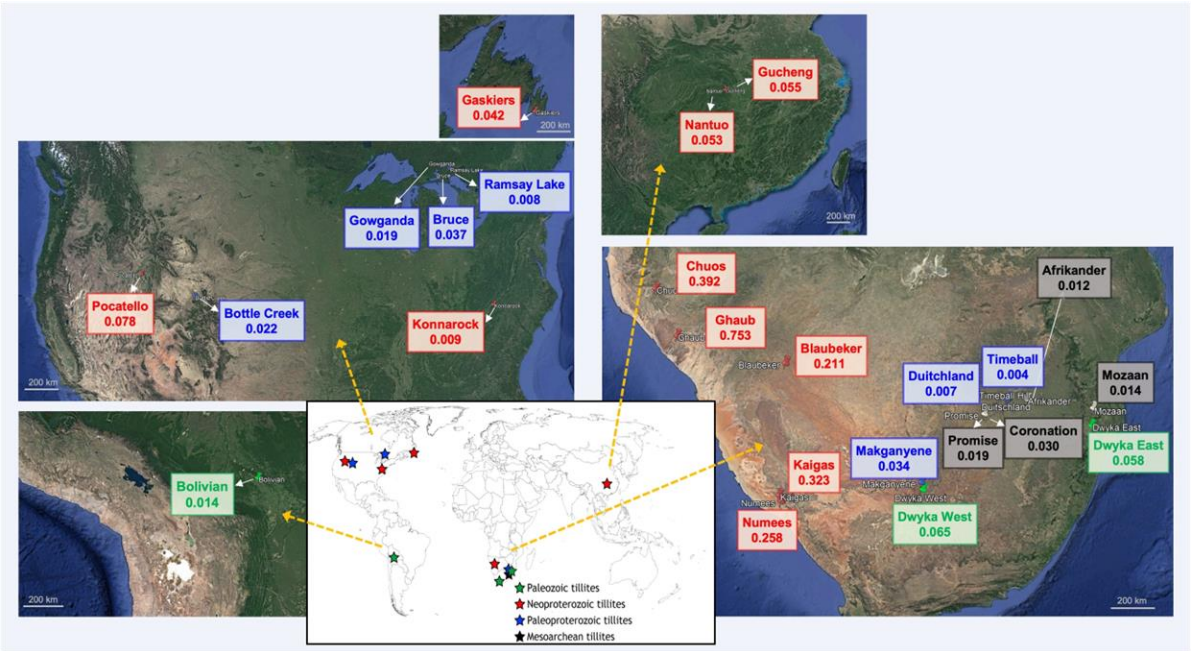

Fig. S5. Iodine concentrations (ppm) in ancient glacial diamictite composites from different localities.

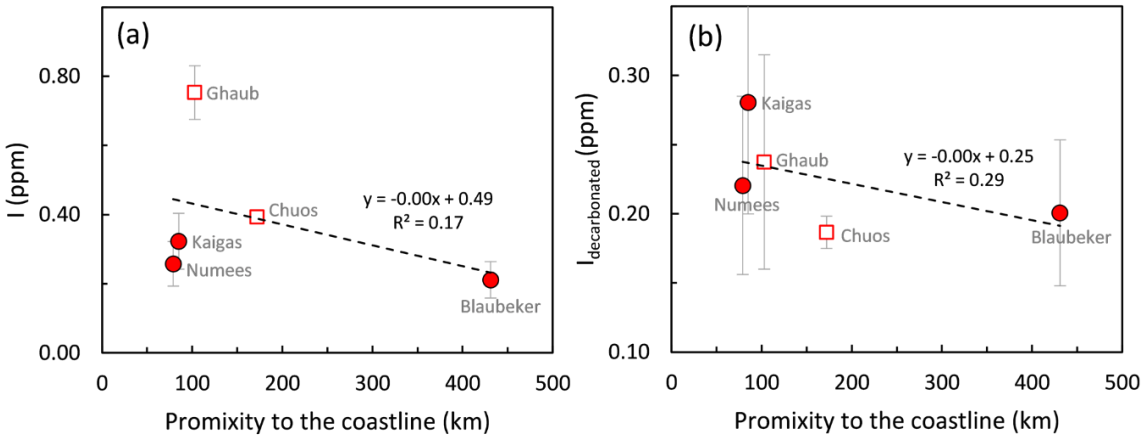

Fig. S6. Iodine **(a)** and $I_{decarbonated}$ **(b)** concentrations (ppm) of the Namibian diamictite composites. The $I_{decarbonated}$ is calculated by deducting the potential I hosted in carbonate (see Fig. 4h and discussion in text) from the total I concentrations. Error bars are 2σ of the measured I concentrations. Two carbonate-rich samples (Ghaub and Chuos, with XRD carbonate content higher than 10 wt.%) are shown as open squares.

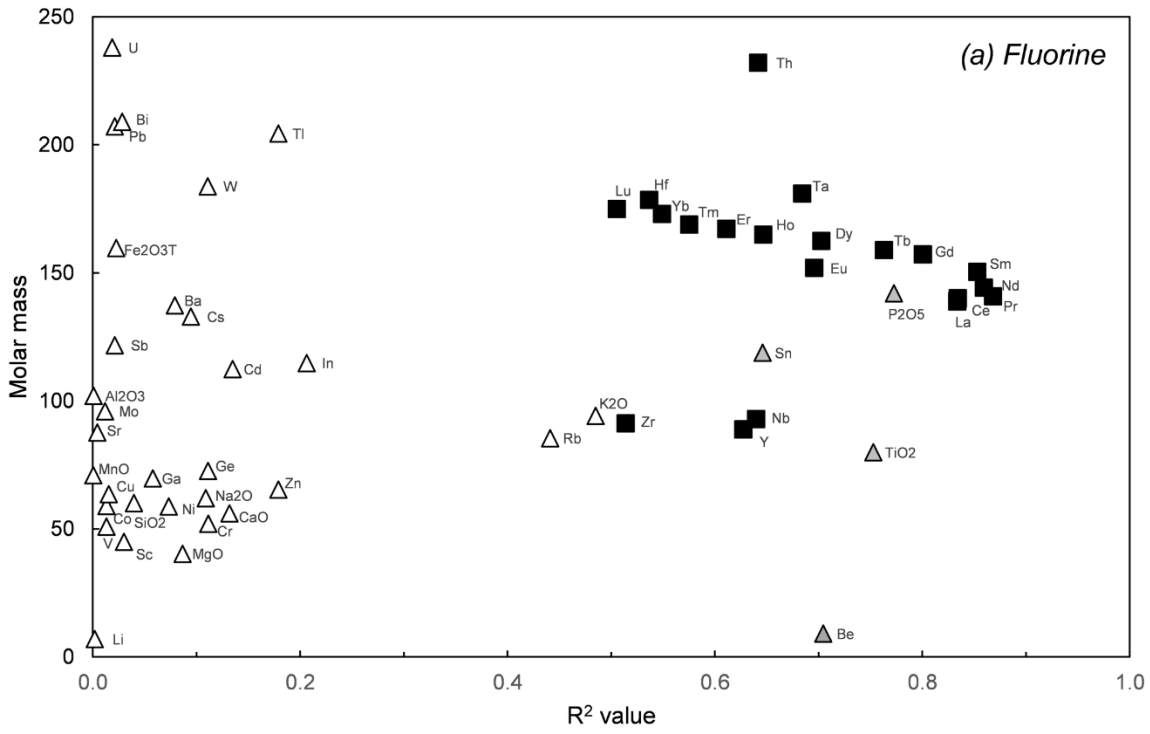

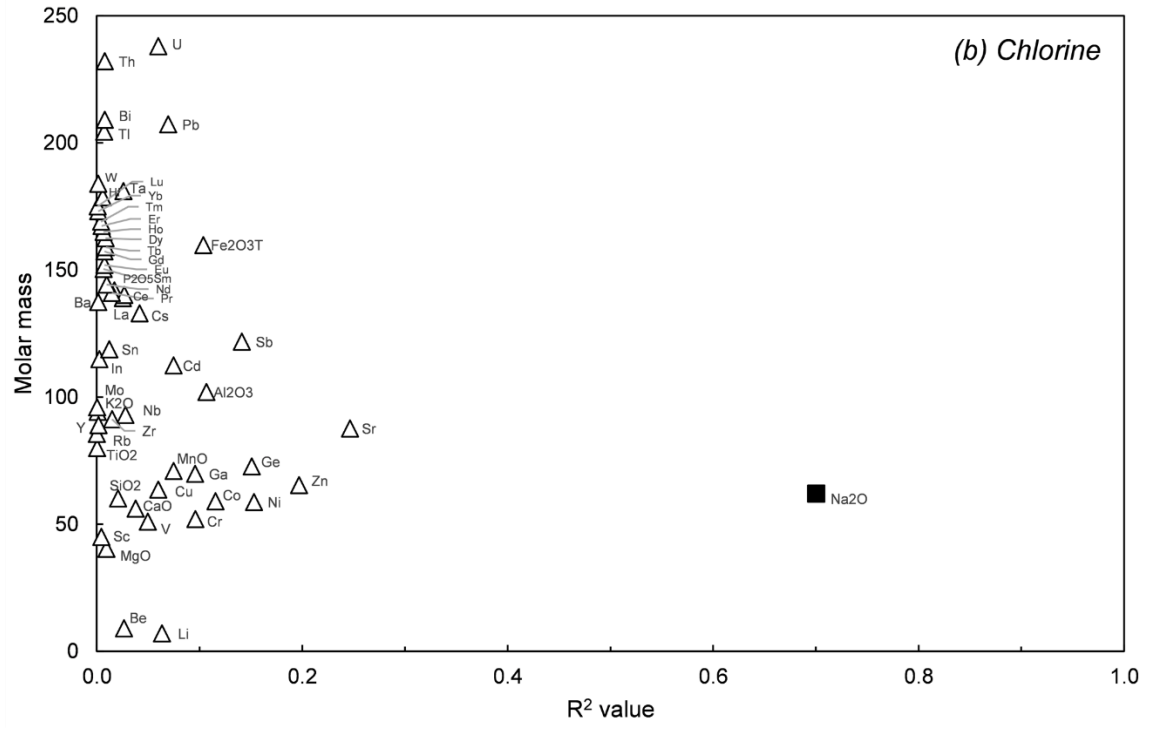

(Fig. S7. continued on the next page…)

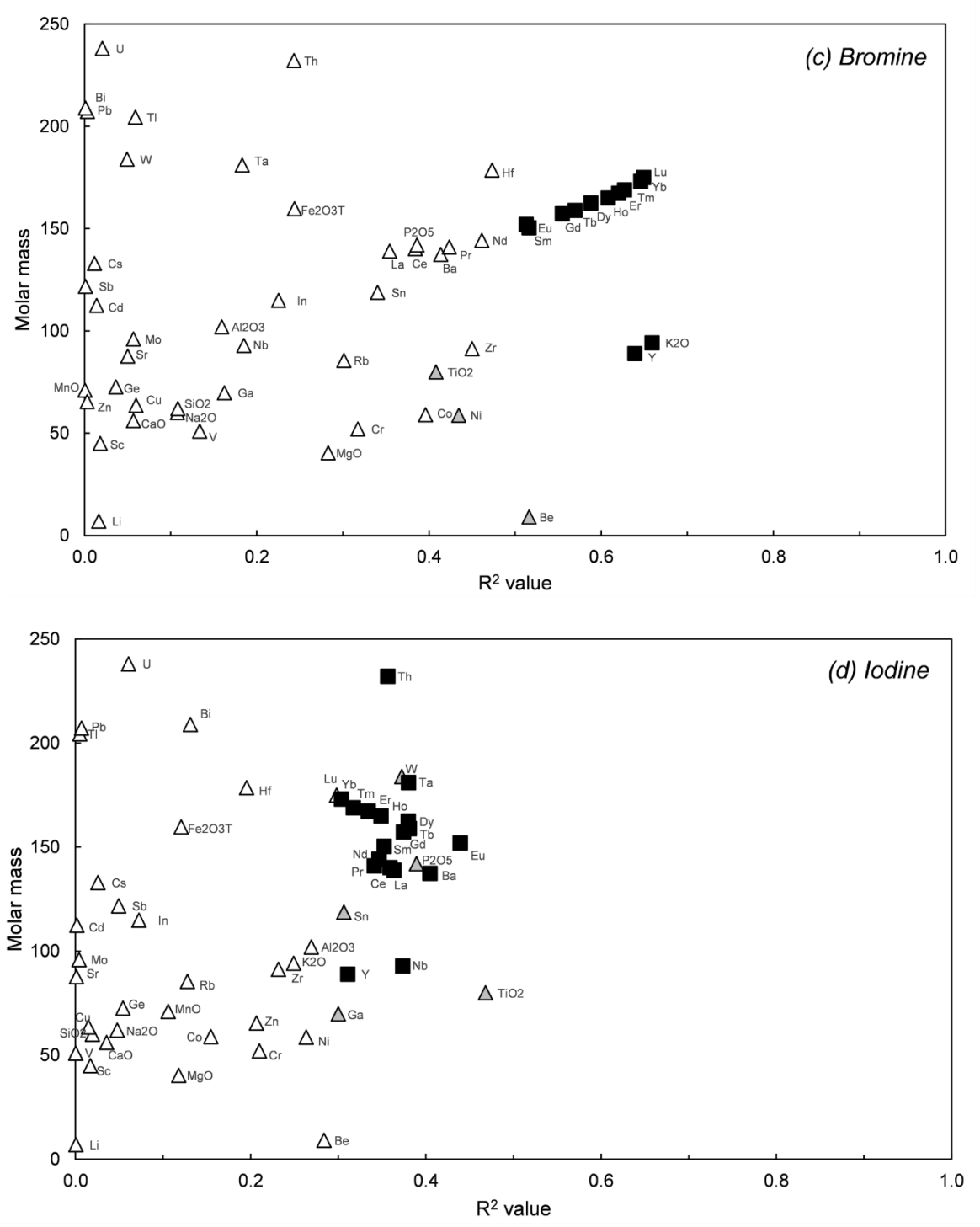

Fig. S7. The distributions of correlation coefficients (i.e., R^2 values) between each halogen element (F, Cl, Br, or I) and 55 other elements in the diamictites. Symbols are the same as in Fig. 8. Note that carbonate-rich diamictites are not included in the above calculations. In addition, the Mesoarchean diamictite composites for F, the Numees for Cl, and the Namibian samples for I are also excluded, due to their distinct halogen concentration(s) (see discussions in the text)

Appendix-3

Determining the uncertainties of estimated halogen concentrations of the UCC

(via the regression approach)

The regression approach has been widely used to determine trace element concentrations of the UCC (McLennan, 2001; Rudnick and Gao, 2003; Hu and Gao, 2008). However, it is often hard to assess the uncertainty of the regression line itself, which makes it challenging to place tight constraints on the uncertainty of the projected element concentration of interest. In order to better constrain the uncertainty of the projected concentration of the element of interest, the bootstrap method, a statistical resampling approach, is adopted in this study. For example, if there are 19 original diamictites used to calculate the regression line between F and La, 19 samples are first randomly selected from the original dataset (allowing samples to be repeatedly selected), and then the resampled 19 samples are used to establish the regression line and calculate a new estimate. The above process is repeated 1,000 times and 1,000 corresponding estimates of F will be obtained. Finally, the compilation of all the above estimates allows us to incorporate the uncertainties on the slopes and intercepts of the regression lines to the final results.

In addition, to take into account the uncertainties of the recommended concentrations of the 55 other elements of the average UCC (Rudnick and Gao, 2003) in our final results, we also perform a second resampling within the above process by choosing one value from 1,000 concentrations of each element in Gaussian distributions defined by the mean value and the standard deviations reported by Rudnick and Gao (2003). The selected concentration is later projected to the determined regression line to calculate the new UCC halogen estimate. As a result, the final mean values and the uncertainties reported in Table 3 and Fig. 8 incorporate the uncertainties from not only the regression

line itself (i.e., from slope and intercept, see above) but also the average concentrations of the UCC estimated by Rudnick and Gao (2003).

Appendix C

Halogen enrichment on the continental surface: a perspective from loess

– Supplementary Information

Samples and Analytical Methods

The 129 loess samples investigated in this study were collected from four continents: Europe (Germany and Switzerland), North America (United States), South America (Argentina), and Asia (Kazakhstan and China). The latitude and longitude of the loess sections, along with references to the original investigations of these units, are given in Table S-1 and plotted in Figure S-1. Data for major elements, rare earth elements (REEs), total organic carbon (TOC), and halogens are reported in this study.

Major Elements and REE Analyses

The samples were powdered in an agate mortar mill (RS200, Retsch, Germany) prior to analysis. Major element concentrations were determined by X-ray fluorescence (RIX2100, Japan) on fused glass disks at Northwest University in Xi'an, China. Reference materials BCR-2 (basalt, USGS) and GSR-3 (basalt, Chinese National Standard) indicate that precision and accuracy are better than 5 %. Rare earth elements were analysed by ICP-MS (Agilent 7900) after high-pressure acid digestion of samples in Teflon bombs at the State Key Laboratory of Geological Processes and Mineral Resources (GPMR), China University of Geosciences, Wuhan. About 50 mg of sample powder was weighed into a Teflon bomb, and then 1 ml of concentrated HNO_3 and 1 ml of concentrated HF were added. The sealed bomb was heated at 190 °C in the oven for 72 hours. After cooling, the solution was evaporated to dryness at ~120 °C. This was followed by adding 1 ml of concentrated HNO_3 and evaporating to dryness again. The resultant salt was re-dissolved by adding 1 ml of HNO_3, 1 ml of Milli-Q water (18.2 MΩ), and 1 ml of 1μg/ml In internal standard solution. The solution was then resealed and heated in the bomb at 190 °C for ~24 hours. The final solution was diluted to ~100 g with 2 % HNO_3 for ICP-MS analysis. Total procedure blanks are below detection limits. The results for reference materials (BCR-2, BHVO-2, AGV-2, and SCo-1) agree well with the recommended values, within 10 % uncertainties. Results for the reference materials are in Park et al. (2012).

Total Organic Carbon Analysis

Organic C measurements were conducted at the State Key Laboratory of Biogeology and Environmental Geology, China University of Geosciences, Wuhan. About 2 g of powdered sample was acidified with 50 % HCl to remove inorganic carbon from carbonates. The residue was rinsed with deionized water to neutralize pH, then centrifuged and dried for 48 hours, before being analysed using the 902 T C–S analyser (Beijing Wanliandaxinke Instruments Co. Ltd.). Based on multiple analyses of AR-4007 (total carbon: 7.62 %, Alpha Resources Inc.), AR-4017 (total carbon: 0.50 ± 0.03 %, Alpha Resources Inc.) and B2152 (total carbon: 1.30 ± 0.09 %, Elemental Microanalysis Ltd.), TOC data are reported with a precision better than ± 0.1 %.

Halogen Analyses and Leaching Experiment

Halogen concentrations of loess are obtained using two different methods: (1) F-Cl-Br analysis by combustion ion chromatography analysis (C-IC) conducted at Fachbereich Geowissenschaften, Universität Tübingen, and (2) Cl-Br-I analysis by NH_4HF_2 digestion and ICPMS analysis (N-ICPMS) conducted at State Key Laboratory of Geological Processes and Mineral Resources, China University of Geosciences, Wuhan. More detailed descriptions of these two methods can be found in Han et al. (2023). Although Cl and Br are both analysed in the above two methods, the measured Cl and Br content in loess by C-IC are often 25-50 % lower than those obtained by N-ICPMS, which is consistent with the results obtained by Han et al. (2023) on glacial diamictites (Fig. S-2). This discrepancy could result from incomplete halogen recovery by pyrohydrolysis (e.g., Marks et al., 2017; Kendrick et al., 2018a; Han et al., 2023). Therefore, we used the F data from C-IC and the Cl, Br, I data from N-ICPMS in this paper to investigate the behaviour of halogens in loess (Table S-1 and Fig. 1).

Halogen leaching experiments were performed on 14 loess samples from various localities (five from Germany, one from the United States, one from Kazakhstan, and seven from China) at State Key Laboratory of Geological Processes and Mineral Resources, China University of Geosciences, Wuhan. For each sample, ~150 mg of sample powder was first mixed with 5 ml Milli-Q water (18.2 MΩ), then sonicated for 5 minutes using ultrasound, and subsequently centrifuged for 7 minutes in a centrifuge. The solid residue was then separated and dried in an oven at 50ºC for 48 hours. Finally, the residual sample powders were dissolved and analysed for Cl-Br-I content using the above N-ICPMS method.

Supplementary Table

Table S-1 Major elements, total organic carbon (TOC), and rare earth elements of loess samples.

Table S-1 is available for download (.xlsx) from the online version of this article at http://doi.org/10.7185/geochemlet.2442.

Supplementary Figures

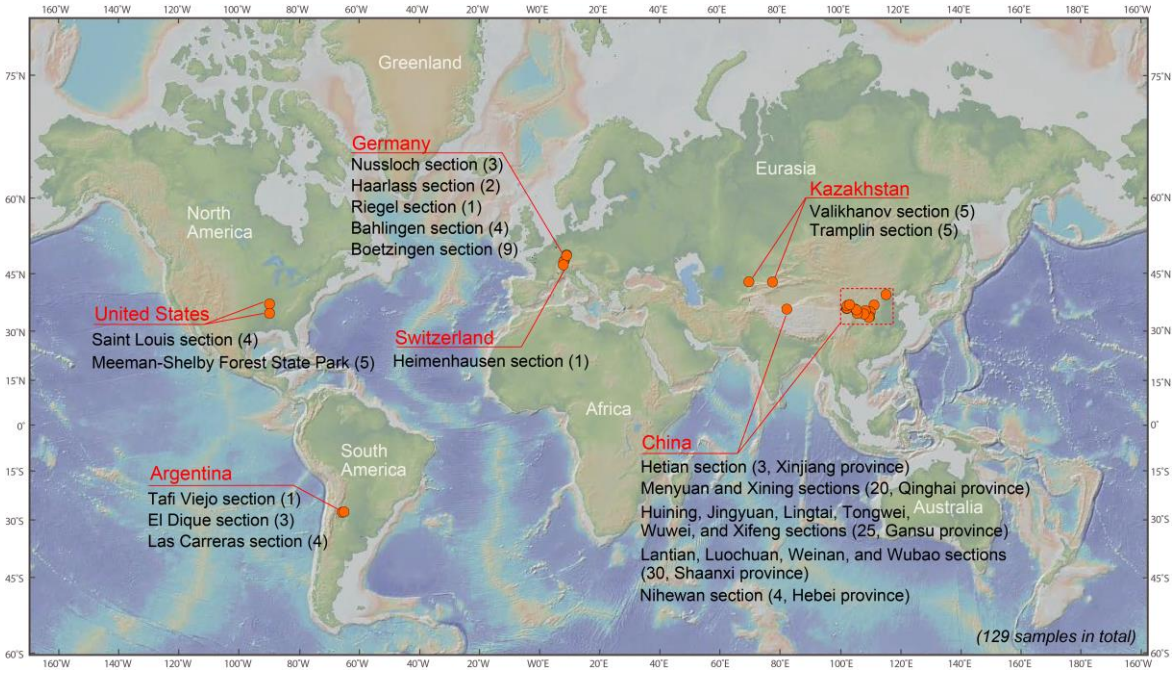

Figure S-1 Distribution of loess samples from this study. The number in parentheses indicates the quantity of samples analysed in each section.

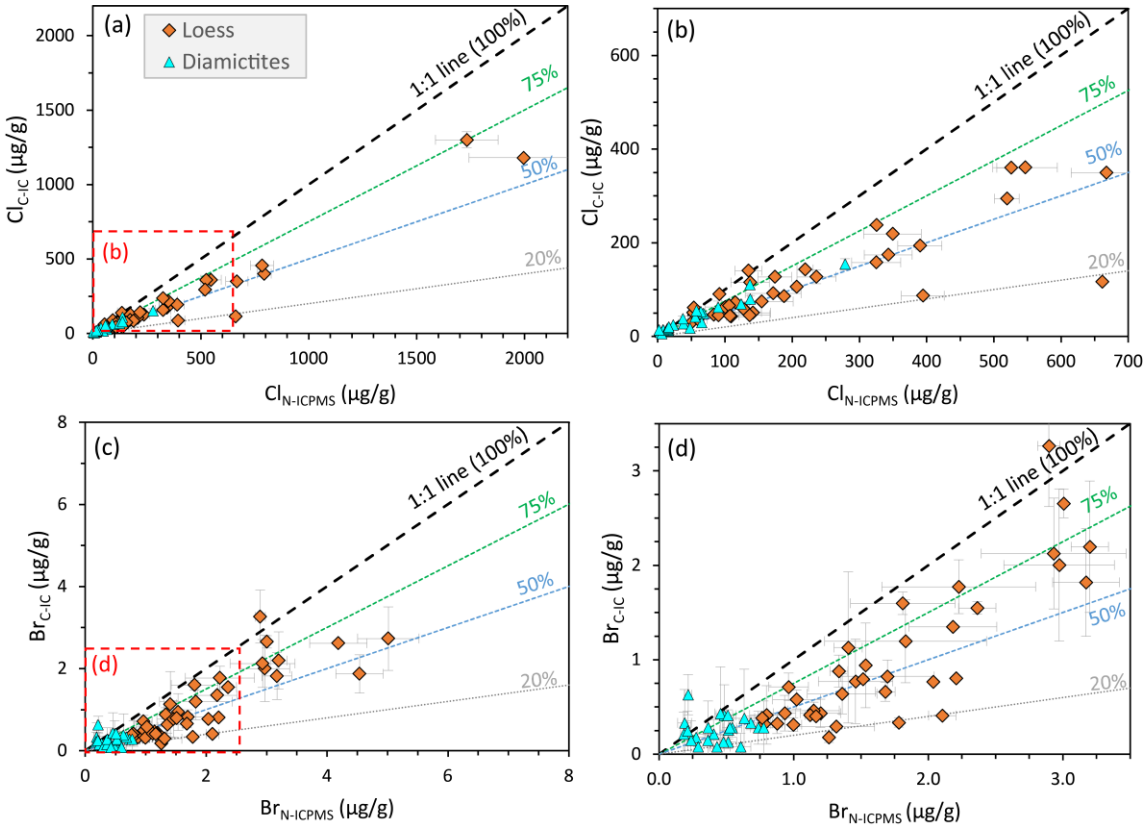

Figure S-2 Comparison of Cl **(a-b)** and Br **(c-d)** results for loess (this study) and glacial diamictite composites (Han et al., 2023) by C-IC and N-ICPMS, respectively. Error bars represent 1σ.

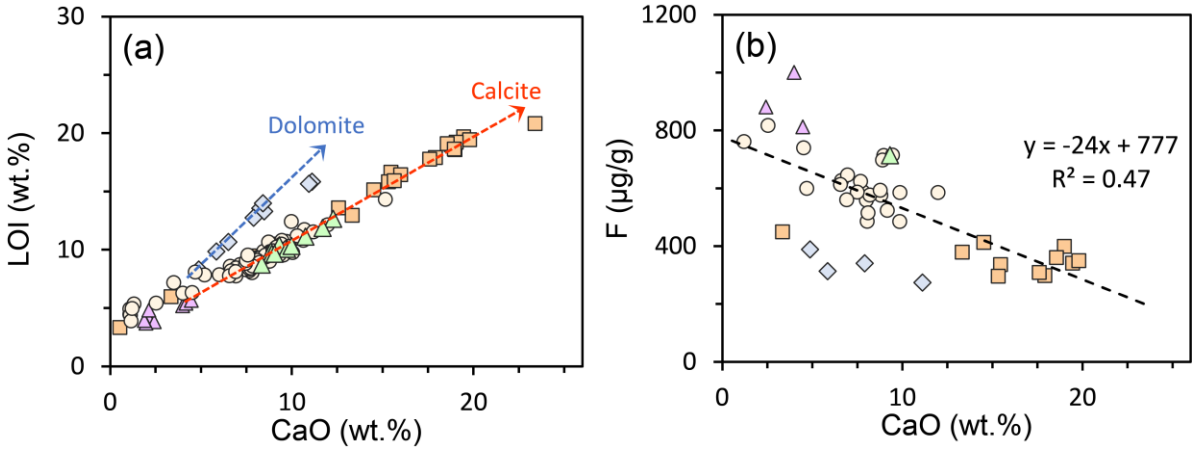

Figure S-3 **(a)** Loss of Ignition (LOI) of loess increases as the CaO content increases. The data follow the trends produced by having variable amounts of calcite (red-dashed line) and dolomite (blue dashed line) in the samples, suggesting that the CaO in loess is mainly controlled by carbonate. **(b)** Fluorine versus CaO content. There is a negative trend between F and CaO, likely due to the dilution of F content in loess samples by carbonate. Symbols as Fig. 2.

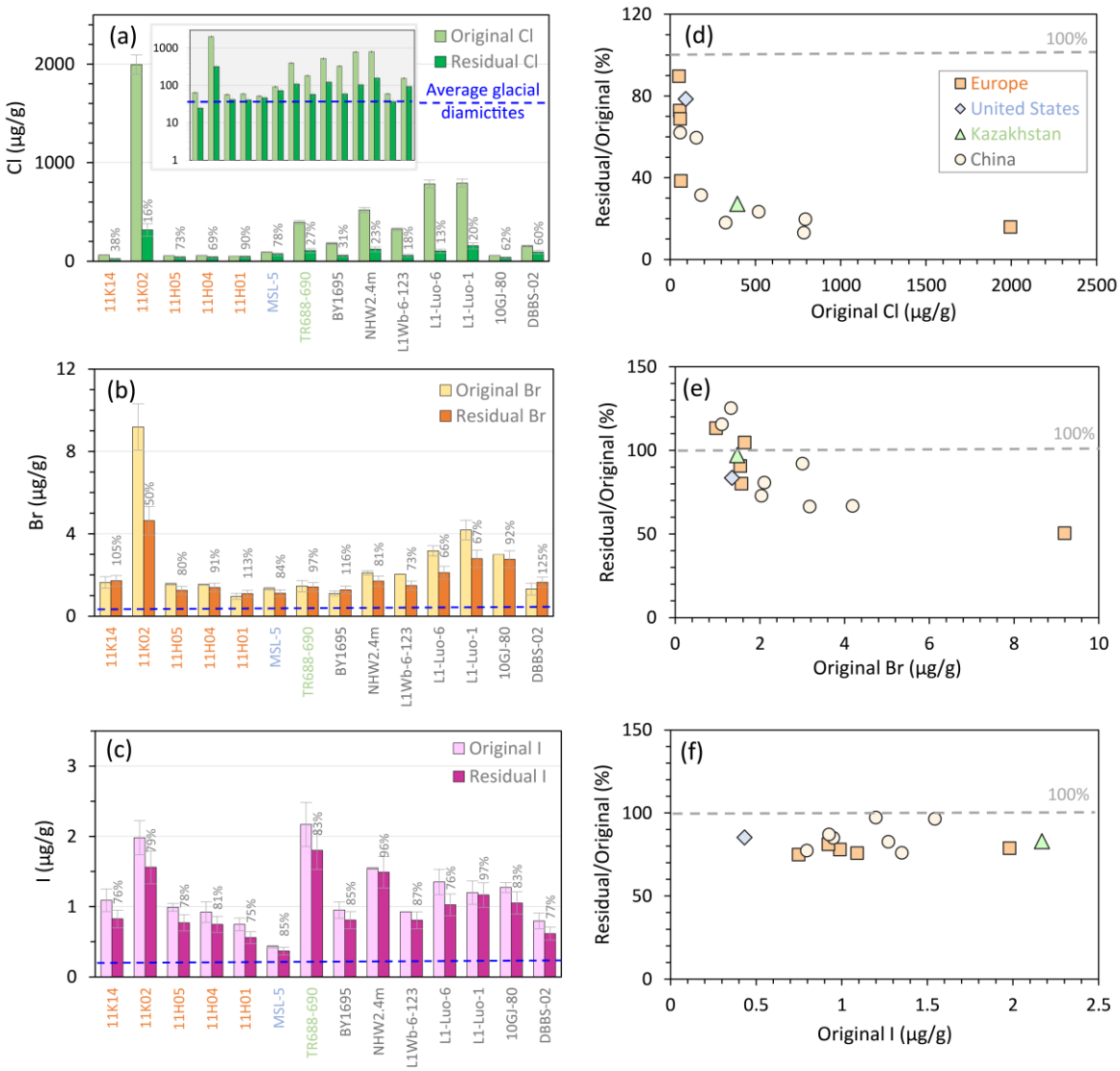

Figure S-4 Leaching experiments on loess samples for Cl, Br, and I. **(a-c)** show the Cl, Br, and I contents of the samples (on the x-axis) both before (original) and after (residual) leaching. The blue dashed lines represent the average Cl-Br-I content of glacial diamictites from Han et al. (2023). The inset figure in **(a)** is in log-scale. In **(d-f)**, the proportion of residual halogen components in the analysed loess samples (y-axis) is plotted against the original halogen concentrations (x-axis).

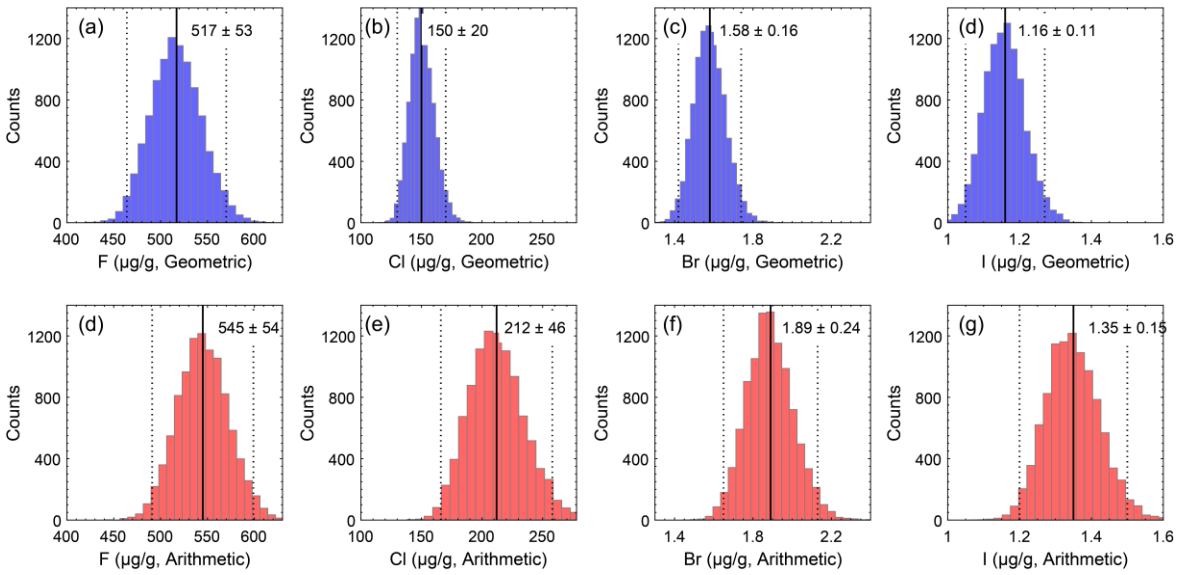

Figure S-5 Bootstrapped geometric **(a-d**, upper panel**)** and arithmetic **(d-g**, lower panel**)** means of loess F-Cl-Br-I data, which are computed using MATLAB, employing 10,000 trials. Each trial represents the geometric or arithmetic mean of a randomly resampled set of the loess data, with replacement allowed. The geometric/arithmetic means for the loess samples (Fig. 1) are determined by averaging the results of the 10,000 bootstrapped trials, shown as vertical black lines (2 standard errors indicated by black dashed lines). The arithmetic means consistently surpass the geometric means due to the skewed distribution of halogen concentrations in loess (Fig. 1).

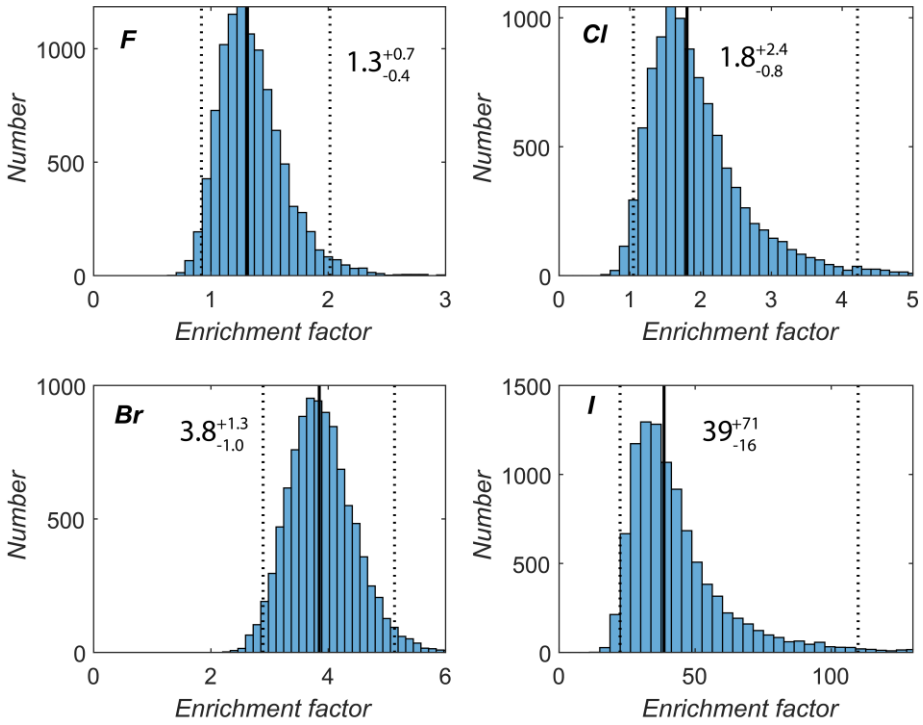

Figure S-6 Enrichment factor of halogens in loess relative to the estimates of the crystalline UCC (394 ± 67 µg/g F, 83 ± 24 µg/g Cl, 0.41 ± 0.04 µg/g Br, and 0.03 ± 0.01 µg/g I, with 2 standard deviations, from Han et al., 2023), calculated by bootstrapping, with 10,000 trials. Each trial represents the median of randomly sampled loess compared to a random composition of the crystalline UCC within its 2 standard deviations. The black line represents the median of the 10,000 bootstrapped trials, and the dashed lines are 95 % confidence interval.

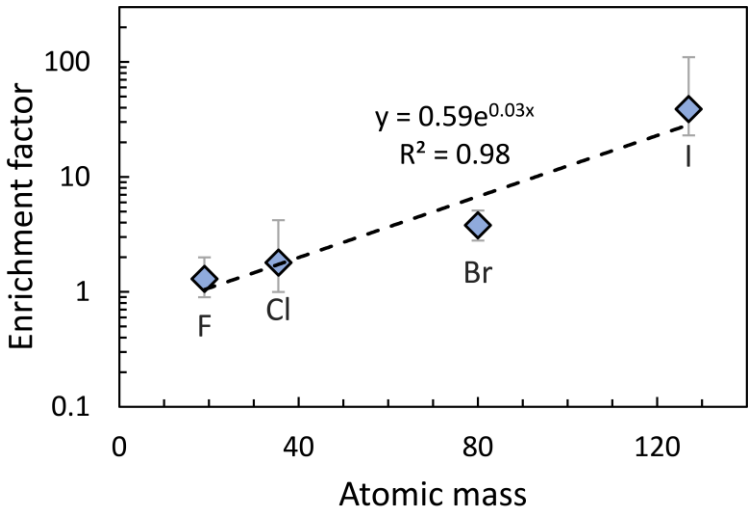

Figure S-7 The halogen enrichment factors in loess increase exponentially with their atomic masses. Error bars of halogen enrichment factors are at 95 % confidence level, see Figure S-6 for further details.

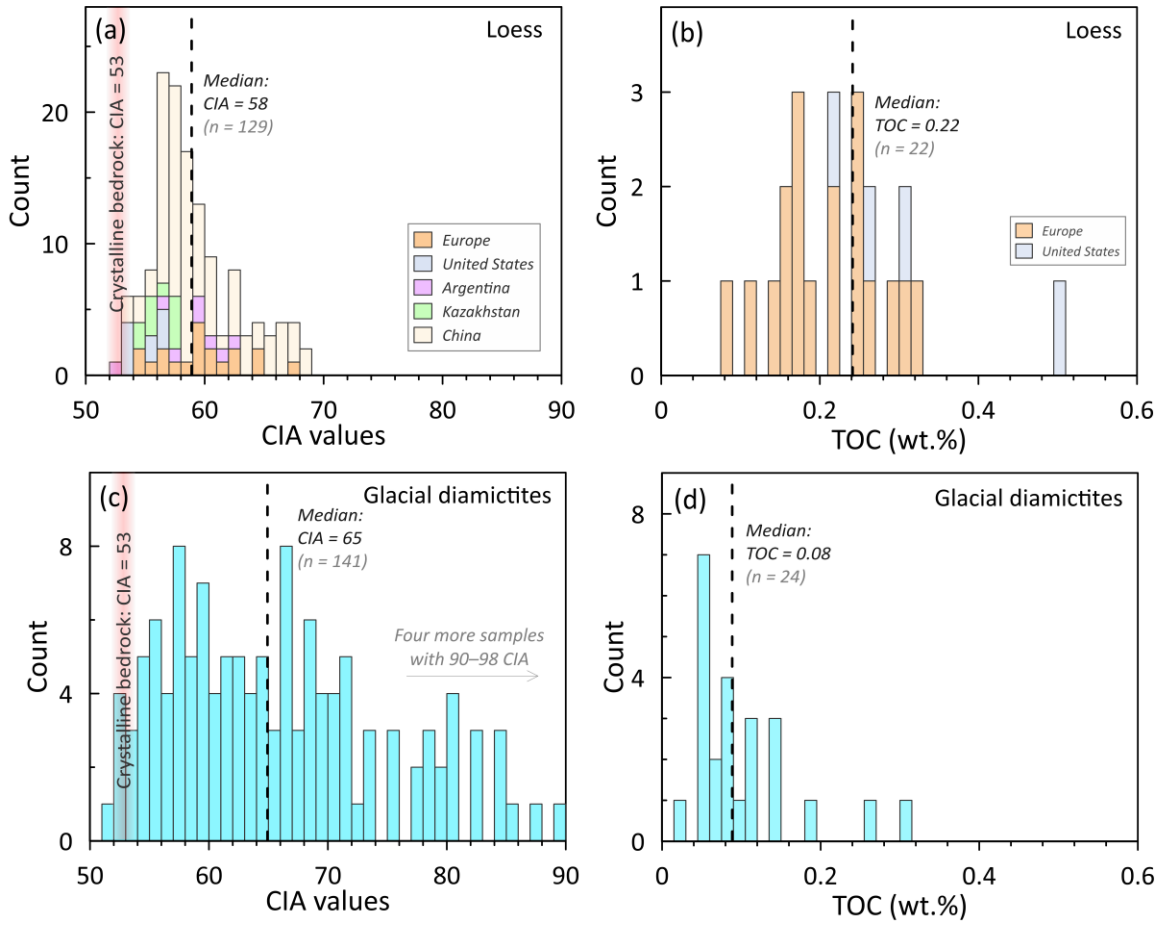

Figure S-8 Comparison of CIA value (chemical index of alteration, CIA = molar Al_2O_3 / (Al_2O_3 + CaO^* + K_2O + Na_2O, where CaO^* is corrected for carbonate and apatite (Nesbitt and Young, 1982) and the carbonate correction is based on the approach of McLennan (1993), **a** and **c)** and TOC results **(b** and **d)** for loess (this study) and glacial diamictite composites, respectively. The CIA values of glacial diamictites are from Gaschnig et al. (2016) for 141 individual glacial diamictite samples, and the TOC data are from Greaney et al. (2020) for 24 glacial diamictite composites. The dashed line in each plot represents the median value for each population, and loess samples generally have limited and lower CIA values but higher TOC than glacial diamictites.

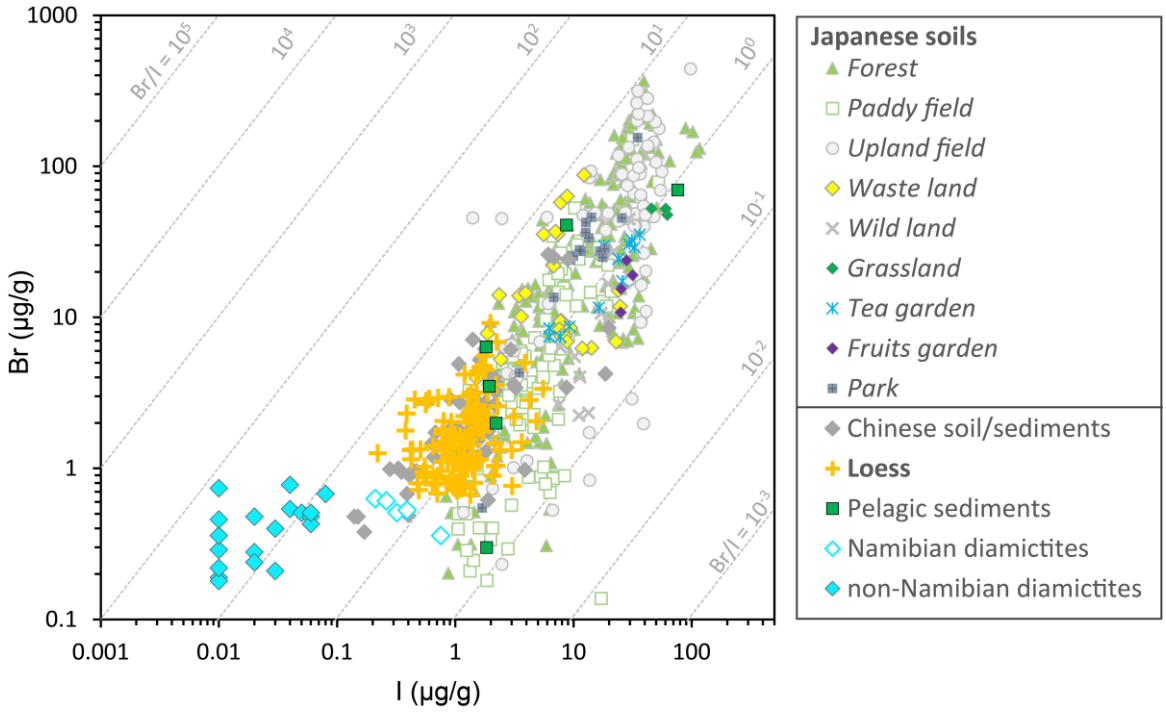

Figure S-9 Br versus I content of Japanese soils (Yamasaki et al., 2015), Chinese soils/sediments (He et al., 2018), loess (this study), pelagic sediments (John et al., 2011), and glacial diamictites (Han et al., 2023). Within the glacial diamictite composites, five samples from Namibia exhibit notably elevated I content and relatively low Br/I ratios (the elevated I content of the Namibian samples is likely due to the presence of carbonate and abundant terrigenous sedimentary rocks in their provenance, see discussion in Han et al. (2023)).

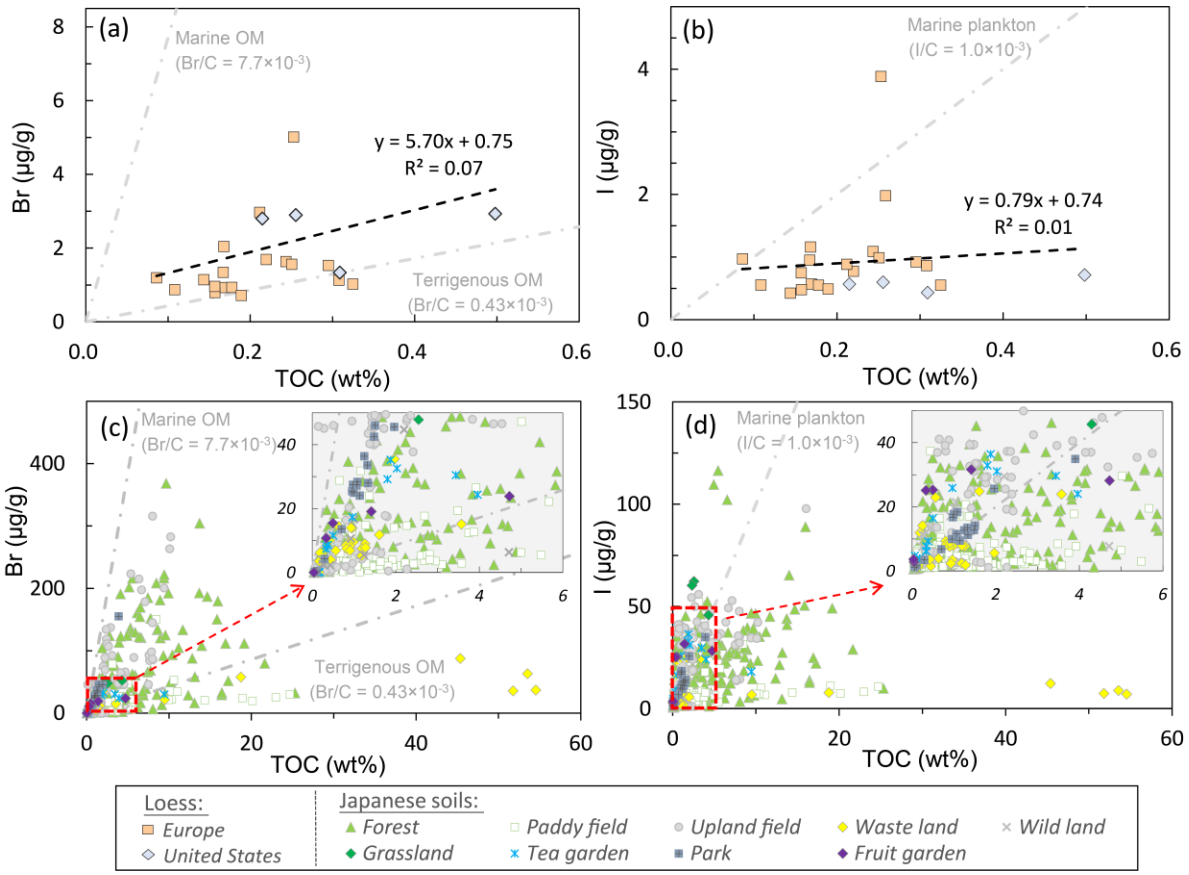

Figure S-10 Br and I versus TOC content of loess samples **(a-b**, this study**)** and Japanese soils (c-d, Yamasaki et al., 2015). In **(a)** and **(b)**, the correlation of Br and I with TOC of the analysed loess samples is indicated by the black dashed line, both showing very poor correlation (R^2 value ≤ 0.1). Br/C ratios for organic matter (OM) of terrigenous and marine sources ($0.43*10^{-3}$ and $7.7*10^{-3}$, respectively, from Mayer et al. (2007)) are plotted as grey dash-dotted lines in **(a)** and **(c)** for comparison. In b and d, the grey dash-dotted line represents the I/C ratio ($1.0*10^{-3}$) of typical marine plankton (Elderfield and Truesdale, 1980).

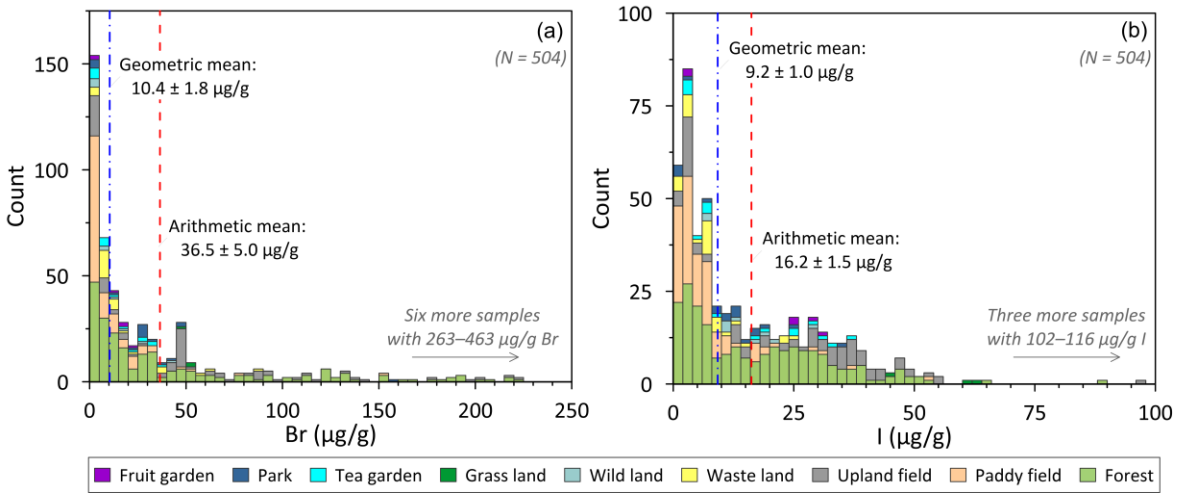

Figure S-11 Bromine and I content in various types of Japanese soil samples (Yamasaki et al., 2015). The blue dash-dotted and the red dashed lines represent the geometric and arithmetic means of the dataset, respectively, along with 2 standard errors. Their calculations are the same as those for the loess data, see Figure S-5 for further details.

Appendix D

Halogen Behavior During High-Grade Metamorphism and Partial Melting in the Deep Continental Crust (Ivrea Zone, NW Italy)

– Supplementary Information

Table S1. Halogen concentration analyses from different labs.

Samples	Lithology	Metamorphic grade	Pyrohydrolysis --- Universität Tübingen*						N-ICPMS --- China University of Geosciences, Wuhan#						Pyrohydrolysis --- UT Austin#			
			F ppm	1σ	Cl ppm	1σ	Br ppm	1σ	Cl ppm	1σ	Br ppm	1σ	I ppm	1σ	F ppm	1σ	Cl ppm	1σ
P1	Metapelite	Amphibolite facies	643	128	54	1.7	-	-	57	11	0.76	0.15	0.10	0.02	-	-	-	-
P2	Metapelite	Amphibolite facies	602	20	21	1.8	-	-	39	8	0.92	0.18	0.09	0.02	-	-	-	-
P3	Metapelite	Amphibolite facies	515	23	46	7.4	-	-	57	1	0.61	0.04	0.02	0.01	510	102	51	10
P4	Metapelite	Amphibolite facies	1116	6	23	0.7	-	-	39	1	0.81	0.03	0.22	0.01	-	-	-	-
P5	Metapelite	Amphibolite facies	945	7	36	2.1	-	-	51	2	0.78	0.06	0.02	0.01	-	-	-	-
P6	Metapelite	Transition Zone	860	17	67	0.7	-	-	69	8	0.52	0.00	0.03	0.003	869	174	102	20
P7	Metapelite	Transition Zone	1145	41	53	0.0	-	-	86	5	0.63	0.06	0.02	0.001	1163	233	103	21
P8	Metapelite	Granulite facies	301	87	161	0.1	-	-	140	28	0.74	0.15	0.02	0.004	309	62	220	44
P9	Metapelite	Granulite facies	650	164	44	0.8	-	-	58	12	0.51	0.10	0.01	0.003	607	121	102	20
P10	Metapelite	Granulite facies	341	84	35	3.3	-	-	63	5	0.79	0.03	0.02	0.001	331	66	61	12
P11	Metapelite	Granulite facies	337	68	57	4.0	0.70	-	68	4	0.12	0.06	0.02	0.003	341	68	77	15
P12	Metapelite	Granulite facies	104	12	68	2.4	-	-	109	22	0.86	0.17	0.02	0.005	101	14	181	1
B1	Metabasite	Amphibolite facies	----------Pending----------						----------Pending----------						654	131	244	49
B2	Metabasite	Amphibolite facies	----------Pending----------						----------Pending----------						74	15	62	12
B3	Metabasite	Granulite facies	197	44	80	3.5	-	-	95	5	0.21	0.07	0.04	0.01	280	56	109	22
B4	Metabasite	Granulite facies	343	39	180	10.2	0.75	0.21	184	9	0.44	0.06	0.16	0.01	351	11	203	2
B5	Metabasite	Granulite facies	206	16	261	5.8	-	-	254	18	0.49	0.21	0.03	0.001	185	37	325	65
L1	Leucosome (MP)	Amphibolite facies	210	21	59	1.6	1.10	-	78	2	0.74	0.01	0.03	0.02	-	-	-	-
L2	Leucosome (MP)	Amphibolite facies	127	0	38	1.9	-	-	57	11	0.38	0.08	0.12	0.02	122	24	82	16
L3	Leucosome (MP)	Transition Zone	15	7	43	8.2	-	-	94	19	1.60	0.32	0.01	0.002	16	3	83	17
L4	Leucosome (MP)	Transition Zone	46	13	75	7.0	-	-	157	2	2.35	0.02	0.01	0.000	48	10	155	31
L5	Leucosome (MP)	Granulite facies	42	4	122	5.4	0.55	0.07	130	1	2.02	0.01	0.17	0.03	-	-	-	-
L7	Leucosome (MP)	Granulite facies	1478	170	101	8.1	-	-	147	29	1.02	0.20	0.03	0.01	-	-	-	-
L8	Leucosome (MP)	Granulite facies	11	2	63	3.7	-	-	117	4	1.43	0.00	0.10	0.01	4	0.8	177	35
L9	Leucosome (MB)	Granulite facies	----------Pending----------						159	32	0.88	0.18	0.04	0.01	-	-	-	-
L10	Leucosome (MB)	Granulite facies	----------Pending----------						221	44	0.81	0.16	0.10	0.02	-	-	-	-

[*] For the pyrohydrolysis analyses conducted at the Universität Tübingen, each sample was analyzed 2-4 times, and the uncertainty represents the calculated one standard deviation from repeated measurements.

[#] For the analyses from the University of Texas at Austin and the China University of Geosciences, Wuhan, the uncertainty represents one standard deviation of duplicate analysis, if available; otherwise, it is estimated as 20% of the measured concentrations (values underlined).

Note that samples B1, B2, L9, and L10 are still awaiting the results from the Tübingen and Wuhan labs.